Physical properties of brightest cluster galaxies and their evolution with redshift

Aline Chu

SORBONNE UNIVERSITÉ

THÈSE DE DOCTORAT

ÉCOLE DOCTORALE N°127
ASTRONOMIE ET ASTROPHYSIQUE D'ILE-DE-FRANCE

Réalisée au sein de

Institut d'Astrophysique de Paris - CNRS

Evolution des propriétés physiques des galaxies centrales les plus brillantes des amas de galaxies

---

Aline Chu

Directrices de thèse:

Dr. Florence DURRET (Institut d'Astrophysique de Paris)
&
Dr. Isabel MÁRQUEZ (Instituto de Astrofísica de Andalucía)

Présentée et soutenue le

7 Décembre, 2022

Devant un jury composé de

Prof. Françoise Combes	Observatoire de Paris	Présidente du jury
Prof. Michael West	Lowell Observatory	Rapporteur
Dr. Rémi Cabanac	Institut de Recherche en Astrophysique et Planétologie	Rapporteur
Dr. Nina Hatch	University of Nottingham	Examinatrice
Dr. Stéphane Arnouts	Laboratoire d'Astrophysique de Marseille	Examinateur

Abstract

Galaxy clusters are the largest gravitationally bound structures of the Universe. At the center of these clusters generally reside the most massive galaxies observable today. These galaxies are refered to as Brightest Cluster Galaxies (BCGs), and are the final products of 10 Gyrs of consecutive galactic mergers in the densest regions of the cosmic web. In this thesis, we focus our attention on these very peculiar objects, excellent tracers of cluster formation, and ideal to study the impact of environmental processes on galactic formation. The characterization of the physical properties of BCGs is important to obtain better knowledge of these galaxies. Previous studies have found contradicting results concerning their growth: while some studies find that they are still evolving today, others find that they may have stopped growing a long time ago. In order to put things in perspective, I present here new catalogues of BCGs which have allowed me to conduct a deeper analysis of the formation of BCGs, thanks to the bigger statistics we reached.

My work on the characterization of the physical properties of BCGs has shown a lack of evolution of their sizes and luminosities in the last 10 Gyrs, hinting at an earlier formation epoch and absence of recent significant growth. However, their structures may have changed over time, as hinted by the observation of an inner component at recent epoch that can not be detected at earlier times. This may only be due to observational biases, but deeper surveys such as the ones expected from the Euclid or the Rubin Observatory's Legacy Survey of Space and Time (LSST) missions should enable us to confirm this morphological evolution. BCGs, because of their central locations, are more likely to undergo mergers in their lifetimes, which leave marks on their shapes. As inferred from their alignments, we confirm the special bond between BCGs and their host clusters.

I also offer new tools for automated detections of BCGs on optical images. These may be applied to large surveys using cluster coordinates available in existing or future catalogues of clusters.

In this manuscript, I also tackle the subject of fossil groups (FGs). We increase the number of known FGs and are carrying on observations in order to confirm the fossil nature of candidate FGs. We find that Brightest Group Galaxies (BGGs) of FGs show an evolution which may be more similar to that of BCGs of clusters than that of BGGs of non-FGs, i.e. normal groups of galaxies, as inferred from the Kormendy relation. However, the stellar evolution of FGs and non-FGs may still be comparable.

Zooming in the central regions of BCGs, we look at the supermassive black holes (SMBHs) harbored at the center of clusters. From the Illustris TNG-300 cosmological simulation and using orbital integration methods, we show that radial mergers of galaxies can kick away the black hole from its central position to distances of a few parsecs to hundreds of kiloparsecs. I discuss the consequences of such an offset on the growth of SMBHs and the impact on the dynamics reigning in the central regions of BCGs and clusters.

The observations and modeling of these large samples of BCGs and BGGs have given us insight on the formation and evolution of clusters and groups at various scales, from that of a large cluster down to the central supermassive black hole. Future instruments and surveys such as Euclid or LSST will provide us with samples of tens of thousands of clusters, and the tools developed here should be useful to analyse such large samples, to derive with a better precision the epoch of formation of clusters and groups.

Abstract

Les amas de galaxies sont les structures gravitationnellement liées les plus grandes de l'Univers. En général, au centre de ces amas, résident les galaxies les plus massives observées aujourd'hui, appelées les galaxies les plus brillantes d'amas (BCG, Brightest Cluster Galaxy). Elles sont le produit de 10 milliards d'années de fusions successives de galaxies dans les régions les plus denses de la toile cosmique. Dans cette thèse, nous nous focalisons sur ces objets très spéciaux, excellents traceurs de la formation de leur amas, et cibles idéales pour étudier l'impact que l'environnement peut avoir sur la formation des galaxies. La caractérisation de ces galaxies est importante pour mieux comprendre ces objets. Plusieurs auteurs trouvent des résultats contradictoires concernant leur évolution: certaines études trouvent que les BCGs évoluent encore aujourd'hui, d'autres pensent qu'elles auraient arrêté d'évoluer il y a bien longtemps. Afin de choisir entre ces deux hypothèses, je présente ici de nouveaux catalogues de BCGs dont le grand nombre d'objets permettra d'effectuer des analyses encore plus profondes sur la formation des BCGs.

Mon travail sur la caractérisation des propriétés physiques des BCGs montre une absence d'évolution de leur taille et de leur luminosité depuis 10 milliards d'années, ce qui suggère une époque de formation qui aurait eu lieu tôt dans l'histoire de l'Univers. Cependant, leur structure aurait pu changer au cours du temps, ce que suggère l'observation d'une deuxième composante dans les galaxies les plus proches de nous. Des relevés d'images plus profonds comme ceux prévus avec les futures missions Euclid et Legacy Survey of Space and Time (LSST) devraient nous permettre de vérifier et confirmer s'il s'agit en effet d'une évolution ou d'un biais observationnel. Les BCGs, grâce à leur localisation centrale, sont plus enclines à subir des fusions durant leur vie, qui les alignent avec leur amas, montrant un lien très particulier entre les deux structures.

Je décris également de nouveaux codes pour la détection automatique des BCGs sur des images optiques, qui peuvent être appliqués sur de grands relevés à partir de catalogues de galaxies.

Dans ce manuscrit, j'aborde aussi le sujet des groupes fossiles (GFs). Nous augmentons le nombre de GFs connus et avons fait des demandes d'observations afin de confirmer la nature «fossile» de candidats GFs. Nous montrons que les galaxies les plus brillantes (Brightest Group Galaxy, BGG) des GFs ont des évolutions qui semblent plus similaires à l'évolution des BCGs d'amas plutôt qu'à l'évolution des BGGs de non-GFs, comme indiqué par la relation de Kormendy des GFs qui se superpose à celle des BCGs d'amas. Les populations stellaires des BGGs de GFs, cependant, ne diffèrent pas beaucoup de celles des BGGs de non GFs.

En zoomant dans la région centrale des BCGs, je m'intéresse aussi au trou noir supermassif (TNSM) qui vit au centre des amas. Grâce aux informations données dans la simulation cosmologique Illustris TNG-300, et avec des méthodes d'intégration d'orbites, nous montrons que des fusions radiales de galaxies peuvent éjecter le trou noir de sa position centrale à des distances allant jusqu'à des centaines de kiloparsecs. Nous discutons des conséquences d'un tel décentrage sur le grossissement des TNSMs et de l'impact que cela peut avoir sur la dynamique qui règne dans les régions centrales des BCGs et des amas.

L'observation et la modélisation de tels échantillons de BCGs et BGGs nous donnent un aperçu de la formation et de l'évolution des amas et des groupes à différentes échelles, depuis les amas de galaxies jusqu'au TNSM. De futurs instruments tels que Euclid et LSST vont nous faire découvrir des dizaines de milliers d'amas, et les outils développés et décrits dans ce manuscrit devraient nous aider à analyser ces grands échantillons, afin de mieux déterminer l'époque de formation des amas et des groupes de galaxies.

Acknowledgements

I would like to start these aknowledgements with these words that someone told me recently, and that resonated very deeply with me:

"A thesis is like a Psyduck that has his head squeezed: it squeezes and squeezes more and more, until all its powers awaken."

Dr. J. Froustey

I have to say that, although quite mystical and intriguing, this statement is right. As more and more knowledge gets put into your head, papers get written and the final move, *Doctor*, gets unlocked. To squeeze Psyduck's head though (i.e. *my* head), many techniques were used and many trainers participated in this three-year long game. And I would like to thank each of them.

First, the jury, or the *Elite 4* and its *Champion*[1], for accepting to hold this position and be part of my adventure, and of course, for giving me the title of Doctor (or *League Champion*). All these discussions we had were very fruitful and insightful, and got me very excited as to what research will bring in the following years. I would also like to thank all the other researchers and engineers I met during these three years. In particular, Valérie de Lapparent, who is in fact the one who got me fascinated with galaxies of all forms and shapes; but also Fréderic Daigne and Patrick Boissé, who have supported me since my Masters' and even before; Christophe Adami, who has been a great tutor throughout my whole thesis and particularly during our observations at the OHP and, of course, thank you for the lemons; I will not forget Patrick Tisserand who offered me unexpected observation time with an Australian telescope between two conversations during our tutoring at Sorbonne Université; the other Patrick (Hudelot), for all these bouldering sessions and for going through the trouble to summarize a one-week long Euclid course into a one hour class; and also many many others who have made all this time at IAP (or elsewhere) extremely nice and pleasant.

Of course, let's not forget about the two most important persons of this thesis, the two that have supported me through all the hardships and encouraged me to go further and beyond without ever putting pressure on me, and who always pushed me to pursue the research I wanted to do: my scientific grandmother and *mi tìa cientìfica*, my two *Professor Oak*, Florence and Isabel. Thank you - and *gracias* - for everything you have done during this thesis. You have taught me a lot and always made time to answer my questions and discuss about everything and nothing. You two have always been present, attentive, and supportive, and I can say that I would have definitely not gone this far without you. Not only professionally but also personally, the time I have spent with you has been nothing short of amazing. All these zoom meetings we had, the many concerts you invited me to, the incredible trip to Granada, the chocolate tarts, and so many others, are all memories that I cherish fondly. From this scientific family, I also want to thank the *brothers*,

[1] I am sorry for all the Pokémon analogies, but knowing my never ending passion for it, Dr. Froustey got me to do it

Florian and Amael, who have been extremely helpful and did not hesitate to make time for me when needed.

I know they have been looking for it, and it's here: to all my fellow IAP trainers, a *huge* thank you ! You have made this adventure fun, exciting, and weird. Our thesis was marked by some very difficult times[2], and I (along with others, I'm sure) was particularly badly affected by it. Meeting you everyday at the lab was the escape I needed, and the push that got me to work hard again. You have become, not only some random trainers that I may have encountered during my adventure, but genuine friends that I hope I will stay in contact with for a long time still. I will never forget the movie nights, restaurants, bars, games, nerf wars, basketball, hikes, bouldering (and my broken ankle)... and all the other stuff that we did, without forgetting all the drama too, of course. Because I know you and know you want your name here: to office and brunch-mate Virginia, the other office-mate Pupu, Frère Bolbol and his cats, princesse bébou Julien, my Burger King associate Warren, pretty boy Marko Polo, and also the heart king Mike, bichette Emilie, Simonono and Valentinana, Axel (please stop putting your fingers in my drinks), banana boy Louis, Amaury, Nai (IT'S CORN), Louise, Simon, Alexandre, Lukas, Quentin, and all the others (I'm sorry, you guys are too many, I can't); Thank you to all of you ! And to the original Psyduck and bébou, the reason why Psyducks are drawn on all white and blackboards in this lab, the patient zero of the *goutte* disease, thank you to Clément who has been my rock for the most part of my thesis. You crack the best jokes, please don't change.

Et enfin, j'aimerais remercier ma famille: en particuler mon frère, mon beau-père, ma grand-mère, et surtout, ma mère. Ces dernières années n'ont pas étées faciles, avec beaucoup de rebondissements, des moments qui n'ont pas étés toujours joyeux... Malgré tout, ma mère m'a toujours mise en priorité, a toujours fait en sorte que je ne manque de rien, et a toujours cru en moi jusque la fin. Ce titre de Docteur, je le dois en grande partie à elle et à tous ses encouragements. Je l'ai dis et redis: merci du fond du coeur.

[2]Yes, I'm talking about the C++.

Contents

List of Figures

List of Abbreviations

AGN	Active Galactic Nucleus
BCG	Brightest Cluster Galaxy
BGG	Brightest Group Galaxy
BH	Black Hole
CFHTLS	Canada-France-Hawaii Telescope Legacy Survey
CFIS	Canada France Imaging Survey
CHEF	Chebyshev-Fourier Function
CMB	Cosmic Microwave Background
DESI	Dark Energy Spectroscopic Instrument
DM	Dark Matter
ESA	European Space Agency
FG	Fossil Group
FP	First Progenitor
HLA	Hubble Legacy Archive
HST	Hubble Space Telescope
ICL	Intra Cluster Light
IFU	Integral Field Unit
IMF	Initial Mass Function
JWST	James Webb Space Telescope
LSB	Low Surface Brightness
LSST	Legacy Survey of Space and Time
MUSE	Multi Unit Spectroscopic Explorer
SDSS	Sloan Digital Sky Survey
SED	Spectral Energy Distribution
SFR	Star Formation Rate
S/N	Signal to Noise ratio
SMBH	SuperMassive Black Hole
SZ	Sunyaev-Zel'dovich
UNIONS	Ultraviolet Near Infrared Optical Northern Survey
VLT	Very Large Telescope
ΛCDM	Lambda - Cold Dark Matter

Color image of the galaxy cluster SMACS 0723 obtained by the James Webb Space Telescope.
Credit: NASA, ESA, CSA, and STScI

Chapter 1

Introduction

From the concentration of small local fluctuations in the primordial field of the Universe, to stars and galaxies, the objects which constitute our Universe were formed by assembling small elements of matter together to form bigger and bigger objects, which in turn merge to create even bigger entities. This is the hierarchical evolution scenario of the Lambda Cold Dark Matter (ΛCDM) cosmology model that is invoked to explain the formation of structures such as galaxy clusters that we observe today.

Galaxy clusters are one of the largest and most massive structures known today (after superclusters of galaxies which are structures of several clusters gravitationally bound together). As so, they are also among the latest structures to assemble, and are believed to have formed from protoclusters, their progenitors, more than 10 Gyrs ago. Clusters are extended structures of about 1 to 2 Mpc, with a mass ranging from 10^{13} $M_{\odot}$ to 10^{15} $M_{\odot}$. They are made of hundreds to thousands of galaxies, and are filled with hot gas (10^{6} - 10^{8} K), bound by gravity. Smaller similar structures, which host less than a hundred galaxies, are referred to as groups of galaxies.

Clusters are located at the intersection of filaments in the cosmic web. The cosmic web is a complex structure which describes the tri-dimensional matter distribution in the Universe. The Universe is mostly empty, or is characterized by very low density regions called voids. Sheets, also referred to as the "walls" of the cosmic web, are 2D structures which surround these voids. Filaments are 1D structures, the starting and ending points of which are located in the sheets, and they connect several clusters i.e. the very dense regions of the Universe identified as the knots in the cosmic web. Filaments are composed of mostly dark energy and dark matter, and also of gas and galaxies which end up falling into clusters. As a result, the cluster grows by constantly accreting matter, and by merging with other smaller groups or clusters that fall into its gravitational potential.

Eventually, all this ordinary matter (baryons) ends up at the bottom of the cluster potential well which is commonly at the center of the cluster. As more and more matter sinks to the central region of the cluster, a supermassive galaxy forms as it accretes all this material. Ultimately, it very often ends up becoming the most massive and the brightest galaxy of the cluster. This galaxy is referred to as the Brightest Cluster Galaxy (BCG hereafter).

BCGs are exceptional objects in the Universe. Not only are they the most massive galaxies that can be observed today, but their properties can teach us to a great extent how the Universe has evolved, and more specifically, how galaxies have formed. BCGs, similarly to their host clusters, grow by accreting matter and merging with other smaller systems through their lives. Their peculiar location makes them particularly interesting objects to study. Indeed, galaxy clusters are very dense regions in the Universe, in which hundreds to thousands of galaxies are trapped in a

volume of a few Mpc^3. BCGs tend to lie very close to the center of the cluster where the number of galaxies is even greater. This is not by chance: as galaxies fall to the bottom of the cluster potential well, they are accreted by the central galaxy, which as a result becomes more massive. The central location of BCGs favors their encounters with other galaxies, and thus, their growth. Hence, BCGs are peculiar objects which were formed in particularly dense environments, and are the results of billions of years of galaxy and cluster mergers that shaped them. BCGs reflect the dynamical processes that govern the formation of their host cluster. Retracing the history of BCGs can enable us to retrace the history of their clusters, as each interaction that happened throughout their lives left an imprint on the central galaxy. As the most massive galaxies that can be found in the sky, and because of their very particular environment, they are also very good probes to test cosmological models and better constrain the parameters defined to explain how the Universe formed and evolved.

My research work at the Institut d'Astrophysique de Paris focuses on these exceptionally bright and massive galaxies, BCGs. Using observations, as well as simulations, I have tried to characterize the properties of BCGs to better understand how these galaxies formed and evolved with time.

This chapter introduces notions that are important for the comprehension of this manuscript. We refer the reader to *From Messier to Abell: 200 years of science with galaxy clusters* by Biviano (2000) for an extensive review on the history of galaxy clusters, *Formation of galaxy clusters* by Kravtsov and Borgani (2012) for a detailed review of our current understanding on galaxy cluster formation, and finally *Extragalactic Astronomy and Cosmology - an Introduction* by Peter Schneider for a very thorough course focused on extragalactic astronomy (Schneider, 2006).

1.1 Galaxy clusters

1.1.1 Discovery of galaxy clusters

Galaxy clusters were first observed by French astronomer Charles Messier in 1784, more than two centuries ago. At this time, the existence of extragalactic objects was still unknown to astronomers, and Messier referred to these galaxies as "nebulæ" because of their extended nature. He noticed a big concentration of nebulæ in the Virgo constellation, as captured on photographic plates. Messier made his observations public in the review *Catalogue des nébuleuses et des amas d'étoiles que l'on découvre parmi les étoiles fixes*. Following his discovery, several other similar systems were identified. For example, the German-British astronomer William Herschel discovered hundreds of nebulæ in the Coma Berenices constellation (Herschel, 1785), which is today most commonly referred to as the Coma cluster. William Herschel, his sister Caroline Herschel, and his son John Herschel identified more than 8000 groups and clusters of galaxies (still referred to as "nebulæ" at their time), which were later published in Herschel (1864) and other papers. In Herschel (1785), William Herschel also mentioned NGC 205, second small satellite of the M31 Andromeda galaxy. The other satellite, M32, was discovered years before by the French astronomer Guillaume Le Gentil. These three galaxies, along with the Milky Way and the two Magellanic Clouds, as well as the Triangulum Galaxy M33 observed by Messier, and other satellites, form the Local Group.

The name "Local Group" was only given in 1936 by American astronomer Edwin Hubble, as he showed that these galaxies belong to the same system. For this, he used the luminosity-period relationship determined by Henrietta Leavitt in 1908 for cepheids. The discovery of cepheids in the Andromeda galaxy in the early 1920s, allowed Hubble to establish the velocity-distance relation also known today as the Hubble law (Hubble, 1929):

$$v = H_0 D \tag{1.1}$$

with v the radial velocity of the object, H_0 the Hubble's constant, and D the proper distance of the object. He proved, using this relation, that nebulæ are in fact not part of our galaxy, and are extragalactic objects.

Few of the greatest contributors to the discovery of clusters include of course Charles Messier, William and John Herschel, but also Swiss astronomer Fritz Zwicky as well as American astronomer George Abell.

In 1961, Zwicky published his *Catalogue of Galaxies and Galaxy Clusters* (Zwicky et al., 1961) which contained about a thousand rich clusters which have at least 50 cluster members with luminosities within 3 magnitudes of the brightest galaxy's magnitude. He is mainly known for his discovery of dark matter in clusters (see Section 1.1.3). Abell built an impressive sample of 2712 clusters in the local Universe detected on red photographic plates, which was published in Abell (1958). From this catalogue, he extracted a subsample of 1682 rich clusters which is estimated to be about 85% complete. This sample is one of the richest samples built, still today, and is still subject to many studies. Zwicky's catalogue, compared to Abell's, could not be used as a statistically homogeneous cluster, as the sizes of the clusters were distance-dependent (Abell, 1962).

1.1.2 Hierarchical evolution scenario

Galaxy clusters were formed from the collapse of small overdensities in the initial density field. Large structures are formed from the accretion and the merging of smaller structures (Gott and Rees, 1975), in a hierarchical way. For example, galaxies are the results of the gathering of globular clusters, which are themselves conglomerations of thousands to millions of stars bound together by gravitation. These galaxies can then form a bigger entity, which, depending on the size of the resulting assembly, can range from a group of galaxies to a cluster of galaxies.

1.1.3 Galaxy clusters as cosmological probes

Although we do not tackle the cosmological aspect of galaxy clusters in this thesis, we briefly present here the role of galaxy clusters as powerful cosmological probes.

Clusters of galaxies are, by definition, systems which bind hundreds to thousands of galaxies by gravitation. They make excellent targets to test cosmological models (Allen, Evrard, and Mantz, 2011), as they can reveal what processes took part in the formation of the large scale structures, and on a smaller scale, can help us understand how galaxies were formed and have evolved.

Almost a hundred years ago, in 1933, Zwicky estimated for the first time the mass of the Coma cluster by applying the Virial theorem to the cluster (see the republication of Zwicky's work in Zwicky, 2009) and showed evidence for unseen matter that he called "Dark Matter" (DM). From the galaxy catalogues published by Hubble and Humason (1931), he noticed a huge velocity

dispersion between the eight galaxies of the Coma cluster that had been observed. He calculated the observed velocity dispersion along the line-of-sight to be about 1000 km/s. He then attempted to determine the velocity dispersion by applying the Virial theorem. He estimated the mass of the cluster by counting the number of observable galaxies in the cluster, and multiplying this number by the average mass of a galaxy. Then, he computed the average potential energy of the system by estimating the physical size of the cluster. Knowing that the 3D radial velocity squared is proportional to the square of the velocity dispersion, this allowed him to determine a velocity dispersion of 80 km/s. From this huge discrepancy between the observed and calculated velocity dispersion, he concluded:

> *"If this would be confirmed, we would get the surprising result that dark matter is present in much greater amount than luminous matter."*

Indeed, the velocity dispersion derived from the Virial theorem was much smaller than the one measured from observations, hinting at an underestimated total mass, and thus, to matter that had not been detected with observations.

Zwicky showed another piece of evidence for the existence of DM four years later, in 1937, by calculating the average mass-to-light ratio of a galaxy in the Coma cluster, again making use of the Virial theorem (Zwicky, 1937). He computed a mass-to-light ratio of around 500, which is enormous as the mass-to-light ratio of an elliptical galaxy should be around 8.5 (Faber and Jackson, 1976; Schechter, 1980; Bacon, Monnet, and Simien, 1985). Once again, he showed that additional mass was needed to explain the dynamics of cluster galaxies. The discovery of DM by Zwicky is explained more in depth in Bertone and Hooper (2018) and in the introduction of Amaël Ellien's thesis[1].

Today's most accepted model, the ΛCDM model, predicts a Universe composed dominantly of dark energy (73%), DM (23%), and only a small fraction of visible baryonic matter (4%) (Komatsu et al., 2011).

The cluster number density evolution in bins of mass and redshift is a strong constrain for cosmological models as it depends on the underlying cosmology. In particular, the observed abundance of galaxy clusters is a powerful test to validate structure formation models (see the review by Kravtsov and Borgani, 2012). Because galaxy clusters are among the largest and most massive bound systems formed from hierarchical clustering, the number of clusters observed is exponentially sensitive to small variations in the different cosmological models used (see Mana et al. 2013 and references therein: Evrard 1989; Frenk et al. 1990; Bahcall, Fan, and Cen 1997). The cluster abundance is linked to the critical density of the Universe, Ω_0, which is defined as the ratio of the mean density observed to the density in a flat Universe. The cluster counts are also a time dependent function and are to be linked with the primordial fluctuations in the density field, which makes it an even greater probe for cosmology (Clerc et al., 2012). In a high density Universe, galaxy clusters would be forming today, thus we would not expect to observe many clusters at high redshifts. On the contrary, in a low density Universe, they would have formed long ago and we would thus expect to observe a large number of clusters at high redshifts (see Biviano, 2000, and references therein). Press and Schechter (1974) were the first to propose a statistical model to predict the abundance of galaxy clusters (or other collapsed objects or systems) as a function of their mass.

[1] https://www.theses.fr/2020SORUS305

The cluster abundance can also give us information on the power spectrum, or the two-point correlation function in Fourier space, which describes the density contrast of the Universe as a function of scale. In other words, the fluctuations in the distribution of galaxies, i.e., on the local density compared to the mean density of the Universe, gives information on the power spectrum of the initial matter distribution that has been amplified by gravity (Baugh, 2000). This function, predicted by simulations, infers how large-scale structures were formed, and was measured on big data surveys such as the Sloan Digital Sky Survey (SDSS) (see for example Hütsi, G. 2006; Gil-Marín et al. 2015; and references cited in Cui et al. 2008 for more examples).

1.1.4 Detection of galaxy clusters

Galaxy clusters are extended structures, identified by a concentration of galaxies in an aperture of 1 or 2 Mpc, that can be observed at multiple wavelengths. The combination of the information brought by multi-wavelength studies completes the frame to understand galaxy cluster formation. Spectroscopy, though, is still needed to confirm the existence of a cluster. This is done by mapping the cluster field with multi-object spectroscopy or with integral field unit (IFU) spectroscopy that enable to obtain redshifts of many galaxies in the cluster's vicinity and to confirm that they are bound together. Before proceeding to spectroscopy, though, clusters need to be identified via imaging, which can be done in several ways. We describe here different methods used to detect galaxy clusters.

Bremsstrahlung effect

Galaxy clusters are dense regions of the Universe filled with hot intracluster gas (10^6 - 10^8 K). Cavaliere, Gursky, and Tucker (1971) first suggested that clusters of galaxies could be associated with extended X-ray sources. Bahcall (1974) also showed that most clusters in the sample she studied present a massive galaxy near the X-ray center. She found a strong correlation between X-ray luminosity and the optical classification of clusters: clusters which have dominant bright cD galaxies (supermassive elliptical galaxies with an extended halo of stars) in their central regions have stronger X-ray emission than clusters that do not. Clusters were also found to present strong correlations between their total mass and their X-ray properties (Kravtsov and Borgani, 2012).

Clusters emit strongly in X-rays due to the Bremsstrahlung effect: the Bremsstrahlung effect, also called the braking radiation or free-free radiation, is an eletromagnetic radiation due to the deceleration of an electron which suffers the strong electric field of a nucleus (Sarazin, 1986). As they interact, the electron slows down, gets deviated and emits a high energy photon in X-rays. The denser the gas, the stronger the radiation. Indeed, the intensity of the radiation is directly proportional to the product of the density of electrons, n_e times the density of protons, n_p. n_p being close to n_e, the intensity is thus proportional to the square of the density of electrons :

$$L_X \propto n_e^2 R_X^3 T_X^{0.5} e^{-h\nu/k_B T_X} \tag{1.2}$$

with L_X, R_X, T_X the X-ray luminosity, radius, and temperature of the cluster; h the Planck constant, k_B the Boltzmann constant, and $h\nu$ the ionisation energy of the electron.

The Bremsstrahlung radiation is brighter as the gas gets hotter. At high temperatures, the Bremsstrahlung effect becomes dominant and the X-ray spectrum resembles a Bremsstrahlung spectrum with a few emission lines, the main characteristic emission line being the strong 6.7 keV

Fe line (Sarazin, 1986). The position and the exact energy of the Fe line are however difficult to measure precisely because of the low resolution of telescopes at high energies, and the need of a high signal to noise ratio. It is also possible to constrain the redshift of an extended X-ray source from its spectrum, without the Fe line, as it presents a break at $e^{-h\nu/k_B T_X}$. If the temperature of the gas was accurately known, we could still determine the redshift of the source, but with a low precision.

At lower temperatures (1 - 2 keV), electrons have a lower velocity, and collisions are thus not as frequent. As a result, the Bremsstrahlung effect is less important, and the emission of recombination lines is more prominent (Sarazin, 1986). The corresponding spectrum is a Bremsstrahlung spectrum with stronger emission lines.

The main advantage of this detection via X-rays is its dependency to the square gas density of the cluster. Clusters being among the densest systems in the Universe, this means clusters detected via their extended X-ray emission are less likely to be subject to projection effects from other systems on the line-of-sight. X-ray detected clusters are thus rarely spurious. This enables to build X-ray surveys of galaxy clusters with very good purity and completeness, although X-ray samples tend to be biased toward massive low-redshift objects.

Sunyaev-Zel'dovich effect

The Sunyaev-Zel'dovich (SZ) effect comes from the distortion of the Cosmic Microwave Background (CMB) due to inverse Compton scattering by high energy electrons in galaxy clusters (Sunyaev and Zeldovich, 1970; Birkinshaw, 1999). It can be observed in the sub-millimeter domain. As hot electrons of the cluster interact with the sea of photons of the CMB in which the cluster is embedded, they transfer energy to the photons of the CMB during the collision. These photons, which originally have low-energy, leave with a smaller wavelength and a boost in energy to the detriment of the electron. The intensity I of the distortion is proportional to the product of the density of electrons n_e in the cluster and to the temperature T integrated along the line of sight (Allen, Evrard, and Mantz, 2011):

$$I \propto \int n_e T dl \tag{1.3}$$

Similarly to the information obtained from X-rays, the SZ effect allows to trace the hot gas of the cluster and therefore, the two methods are complementary. Indeed, X-rays provide information on the density of the gas, whereas the SZ effect gives information on the thermal pressure of the gas. Using these two properties, it is possible to determine other dynamical properties such as temperature, entropy or mass of clusters (Pointecouteau, 2020). The SZ signal of a cluster is not affected by cosmological dimming which reduces the surface brightness of sources by a factor $(1+z)^4$. Consequently, the SZ effect enables to detect structures independently of their distance, and thus, of their redshift. Hence, it can be used to detect massive clusters at high redshifts (Allen, Evrard, and Mantz, 2011). It is however less effective in detecting intermediate-mass clusters as, contrary to the Bremsstrahlung effect, its dependency to the gas density is only linear.

1.1.5 Intra Cluster Light (ICL)

The origin of intra cluster light (ICL) comes from galactic interactions inside a cluster: as galaxies interact with each other, and following the violent event of a galactic merger, stars from the

galaxies get stripped from their host galaxies and settle as a very faint and extended component of the cluster. These stars are not bound gravitationally to the galaxies anymore, but are instead trapped in the potential of the whole cluster. The ICL appears mostly concentrated around the central massive galaxy, at the center of the cluster, which is where most of the principal mergers are happening. ICL appears mostly red, similarly to the stars in the cluster, indicating that stars from the ICL are not likely to have been formed in-situ.

FIGURE 1.1: Optical image of the galaxy cluster Abell S1063 obtained with the Hubble Space Telescope. The central galaxy (the BCG) appears surrounded by a very diffuse light (here, in blue) which corresponds to the ICL. Credit: NASA, ESA, and M. Montes (University of New South Wales, Sydney, Australia)

Due to its nature, ICL has a very faint surface brightness and as a result is very difficult to detect. Long exposure times are needed in order to detect this component, as its surface brightness is usually fainter than $\mu > 26.5$ mag/arcsec^2 in the V band (Holmberg, 1958). It becomes even fainter at higher distances due to cosmological dimming. As a result, most studies of the ICL have been done on massive local clusters such as the Virgo cluster or the Coma cluster (see for example Mihos et al., 2005; Castro-Rodriguéz, N. et al., 2009; Jiménez-Teja, Y. et al., 2019; Gu et al.,

2020). Not only is it difficult to detect, but separating it from the other cluster components is also a complex task. Indeed, the stars which compose it form a very extended and diffuse light halo around the central galaxy, and can meddle with its extended envelope. Differentiating what is part of the galaxy and what is not is important in order to model correctly the size and luminosity of the galaxy, the profile of which can otherwise be contaminated by ICL. This can be seen on the image of the cluster Abell S1063 in Figure 1.1. The ICL, visible as the blue diffuse and extended light, surrounds the central galaxy and blurs its borders.

Different methods are used to extract the ICL, the most effective one being via spectroscopy. Authors have found an effective method to separate ICL from the halo of the galaxy by measuring the velocity dispersion as a function of the distance to the central galaxy (see Kluge et al. 2021 and references therein: Dressler 1979; Carter et al. 1981; Ventimiglia et al. 2010; Toledo et al. 2011; Arnaboldi et al. 2012; Melnick et al. 2012; Murphy, Gebhardt, and Cradit 2014; Bender et al. 2015; Barbosa et al. 2018; Loubser et al. 2018; Spiniello et al. 2018; Gu et al. 2020). They find that the stellar velocity dispersion starts to increase in the outskirts of the central galaxy, and sometimes reaches the velocity dispersion of the cluster. This hints at the presence of stars which do not belong to the central galaxy in the outer halo.

Since spectroscopy is not easily accessible, algorithms have been developed in order to extract the ICL directly from imaging. These algorithms rely on various methods in order to bring out low surface brightness features. One of the existing methods, which was implemented in the algorithm `CICLE` developed by Jiménez-Teja and Dupke (2016) used in one of our studies, relies on the modeling of the luminosity profiles of the sources in the field which, once subtracted, return an image with only the ICL remaining. The `DAWIS` code developed by Ellien et al. (2021) based on the decomposition on wavelet functions, considers all structures with a size above a given scale as ICL. These two algorithms will be more detailed in Chapter 2 and Chapter 3 respectively. Others, instead of considering the size, use the surface brightness as an indicator. The typical surface brightness threshold is $\mu = 26.5$ mag/arcsec^2 in the V band (Holmberg, 1958).

However, different detection methods return different ICL fractions. The ICL fraction is defined as the ratio of the integrated flux of the ICL over the total integrated flux of the cluster. As the formation of the ICL is directly linked with the formation of the cluster, we can expect a dependence of the ICL fraction with the number and nature of mergers a cluster may have experienced; and more importantly, with the cluster mass or dynamical state (Rudick, Mihos, and McBride, 2011; Jiménez-Teja et al., 2018; Kluge et al., 2020).

1.2 Galaxies in clusters

1.2.1 Morphological types of galaxies and segregation

Galaxies come in various shapes and colors. Their different characteristics indicate that all galaxies were not formed in the same way, and questions arise regarding their evolution. The need to classify them became very rapidly apparent to understand galaxy evolution. In 1926, astronomer Edwin Hubble invented the Hubble Sequence, which allows to classify galaxies visually according to their morphology (Hubble, 1926a; Hubble, 1926b; Hubble, 1927). At first, the classification was only done by eye, but as new observational instruments developed, it became more and more

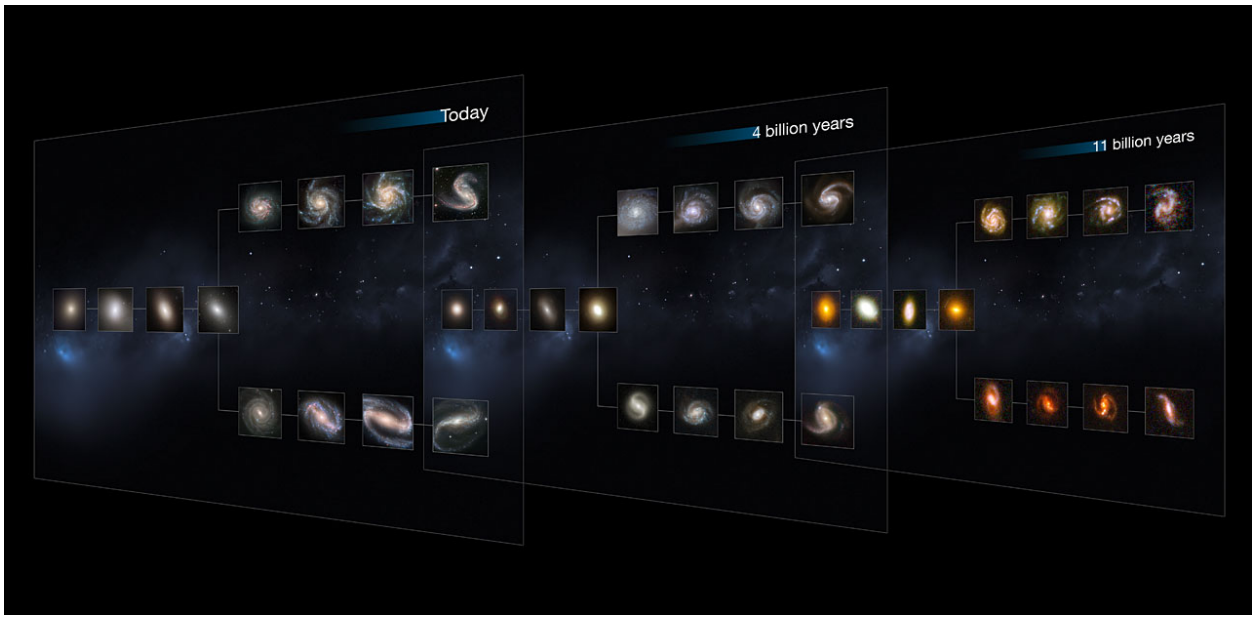

FIGURE 1.2: The Hubble Sequence throughout the Universe's history. Credit: NASA, ESA, M. Kornmesser

precise with other physical criteria. We distinguish four main categories as seen in Figure 1.2 (from left to right): elliptical, lenticular, spiral, and irregular galaxies.

- Elliptical galaxies are, as their name suggests, galaxies which have ellipsoidal 2D profiles, and they are categorized depending on their ellipticity (ϵ = 1 - a/b with a the major axis of the galaxy and b the minor axis). The ellipsoidal shape was (erroneously) explained in some part by their rotation which, due to centrifugal forces, was thought to push stars outwards and thus flatten the profile of the galaxy. Ellipticals, however, are known to have very low rotational velocities (which is even more true for massive ellipticals), so their spin does not play a big role in the shaping of these galaxies (Binney, 1976; Jedrzejewski and Schechter, 1989). Their morphology can be mainly explained by the anisotropic motions of their stars: stars in elliptical galaxies follow ellipsoidal orbits, and are characterized by anisotropic random velocities (Schneider, 2006). Ellipticals have very little or no gas left in their vicinities. As a result, they do not have any ongoing star formation, and let their stellar population age increase. These quiescent galaxies are characterized by an old and red stellar population. Some would even define them as "dead" galaxies, which can be debatable. Their size range is very broad: on one hand, some elliptical galaxies can be as small as a fraction of the radius of the Milky Way, of the order of a few kiloparsecs; on the other hand, they can also constitute the most massive and largest galaxies in our Universe, with sizes reaching hundreds of kiloparsecs and masses up to 10^{13} $M_{\odot}$.

- Spiral galaxies are composed of a bulge, a flat rotating disk, and spiral arms in the disk. They are classified according to the ratio of light contained in the bulge over the light in the disk. The arms are composed of gas and dust, and more specifically HII regions, which are sites of active star formation, and are characterized by a young, hot and blue stellar population. Bulges contain redder and older stars than disks. Two-thirds of spiral galaxies present a bar in their center (Lee, Ann, and Park, 2019). Our galaxy, the Milky Way, belongs to the class

of barred spirals. The presence of a bar can affect the motions of the matter (stars, gas or dust) present in the disk and may play a key role in the dynamical evolution of spirals (Vera, Alonso, and Coldwell, 2016). For example, some matter can travel from the disk to the center of the bulge through these bars which can trigger starburst events in the bulge (see Nair and Abraham, 2010, and references therein).

- Lenticular galaxies are an intermediate category between ellipticals and spiral galaxies. Like ellipticals, they appear elongated and have low star formation rates (SFR), i.e the stellar mass formed per year; due to the lack of gas in their disk, but they also have a very prominent bulge which is well distinguishable from the disk, and sometimes shows traces of a bar similar to that of barred spirals.

- Irregular galaxies are galaxies which do not have a regular shape, and in most cases they are still forming. They are often small (e.g dwarf galaxies).

Other morphological types exist, such as dwarf galaxies, starburst galaxies, or others with more exotic names such as blueberry galaxies, greenpea galaxies or even jellyfish galaxies... Those are subcategories in the galactic classification which present different morphologies and physical and dynamical properties, and will not be detailed in this thesis.

The main morphological types can also be identified by their colors in a color-magnitude diagram such as the one shown in Figure 1.3. On this diagram, two principal peaks can be distinguished: the blue cloud (represented by blue points) and the red sequence (represented by red points). This is the bimodal color distribution of galaxies (Baldry et al., 2004; Menci et al., 2005). These two regions are mostly populated by blue spiral galaxies and red elliptical galaxies respectively. In between resides the green valley (represented by the green points), which represents a transitional region between the blue cloud and the red sequence. This diagram gives, in other words, the SFR as a function of the galactic morphological type. Bluer colors indicate the presence of new young stars, hence a high SFR; and red colors trace the presence of old passively evolving stars, hence a low SFR.

Late-type galaxies (spirals and irregulars) constitute approximately 60% of the total population of galaxies in the Universe, whereas the remaining 40% are constituted by early-type galaxies (ellipticals and lenticulars). The terms "early-type" and "late-type" galaxies originate from the Hubble sequence, as Hubble thought that ellipticals and lenticular-like galaxies would form first, hence an early formation, and would then evolve into spirals or irregular galaxies, hence a late formation. This was proven to be false, as the effects of interactions between galaxies became better and better understood with time.

Indeed, whereas they are a minority overall, early-type galaxies dominate the galaxy population in dense environments such as clusters and groups of galaxies, whereas late-type galaxies dominate in environments of average or low density such as the field. This is the morphology-density relation that was first brought up by Hubble's observations (Hubble, 1936). He noticed that "the density of the cluster diminishes as the most frequent type advances along the sequence of classification". This relation was confirmed by Dressler (1980), who demonstrated the well-defined relationship between the local galaxy density and the galaxy morphological type. He showed that, as Hubble remarked years before him, the population of ellipticals and lenticulars increases with density, whereas the population of spirals decreases with density. Rood et al. (1972) also found that rich clusters such as the Coma cluster are dominated by ellipticals and lenticulars.

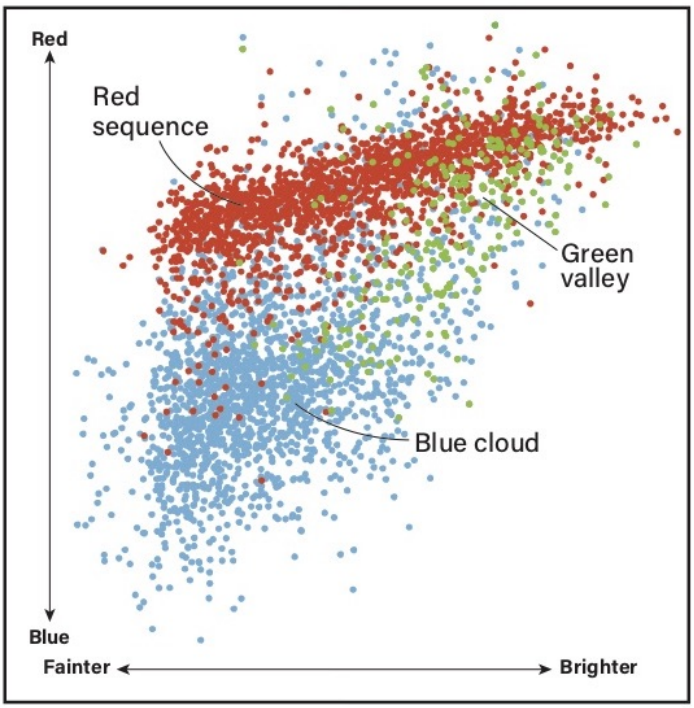

FIGURE 1.3: Color-magnitude diagram of a population of galaxies showing the three main regions: the blue cloud, the green valley, and the red sequence. Credit: Astronomy: Roen Kelly, after Gavazzi, G. et al. (2010)

This was also noted by Oemler (1974) who defined density as the significant physical parameter to determine the galaxy population of a cluster.

So, where does the morphology-density relation come from?

Galaxy clusters are high-density environments, which means that collisions, mergers or interactions between galaxies must be more frequent than in the field. Very early, astronomers understood the importance of collisions to explain the evolution of galaxies. More importantly, Spitzer and Baade (1951) suggested that collisions between two galaxies would be the main mechanism to transform the morphology type of a galaxy into another one. They detailed how collisions would expel all interstellar matter out of the galaxies, thus preventing the formation of population I stars (highly luminous and young stars which can be found in the star forming arms of spirals), and leaving galaxies in clusters with only population II stars (old red stars). Zwicky (1937) had already mentioned such a discrepancy as he stated that collisions could lead to the disruption of certain "nebulæ", and that would be the reason why field galaxies differ morphologically from cluster galaxies.

Whereas gas or stars can be ejected during mergers, these violent events can also provoke intense star formation, as gas in molecular clouds can get compressed as the two galaxies approach and then coalesce. Shock waves can also appear, which can trigger starbursts in molecular clouds located in the outskirts of the galaxy (Sobral et al., 2015; Stroe et al., 2015). It is commonly believed that elliptical galaxies form by the merger of two spiral galaxies of similar masses (Toomre, 1977). As the merger happens, the gravitational potential of the two galaxies transforms, and the stars

get scattered in a random fashion. Due to the interaction, spiral arms are pulled away more and more as each galaxy passes by the other, and eventually get destroyed in the process, losing their "spiral" characteristic. As the result, as the merger relaxes, what were originally two spiral galaxies become one massive elliptical galaxy.

Additionally, clusters in very dense environments were shown to host a supergiant galaxy in their center (Morgan and Lesh, 1965). These supergiant galaxies were missing in poor groups and poor clusters, as well as in the field. The existence of these very massive galaxies in the center of clusters is directly linked to the higher galactic density in the cluster center. In 1943, Chandrasekhar (1943a) published his theory of dynamical friction which describes how astrophysical objects in motion which undergo the gravitational force of their environment lose energy and decelerate as a result. A simplified version of the Chandrasekhar dynamical friction force is given as:

$$F_{dyn} \approx c\frac{G^2M^2\rho}{v_M^2} \tag{1.4}$$

with G the gravitational constant, M the mass of the object, ρ the density of the medium through which the object is passing through, and v_M the velocity of the object. As they slow down, objects subject to dynamical friction move towards the center of the cluster where the density is greater, thus increasing the chances of collisions with other galaxies. The massive central galaxy is the ending point of all galaxies trapped in the gravitational potential of the cluster, and it will "cannibalize" or merge with these other systems. The Chandrasekhar dynamical friction also plays a role in the transformation of spiral galaxies to an elliptical galaxy following a collision: stars, because of dynamical friction, sink down to the center of the galaxy, and adopt random anisotropic orbits, which explains the final ellipsoidal profile of the resulting galaxy.

1.2.2 The red sequence

The dominant population of galaxy clusters consists of elliptical and lenticular galaxies which are mainly located towards the center of the cluster, whereas late-type galaxies are mainly found in the outskirts. These early-type galaxies, as we described, are quiescent galaxies with an old stellar population which does not get renewed. This is why, when looking at clusters through a telescope or on color images, one can distinguish an overdensity of red galaxies at the location of the cluster. These galaxies have no gas left, have similar properties as they grew in the same environment, and are at the same distance (redshift). As a result they have very similar red colors, and they constitute what is called the red sequence of the cluster. The red sequence can be extracted from a color-magnitude diagram (Baum, 1959; de Vaucouleurs, 1961), an example will be given in Chapter 2. The color-magnitude diagram presents a very small dispersion due to the similar nature of the galaxies which constitute it. The depth and the slope of the sequence can also provide us with information on the formation of the cluster: indeed, with time, as the gas gets consumed and galaxies are left with no material to induce new star formation, the stellar population will evolve passively and all galaxies will evolve to resemble each other. Consequently, the red sequence will become narrower and narrower as it ages. The slope of the sequence, on the other hand, is related to the metallicity of the stellar population. Indeed, more massive ellipticals contain more massive stars, in which are formed heavier elements. As a result, the metallicity increases with the mass of the galaxy.

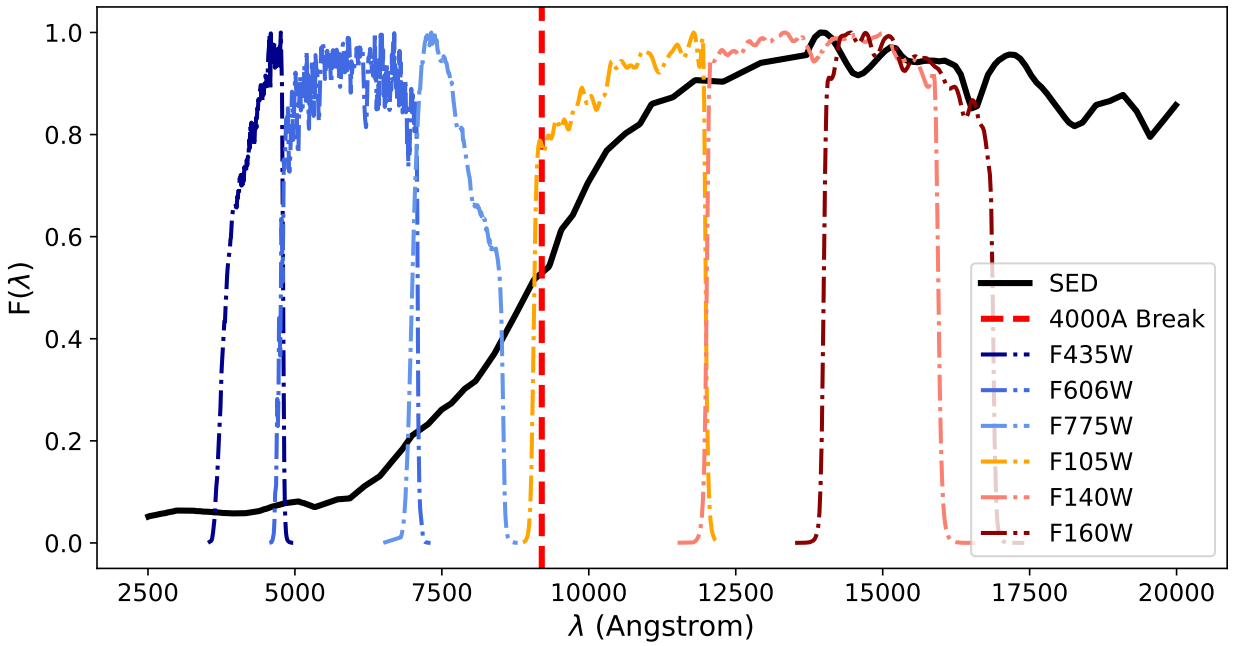

FIGURE 1.4: Illustration of the SED of a typical cluster elliptical galaxy at redshift $z = 1.3$ (black solid line). The dotted red vertical line represents the 4000 Å break redshifted to the cluster's redshift. The filter transmissions are normalized to 1, and are shown as dash dotted lines: (from left to right, from the bluest to the reddest colors) $F435W$, $F606W$, $F775W$, $F105W$, $F140W$ and $F160W$.

The red sequence is an excellent tool to indicate which galaxies are likely to be members of the cluster, if no spectroscopy is available. Looking for the red sequence is equivalent to determining which galaxies are at the same redshift. The downside, however, is the need for appropriate filters in order to compute a color that will best remove interlopers (galaxies in the background and foreground).

The Spectral Energy Distribution (SED) of an elliptical galaxy (see Figure 1.4) is characterized by a strong 4000 Å break. The 4000 Å break is caused by the absorption of high energy radiation from metals in the atmosphere of the red stars which compose the galaxy. Young stars are mostly hot and emit in the bluer wavelengths, whereas old stars are cold and emit in the redder wavelengths. As can be seen in Figure 1.4, the 4000 Å break, marked by a red dotted line, represents a separation between the population of young and hot stars dominant in the bluer side of the spectrum, that only represents a small fraction of the stellar content of passive galaxies, and the population of old and cold stars that is dominant on the redder side. The spectrum before and after the break is mostly flat, it is thus necessary to select two filters which do not both fall on the same flat part of the SED in order to compute a color that efficiently extracts the red sequence. Indeed, in that case, the color computed by the difference of magnitudes in two different filters $(blue - red)$ would be null. The break, which gives the most information regarding the redshift of the galaxy, would not be contained between the two filters considered, and would not enable us to determine the redshift of the galaxy. For a galaxy at redshift $z = 1.3$, for example, taking filters from the Hubble Space Telescope (HST) ACS and WFC3 instruments, both the colors $(F435W - F606W)$ and $(F140W - F160W)$ would be equal to zero. However, they characterize two very different stellar populations: the first filter captures the younger stars whereas the second one captures the older

stars. Using only these colors would thus not enable us to know if this galaxy is at low or high redshift. Similarly, choosing two filters which are on two extremes of the SED will not enable us to constrain the break very well. Indeed, taking the same example, the color $(F435W - F160W)$ would contain the break; however, because both filters fall on flat regions of the SED, all galaxies between redshifts 0.8 and 1.8 will have the same colors. This is why it is preferable to consider two filters which are not too far from each other (without superposition) and at least one of the two should be close to the break, preferably in the redder side of the SED (in order to have the best signal to noise possible). The best case scenario would be to have one filter which contains the beginning of the break, and the other one the end of the break. In the case shown in Figure 1.4, the best would hence be the $(F775W - F105W)$ color.

This condition is particularly difficult to meet for very low redshift ($z < 0.1$) and high redshift ($z > 1$). At $z < 0.1$, the break is very narrow and may become below visible filters, and is thus hard to constrain via optical data (but UV can be used). At $z > 1$, infrared becomes necessary.

1.2.3 Black holes in massive galaxies

The existence of black holes (BHs) was first speculated by John Mitchell in 1783 as he speculated that a sufficiently massive star would have enough gravity to stop light from escaping. BHs are defined as objects so massive and compact that their gravitational curvature would close space-time locally so that no matter or light could escape. The event horizon of a BH was defined by Rindler (1956) as "a frontier between things observable and things unobservable". In other words, light that crossed the event horizon can not escape and reach us, and can thus not be observed. The characteristic radius of the event horizon of a BH is the Schwarzschild radius defined as:

$$r_s = \frac{2GM_{BH}}{c^2} \tag{1.5}$$

with G the gravitational constant, M_{BH} the mass of the BH and c the speed of light.

BHs have masses that can range from a few solar masses (stellar BHs) to more than a million or even a billion solar masses (supermassive BHs). Massive galaxies were found to host supermassive black holes (SMBHs) in their centers. The BH at the center of our galaxy, Sagittarius A, is a SMBH with a mass equivalent to more than 4 million Suns concentrated in a radius of about 51.8 million kilometers (or, as the NASA website states, that mass "would fit inside a very large ball that could hold a few million Earths"). These extremely dense objects play a large role in the shaping of their host galaxies (see the review in Cattaneo et al., 2009). Some galaxies may present a very bright nucleus, caused by an accreting SMBH. As SMBHs accrete matter, they convert and release the gravitational energy produced by the absorption of material into radiation, radio plasma jets or winds, in the interstellar medium. The resulting jets can reach velocities of 1000 km/s with released energy amounting to 10^{45} erg/s (see Fabian, 2012). In these forms, the released energy can heat dynamically the surrounding gas, preventing the collapse of cold gas into new stars. These galaxies are called active galactic nuclei (AGN). From simulations, AGN feedback was found to be able to regulate the star formation in host galaxies, and also affects their sizes, masses, stellar surface densities or stellar ages (Rosito et al., 2021). More specifically, SMBHs may have contributed greatly to the quenching of star formation in elliptical galaxies.

The quenching may have happened already before the cluster was even formed. Massive elliptical galaxies were shown to have had most of their stars formed in-situ a long time ago. Simulations such as those by De Lucia and Blaizot (2007) find that 80% of the stellar population was already formed before $z = 3$, and are in agreement with observations by Thomas et al. (2010) who state that most of the stars were already born by $z = 2$. The chemical composition of elliptical galaxies also hints at a brief formation epoch that would have happened long ago. SMBH feedback, which is a very intense and rapid event, represents a very good candidate to explain the rapid quenching of elliptical galaxies.

Ultimately, the growth of the central SMBH and bulge of massive elliptical galaxies appear to be closely linked, as are the SMBH masses with the galaxy bulges' stellar masses (Magorrian et al., 1998; Marleau, Clancy, and Bianconi, 2013) and velocity dispersions (Gebhardt et al., 2000; Ferrarese and Merritt, 2000; Gültekin et al., 2009; Ding et al., 2022). The SMBH and the bulge of elliptical galaxies grow together by accreting the same surrounding gas. What is still unclear, however, is whether the growths stop because of the deficit of gas due to star formation, or due to the SMBH that would have ejected all the gas outside the galaxy (Cattaneo et al., 2009).

On a larger scale, SMBHs are also believed to regulate the star formation at the center of galaxy clusters. Clusters are huge reservoirs of gas and emit strongly in X-rays, even more so in their central region which tends to be denser. Hence, they lose energy proportionally to the number of photons that is being released. The core of the cluster, as a consequence, is supposed to cool all the more rapidly, leading clumps of gas to collapse together, then followed by the start of a new period of star formation. However, observations show that the SFR measured at the core of galaxy clusters is much below what is expected by hydrodynamical numerical simulations that only take into account gravitational collapse or SN feedback as the main clustering processes (Kravtsov and Borgani, 2012). This means that there exist heating processes that would prevent the gas from cooling too rapidly, and thus, from forming stars. This problem, also known as the cooling flow problem, is commonly solved by considering a central AGN at the center of the cluster, where the brightest galaxy usually lies, with feedback that would dynamically heat the core. It was found in several studies that AGN feedback enables reduction of the SFR obtained in simulations in the cores of clusters, and reduces the hot gas content in groups to values more comparable to those actually observed. But, we can note that the simulations used in these studies only inject energy phenomenologically. Even though they show that AGNs do produce enough energy for quenching, the actual physical process is not simulated from first principles. Taking into account AGN feedback, stellar masses of BCGs are now better calculated, and so are the metallicity profiles and the relation between X-ray luminosity and temperature (see Kravtsov and Borgani, 2012, and references therein).

1.2.4 Brightest Cluster Galaxies (BCGs)

Brightest cluster galaxies (BCGs) are exceptionally bright objects which are believed to lie at the bottom of the cluster potential well and reflect the dynamical processes that govern the formation of their host cluster. Similarly to their host clusters, BCGs, being the most massive galaxies, are also the result of hierarchical merging with smaller galaxies which get cannibalized by the central galaxy, contributing to its growth. They are, by definition, the brightest galaxy of their cluster, and to make the link with Section 1.2.2, the brightest of the red sequence galaxies. BCGs are usually described as massive cD galaxies. Since they are elliptical galaxies, BCGs are generally known as

having an old and passive stellar population, and quenched star formation from their lack of gas. They are however different from other "normal" ellipticals. In fact, Tremaine and Richstone (1977) and Dressler (1978) found that the BCG luminosity was determined by "some special process" and not by a statistical sampling of a universal luminosity function. The luminosity function, which should rather be referred to as a luminosity distribution, is defined as the relative number of galaxies in a given luminosity bin. For instance, the Schechter luminosity function is a good first approximation of the total luminosity distribution of galaxies (Schechter, 1976). Moreover, BCGs, contrary to elliptical galaxies, present an extended envelope in their surface brightness profiles (Oemler, 1976; Schombert, 1986). These galaxies were formed through several dynamical and environmental processes, including galactic cannibalism, cooling flows from the central AGN and dynamical friction. The relative importances of these processes in the shaping of these galaxies however is still not well constrained (see Castignani et al., 2020, and references therein).

Simulations show that most of the stars of BCGs have been formed in-situ during intense starburst events that would have happened more than 11 Gyrs ago (De Lucia and Blaizot, 2007). The stars formed in progenitor galaxies before they were captured by the potential of the clusters and merged to create today's BCG. Following these events would be a phase of dry and wet mergers during which even more stars are born, increasing the stellar mass of the BCG (Cooke et al., 2019). Eventually, all the gas gets consumed or ejected during these violent interactions, leaving the resulting galaxy (the BCG) with little to no gas left. The BCG continues its growth mainly through dry mergers, as most of the galaxies in the cluster vicinity are now passive elliptical galaxies, which should render the start of a new starburst impossible. Observationally, though, a few clusters have been shown to still have a huge reservoir of molecular gas with $SFR > 100\ \mathrm{M}_{\odot}/\mathrm{yr}$ (see McDonald et al., 2016; Fogarty et al., 2019; Castignani et al., 2020). The existence of these star forming BCGs questions our understanding on the formation and evolution of these galaxies.

Because of their central locations, they are more likely to experience mergers in their lifetimes and they thus represent the final products of hierarchical evolution at the galactic scale. On a cosmological point of view, galaxy clusters are perfect laboratories to study the effect of environmental processes on the formation of galaxies (Spitzer and Baade, 1951), and BCGs allow us to infer how these processes can affect the dynamics and the growth of galaxies. For example, Spitzer and Baade (1951) mention how astrophysical signatures of mergers such as streams or tails can allow to test physical models. As BCGs grow at the same time as their host clusters, they also have properties which are very closely linked to those of their host clusters (Lauer et al., 2014). As such, BCGs are excellent tracers of their host cluster history, and they also represent the most massive galaxies of the Universe, thus imposing upper limits on the evolution of the properties of galaxies in simulations. In this thesis, more specifically, we measure how the physical properties of BCGs evolve (or not) with time. This evolution, as well as other scaling relations such as the Kormendy relation (Kormendy, 1977), which we try to refine with statistically bigger samples, are to be verified by simulations and can thus enable us to better constrain the cosmological parameters and physical processes involved in models used to better probe galactic evolution.

In this thesis, we analyze four different samples. Three of them are chosen for observational studies: the first one (see Section 2.1) consists in a sample of 149 BCGs between redshift 0.1 and 1.8 with HST data; the second one (see Section 2.2) represents a statistically significant bigger sample of 1371 BCGs up to redshift 0.7 detected in the Canada-France-Hawaii Telescope Legacy Survey (CFHTLS); and finally the third one (see Chapter 3) is a sample of about 30 brightest galaxies of

fossil groups from the SDSS.

Although it is commonly thought that BCGs lie at the bottom of the cluster potential well, which is expected to be located in the center of the cluster, observations have shown that offsets between the BCG and the cluster center as defined by X-rays were common (see Patel et al., 2006; Hashimoto, Henry, and Boehringer, 2014; De Propris et al., 2020; Chu, Durret, and Márquez, 2021). This motivated our last study (see Chapter 4), which is based on a sample of 370 BCGs from the Illustris-TNG300 simulation, to investigate the effect of mergers on offsets between the BCG and its SMBH.

Chapter 2

Evolution of the physical properties of BCGs through time

2.1 Detection and photometric properties of BCGs observed with the Hubble Space Telescope

Large samples of BCGs are necessary in order to obtain statistically significant information on their properties to infer their formation and evolution. In this study, we built a sample of BCGs observed in the optical to near infrared with the HST instruments ACS and WFC3 respectively. Our sample was constructed with the only criterium that HST images were available. We used existing and already published samples from Whiley et al. (2008), Lidman et al. (2012), Lin et al. (2013), Lauer et al. (2014), Bai et al. (2014), van der Burg et al. (2014), McDonald et al. (2016), Bellstedt et al. (2016), Zhang et al. (2016), West et al. (2017), Durret et al. (2019), DeMaio et al. (2019), Cerulo, Orellana, and Covone (2019) and Kluge et al. (2020). The resulting catalogue constituted one of the largest samples of BCGs observed with HST to date (149 BCGs), and one of the samples which covers the largest redshift interval (up to z = 1.8). Another particularity of this sample is that all clusters have a spectroscopic redshift available in the literature. The exquisite spatial resolution of the HST images and the wide redshift coverage of our sample allow a detailed study of the evolution of the physical properties of these BCGs and hence to retrace their histories.

2.1.1 Construction of the BCG catalogue, automatic detection method

Catalogues of BCGs are not as common as catalogues of galaxy clusters. In order to build our own catalogue of BCGs, it was necessary to first retrieve catalogues of clusters and elaborate our own procedure to detect the BCGs. BCGs are here identified as the most massive elliptical galaxies in the clusters. Based on the cluster coordinates from the samples above, I retrieved images available in the optical and near infrared of the clusters from the Hubble Legacy Archive (HLA), and wrote an algorithm in order to identify the BCG on these images. Indeed, the images contain many things that are not what we look for: stars, artifacts (trails of satellites, diffraction spikes from bright stars, instrument defects), but also galaxies which are not part of the cluster, and which can be in the foreground or in the background. These galaxies in particular are difficult to filter out in the absence of spectroscopic data. Knowing that most objects in the field would lack spectroscopic redshifts, we decided to use only photometric criteria to classify objects in the sky into two categories: interlopers and cluster members.

The extraction of sources and their photometric properties was done using the software `Source Extractor` (Bertin and Arnouts, 1996), which is a program that builds photometric catalogues of objects detected on an astronomical image. The separation between point sources and extended objects is easily done using the corresponding parameter (CLASS_STAR). Two main properties were used to distinguish interloper galaxies in a first step. On one hand, edge-on spiral galaxies appear very elongated along the line of sight, we thus use the measured projected ellipticity to filter these out. On the other hand, foreground galaxies, because of their closeness, can appear bright in the sky. However, using their apparent magnitude directly to identify them is hazardous as BCGs at a given redshift can vary in luminosity by several magnitudes. In order to distinguish foreground galaxies from other objects at the right redshift, we compute what we refer to as a "pseudo" absolute magnitude: this absolute magnitude is not the real absolute magnitude of the object as it is not computed at its redshift but at the cluster's redshift. Foreground galaxies, by their pseudo absolute magnitude, will appear much too bright. They are thus excluded.

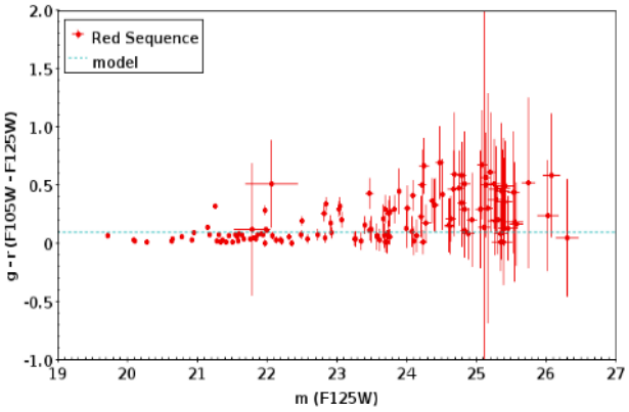

FIGURE 2.1: Red sequence of a cluster on a color-magnitude diagram. Red points correspond to the colors of galaxies in the field, the blue dotted line shows the expected color of an elliptical galaxy at the cluster's redshift. Cluster members show a very tight relation in this diagram.

However, this is not enough and is only efficient in removing bright foreground objects. In order to get rid of all remaining contaminations, we extract the red sequence of the cluster. The red sequence, as was described in Chapter 1, enables us to identify the elliptical cluster members only based on their colors. It can be traced on a color-magnitude diagram such as the one shown in Figure 2.1 which shows the small dispersion of colors of the bright galaxies in the field. Accurate photometry on fainter objects is more difficult, leading to higher uncertainties and color dispersion. We can note the bias towards redder objects at $m_{F125W} > 23$ which is more likely due to contaminations by farther objects. This diagram also indicates by the blue dotted line the typical color of an elliptical galaxy at the cluster's redshift. To serve as a model, we make use of the SED of an elliptical galaxy from Bruzual and Charlot (2003). Based on this model, we can determine the expected color of an elliptical galaxy at the cluster's redshift (see Figure 1.4), which is known here. When compared with observations, the red sequence can be extracted by removing all objects which have colors too different from the model. The color used is adapted depending on the cluster's redshift and the filters available.

In Figure 2.2 the three different steps of the detection method are described: from left to right,

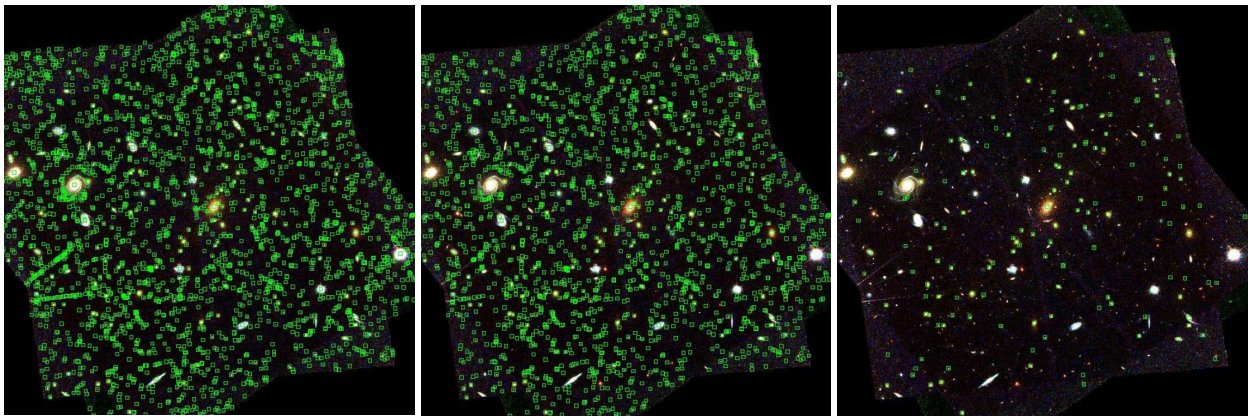

FIGURE 2.2: From left to right: MACS J1115.8+0129 (z = 0.349) (z = 0.45): all sources detected by SExtractor, removal of stars and bright foreground sources, extraction of the red sequence of the cluster.

(1) the whole catalogue returned by `Source Extractor`, (2) after removing stars and bright foreground galaxies, and finally, (3) after selecting the red sequence. Very obviously, the most important step is the extraction of the red sequence, which efficiently selects the red galaxies of the cluster and removes other interlopers from the remaining catalogue. In theory, the BCG of the cluster would be the brightest of the red sequence. Practically, some interlopers with similar colors may remain, and therefore the brightest galaxy is not necessarily a member of the cluster. We thus also look at the galaxy density around each galaxy to remove galaxies which appear isolated (i.e. the density of galaxies in a certain aperture around them appears too low compared to the defined threshold).

All detections were carefully checked by eye to confirm whether the BCG assigned automatically by the algorithm was correctly chosen, using X-ray data if available as well as spectroscopic redshifts if any. This method was shown to be very efficient to detect red BCGs, as all red BCGs in the sample were correctly detected by the algorithm. This algorithm can be applied to any survey as long as it is in the optical and/or infrared, two photometric bands at least are available, and the cluster redshifts are confirmed via spectroscopy. The fact that this method has been automatized and only relies on photometry (except for the cluster's redshift) is also a big advantage for large surveys. This tool enables to obtain a large catalogue of "candidate" BCGs (technically, a BCG is still a candidate until it has been observed with spectroscopy and its redshift confirmed), and as result, to increase the statistics on BCG studies.

2.1.2 Luminosity profiles

The luminosity profile of each BCG was then modeled with the `GALFIT` software, an algorithm which fits 2-D analytic functions to objects on digital images (Peng et al., 2002). The Sérsic profile (Sérsic, 1963) was shown to be a really good match for the surface brightness profile of elliptical galaxies:

$$I(R) = I_{\mathrm{e}} \exp\left\{-b_{\mathrm{n}}\left[\left(\frac{R}{R_{\mathrm{e}}}\right)^{1/n} - 1\right]\right\} \tag{2.1}$$

with R_e, I_e, R and b_n the effective radius (radius which encloses half of the total luminosity of the galaxy), the surface brightness enclosed in a radius R_e, the radial distance from the center, and a constant depending on the Sérsic index n, respectively. The Sérsic profile is a generalized version of the de Vaucouleurs profile which corresponds to a Sérsic index $n = 4$. The exponential profile is obtained by fixing $n = 1$. The Sérsic profile becomes steeper at higher radii with decreasing n.

A mask, a PSF, as well as the image of the cluster are given to `GALFIT` with the coordinates of the BCG and initial guesses for the apparent magnitude, effective radius, ellipticity, and Sérsic index of the BCG. Two models were applied to each BCG: a model with a single Sérsic component, and a model with two Sérsic components. The addition of a second component was done in an attempt to better model the brighter inner structure of the BCG. The choice between the two models was then done via the statistical F-test (Margalef-Bentabol et al., 2016).

2.1.3 Results

Results returned by `GALFIT` show no clear evolution up to redshift $z = 1.8$ for the rest-frame absolute magnitude, effective radius, Sérsic index or ellipticity of BCGs with time. This implies that BCGs were already formed long ago, before $z = 1.8$, and have evolved passively since. We also show that the Kormendy relation (Kormendy, 1977), defined for elliptical galaxies, is also very well defined for BCGs. The Kormendy relation is a scaling relation that links the mean effective surface brightness to the effective radius. It indicates that bigger galaxies tend to be less concentrated than smaller galaxies. We also show that BCGs modeled with two Sérsic profiles are mostly at lower redshift ($z < 0.4$) but this is not due to the lower resolution resulting from larger physical scales at farther distances. The presence of a double component mainly at lower redshift may hint at the late formation of a disk or a bulge. However, observational biases may also come into play. We discuss this further in Chu et al. (2022) (see Section 2.2).

We also study the alignment of BCGs with their host clusters, and show that 70% of BCGs at $z < 0.9$ are aligned with their host clusters within 30 degrees. This confirms previous results found by other authors such as West et al. (2017) and Durret et al. (2019) among others. This alignment may be evidence for the effect of mergers on the central galaxy which gets aligned by tidal interactions as galaxies which are going to merge with the BCG fall along cosmic filaments. We also estimate the fraction of blue BCGs to be 2%. Blue BCGs are defined as BCGs with negative colors: the difference between the magnitudes measured in two chosen filters $blue - red < 0$. The existence of these blue BCGs is interesting in view of the definition of a BCG: BCGs are supposed to be red quiescent galaxies with a passive, old stellar population. This blue color hints at the presence of young stars, and thus, at star formation in the galaxy. These galaxies are still very rare, but studying them can yield information on the processes which can trigger a new epoch of star formation. They can help us to understand how these galaxies resulting from many mergers which should have consumed or ejected all their gas long ago can still have some gas remaining (see Castignani et al., 2020, for an extensive study of 19 CLASH BCGs with high molecular gas content).

In this study, we also analyze how the properties of BCGs evolve with their host cluster properties (mass, position of the BCG from the X-ray peak) and find no correlation between them. We do not find any correlation depending on the cluster-BCG alignment either (the mass of the clusters were derived either from the richness of the cluster, or were taken in the literature and hence come from different methods for estimating the mass).

In summary, this study gives new insights on the origin and evolution of BCGs using a large sample which covers a wide redshift range, up to redshift $z = 1.8$. We offer here a new tool to detect and model automatically the luminosity profiles of BCGs, which can be applied to any imaging data set. Among the contradicting results regarding the evolution of BCGs through time, we agree with Stott et al. (2011) and Bai et al. (2014), as we do not find any significant growth in size or luminosity for BCGs during the last 10 Gyrs. We however find an inner structure mostly at lower redshift which may hint at an inside-out growth scenario of BCGs with time, as proposed by Bai et al. (2014), Lauer et al. (2014) or Edwards et al. (2019).

2.1.4 The paper

A&A 649, A42 (2021)
https://doi.org/10.1051/0004-6361/202040245

Astronomy & Astrophysics

Physical properties of brightest cluster galaxies up to redshift 1.80 based on HST data⋆

A. Chu[1], F. Durret[1], and I. Márquez[2]

[1] Sorbonne Université, CNRS, UMR 7095, Institut d'Astrophysique de Paris, 98bis Bd Arago, 75014 Paris, France
e-mail: aline.chu@iap.fr
[2] Instituto de Astrofísica de Andalucía, CSIC, Glorieta de la Astronomía s/n, 18008 Granada, Spain

Received 26 December 2020 / Accepted 28 January 2021

ABSTRACT

Context. Brightest cluster galaxies (BCGs) grow by accreting numerous smaller galaxies, and can be used as tracers of cluster formation and evolution in the cosmic web. However, there is still controversy regarding the main epoch of formation of BCGs; some authors believe they already formed before redshift $z = 2$, while others find that they are still evolving at more recent epochs.
Aims. We study the physical properties of a large sample of BCGs covering a wide redshift range up to $z = 1.8$ and analyzed in a homogeneous way, to see if their characteristics vary with redshift. As a first step we also present a new tool to determine for each cluster which galaxy is the BCG.
Methods. For a sample of 137 clusters with HST images in the optical and/or infrared, we analyzed the BCG properties by applying GALFIT with one or two Sérsic components. For each BCG we thus computed the Sérsic index, effective radius, major axis position angle, and surface brightness. We then searched for correlations of these quantities with redshift.
Results. We find that the BCGs follow the Kormendy relation (between the effective radius and the mean surface brightness), with a slope that remains constant with redshift, but with a variation with redshift of the ordinate at the origin. Although the trends are faint, we find that the absolute magnitudes and the effective radii tend to become respectively brighter and bigger with decreasing redshift. On the other hand, we find no significant correlation of the mean surface brightnesses or Sérsic indices with redshift. The major axes of the cluster elongations and of the BCGs agree within 30° for 73% of our clusters at redshift $z \leq 0.9$.
Conclusions. Our results agree with the BCGs being mainly formed before redshift $z = 2$. The alignment of the major axes of BCGs with their clusters agree with the general idea that BCGs form at the same time as clusters by accreting matter along the filaments of the cosmic web.

Key words. galaxies: clusters: general – galaxies: bulges

1. Introduction

Galaxy clusters are the largest and most massive gravitationally bound structures observed in the Universe. They are the perfect probes to test cosmological models and help us better understand the history of the Universe as they will constrain the limits of observed physical parameters through time, such as mass or brightness, in numerical simulations (Kravtsov & Borgani 2012). The Λ cold dark matter (ΛCDM) model proposes a hierarchical evolution scenario starting from small fluctuations that assemble together via the gravitational force, and grow to form bigger and bigger structures. As a result, galaxy clusters are the latest and most massive structures to have formed.

Clusters are believed to be located at the intersection of cosmic filaments, and to form by merging with other smaller clusters or groups of galaxies, and by constantly accreting gas and galaxies that preferentially move along cosmic filaments and end up falling towards the center of the gravitational potential well, which often coincides with the peak of the X-ray emission (see De Propris et al. 2020, and references therein). Generally, the brightest galaxy in the cluster, the brightest cluster galaxy (BCG) lies at the center of the cluster. It is usually a supermassive elliptical galaxy that is formed and grows by mergers with other galaxies, and can be up to two magnitudes brighter than the second brightest galaxy. This property makes BCGs easily recognisable. BCGs have often been referred to as cD galaxies (i.e., supergiant ellipticals with a large and diffuse halo of stars). Since their properties are closely linked to those of their host cluster (Lauer et al. 2014), they can be extremely useful to trace how galaxy clusters have formed and evolved. BCGs tend to be aligned along the major axis of the cluster, which also hints at the close link between the BCG and its host cluster (Donahue et al. 2015; Durret et al. 2016; West et al. 2017; De Propris et al. 2020). This alignment suggests that the accretion of galaxies may occur along a preferential axis, with galaxies falling into clusters along cosmic filaments.

Most of the stars in today's BCGs were already formed at redshift $z \geq 2$ (Thomas et al. 2010). BCGs, especially the most massive ones, can present an extended halo made of stars that were stripped from their host galaxy during mergers, and form the intracluster light (ICL). When measuring photometric properties of galaxies, some parameters such as the BCG major axis can be difficult to measure accurately as the separation between the ICL and the external envelope of the BCG is not clear. However, the ICL is a very faint component, and as we are observing bright galaxies the ICL should not strongly affect our study, so the ICL is not considered in this paper.

⋆ Full Tables 1–4 are only available at the CDS via anonymous ftp to cdsarc.u-strasbg.fr (130.79.128.5) or via http://cdsarc.u-strasbg.fr/viz-bin/cat/J/A+A/649/A42

The evolution of BCG properties with redshift is of interest in the study of cluster formation and evolution, but this topic remains quite controversial. Some authors report no evolution of the sizes of the BCGs with redshift (see Bai et al. 2014; Stott et al. 2011, and references therein). Stott et al. (2011) found that there was no significant evolution of the sizes or shapes of the BCGs between redshift 0.25 and 1.3; instead, Ascaso et al. (2010) found that although the shapes show little change, they have grown by a factor of 2 in the last 6 Gyr. Bernardi (2009) found a 70% increase in the sizes of BCGs since $z = 0.25$, and an increase of a factor of 2 since $z = 0.5$.

Bai et al. (2014) found that while the inner region of the galaxies does not grow much, the light dispersed around the BCG forms the outer component, resulting in a shallow outer luminosity profile. This is an indication of an inside-out growth of BCGs: the inner component forms first and then stops growing while the outer component develops. Edwards et al. (2019) gave more evidence to justify this inside-out growth of BCGs by showing that the stars in the ICL are younger and less metal rich than those in the cores of the BCGs. They also showed that the most extended BCGs tend to be close to the X-ray center. This last statement is supported by Lauer et al. (2014), who added that the inner component would have already been formed before the cluster, while the outer component, the envelope of the BCG, is formed and grows later. Numerical simulations with AGN suppressed cooling flows show that about 80% of the stars are already formed at redshift $z \approx 3$ in the BCG progenitors that merge together to form today's BCGs (De Lucia & Blaizot 2007). Cooke et al. (2019a) found that BCG progenitors in the COSMOS field have an active star formation phase before $z = 2.25$, followed by a phase of dry and wet mergers until $z = 1.25$ that leads to more star formation and increases the stellar mass of the progenitors, after which the stellar mass of progenitors mainly grows through dry mergers, and half of the stellar mass is formed at $z = 0.5$. Similarly, Cerulo et al. (2019) did not find significant stellar mass growth between $z = 0.35$ and $z = 0.05$, suggesting that most of the BCGs stellar masses were formed by $z = 0.35$. Durret et al. (2019) observed a possible variation with redshift of the effective radius of the outer Sérsic component of BCGs for 38 BCGs in the redshift range $0.2 \leq z \leq 0.9$, agreeing with a scenario in which BCGs at these redshifts mostly grow by accreting smaller galaxies.

Several conflicts also arise on the growth of the stellar masses of the BCGs. Collins & Mann (1998), Collins et al. (2009), and Stott et al. (2010) found little to no evolution. On the other hand, other studies found a strong evolution in the stellar masses of BCGs since redshift $z = 2$ (Aragon-Salamanca et al. 1998; Lidman et al. 2012; Lin et al. 2013; Bellstedt et al. 2016; Zhang et al. 2016).

In the present paper we characterize how the properties of BCGs have evolved since $z = 1.80$, based on HST data to have the best possible spatial resolution, which is particularly necessary at high redshift. When dealing with a large amount of data, identifying the BCG of a cluster to build a sample can be a long task. This is why we present here a method based on several photometric properties of the BCGs that will allow us to detect BCGs automatically. We analyzed a sample of 137 galaxy clusters, covering the redshift range $0.187 \leq z \leq 1.80$ and various types of BCGs, including star forming BCGs (SF BCGs), interacting BCGs, hosts of possible AGNs, and supercluster members.

The present paper covers a large redshift range with one of the largest samples observed with HST (see Fig. 1, which is described in more detail in the next section). This will enable us to obtain more significant statistics on the evolution of BCG properties.

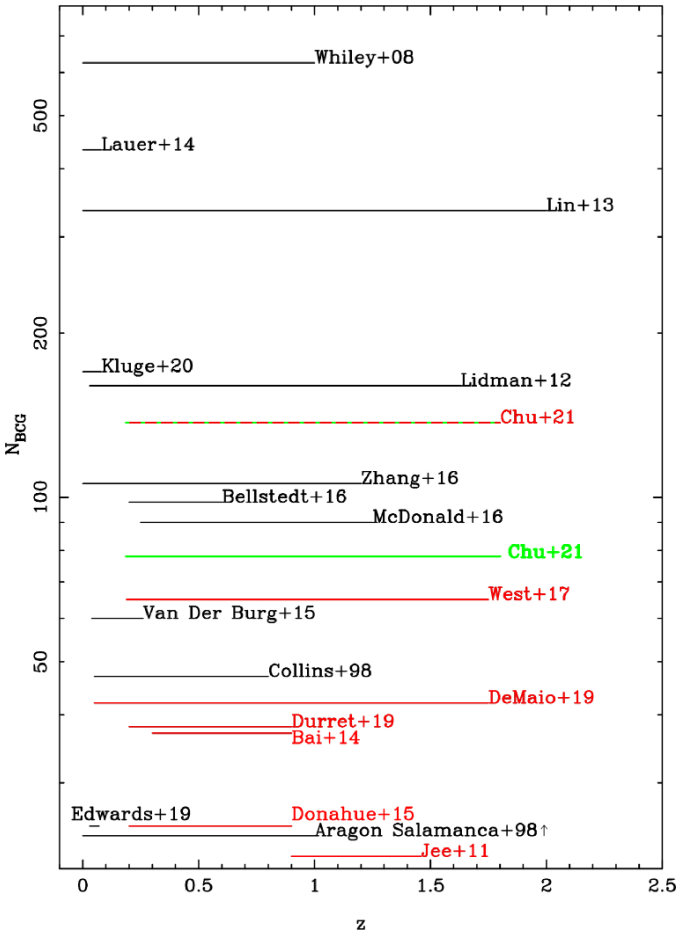

Fig. 1. Comparison of the various samples of BCGs found in the literature, considering the redshift range, the number of galaxies analyzed, and the type of data used. Only samples with at least 20 objects are represented here. Cerulo et al. (2019) with a sample of 74 275 BCGs is not represented here for reasons of legibility. The samples represented in black use ground-based telescope data, space-based data excluding HST, or a mix of ground-based and space-based data, while those in red only use HST data. Our initial sample is represented by the red and green dashed line, and our final BCG sample is in green (see Sect. 4).

The paper is organized as follows. We describe the data in Sect. 2, the method to automatically detect the BCGs in Sect. 3, and the modeling of their luminosity profiles in Sect. 4. The results obtained as well as a short study of the link between the BCG masses, the distance between the BCG and the X-ray center of the cluster, and the physical properties are given in Sect. 5. A final discussion and conclusions are presented in Sect. 6.

Throughout this paper, we assume $H_0 = 70\,\mathrm{km\,s^{-1}\,Mpc^{-1}}$, $\Omega_M = 0.3$, and $\Omega_\Lambda = 0.7$. The scales and physical distances are computed using the astropy.coordinates package[1]. Unless specified, all magnitudes are given in the AB system.

2. Sample and data

2.1. Sample

The sample studied in this paper consists of 137 galaxy clusters with HST imaging taken from Jee et al. (2011),

[1] https://docs.astropy.org/en/stable/coordinates/

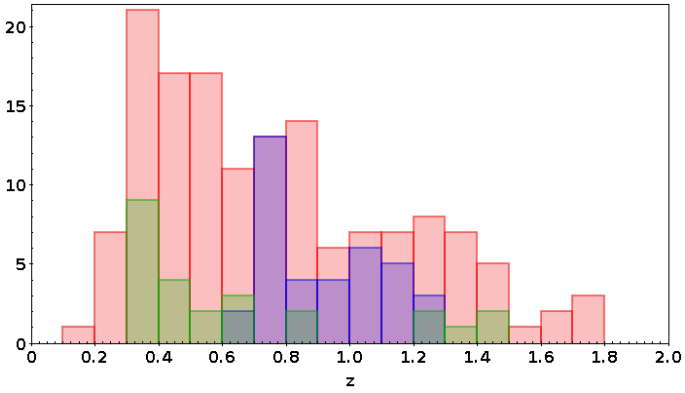

Fig. 2. Histogram of the redshifts of the 149 BCGs in our sample. The red histogram shows all the BCGs studied, while the blue histogram (37 BCGs) shows those observed in rest frame filters that are too blue compared to the 4000 Å break (see Sect. 3). The green histogram (25 BCGs) shows all BCGs with an important inner component (see Sect. 4).

Postman et al. (2012a), Bai et al. (2014), Donahue et al. (2015), West et al. (2017), DeMaio et al. (2019), Durret et al. (2019), and Sazonova et al. (2020). We also add five more distant clusters at $z \geq 0.8$, as well as the cluster Abell 2813 at $z = 0.29$. Among them, we identify 12 clusters that have in their center two BCGs similar in magnitude and size (see Sect. 3). As a result, our final BCG sample contains 149 BCGs; the number of BCGs is not equal to the number of clusters studied because of the clusters with two BCGs. This sample is a good representation of the most massive BCGs in the range $0.1 \leq z \leq 1.80$. The redshift distribution is shown in Fig. 2.

All of these clusters have data available from the *Hubble* Space Telescope, obtained with the Advanced Camera for Surveys (ACS) in optical bands and/or the Wide Field Camera 3 (WFC3) in infrared bands, resulting in good-quality images. This allows us to perform accurate photometry with relatively good precision, and to treat all the BCGs in a homogeneous way. Contrary to other studies such as Bai et al. (2014), we do not exclude from our study clusters with bright nearby objects that may hinder our measurements near the BCG area. We also identify in our sample two clusters that host blue BCGs (negative rest frame blue-red color), with active star forming regions inside the BCGs. These two BCGs will be described in more detail in Sect. 3.

Our sample covers a large redshift range, which will enable us to trace the history of cluster formation through time. Figure 1 shows the comparison of the sample sizes and redshift ranges between different studies done on BCGs[2]. Cerulo et al. (2019) studied a sample 74 275 BCGs from the SDSS in the redshift range $0.05 \leq z \leq 0.35$, and is not represented in this figure for better legibility. Most large studies, especially those with HST data (represented in red), were done exclusively on local BCGs ($z \leq 0.1$) (Lauer et al. 2014; Cerulo et al. 2019), while farther clusters and BCGs were limited to relatively small samples ($N \leq 45$) (Bai et al. 2014; DeMaio et al. 2019; Durret et al. 2019) and/or used ground-based data (represented in black). Our sample contains more clusters and BCGs at high redshifts ($z \geq 0.7$) than that of Lidman et al. (2012) (73 and 33, respectively). With the present study, we therefore almost double the previous samples and cover a larger range in redshift. This enables us to obtain more significant statistics on the evolution of BCG properties.

Lidman et al. (2012), Lin et al. (2013), West et al. (2017), and De Propris et al. (2020) mainly focus on the alignment of BCGs with their host cluster and on the evolution of the BCG stellar masses. Our work constitutes a deeper analysis since we also study the luminosity profiles of the BCGs.

2.2. Retrieving data and cluster information

We retrieved all the FITS images from the *Hubble* Legacy Archive (HLA[3]). We looked for combined or mosaic images according to what is available, and downloaded stacked images directly from the HLA. To avoid handling such heavy files, we first cropped these images, defined the new center on the cluster coordinates found in NED, and created a new image that was 1.2 Mpc wide. Linear scales (arcsec Mpc^{-1}) were determined from the cluster redshifts in the literature (from Jee et al. 2011; Postman et al. 2012a; Bai et al. 2014; Donahue et al. 2015; West et al. 2017; DeMaio et al. 2019; Durret et al. 2019; Sazonova et al. 2020, or were found in NED for the five other clusters we added). Cluster information can be found in Table 1. It was necessary to add the keywords "GAIN" and "RDNOISE" in the header of the FITS images, to be used later by SExtractor or GALFIT. As the images are in units of electrons s^{-1}, we set the GAIN to 1 and multiplied the images by the total exposure time (EXPTIME) to get back to units in electrons. Single exposure images were summed with AstroDrizzle to get the final combined images. We also retrieved the associated weight maps (wht fits) obtained applying the inverse variance map (IVM) option of AstroDrizzle.

3. Procedure for the detection of the BCG

The definition of the BCG that we use throughout this paper is the following. The BCG is the brightest galaxy in the cluster that lies close to the cluster center, defined as the center of the cluster member galaxy distribution. Generally, the cluster center is defined as the X-ray center of the cluster as X-rays trace the mass distribution better. However, it is difficult to obtain X-ray data, particularly at high redshifts. If a large sample is considered, most probably a good fraction of the clusters do not have X-ray data available. Moreover, it has been shown in several studies (Patel et al. 2006; Hashimoto et al. 2014; De Propris et al. 2020) that BCGs are often displaced from the X-ray center. For these reasons, and anticipating future works with much larger samples, we use a definition that is independent from X-rays and only relies on optical and infrared photometric data. We define the center as that of the spatial distribution of cluster galaxies (as in Kluge et al. 2020). X-ray coordinates are only available for 68 out of the 137 clusters in our sample (see Table 4). These X-ray positions are only used to study whether or not the BCG properties correlate with their position relative to the X-ray center (see Sect. 5).

3.1. Method for detecting red BCGs

The method applied to automatically select red BCG is schematically summarized in Fig. 3, and is described in detail below. The

[2] By increasing number of BCGs: Bai et al. (2014), Durret et al. (2019), DeMaio et al. (2019), van der Burg et al. (2015), West et al. (2017), McDonald et al. (2016), Bellstedt et al. (2016), Zhang et al. (2016), Lidman et al. (2012), Kluge et al. (2020), Lin et al. (2013), Lauer et al. (2014), Whiley et al. (2008), and Cerulo et al. (2019).

[3] https://hla.stsci.edu/

Table 1. Sample of the 149 BCGs studied in this paper.

Name	RA_{BCG} (J2000)	Dec_{BCG} (J2000)	Redshift	Class	Instrument	Filter	Scale (kpc/″)	Color
SPT-CLJ0000–5748	0.2504	−57.8093	0.702	1	ACS_WFC	$F814W$	7.128	$F606W-F814W$
Cl0016+1609	4.64	16.4378	0.5455	1	ACS_WFC	$F850LP$	2.83	$F606W-F775W$
SpARCS-J0335	8.9571	−43.2065	1.335	1	WFC3_IR	$F140W$	8.353	$F105W-F140W$
ACO2813	10.8528	−20.6282	0.2924	1	ACS_WFC	$F814W$	4.368	$F435W-F606W$
ACO2813	10.8548	−20.6169	0.2924	2	ACS_WFC	$F814W$	4.368	$F435W-F606W$
XDCPJ0044–2033	11.0236	−20.5651	1.59	1	WFC3_IR	$F160W$	8.42	$F105W-F140W$
RXJ0056–27	14.2374	−27.675	0.56	1	ACS_WFC	$F814W$	6.449	
SPT-CLJ0102–4915	15.721	−49.2528	0.87	1	WFC3_IR	$F105W$	7.681	$F625W-F775W$
SPT-CLJ0102–4915	15.7409	−49.2719	0.87	2	ACS_WFC	$F850LP$	7.681	$F625W-F775W$
RXJ0110+19	17.5758	19.6387	0.317	1	ACS_WFC	$F814W$	4.617	
...	...	...	...	...	...	...	...	...

Notes. The columns are: full cluster name, coordinates of the BCG, redshift, class of the BCG (if two BCGs are defined for a cluster, class 1 represents the brighter of the two), instrument, filter used to model the luminosity profile of the BCG (see Sect. 4), associated scale, color computed to extract the red sequence of the cluster (see Sect. 3). The BCGs with no values in the last column only had data in one filter, and their coordinates were taken from the literature. The full table is available at the CDS.

efficiency of the method is discussed in Sect. 3.1.4. Blue BCGs are mentioned in Sect. 3.2.

3.1.1. Rejection of foreground sources

In order to differentiate the BCG from other objects in the field, we need to identify which objects are part of the cluster and which are not. We describe below our method for detecting the BCGs among all the contaminations (stars, foreground and background galaxies, artifacts) in our images.

Measurements with SExtractor (see Bertin & Arnouts 1996, for more details on the parameters) were done using two different deblendings (parameters DEBLEND_MINCOUNT = 0.01 and DEBLEND_MINCOUNT = 0.02). The smallest deblending parameter (i.e., the finest deblending) is sufficient to separate two nearby galaxies without fragmenting excessively spiral galaxies in the foreground, and provides the most accurate measurements. However, BCGs can present a very diffuse and luminous halo which may be associated with ICL. We found that, in the presence of nearby bright sources in the region of the BCG, SExtractor would detect only those foreground sources and process the BCG halo as a very luminous background. We therefore decided to run SExtractor in parallel with a coarser deblending to take this into account. The two catalogs obtained with two different deblending parameters are then matched; we keep the values obtained with the finer deblending, and add all new objects detected using a coarser deblending.

We computed the magnitude at which our catalog is complete at 80%, $m_{80\%}$. To achieve this we plot the histogram in apparent magnitudes and fit the distribution up to the magnitude at which the distribution drops. By dividing the number of detected sources by the total number of sources expected to be detected in a magnitude bin (given by the fit), we compute the completeness of the catalog at each bin. We can then determine $m_{80\%}$, and make a cut in apparent magnitude to reject all galaxies with $m \geq m_{80\%} + 2$, as the photometry would not be accurate for these faintest objects.

Our procedure to reject the various contaminations is as follows. First, we query in NED for all the sources in the region of the cluster and reject all those with a spectroscopic redshift that differs by more than 0.15 from the cluster redshift ($|z - z_{spec}| > 0.15$). We identify bad detections by their magnitude values, which get returned as MAG = 99.99 by SExtractor. All point sources or unresolved compact galaxies are eliminated using the parameter CLASS_STAR ≥ 0.95 in SExtractor, which requires a point spread function (PSF) model to be fed into SExtractor, created with PSFex (Bertin 2011). Most foreground galaxies can be identified by their excessively bright absolute magnitude when computed from their MAG_AUTO magnitude and assuming they are at the cluster redshift. We thus exclude all sources with an absolute magnitude MAG_ABS ≤ −26.

We can identify edge-on spiral galaxies, which appear very elongated. They can be filtered by making cuts in elongation (defined in SExtractor as the ratio of the galaxy's major to minor axis). As we explain in Sect. 3.1.2, we consider two different filters. We define two different cuts depending on the filter we are looking at: in the bluest filter we apply the criterion ELONGATION ≤ 2.3, and in the reddest filter ELONGATION ≤ 2.6. The latter limit may seem quite high to filter efficiently all edge-on spiral galaxies. However, because of deblending issues, measuring with precision the lengths of the major and minor axes of the sources can be difficult, and will sometimes lead to a very elongated object. A very bright and elongated halo around the BCG, which can be linked to the ICL, will possibly return a high a/b axis ratio. This is the case for the BCG in RX J2129+0005, which has the highest a/b elongation (in the $F606W$ filter) measured in our sample, reaching $a/b = 2.57$ (see Fig. 4). As the reddest filter is more sensitive to the ICL, we prefer to define a limit that is not too strict on this filter. It does not eliminate all edge-on galaxies (which would need a lower limit), but we cannot take the risk of filtering out any of the BCGs we are looking for. This is the reason why we define a different stricter limit on the bluest filter, as it is more sensitive to the blue stellar population present in the disk of spiral galaxies, and less to the ICL.

3.1.2. Selection of red cluster galaxies

Early-type galaxies in clusters are usually easily recognizable by their red color, since they are mostly red elliptical galaxies, without star formation. While blue spiral galaxies also exist inside the cluster, they are a minority, and red elliptical galaxies draw a red sequence in a color-magnitude diagram, which has a low dispersion. We thus apply a filter in color in order to only keep the red galaxies that form the red sequence.

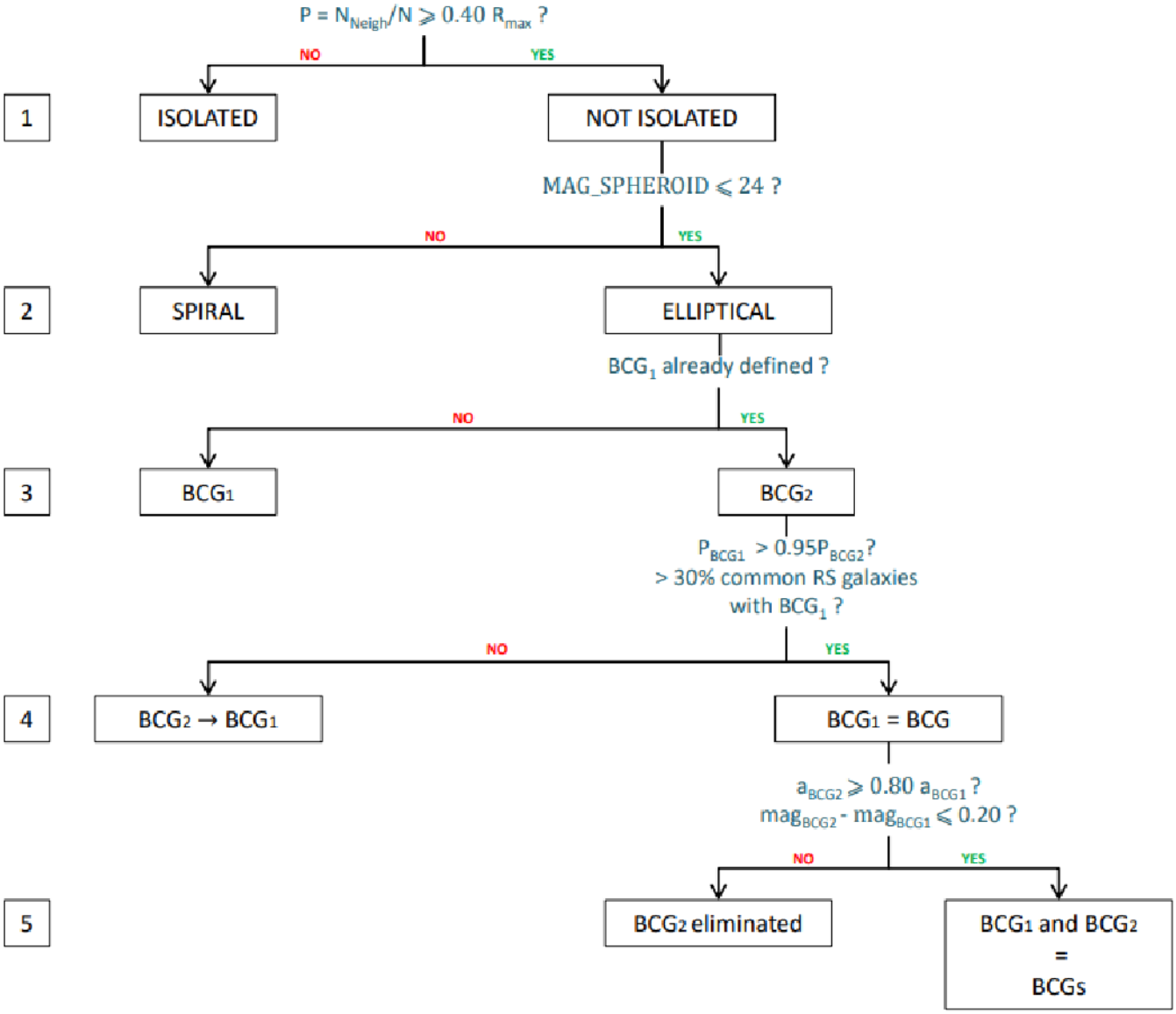

Fig. 3. Flowchart showing how BCGs are automatically selected, in the case of a rich cluster (see description of the method for our definition of a rich cluster). Values may change for less rich clusters (see Sect. 3.1.3).

To extract all the red early-type galaxies in a cluster at redshift z, we model their color using a spectral energy distribution (SED) template from Bruzual & Charlot (2003). The model is similar to the one used by Hennig et al. (2017): a single period of star formation beginning at redshift $z_f = 5$, with a Chabrier IMF and solar metallicity, that decreases exponentially with $\tau = 0.5$ Gyr. However, it differs from the Hennig et al. (2017) model on the star formation redshift; we chose a higher z_f to better model clusters at higher redshifts, while Hennig et al. (2017) limit their study to redshift $z = 1.1$. We reject all blue galaxies (blue-red ≤ 0) and all galaxies whose measured (blue-red) color differs by more than 0.60 mag from the model. While the red sequence of a cluster presents a rather narrow color-magnitude relation, and therefore very little dispersion, this large limit of 0.60 was fixed in order to take into account photometric uncertainties due to deblending issues, redshift uncertainties, or simply to the accuracy of the model used (Charlot, priv. comm.). The color is computed considering a fixed aperture of 35 kpc in diameter (parameter MAG_APER), which is large enough to contain all of the galaxy's light. All magnitudes are K-corrected (K-correction values from the EZGAL BC03 computed model), and we also take into account galactic extinction. Dust maps were taken from Schlegel et al. (1998), and reddening values for the ACS and WFC3 bandpasses were taken from Schlafly & Finkbeiner (2011), considering a reddening law $R_V = 3.1$. The colors computed depend on the filters available and on the redshift of the cluster. The color computed for each cluster can be found in Table 1.

The rest frame (blue-red) color to compute is defined as the color based on two magnitudes with the smallest wavelength difference that bracket the 4000 Å break at the cluster redshift. Depending on what filters are available for each cluster, the selected filters will differ. An example is given in Fig. 5 for a cluster at $z = 1.322$; in this case the filters bracketing the 4000 Å break are $F814W$ and $F105W$[4]. In the cases where the two optimal filters are not available, the color used to trace the red sequence galaxies at different redshifts may not be

[4] The colors $F606W-F625W$ and $F775W-F814W$ were excluded as the two filters are very close to each other.

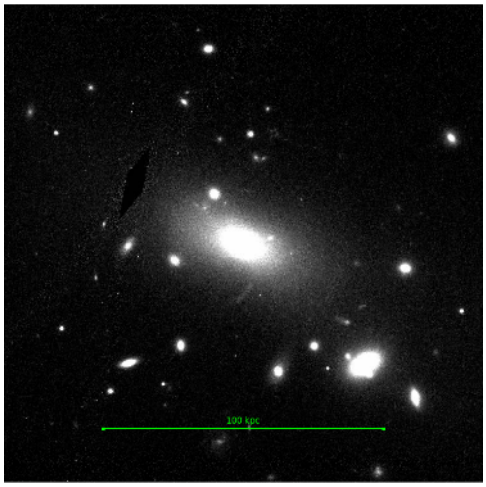

Fig. 4. BCG in RX J2129+0005 at redshift $z = 0.234$. The extended and luminous halo makes it difficult to accurately estimate the a/b axis ratio. In this case the major axis has most likely been overestimated, as the diffuse light is extended along this axis. The image was taken with the $F775W$ ACS filter.

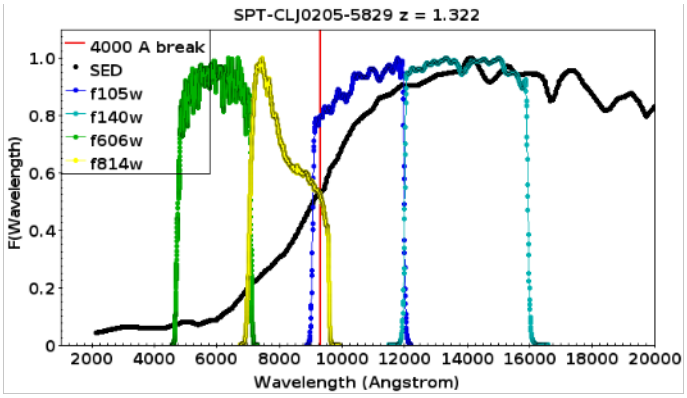

Fig. 5. SED of an elliptical galaxy from the CFHTLS (black solid line) redshifted at the cluster's redshift (SPT-CL J0295–5829, $z = 1.322$). The filter transmissions are normalized to 1 for better visualization, and the break at 4000 Å is shown as a red vertical line for reference. In this case the chosen (blue-red) rest frame color is $F814W-F105W$, and the filter chosen for the final step (modeling the luminosity profile with GALFIT) is $F140W$ (see Sect. 4).

efficient; for instance, the use of the color ($F606W-F140W$) would not optimize the selection as a galaxy at higher redshift ($z = 1.65$ for example) than the cluster redshift (here $z = 1.322$) would have the same color and would not be filtered out.

3.1.3. Rejection of spiral and isolated galaxies

The cut in colors is an important step that allows us to remove most of the spiral galaxies and to maximize the number of ellipticals in our catalogs. However, a few foreground galaxies may still remain, and we describe here the method used to remove them.

The algorithm described hereafter is applied to every single galaxy, from the brightest to the faintest, until the cluster BCG is found. We refer the reader to the sketch shown in Fig. 3. The procedure includes the following steps:

– Step 1: For each cluster we sort the catalog from the brightest to the faintest galaxies, and going down their brightnesses, we exclude galaxies that are too isolated from the rest. We define the BCG as the brightest elliptical galaxy at the center of the galaxy density distribution. To calculate the center we compute $N_{\rm Neigh}$, the number of cluster members (i.e., red sequence galaxies) found in a fixed aperture of 200 kpc radius centered on each galaxy in the final catalog, and note $N_{\rm max}$ the maximum number computed. If N is the total number of red sequence galaxies whose colors fall within 0.60 mag from the model, and $N_{\rm Neigh}$ is the number of neighbors of a given galaxy in an aperture of 200 kpc, we consider that a galaxy is isolated and unlikely to be the BCG if the ratio $P = N_{\rm Neigh}/N$ is lower than 40% of $P_{\rm max} = N_{\rm max}/N$.

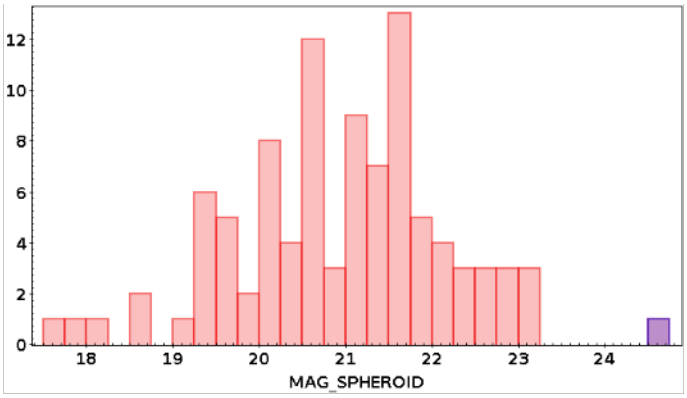

Fig. 6. Histogram of the modeled bulge magnitudes (parameter MAG_SPHEROID) returned by SExtractor. All BCGs are shown in red; the blue bin represents a spiral galaxy close to the cluster ClG J1604+4304 (see Step 2).

Considering that we cropped our images to cover a projected area of $1.2 \times 1.2\,{\rm Mpc}^2$, the aperture of diameter 400 kpc taken here represents one-third of the side of the images. This is small enough to detect high-density areas on the image, and big enough to work on clusters with a high spatial extent. After several trials adopting different values, the value of 200 kpc radius is the one that works best. Less than 200 kpc becomes too small for extended clusters, while a larger radius makes it difficult to detect the smaller density fluctuations, as the covered area becomes large. The limit defined at $R_{\rm lim} = 0.40\,R_{\rm max}$ was also determined after several tests. This condition takes into account the cluster richness and spatial extent, as well as the possible offset of the BCG relatively to the cluster center.

– Step 2: The next step consists in filtering out the last spiral galaxies that remain among the potential BCG candidates. We run SExtractor to model the potential BCG with a bulge and a disk component. We find that spiral galaxies have a very faint bulge (parameter MAG_SPHEROID); as can be seen in Fig. 6, a spiral galaxy (shown in blue) near the cluster ClG J1604+4304 prevented us from successfully detecting the BCG. We see a gap in magnitude between the spiral galaxy and the other BCGs (which are not all pure ellipticals). This enables us to define a new cut in magnitude to remove these remaining spirals: MAG_SPHEROID ≤ 24.

– Step 3: If a galaxy complies with these conditions (i.e., not being isolated and not being a spiral), we keep it as $\rm BCG_1$ if no other BCG candidate was found before, and as $\rm BCG_2$ otherwise. We do not proceed to the next step until a $\rm BCG_2$ is defined.

– Step 4: We check if there are more red sequence members in the same aperture for $\rm BCG_2$ than the number defined in Step 1 for $\rm BCG_1$ by comparing their $P_{\rm Neigh}$ ratios (defined in Step 1). We denote them $P_{\rm BCG1}$ and $P_{\rm BCG2}$. If $P_{\rm BCG1} \leq 0.95\,P_{\rm BCG2}$, and if

less than 30% of $N_{\mathrm{Neigh,BCG2}}$ are in common with $\mathrm{BCG_1}$, $\mathrm{BCG_1}$ is eliminated and we define $\mathrm{BCG_2}$ as the new $\mathrm{BCG_1}$.

The factor of 95% ensures that the overdensity in which $\mathrm{BCG_2}$ lies is significantly richer than the one in which $\mathrm{BCG_1}$ is. The second criterion on the number of galaxies common to $\mathrm{BCG_1}$ and $\mathrm{BCG_2}$ is to make sure that we are not replacing a BCG that is not at the very center of the cluster by another galaxy that is closer. This criterion is necessary to avoid eliminating BCGs that are a little offset from the center of the cluster where the density is higher. It allows us to check that the two galaxies are not in the same area in the sky; in other words, we check that $\mathrm{BCG_2}$ does not belong to the same clump (overdensity) as $\mathrm{BCG_1}$, or that the two galaxies do not belong to the same cluster.

– Step 5: This step is taken only if $\mathrm{BCG_2}$ is defined, otherwise we repeat the previous steps until it is found. If $\mathrm{BCG_1}$ and $\mathrm{BCG_2}$ are similar in size (ratio of the major axes $a_{\mathrm{BCG2}}/a_{\mathrm{BCG1}} \geq 0.80$) and brightness (magnitude difference $\mathrm{mag_{BCG2}}-\mathrm{mag_{BCG1}} \leq 0.2$), we keep both $\mathrm{BCG_1}$ and $\mathrm{BCG_2}$ as the BCGs of the cluster. Otherwise, $\mathrm{BCG_2}$ is eliminated and $\mathrm{BCG_1}$ is defined as the BCG.

The values above do not always work for poor clusters (i.e., when the number of cluster members is low or when the density of red sequence galaxies is low). There is no problem when all the cluster members are concentrated in the same area (with a size comparable to the previously defined aperture); however, if the members are dispersed over the sky and cover a large area, an aperture of 200 kpc radius becomes too small to detect density fluctuations on the sky. We thus differentiate these clusters by their number of red sequence members, N, and by the previously defined parameter P_{max} (see Step 1). We separate the poor clusters with $P_{\mathrm{max}} \leq 0.25$ and $N \leq 100$ (very extended clusters with no important density clumps), and $P_{\mathrm{max}} \leq 0.5$ and $N \leq 40$ (low number of red sequence galaxies, extended spatial distribution). We were not able to correctly determine the BCGs for these clusters by defining a 200 kpc radius aperture, so for these poorer clusters, we consider a bigger aperture of 500 kpc radius. To take into account the bigger aperture, we also modify the second criterion in Step 4. We check that the two BCGs candidates, $\mathrm{BCG_1}$ and $\mathrm{BCG_2}$, have less than 50% galaxies in common in the same aperture to guarantee that they are not both residing in the same cluster.

3.1.4. Results for detected red BCGs

Among the 137 clusters in our sample, 50 clusters only had one filter available, and were thus excluded from this procedure. For these 50 clusters without available colors, we visually checked the images to determine the BCG, and checked with X-ray maps or other studies before adding them to the final sample.

In order to assess the efficiency and accuracy of our detection method, we checked each detection visually and compared it with other studies and with any X-ray map we could find. We compared the X-ray map to the position of the detected BCG to make sure that it is not too far from the X-ray peak (but not necessarily located at the peak, in a radius of about 200 kpc).

During this verification, we found that our detection differs from that of Durret et al. (2019) and Bai et al. (2014) for the BCGs in MACS-J0717.5+3745 and SpARCS-J0224, respectively. MACS-J0717.5+3745 presents a very complex structure because is it undergoing multiple mergers (see Limousin et al. 2016; Ellien et al. 2019, and references therein). Durret et al. (2019) define the BCG as the one in the southern structure; instead, we detected a brighter galaxy in the northern structure, which we define as the BCG. We decided to keep our detection as it lies near the X-ray peak in the northern structure and is surrounded by galaxies at the cluster's redshift. We found, by checking visually, that the BCG in SpARCS-J0224 defined in Bai et al. (2014) is a spiral galaxy. We thus choose to keep our detection, which is an elliptical galaxy located just south of their detection.

A few star forming BCGs can be found in our sample. We find red BCGs with a very high star formation rate (SFR), for example MACS J0329.6–0211 at $z = 0.45$. This BCG has an almost starburst level of UV continuum and star formation (Donahue et al. 2015). Images of this BCG in the UV continuum and Hα–[NII] lines are given by Fogarty et al. (2015), illustrating the distribution of star formation throughout the galaxy. The high SFR of about $40\,M_{\odot}\,\mathrm{yr}^{-1}$ was confirmed by Fogarty et al. (2017), based on *Herschel* data. Green et al. (2016) also indicate that this galaxy hosts an AGN, and is quite blue (blue-red = −0.71), with strong emission lines and a rather high X-ray luminosity of 11.85×10^{44} erg s^{-1}.

Overall, all the red BCGs, even those that are not pure elliptical BCGs or those with colors that are not optimized because of the lack of available filters, were successfully detected with our method. We successfully detect 97% of the BCGs in our sample, and all the red BCGs are found. The method is effective in detecting red BCGs presenting different morphologies and characteristics (mergers, star forming, traces of dust in the core, disturbed).

It should be noted, however, that this method may be less reliable for poorer clusters (as defined in the previous subsection). As we were conducting several tests, trying different values of apertures in which we computed the number of red sequence galaxies or the threshold below which galaxies are considered isolated, we found that the detection efficiency for poorer clusters was more sensitive to these parameters. As this method relies on the density of red sequence galaxies in a small aperture, BCGs that are a little offset from the density peak (which is more difficult to calculate for poor clusters with an extended spatial distribution) could be eliminated, and rejected as being isolated from the other red sequence galaxies.

It is also important to note that, in the presence of more than one cluster (i.e., two clusters interacting with each other) or in the case of superclusters, only the brightest galaxy of one substructure will be detected. For MACS-J0717.5+3745 for example, the BCG of the northern clump is the brightest, and thus is the one detected by our algorithm.

3.2. Finding blue BCGs

Out of the 98 BCGs (87 clusters, 11 clusters with two BCGs) in our sample that we tried to detect, we find two peculiar BCGs with blue colors. Most brightest cluster galaxies are quiescent galaxies, and their dominant stellar population is typically red and old. As they grow by undergoing mergers through time, all their gas is consumed, and we expect the star formation to be quenched or suppressed. However, we do observe, both today and in the distant universe, BCGs with intense UV emitting filaments or knots, hinting at active star formation. Cerulo et al. (2019) found that 9% of their sample of massive BCGs in the redshift range $0.05 \leq z \leq 0.35$ from the SDSS and WISE surveys have blue colors (which they define as galaxies with colors 2σ bluer than the median color of the cluster red sequence), and are star forming. What we refer to from now on as star forming BCGs (SF BCGs), to date have only been observed in cool core clusters. Their morphology can be quite different from that of a simple elliptical galaxy, as was stated before. These galaxies can

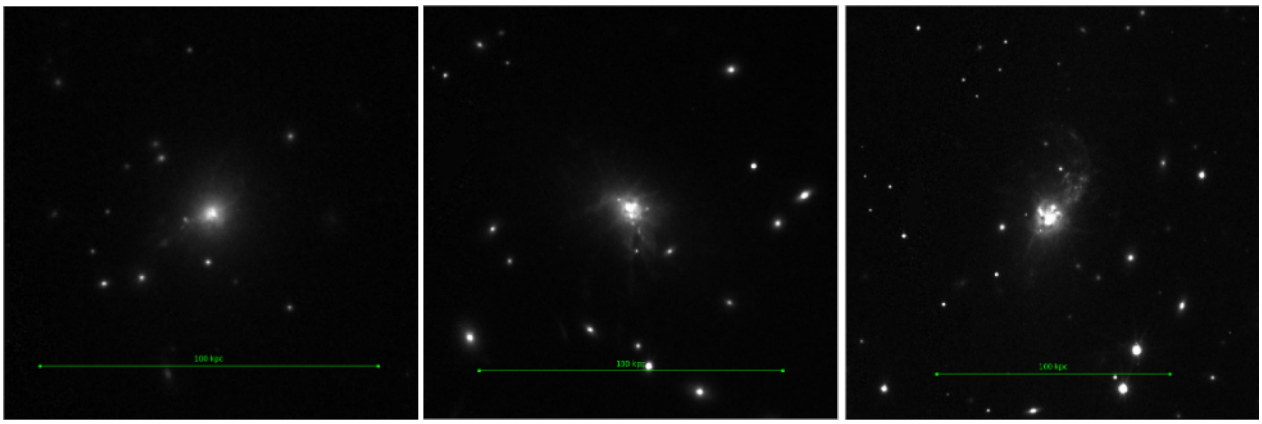

Fig. 7. *From left to right*: MACS J0329–0211 ($z = 0.45$), an example of a red star forming BCG; RX J1532+3020 ($z = 0.3615$) and MACS J1932–2635 ($z = 0.352$), the only two blue star forming BCGs in our sample.

appear disturbed, with a complex structure showing a possible recent or ongoing merger. Such examples of SF BCGs show that BCGs are not all simple ellipticals.

Two BCGs, RX J1532+3020 ($z = 0.3615$) and MACS J1932–2635 ($z = 0.352$), were not correctly detected as they are cool core BCGs with an extremely active star forming center, so they were eliminated because of their blue colors. These two BCGs were identified by eye and added manually, after checking and confirming with other studies. Their images are shown in Fig. 7.

These two BCGs are the only blue BCGs in our sample (blue meaning a negative rest frame blue-red color) out of the 98 BCGs for which we compute a color. In comparison with other studies, we find a few other BCGs that are star forming but still red.

RX J1532+3020 is one of the most extreme cool core galaxy clusters observed today, as well as one of the most massive. An intensive study by Hlavacek-Larrondo et al. (2013) shows the existence of a western and an eastern cavity, which are used to quantify the AGN feedback at the center of the galaxy. These authors estimated that this feedback would release at least 10^{45} erg s^{-1}, which would prevent the intracluster medium (ICM) from cooling, and would then allow us to solve the cooling flow problem in cool core clusters. The BCG of this cluster is a radio loud galaxy that, in its central regions, presents UV filaments and knots, as well as traces of dust, hinting at recent star formation, with a SFR of at least $100\,M_\odot\,\mathrm{yr}^{-1}$ (Castignani et al. 2020). A strong and broad Lyman-α emission and stellar UV continuum, and no other emission lines, have been observed by Donahue et al. (2016). CO with a large reservoir of molecular gas and with a high level of excitation have also been detected by Castignani et al. (2020).

MACS J1932–2635 is another cool core cluster with a huge reservoir of cold gas in the core, of mass $(1.9 \pm 0.3) \times 10^{10}\,M_\odot$, which makes it one of the largest reservoirs observed today, in which Fogarty et al. (2019) detected CO emission as well as UV knots and Hα filaments around the BCG. They measured a SFR of $250\,M_\odot\,\mathrm{yr}^{-1}$, and also observed an elongated tail that extends to the northwest, with traces of cold dust in the tail, which they suspect might be caused by a recent AGN outburst.

In order to detect these blue BCGs, we would have to relax the condition on the color. However, this condition is necessary in order to remove most of the spiral galaxies, and we find that allowing galaxies with blue colors would make the method much less reliable as the red sequence would be ill-defined. Our method is thus only reliable to detect red BCGs, even if they are not pure ellipticals (star forming or merging galaxies, for example).

4. Luminosity profiles

We fit 2D analytical models on sources with GALFIT (Peng et al. 2002). Once the BCG is defined, we run SExtractor one last time to return model fit parameters in the available filter closest to the $F606W$ rest frame at redshift z (see Fig. 5), which is at a wavelength above the 4000 Å break and thus in the spectral region where we get the highest flux. The chosen filters can be found in Table 1. We note that there are 37 BCGs out of the 149 for which HST data are not available in the $F606W$ rest frame or redder. The reddest filter is either bluer than the 4000 Å break or contains it, which means that not only are we looking at the oldest, reddest star population, but also at the youngest bluest stars. These BCGs are indicated by blue squares in the plots. The redshift distribution of all our BCGs is plotted in Fig. 2; the blue histogram represents the clusters with filters which are bluer than the 4000 Å break. These clusters observed in filters that are too blue are mainly between redshifts 0.7 and 1.2.

4.1. Masking

We first need to mask all the neighboring sources. We take the SEGMENTATION map returned by SExtractor, and unmask the BCG (which is identified by an identification number), and also mask any blank region on the image. Because of deblending issues, it is more than likely that other objects, projected on the BCG, need to be masked.

We use sharp divided images to detect any neighboring objects that pollute the signal. Sharp divided (SD) images (see e.g., Márquez et al. 1999, 2003) are obtained by dividing the images by the median filtered corresponding images. This brings out all the small neighboring sources that may have been hidden by the luminous halo of the BCG. We run SExtractor (again) on this SD image, and mask all the objects that are farther than 0.5 arcsec from the BCG coordinates (an example is given in Fig. 8), which is the minimum distance required to avoid masking the BCG center. As can be seen in Fig. 8, the sources masked based on the SD image detection seem larger on the final mask than in the SD images, as the SD image does not show the true sizes of the objects. We apply a factor of 6 to the minor and major axes of the sources detected by SExtractor on the SD image to create our final mask. This factor allows us to include all the

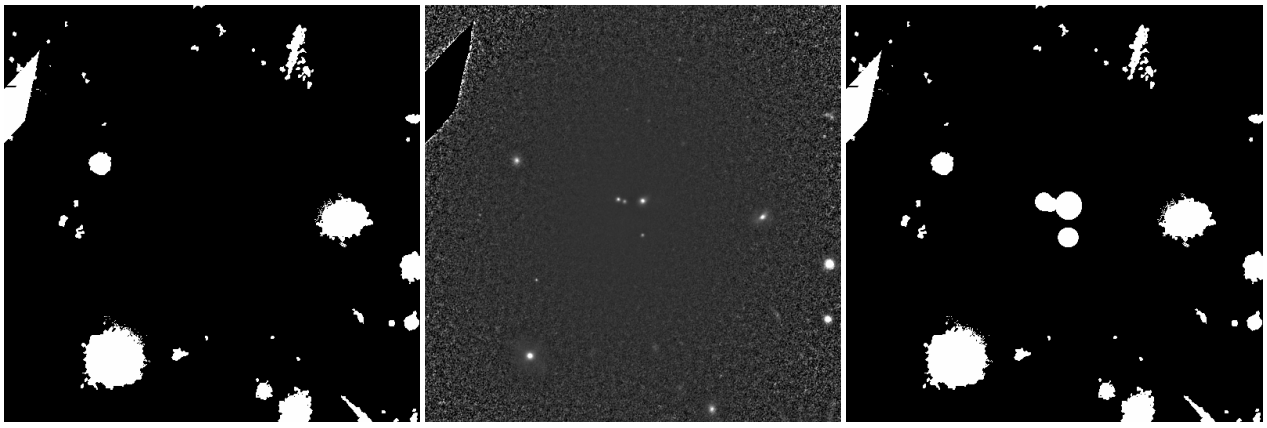

Fig. 8. Example of the BCG in the cluster Abell 2261, at $z = 0.224$. *Left*: segmentation map returned by SExtractor, with the BCG unmasked. The pixels with a value of 1 are masked; those with a value of 0 are unmasked. *Middle*: sharp divided image in which four knots in the core appear. These knots were drowned in the light of the BCG and are now visible. *Right*: final mask (including the central objects).

luminosity of the sources and to mask them efficiently. If necessary, we identify by eye and draw the regions to be masked ourselves in SAOImage DS9 and create a new mask.

4.2. PSF model

To obtain a successful model of the galaxy profiles that also works for the inner regions, an accurate description of the PSF is needed. While the PSF we used for the photometry may have been sufficient to distinguish stars from galaxies, GALFIT requires the PSF to meet a number of criteria: it must have a very high S/N and a flat and zero background (otherwise any pattern in the background will appear on the model image when convolved with the PSF); it should match the image (e.g., diffraction rings and spikes, speckle pattern); and it should be correctly centered (see GALFIT Technical FAQ).

We first subtract from the images the sky background, which is determined by masking all sources and blank areas on the cluster image, using the routine calc_background with a 3σ clipping method. We then use PSFex, and make a selective sample of the stars that will go into making the PSF. We select all point-like sources with FLAGS = 0, MAG_AUTO ≤ 21, ELONGATION ≤ 1.1, CLASS_STAR ≥ 0.98, $S/N \geq 20$, and an isophotal print ISOAREA_IMAGE ≥ 20 pixels.

Since we work on HST observations that cover a small field of view, there may not be many bright stars in the field of the cluster that we could use to compute a PSF. We tried to take several faint stars and stack them to increase the S/N of the PSF. However, we find that this often results in a PSF with an uneven background that stands out during the model fitting returned by GALFIT, and this usually ends up being a bad fit (too large effective radius, large uncertainties). Since we are working on space observations, the PSF does not vary much, and though it may vary with time, the variations should not be significant (see Martinet et al. 2017). This means that we can replace the PSF for a given filter by another one in the same filter with a better S/N. Higher S/N PSFs return better fits.

Modeled and theoretical PSFs are available for ACS/WFC and WFC3/IR. However, according to the GALFIT Technical FAQ[5], the profiles obtained with models may not be realistic for space-based images, so we prefer to use observed PSFs.

[5] https://users.obs.carnegiescience.edu/peng/work/galfit/TFAQ.html

4.3. Profile fitting

We use GALFIT to fit two different models to our BCGs: a single Sérsic component or two Sérsic components, to allow different contributions from the inner and outer parts of the galaxies. We also tried to apply other models or combinations of models including a de Vaucouleurs profile, but they always provided worse results (i.e., they gave a worse χ^2, and about 30% of the BCGs were not well fitted with one or two de Vaucouleurs profiles), so here we only discuss the results with Sérsic fittings.

It is necessary to give GALFIT an estimate of all the initial parameters: the effective surface brightness or total magnitude, the effective radius (the radius at which half of the total light of the galaxy is contained), and the elongation or the position angle (PA) of the BCG. These initial guesses are taken from the SExtractor catalogs: MU_EFF_MODEL or MAG_AUTO, FLUX_RADIUS, ELONGATION, and THETA_IMAGE. We did not have an estimate of the BCG Sérsic index, so we started from the value corresponding to the de Vaucouleurs profile: $n = 4$. If the fitting does not converge, we try different Sérsic indices in the range 0.5−10. For the second Sérsic component that accounts for the inner part, the following parameters are considered: MU_EFF_SPHEROID, SPHEROID_REFF_IMAGE, SPHEROID_SERSICN, and SPHEROID_THETA_IMAGE. The suffix SPHEROID refers to the bulb component when SExtractor tries to model a disk and a bulb to a galaxy. We consider an elongation (minor-to-major axis ratio, b/a) of 0.90 for the inner part, as an initial guess. The region to fit is a box that is $2.5\,r_{\rm Kron}$ wide (cf. GALFIT FAQ), $r_{\rm Kron}$ being the Kron radius returned by SExtractor. This is large enough to contain all the light from the BCG as well as some sky background, and is a good compromise to obtain good fits of our galaxies.

We first run GALFIT to fit the BCGs with one Sérsic component. If it does not manage to converge with a Sérsic index of $n = 4$, we try different values between 0.5 and 10 until it converges to a meaningful fit, and reject any fit with returned effective radius larger than half the size of the fitting region, which is to say $R_{\rm e} \leq 2.5\,r_{\rm Kron}/2$ pixels. We then use the output parameters as initial guesses to fit the outer part of the galaxy and add another Sérsic component to fit the inner part of the galaxy. If it does not converge towards meaningful values, we increment the Sérsic index until it manages to fit the BCG. For pairs of BCGs (two brightest cluster galaxies with similar sizes and magnitudes), we fit both of them simultaneously.

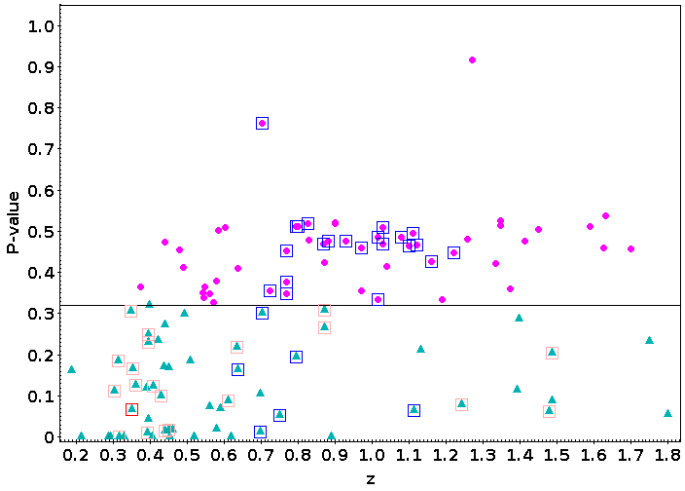

Fig. 9. Distribution of P-values as a function of redshift considering a model with one Sérsic component (magenta), and a model with two Sérsic components (cyan). BCGs that could not be fitted by either model are not included.

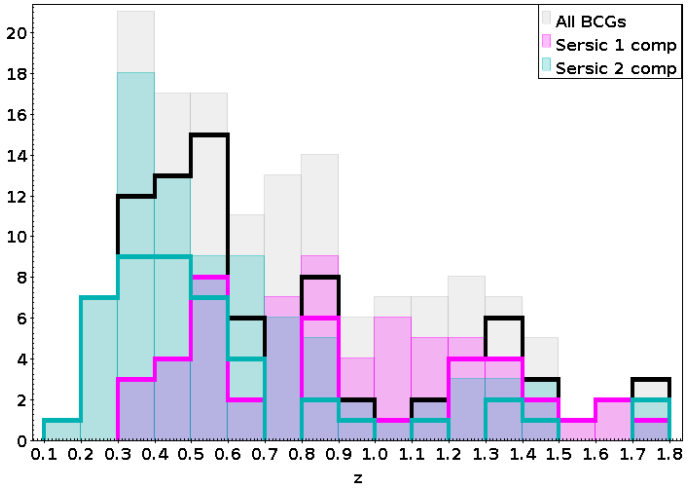

Fig. 10. Distribution of redshifts for each model: a single Sérsic component (magenta) and two Sérsic components (cyan). The overall distribution is shown in gray. The semi-filled histograms represent the initial sample, and the unfilled histograms only contain BCGs with appropriate data.

4.4. Choice of best fit model

The quality of the fit can be estimated from the reduced χ^2 (χ^2_ν), which should be close to 1. From our results we find that $\chi^2_\nu > 1.2$ and $\chi^2_\nu < 0.8$ often indicate a bad fit. This happens when the model used to fit the BCG is not adapted, or when the initial parameters given are bad estimates. In this case, GALFIT may also not have converged and/or crashed. To decide whether a second component is really necessary to fit the BCG, or if one component gives equally good results, we use the F-test (Simard et al. 2011; Margalef-Bentabol et al. 2016). As stated in Bai et al. (2014), as the background noise is not Gaussian, the meaning of χ^2_ν is not as significant, and when comparing two models a χ^2_ν closer to unity does not necessarily mean that it is a better fit. So we prefer to use an F-test.

The F-test states that if the P-value, determined from the F-value and the number of degrees of freedom, is lower than a probability P_0, then we can reject the null hypothesis and consider that the second model gives a significantly better result than the simpler one. The F-value is defined as the ratio of the reduced chi-squared values of the two models. GALFIT returns the χ^2 and the χ^2_ν of the fit, but instead of directly considering the output χ^2_ν computed by GALFIT, we compute χ^2_ν as

$$\chi^2_\nu = \frac{\chi^2}{n_{\mathrm{d.o.f.}}} \tag{1}$$

with $n_{\mathrm{d.o.f.}}$ the number of degrees of freedom, which is defined here as the number of resolution elements, n_{res}, minus the number of free parameters in the model, n_{free}. n_{res} can be calculated as (see Simard et al. 2011; Margalef-Bentabol et al. 2016)

$$n_{\mathrm{res}} = \frac{n_{\mathrm{pixels}}}{\pi\theta^2}, \tag{2}$$

where n_{pixels} is the number of unmasked pixels used for the fitting, and θ is the full width at half maximum (FWHM) of the given PSF in units of pixels, and $n_{\mathrm{d.o.f.}}$ is then

$$n_{\mathrm{d.o.f.}} = n_{\mathrm{res}} - n_{\mathrm{free}} - 1. \tag{3}$$

The P-value is then calculated with the routine f.cdf from scipy.stats in python. We set $P_0 = 0.32$, which represents a 1σ threshold value (Margalef, priv. comm.).

We show the distribution of P-values as a function of redshift in Fig. 9. A P-value $\leq P_0$ means that we need a second component to correctly model the BCG light distribution. We do not represent in this plot the BCGs that could not be fitted by either model: 9 BCGs could only be fitted with a single component, 22 could only be fitted with two components, 2 could only be fitted by fixing the Sérsic index $n = 4$ (de Vaucouleurs profile), and 2 BCGs could not be fitted or returned a poor fit for either of the models. In Fig. 10 it appears that BCGs that need a second component to obtain a good fit tend to be at lower redshifts (peak at $z = 0.3$), while the distribution for those that were well fitted with a single component is flatter. We also find BCGs with a model with two Sérsic profiles at higher redshifts (14 BCGs at $z \geq 1.0$). If the chosen model depended on the distance, we would have expected not to have two component BCGs at higher z, which is not the case.

We must remember that part of our sample (37 BCGs) is studied in a too blue rest frame filter, and for these clusters we are not looking at the same star population. Without taking into account those observed in too blue filters, we find that 55 out of 72 BCGs (76%) at redshift $z \leq 0.8$ need a second component, while the trend is reversed at $z > 0.8$, as 23 out of 38 BCGs (61%) can be nicely modeled with only one component. We also find that most of the BCGs observed with too blue filters (62%) can be modeled with only one Sérsic.

We also want to discover if the existence of these two distinct populations (BCGs with two components at low z, and BCGs with a single component throughout redshift), with a limit around redshift $z = 0.8$, may be due to the fact that BCGs at higher redshifts are less resolved than their lower redshift counterparts. To test this hypothesis, we bring a sample of 44 BCGs at redshifts $z \leq 1.0$ to a common physical scale at redshift $z = 1.2$. We smooth the images with a Gaussian and repeat the previous steps. The σ_{gauss} of the Gaussian to apply is calculated as

$$\sigma_{\mathrm{gauss}} = \sqrt{(\sigma^2_{z=1.2} - \sigma^2_{z,\mathrm{cluster}})}$$

with $\sigma_{z,\mathrm{cluster}}$ computed from the FWHM of the image we want to degrade, and $\sigma_{z=1.2}$ the σ at the reference redshift $z = 1.2$, which was computed as

$$\sigma_{z=1.2} = \sigma_{z,\mathrm{cluster}} * \frac{\mathrm{pixscale}_{z=1.2}}{\mathrm{pixscale}_{z,\mathrm{cluster}}}.$$

Of the 44 BCGs at $z \leq 1.0$ on which we did this test, 30 returned results similar to those obtained with the original (unsmoothed) images. We also found that seven BCGs that were better fitted with two Sérsic components can be modeled just as well, according to the F-test, with only one Sérsic after smoothing the images. Surprisingly, the opposite also happened for seven other BCGs: four could not initially be fitted with two components and the other three were close to the P-value limit, $P_{\mathrm{lim}} = 0.32$. As 68% of the tested BCGs showed no significant difference, we can confirm that the lack of resolution for the farthest BCGs does not cause the absence of an inner component for BCGs at higher redshifts.

4.5. BCGs observed in too blue filters

In all that follows, when considering together the results from BCGs better fit with one or two Sérsic components, we consider the values obtained for the outer Sérsic component ($R_{\mathrm{e,out}} \geq R_{\mathrm{e,in}}$).

As stated before, we have 37 BCGs observed in too blue filters (relative to the 4000 Å break). We must determine if they can be taken into account in our final study. For this, we run a test on 40 clusters with filters available on the blue side of the 4000 Å break as well as appropriate red filters, to check if the returned parameters vary depending on the filters chosen. We find that the absolute magnitude and mean effective surface brightness become fainter as the filter gets bluer. However, the dispersion is too big to simply correct for the offset to bring the BCGs observed in too blue filters to the appropriate red ones, perhaps because the filters on the blue side of the break do not always fall in the same spectral region on the SED (as the SED varies with redshift, and not all clusters were observed with the same filters). The effective radii can have their sizes halved when observed with too blue filters. As for the Sérsic indices, we find that the BCGs that need a second component tend to have Sérsic indices in bluer filters consistent with those measured in the appropriate red filters. The BCGs which could be fitted with only one Sérsic have indices that vary without any clear pattern. These observations show that we cannot directly consider together the measurements obtained looking at different parts of the SED. Therefore, we chose to exclude the BCGs observed in too blue filters in what follows.

We find however that the position angles (PA) of the BCGs are not affected and remain consistent regardless of the filter chosen (see Fig. 11). The PAs of these BCGs will thus be kept. Only one point presents a big difference between the two values ($\mathrm{PA_{red}}$–$\mathrm{PA_{blue}} > 120°$). We found that the ICL associated with this BCG is more extended in the reddest filter; Ellien et al. (2019), also show that the ICL tends to be more extended in redder filters. The other BCGs with a significant difference between the values measured in the two different filters are circular in shape ($b/a > 0.80$), so the PAs are ill-defined, which also explains the huge error bars.

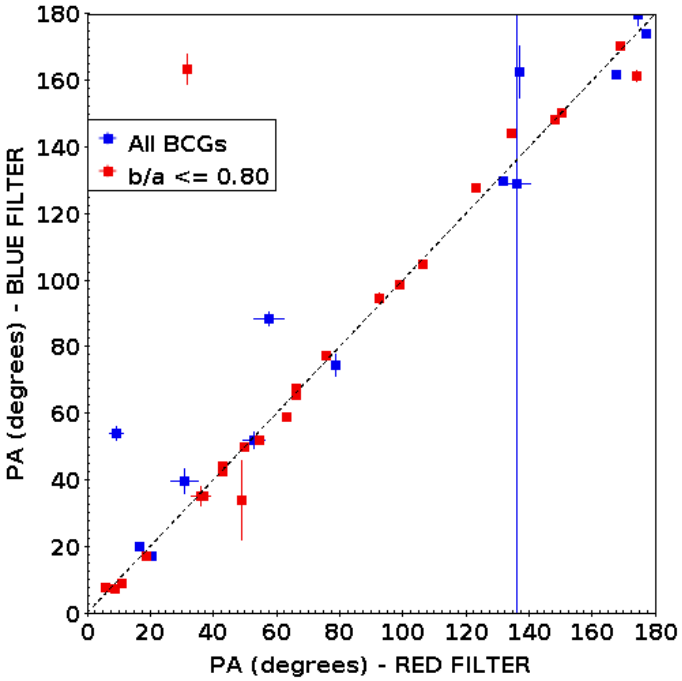

Fig. 11. PA measured in the appropriate red filter (x-axis), and measured in a too blue filter (y-axis). In red are BCGs with elongations $b/a \leq 0.80$.

5. Results

As explained above, we tried fitting the BCGs with one or two Sérsic profiles. In the following the values plotted are those from the best model determined using the F-test (see previous section). The resulting parameters are summarized in Tables 2 and 3.

Two BCGs were not properly fitted by either model, but were correctly fitted by fixing the Sérsic index $n = 4$ (corresponding to a de Vaucouleurs profile). We thus kept the parameters obtained with this fit. Two other BCGs were not correctly fitted by either model, and were thus excluded, bringing our sample size to 147 BCGs.

We summarize the total number of galaxies that were fit with each model:

– Sérsic (1 component): 63 BCGs;
– Sérsic + Sérsic (2 components): 84 BCGs.

Without taking into account the BCGs observed in too blue filters we have:

– Sérsic (1 component): 40 BCGs;
– Sérsic + Sérsic (2 components): 70 BCGs.

In all the plots shown in this paper, the BCGs better fitted with two Sérsic components will be represented with triangles, and those fitted with only one component with diamonds.

Before drawing conclusions, we need to know if we can consider together the results from BCGs better fit with one and with two Sérsic components. In principle, the two subsamples can be put together if, for the two components, we assume that the outer component contains most of the light of the BCG and that the outer profile represents well enough the overall luminosity of the galaxy. The more important the contribution of the inner component to the total luminosity of the BCG is, the less accurate this statement will be. If an inner component is required to model the BCG, then the resulting outer profile obtained when fitting two components may not be comparable to a profile obtained with only one component.

We show the histogram of the ratio of the inner component to total fluxes for the 70 BCGs requiring two Sérsic components (see Fig. 12), and find that 24 BCGs present a very important inner component, which can contribute up to 30% of the total luminosity of the galaxy. If we choose to ignore these 24 BCGs, no obvious difference can be seen in the overall

Table 2. Parameters obtained from fitting the luminosity profiles of the BCGs with GALFIT.

Name	Class	Model	M_{ABS} (mag)	$\langle\mu_e\rangle$ (mag arcsec^{-2})	R_e (kpc)	n	b/a	PA (degrees)	Alignment (degrees)
SpARCS-J0335	1	Sérsic	−26.088	25.034	57.488	8.7	0.88	158	4
XDCPJ0044–2033	1	Sérsic	−25.073	23.119	12.944	3.39	0.36	11	63
CLJ0152–1357	1	Sérsic	−24.859	23.471	21.802	3.59	0.7	49	
CLJ015244.18–135715.84	2	Sérsic	−24.378	22.698	12.74	4.24	0.75	42	
CLJ015244.18–135715.84	1	Sérsic	−24.478	22.343	11.331	7.96	1.0	10	
RCSJ0220–0333	1	Sérsic	−24.511	23.111	10.804	4.08	0.75	24	64
RCSJ0221–0321	1	Sérsic	−23.916	22.257	5.667	0.88	0.61	111	63
RCSJ0221–0321	2	Sérsic	−24.566	23.098	11.261	5.43	0.74	21	27
XLSSJ0223–0436	1	Sérsic	−24.675	23.103	8.146	4.52	0.74	47	69
...	...	...	...	...	...	...	...	...	...
SPT-CLJ0000–5748	1	Sérsic2	−25.601	24.306	47.94	1.85	0.53	162	8
ACO2813	1	Sérsic2	−24.891	23.516	49.81	4.7	0.72	175	
ACO2813	2	Sérsic2	−24.894	23.362	46.464	1.3	0.53	148	
RXJ0056–27	1	Sérsic2	−24.641	23.613	28.883	1.83	0.64	94	
SPT-CLJ0102–4915	1	Sérsic2	−24.87	22.478	13.894	1.62	0.87	118	29
SPT-CLJ0102–4915	2	Sérsic2	−25.753	22.069	15.653	1.26	0.57	134	13
RXJ0110+19	1	Sérsic2	−24.411	22.709	26.043	1.1	0.72	44	
Abell209	1	Sérsic2	−24.327	21.734	19.715	2.05	0.71	134	23
SPT-CLJ0205–5829	1	Sérsic2	−25.701	26.197	82.853	1.09	0.33	32	8
XMMXCSJ022045.1–032555.0	1	Sérsic2	−24.403	21.638	16.486	2.34	0.91	65	
...	...	...	...	...	...	...	...	...	...

Notes. Only the parameters obtained for the chosen model are shown. If fitted by two Sérsic profiles, the parameters of the outer component are given (the parameters for the inner component are then given in Table 3). The columns are: full cluster name, class of the galaxy, best model (Sérsic is a model with a single component, Sérsic2 is a model with two components, and Sérsic* fixes the Sérsic index $n = 4$), absolute magnitude, mean effective surface brightness, effective radius, Sérsic index, elongation (ratio of the major to minor axis), position angle, alignment of the BCG with its host cluster. The full table is available at the CDS.

Table 3. Parameters obtained for the inner component, for BCGs fitted with two Sérsic profiles.

Name	Class	$M_{ABS,inn}$ (mag)	$\langle\mu_{e,inn}\rangle$ (mag arcsec^{-2})	$R_{e,inn}$ (kpc)	n_{inn}	b/a_{inn}	PA_{inn} (degrees)
SPT-CLJ0000–5748	1	−23.363	22.079	6.133	1.18	0.66	−6
ACO2813	1	−22.077	19.314	1.968	0.37	0.76	−3
ACO2813	2	−23.127	21.373	8.236	2.03	0.87	−45
RXJ0056–27	1	−23.153	22.119	7.314	4.47	0.89	−32
SPT-CLJ0102–4915	1	−23.625	19.466	1.956	1.6	0.73	−12
SPT-CLJ0102–4915	2	−24.621	19.962	3.521	1.54	0.47	−48
RXJ0110+19	1	−23.367	19.475	3.634	2.32	0.92	23
Abell209	1	−20.251	17.611	0.452	1.28	0.93	68
SPT-CLJ0205–5829	1	−24.978	23.76	19.333	7.67	0.72	−19
XMMXCSJ022045.1–032555.0	1	−21.69	18.129	0.939	1.51	0.72	67
...	...	...	...	...	...	...	...

Notes. The columns are: full cluster name, class of the galaxy, absolute magnitude, mean effective surface brightness, effective radius, Sérsic index, elongation (ratio of the major to minor axis), position angle. The full table is available at the CDS.

relations observed in the following. However, we prefer to exclude them as the outer profile may not be comparable to the profile obtained with a single component modeling most of the light of the galaxy. After excluding the galaxies with a very bright inner component and those observed in too blue filters, we obtain the final numbers:

– Sérsic (1 component): 40 BCGs;
– Sérsic + Sérsic (2 components): 46 BCGs.

In the following plots, BCGs observed in too blue filters are indicated by blue squares, and those fit with two Sérsic profiles and with an important inner component are indicated by light pink squares. We also identify the blue SF BCGs (cf. Sect. 3) with red squares and pairs of BCGs with black triangles.

5.1. Evolution with redshift

In order to study the evolution of the BCGs, we consider the dependence of the derived parameters as a function of redshift.

The absolute magnitudes of the BCGs, computed from the total apparent magnitudes (see Table 1 for the filters considered)

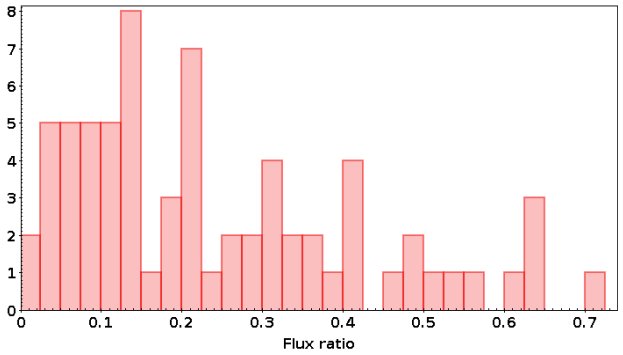

Fig. 12. Histogram of the ratio of the flux of the inner component to the total flux of the BCG, for clusters better fit with two components. Clusters observed in too blue filters are excluded in this plot.

calculated by GALFIT, despite the very big dispersion (4 mag thoughout redshift) tend to become brighter with redshift (see Fig. 13, left). The trend is faint, and can be quantified with a correlation coefficient $R = -0.29$ and a p-value $p = 0.006563$ (calculated from the coefficient R and the number of data points N[6]). By taking a significance level of $\alpha = 0.05$, we show that we can reject the null hypothesis ($p < \alpha$) and conclude that the trend is significant.

There is a moderate trend for BCGs to grow with time (Fig. 13, right), as those with the smallest effective radii are at higher redshifts ($z \geq 1.2$). The trend in logarithmic scale is quantified by a correlation coefficient $R = -0.40$, and with a p-value of $p = 0.000142$. BCGs observed in too blue filters generally have smaller effective radii than the others at a given redshift. Those with an important inner component contribution do not appear to occupy a special place in these relations.

The mean effective surface brightness (Fig. 14) shows no significant evolution as a function of redshift ($R \ll 0.1$), with a very large dispersion (spanning 6 mag at $z \geq 1.25$). Seven BCGs at higher redshifts ($z \geq 1.4$) can be seen among the galaxies with the brightest mean effective surface brightnesses ($\langle\mu\rangle \leq 22$ mag arcsec^{-2}). We confirm that nothing peculiar was observed with these BCGs. Those observed in too blue filters and those with an important inner component contribution do not occupy a specific place in the relation.

The vertical gradient in color in Fig. 14 shows that the large dispersion is also linked to the effective radius. As we go towards the biggest BCGs (increasing effective radii), the relation is shifted towards the fainter mean effective surface brightnesses. This is to be linked with the Kormendy relation, which is shown in Sect. 5.2.

Finally, there is no correlation between the Sérsic index and redshift (Fig. 15, left). However, in the right panel, we see two different populations: the BCGs that were modeled with only one component generally have high Sérsic indices with a strong peak at $n_{1\mathrm{comp,mean}} = 4$ (without considering the BCGs observed in too blue filters), while the BCGs that were better modeled with two Sérsic components with lower Sérsic indices show a peak at $n_{2\mathrm{comp,mean}} = 2.0$.

5.2. Kormendy relation

The Kormendy relation (Kormendy 1977) links the (mean) effective surface brightness of elliptical galaxies to their effective radius. This relation is plotted in Fig. 16. The different colors represent different redshift bins: $z \leq 0.3$, $0.3 < z \leq 0.5$, $0.5 < z \leq 0.9$, $0.9 < z \leq 1.3$, and $z > 1.3$. We show that all the BCGs seem to follow the Kormendy relation with the same slope, but the ordinate at the origin of the line decreases with increasing redshift.

While applying a linear regression to the relation obtained in each redshift bin ($R > 0.80$, $p < \alpha$), we find that the slope remains quite constant at all redshift bins, $m = 3.33 \pm 0.73$, whereas the ordinate at the origin varies as $c = 2.15 * z + 16.65$.

5.3. Inner component

The sample requiring an inner component consists of 46 BCGs. We find that the inner component follows a Kormendy relation (Fig. 17), and is a continuation of the Kormendy relation shown in Fig. 16 at brighter mean effective surface brightness and smaller effective radius ($R_{\mathrm{e,inn}} \leq 20$ kpc).

We observe a very faint trend for the inner components to have brighter surface brightnesses with decreasing redshift, but the trend is not significant ($R = 0.27$, $p = 0.06237 > \alpha$). We do not find any clear correlation (correlation coefficient $\leq$0.2) between redshift and the absolute magnitude, effective radius, or Sérsic indices of the inner component of the BCGs.

5.4. Alignment of the BCG with its host cluster

Some studies have shown that BCGs tend to have a similar orientation, or PA, to that of their host cluster (West et al. 2017; Durret et al. 2019). As a comparison, we reproduce this study and compare our results with those of these two papers. The PA of the host clusters are taken from West et al. (2017) (computed from the moments of inertia of the distribution of red sequence galaxies) and Durret et al. (2019) (computed from density maps of red sequence galaxies), and the PAs of the BCGs are measured here with GALFIT. If measurements are given in both papers, the $\mathrm{PA_{cluster}}$ in Durret et al. (2019) was used, unless the $\mathrm{PA_{cluster}}$ is ill-defined (when the clusters are circular in shape), in which case the PA from West et al. (2017) was used. We did not measure the PA of the host clusters for the clusters that are not presented in the above-quoted papers as our images are not large enough to accurately measure the full extent and shape of the cluster.

We include all BCGs for which the PA of the cluster was measured (73 BCGs), including those observed with too blue filters, as the PA measured by GALFIT is the same regardless of the filter (see Fig. 11). We show the histogram of the alignment between the BCGs and their host clusters (defined as the difference of PA between that of the cluster and the BCG) in Fig. 18.

We find that 39 BCGs (53%) are aligned with their host cluster with a difference smaller than 30°. This already shows a tendency for BCGs to align with their host clusters, as a random orientation of the BCGs would result in a flat distribution. BCGs with the highest PA difference tend to be circular in shape (elongation $= b/a \approx 1$, for which it is more difficult to measure a PA, resulting in high uncertainties). We thus chose to exclude all BCGs with axis ratio $b/a \geq 0.8$, in order to eliminate BCGs with ill-defined PAs, as shown in red in the histogram. We then find that 32 out of 58 of BCGs are aligned with their host cluster within 30°, slightly increasing the percentage to 55%. There is a secondary peak between a PA difference of 30 to 40°, mainly corresponding to BCGs at redshift $z \geq 0.9$. At such high redshifts, galaxies appear smaller, and therefore the accuracy of the measured PA is probably worse. If we only consider galaxies at $z \leq 0.9$ (blue histogram), we find that 22 BCGs out of 30 (73%)

[6] https://www.socscistatistics.com/pvalues/pearsondistribution.aspx

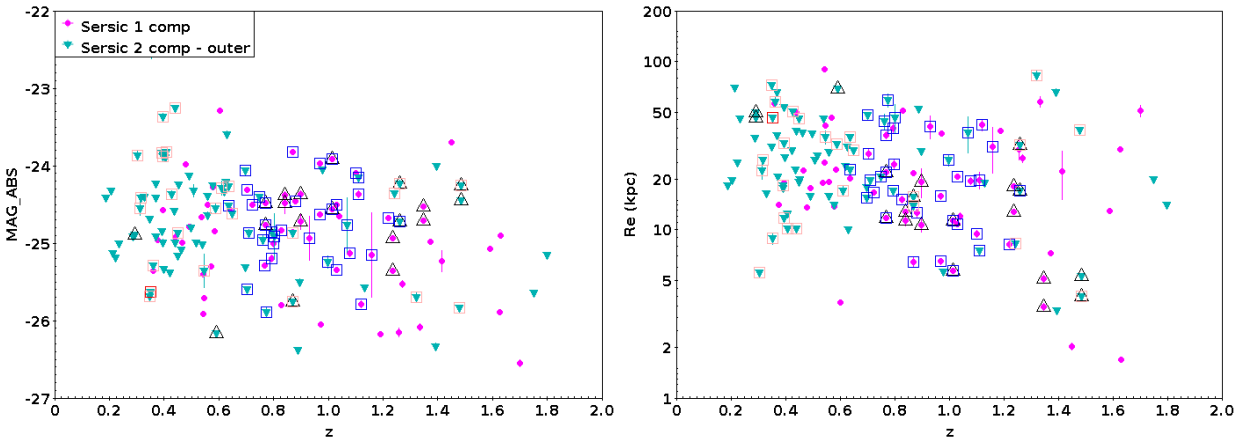

Fig. 13. *Left*: absolute magnitude and *Right*: effective radius in logarithmic scale as a function of redshift. Cyan triangles are BCGs fit by two Sérsic components (the outer component is considered), while the magenta points are BCGs fit with only one Sérsic component. Blue squares represent the BCGs observed in too blue filters, red squares are SF BCGs (see Sect. 3), black triangles are pairs of BCGs, and the light pink squares are BCGs with an important inner component contribution.

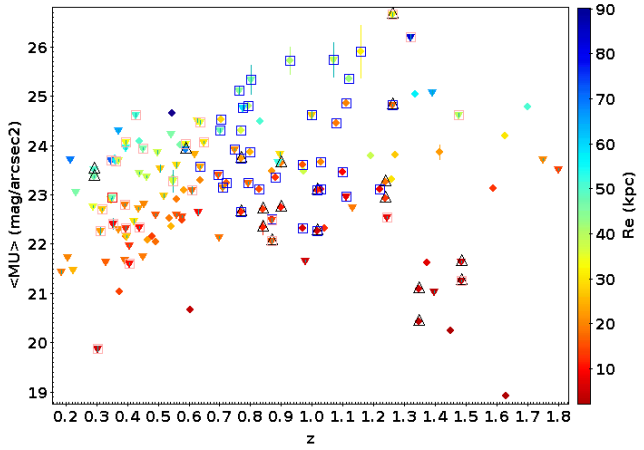

Fig. 14. Mean effective surface brightness as a function of redshift (color-coding as in Fig. 13). Additional information on the effective radii of the BCGs is shown on the right of the figure.

align with their cluster within less than 30°. This shows that most BCGs tend to align with their host cluster at least at $z \leq 0.9$.

5.5. BCG physical properties as a function of host cluster properties

We browsed the available bibliography to retrieve the cluster masses and X-ray center coordinates. The corresponding data can be found in Table 4. We preferred lensing-based mass estimates if they were available. We brought all the masses to M_{200}, applying the conversion factor between M_{500} and M_{200}: $M_{500} = 0.72\,M_{200}$ (Pierpaoli et al. 2003).

We show the richness of the cluster as a function of redshift and cluster mass in Fig. 19. The richness N of the cluster is defined here as the number of red sequence galaxies (found in Sect. 3) in an aperture of 500 kpc radius around the BCG. We obtain different values of N for two different BCGs in the same cluster because the richness is computed in an aperture centered on each BCG.

As can be seen in Fig. 19 (left panel), clusters seem to become richer with decreasing redshift (correlation coefficient in logarithmic scale $R = -0.70$ and p-value of $p < 10^{-5}$). Clusters at higher redshifts ($z \geq 1.0$) have a lower richness, with a number of detected red sequence galaxies $N \leq 60$. The right panel also shows that the most massive clusters are also the richest, and the high-redshift clusters (blue points on the plot) with a low richness are also the least massive ($M_{200,c} \leq 5 \times 10^{14}\,M_{\odot}$). This low value of N could in principle be due to the depth of our images as we have a bias due to the distance: at higher redshifts it is more difficult to detect objects, and only the brightest ones can show up.

However, when looking at Fig. 20, the left panel shows that we do not observe very massive clusters at high redshifts. So we have no bias due to the distance of the galaxies when measuring cluster masses: the masses are measured via lensing or derived from X-ray or SZ maps, which are independent of distance. Thus, we conclude that clusters become richer with time, and this result is not due to the depth of our images. However, although we only observe very massive clusters at lower redshifts ($M_{200,c} \geq 30 \times 10^{14}\,M_{\odot}$ at $z \leq 0.8$), the masses of the clusters do not vary much with time ($R < 0.20$). The right panel shows that the very massive clusters only host bigger BCGs: clusters with masses $M_{200,c} \geq 25 \times 10^{14}\,M_{\odot}$ only have BCGs with effective radii $R_e \geq 30$ kpc. We find no correlation ($R \leq 0.2$) between the BCG surface brightnesses or Sérsic indices and the cluster masses.

Using the relation given in Bai et al. (2014), we compute an estimate of the BCG masses from the cluster masses: $M^{*}_{\rm BCG} \propto M^{0.6}_{\rm cluster}$. We find that the most massive BCGs are also the biggest (moderate correlation with $R = 0.46$ and $p = 0.00007$) and also tend to be brighter ($R = -0.32$, $p = 007353$). No correlation between the BCGs masses and redshift is seen ($R < 0.20$).

We also study how the BCGs behave depending on their offsets to the cluster X-ray center. We exclude superclusters and clusters that present several substructures and/or several BCGs. We show the histogram of the offsets in Fig. 21, top left panel. We find that 31 out of 61 (51%) are within a 30 kpc radius range from the X-ray center of the cluster, showing that BCGs tend to lie close to the cluster X-ray centers. The two star forming BCGs that have undergone recent mergers and are not at equilibrium are also located at the center of the cluster ($D_X \leq 10$ kpc). We confirm, however, that there can be a significant offset between the two: 12 out of 61 BCGs (20%) present an offset bigger than 100 kpc. Although the corresponding plots are not shown here,

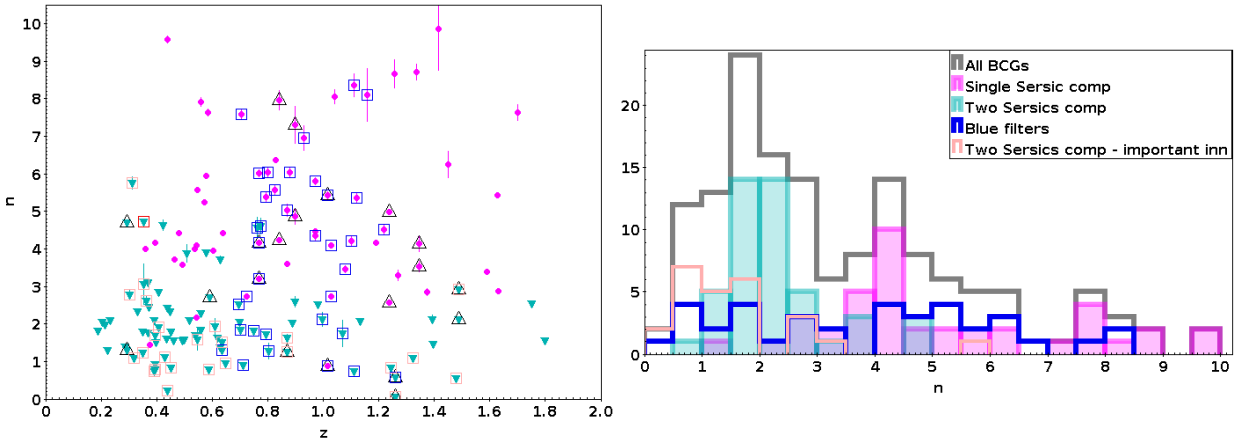

Fig. 15. *Left*: Sérsic indices as a function of redshift (see Fig. 13 for color-coding). *Right*: distribution of the Sérsic indices. All BCGs are represented in the gray histogram. The magenta and cyan histograms represent the distributions obtained with one and two components, respectively, only for the BCGs with appropriate data. The blue and lighter pink histograms represent BCGs observed in too blue filters and with an important inner component, respectively.

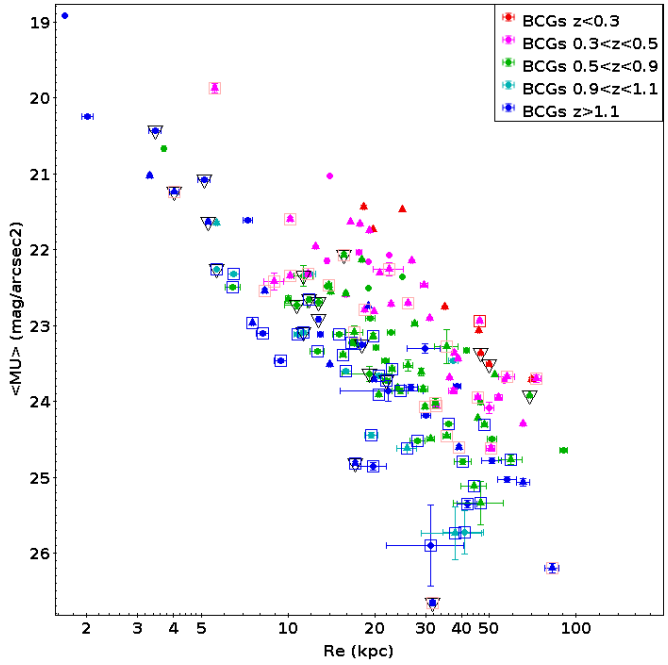

Fig. 16. Kormendy (1977) relation using the parameters obtained with one Sérsic component and the outer component of the two Sérsic component model. Different colors represent different redshift bins. Symbols are the same as in Fig. 13.

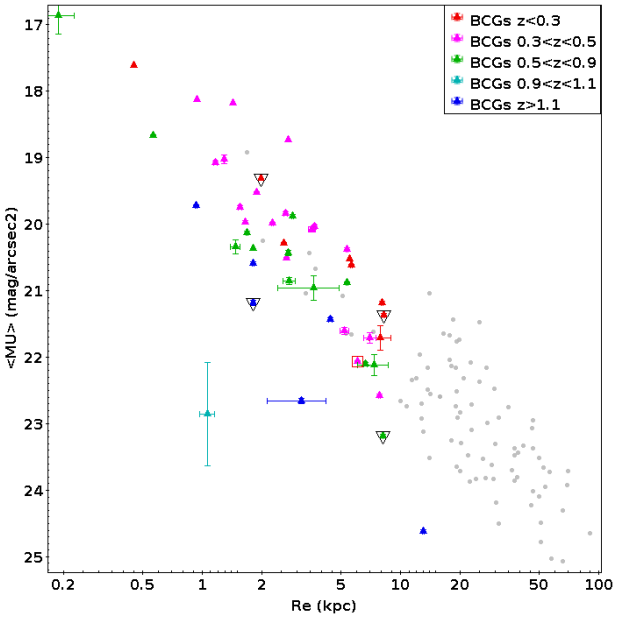

Fig. 17. Same as Fig. 16, but for the inner component of BCGs fitted with two components. The gray points are the same as in Fig. 16.

we find no correlation between the offset and the absolute magnitude, effective radius, or Sérsic index of the BCGs, or with the alignment previously computed.

As can be seen in the top right and bottom left panels of Fig. 21, however, the more massive and richer the cluster (or the BCG, as we converted the cluster masses to BCG masses), the closer the BCG is to the X-ray center of the cluster; the objects with the biggest offets (≥100 kpc) have mass $M_{\rm cluster} \leq 10 \times 10^{14}\,M_{\odot}$ and richness $N \leq 100$. We also find that there is a moderate correlation between the offset and the mean effective surface brightness of the BCG (see Fig. 21, bottom right); BCGs tend to have brighter mean effective surface brightnesses the closer they are to the X-ray center (in logarithmic scale, $R = 0.34$, $p = 0.0395$).

We also analyzed whether the most luminous BCGs are special (see Lin et al. 2010; Lauer et al. 2014). We studied the distribution of the difference in magnitude between the BCGs and the second ranked galaxies of the clusters. We found that the distribution was continuous, with most BCGs having a difference smaller than one magnitude with the second ranked galaxy. By selecting BCGs that are at least 1 mag brighter than the second ranked galaxy of the cluster (9 BCGs), we find that the most luminous BCGs do not occupy a specific place in the observed relations.

6. Discussion and conclusions

Our work deals with the largest sample (to our knowledge) of BCGs with HST imaging, covering a broad redshift interval from $z = 0.1$ to $z = 1.8$ (see Fig. 1), thus enabling us to trace the evolution of BCGs through time. Our sample is larger than most

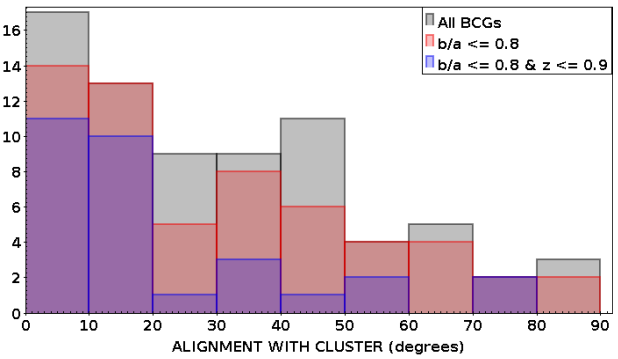

Fig. 18. Difference between the PA of the cluster (see West et al. 2017; Durret et al. 2019) and that of the BCG, as returned by GALFIT. Only clusters found in West et al. (2017) and Durret et al. (2019) are included here. The histogram is to be compared to that shown in West et al. (2017) as a way to check that our results agree with theirs. All BCGs are represented in the gray diagram, while only those with an axis ratio $b/a \leq 0.8$ are included in the red diagram. We also exclude all BCGs at redshift $z > 0.9$ on the blue histogram.

studies found in the literature based on HST images, such as Bai et al. (2014), DeMaio et al. (2019), and Durret et al. (2019). We studied the luminosity profiles of these galaxies and how they evolve as a function of redshift. HST images allowed us to perform profile fitting with precision, and GALFIT returns accurate parameters from model fitting.

We developed a new tool to detect automatically red BCGs on optical images. We successfully detected all the red BCGs regardless of their peculiar characteristics (see Sect. 3). We did not manage to detect in this way the blue BCGs, which represent here only 2% of our sample.

We then proceeded to model the luminosity profiles of these automatically detected BCGs, as well as those that have only one filter available, bringing this sample to 149 BCGs. We removed all BCGs observed in too blue filters as well as BCGs better modeled with two components for which the inner component has an important contribution to the total luminosity of the galaxy. Our final sample consisted of 86 BCGs.

We studied how the photometric properties of BCGs correlate with redshift, and despite the weak but significant correlation we find that the absolute magnitude presents a faint trend of becoming brighter with time.

We show that there is a faint trend (see Fig. 13, right) for BCGs to become bigger with decreasing redshift. This is the behavior we expect for galaxies that grow in size with time by accreting gas and merging with other smaller galaxies. This trend was also observed in Durret et al. (2019) up to redshift 0.9, and can be confirmed up to redshift $z = 1.8$. Based on this relation, we find that BCGs grow by more than a factor of 3 between redshifts 1.8 and 0.1. The dispersion can be linked with the Kormendy relation: galaxies with higher surface brightnesses have smaller effective radii.

We find no strong correlation between the other photometric properties (surface brightness or Sérsic index) of the BCGs and redshift. This is in agreement with Bai et al. (2014) who do not find any correlation between the magnitude or the mean surface brightness of the BCGs and redshift, up to redshift $z = 0.9$. We add that no evolution can be observed up to redshift $z = 1.8$.

Although we only observe massive clusters at lower redshifts ($M_{200,c} \geq 30 \times 10^{14}\, M_\odot$ at $z \leq 0.8$), overall the masses of the clusters do not correlate with redshift. The growth of the cluster is mainly to be linked with the cluster richness (Fig. 19); clusters become richer with time, and we find that the number of red sequence galaxies in an aperture of 500 kpc centered on the BCG increases by almost a factor of 10 between $z = 1.8$ and $z = 0.1$. We confirmed that the low richness we measured at higher redshift is not due to the depth of our images. This growth mainly seems to be happening at $z \leq 1.0$ as we do not observe a significant variation of the richness of the clusters before that time.

We used the relation found in Bai et al. (2014) to compute the BCG masses from the cluster masses, based on the relation found by Bai et al. (2014). We find that bigger BCGs are also more massive (see Fig. 19): $R_e \propto 4.42 \times M_{BCG}$, but the masses do not show a significant growth with redshift.

We thus find that the sizes of the BCGs grow faster than their masses in the same redshift range. Although we do not find that the masses of the BCGs grow significantly with time, whereas Bai et al. (2014) finds a factor of 2 since $z = 2$, we agree that the sizes have grown significantly faster than the masses in the same redshift range. Bai et al. (2014) find that the sizes grow more than twice as fast as the masses. We confirm that the masses and sizes of BCGs do not grow at the same rate. This is in favor of a scenario in which BCGs grow thanks to minor dry mergers at the later stages of their formation and evolution. A growth mainly due to major dry mergers would indeed make the sizes and masses grow at the same rate.

To summarize, we can say that the sizes of the BCGs, as well as the richnesses of the clusters, evolve with redshift: clusters become richer with time and, at the same time, BCGs undergo dry mergers that increase their sizes.

Another interesting result is the distribution of Sérsic indices (see Fig. 15) that shows two different populations, one with low Sérsic indices mainly at low redshift ($z \leq 0.8$) and one with high Sérsic indices. The limit is also to be linked to the fact that BCGs at lower redshifts often require a second component to correctly take into account the brighter core of the galaxy. We find that BCGs better modeled with two components have a peak Sérsic index $n = 2$, while those that were fit with a single component have a peak at $n = 4$. Those modeled with only one Sérsic component are thus comparable to pure elliptical galaxies which can be well modeled with a deVaucouleurs profile. This slightly differs from the results shown in Bai et al. (2014) who find a median value of $n = 5.7$. However, Bai et al. (2014) only fit a single Sérsic profile to all the BCGs in their sample. If we only look at the distribution we obtained for BCGs modeled with a single component, we find that this distribution is more comparable to that of ETGs shown in their paper. Another difference with that study is related to the filters chosen to model the luminosity profiles of the BCGs. While we consider the same spectral region of the SED for all clusters in order to only look at the same old red stellar population at all redshifts, Bai et al. (2014) observe all BCGs with the ACS $F814W$ filter, which we find is already too blue for clusters at redshifts $z \geq 0.57$. We also showed, by studying the parameters obtained in two different filters for a sample of BCGs, that the parameters vary depending on the part of the SED you look at: when looking at a bluer filter the absolute magnitude and mean effective surface brightness become fainter, the effective radius becomes smaller, and the Sérsic indices vary without any clear trend.

Finally, we find that the Kormendy relation (Kormendy 1977) is also a function of redshift, with the relation shifted towards fainter mean effective surface brightnesses at higher redshifts. This relation shows that, at the effective radius, smaller galaxies are brighter and denser than the bigger ones. The slope of 3.33 ± 0.73 measured with our sample remains constant with redshift. Our value is in good agreement with that given in

Table 4. Cluster properties.

Name	$RA_{cluster,X}$ (J2000)	$Dec_{cluster,X}$ (J2000)	Ref	$M_{200,c}$ $10^{14}\,M_\odot$	Method	Ref	$PA_{cluster}$ (degrees)	Ref
SPT-CLJ0000–5748	0.25	−57.8093	1	$6.04^{+1.61}_{-1.61}$	SZ	1	170 ± 22	2
Cl0016+1609				$25.76^{+6.66}_{-6.66}$	WL	3	35 ± 0	4
SpARCS–J0035	8.9588	−43.2029	5	$2.5^{+0.9}_{-1.0}$	$\sigma-M_{200}$	6	154 ± 8	2
ACO2813	10.8519	−20.6229	7	$8.17^{+1.91}_{-1.61}$	WL	8		
XDCPJ0044–2033	11.022	−20.5665	9	$3.98^{+1.58}_{-1.58}$	X	10	128 ± 49	2
RXJ0056–27	14.2338	−27.67	11	$2.84^{+1.59}_{-1.59}$	WL	3		
SPT-CLJ0102–4915	15.734	−49.2656	1	$25.4^{+4.9}_{-4.9}$	WL	3	147 ± 2	2
RXJ0110+19	17.575	19.6397	11	$2.36^{+1.22}_{-1.22}$	WL	3		
Abell209	22.969	−13.6108	12	$9.5^{+0.7}_{-0.7}$	Lens	13	131 ± 0	4
CLJ0152–1357	28.1712	−13.9686	14	$14.0^{+4.6}_{-4.6}$	WL	15		
...	...	...	...	...	...	...	...	...

Notes. The columns are: full cluster name, X-ray coordinates of the cluster, mass of the cluster, method used to measure the mass of the cluster, PA of the cluster. The full table is available at the CDS.

References. (1) Chiu et al. (2015); (2) West et al. (2017); (3) Sereno (2015); (4) Durret et al. (2019); (5) Fassbender et al. (2011); (6) van der Burg et al. (2014); (7) Bartalucci et al. (2019); (8) Okabe & Smith (2016); (9) Tozzi et al. (2015); (10) Cooke et al. (2019b); (11) Hoekstra et al. (2010); (12) Postman et al. (2012b); (13) Merten et al. (2015); (14) Sayers et al. (2019); (15) Martinet et al. (2016); (16) DeMaio et al. (2019); (17) Jee et al. (2011); (18) Andreon et al. (2014); (19) Zitrin et al. (2012); (20) Stott et al. (2010); (21) Czakon et al. (2015); (22) Herbonnet et al. (2020); (23) Sereno & Zitrin (2011); (24) Brodwin et al. (2015); (25) Chan et al. (2019); (26) Jee et al. (2005); (27) Hicks et al. (2013); (28) Just et al. (2019); (29) Hicks et al. (2008); (30) Noble et al. (2011); (31) Gonzalez et al. (2015); (32) Dahle (2006); (33) Guennou et al. (2014); (34) Jørgensen et al. (2018); (35) Santos et al. (2012); (36) Jee et al. (2017); (37) Mo et al. (2016); (38) Martini et al. (2013); (39) Richard-Laferrière et al. (2020); (40) Sereno & Covone (2013); (41) Lidman et al. (2012); (42) Sanders et al. (2017); (43) Donnarumma et al. (2009).

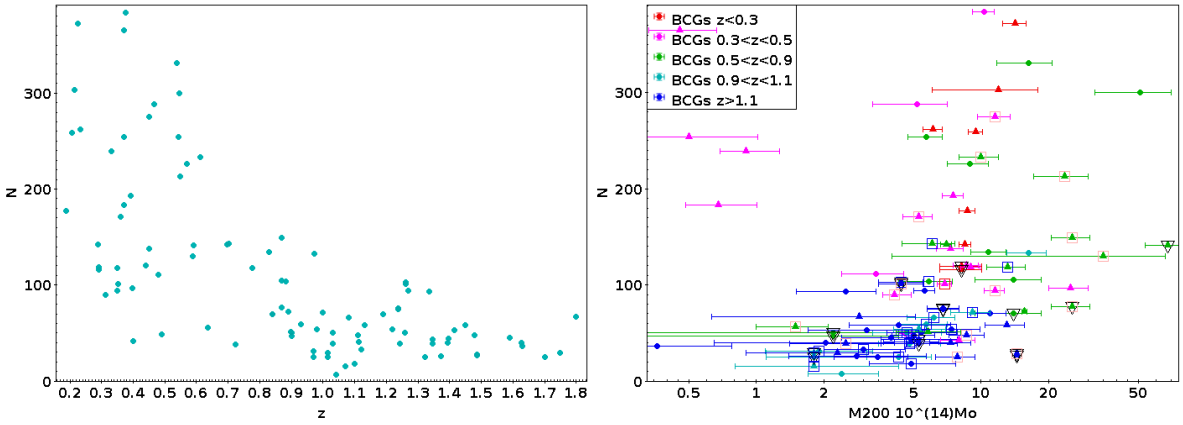

Fig. 19. *Left*: richness of the cluster (see text) as a function of redshift. *Right*: richness of the cluster as a function of its mass $M_{200,c}$. The colors represent different redshift bins.

Bai et al. (2014),

$$\langle\mu\rangle = (3.50 \pm 0.18)\log R_e + (18.01 \pm 0.23),$$

and agrees within one σ with the value given in Durret et al. (2019),

$$\langle\mu\rangle = (2.64 \pm 0.35)\log R_e + (19.7 \pm 0.5).$$

It should be noted that cosmology or selection effects might be contributing to the results in Fig. 13, which shows a trend for BCG sizes and luminosities to increase with time. Despite its faintness, the contribution of the ICL should be taken into account. The ICL blends with the envelope of the BCG, making it difficult to differentiate the galaxy from the ICL, and this may affect our measurements (in particular those of the effective radii and Sérsic indices). The ICL might contribute at some level to measured sizes and luminosities of galaxies at low redshifts, yet might be missed in high-redshift clusters because of cosmological surface brightness dimming, or perhaps because the ICL has not yet developed in these young clusters. A concern comes from the value of the background, as GALFIT is sensitive to it, but its computation is limited by the sizes of the images (even without cropping).

We broaden the work by West et al. (2017) and Durret et al. (2019) on the alignment of BCGs with their host clusters. We removed BCGs with ill-measured position angles due to their circular shape, as well as BCGs at higher redshifts, $z \geq 0.9$, as they would appear smaller on the CCD, and would thus be less resolved and have less accurate measured PAs. This enables us to conclude that BCGs tend to align with their host cluster at least at $z \leq 0.9$, as after this selection 73% of the remaining BCGs are aligned with their host cluster within 30°. This is a

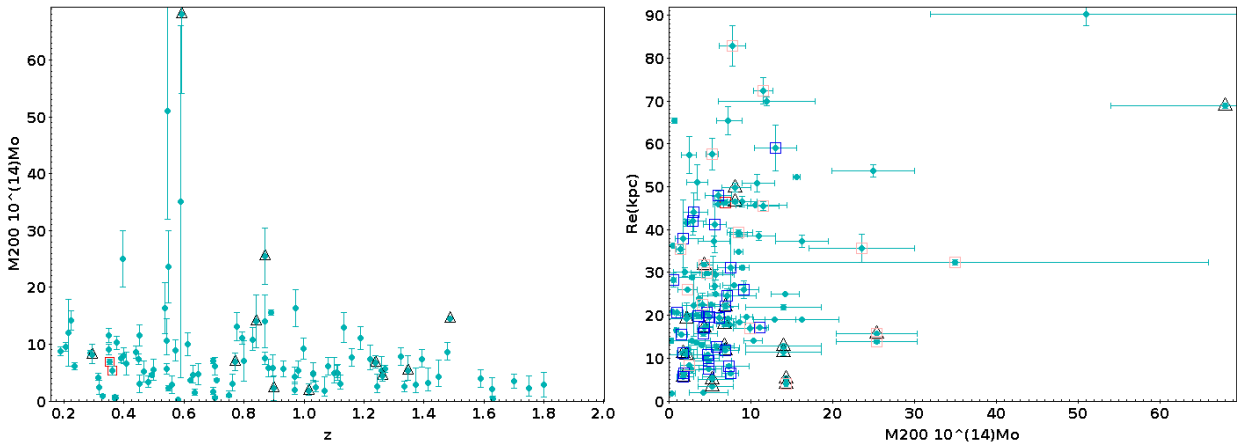

Fig. 20. *Left*: cluster mass M200 (in units of 10^{14} $M_{\odot}$) as a function of redshift. *Right*: BCG effective radius as a function of cluster mass.

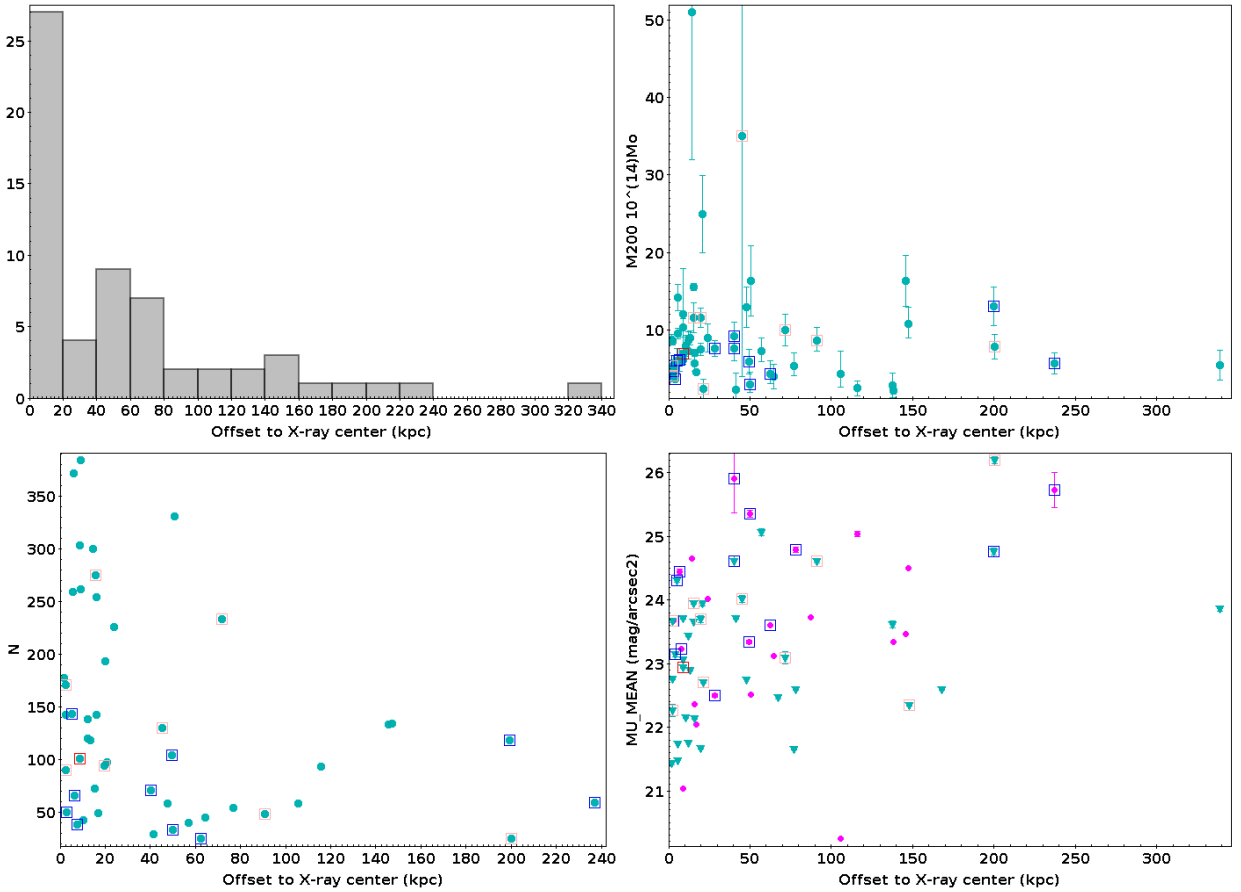

Fig. 21. *Top left*: histogram of the offsets between the BCG and the X-ray center. *Top right*: masses $M_{200,c}$ of the clusters as a function of the offsets between the BCG and the cluster X-ray center. *Bottom left*: richness of the cluster as a function of the offsets between the BCG and the cluster X-ray center. *Bottom right*: mean effective surface brightness of the BCGs as a function of the offsets between the BCG and the cluster X-ray center.

tighter alignment than that reported by Durret et al. (2019), who found an alignment for 12 out of 21 BCGs (57%) between redshifts 0.21 and 0.89. Okabe et al. (2020) study the alignment of 45 dark matter (DM) haloes and their BCGs up to $z = 0.97$, and find that BCGs tend to be well aligned with their DM haloes, with a mean difference of 22.2 ± 3.9°. A similar study was done by Ragone-Figueroa et al. (2020) on the alignment of BCGs both with the distribution of cluster galaxies and DM haloes, by analyzing cosmological hydro-simulations of 24 clusters. They find a strong alignment at $z < 2$, and add that relaxed clusters tend to host BCGs that align with the major axis. Similar conclusions are made by De Propris et al. (2020), who show that BCGs are generally aligned with the host cluster even when the offset between the BCG and the X-ray center is significant.

Cerulo et al. (2019) found that 9% of the BCGs between $0.05 \leq z \leq 0.35$ have colors bluer than 2σ of the median color of the cluster red sequence. During this study we found two peculiar blue BCGs in our sample. Apart from their colors and

complex structures, these two peculiar BCGs do not have photometric properties different from the other BCGs. It would be interesting to continue this study by considering a larger sample of star forming blue BCGs to see where they lie in the previous plots.

We plan to apply the method described in this paper to more than a thousand clusters from the Canada-France-Hawaii Telescope Legacy Survey (CFHTLS), detected by Sarron et al. (2018), up to redshift $z = 0.7$. This will enable us to better evaluate the accuracy of our BCG detection method on ground-based data, and although the resolution will not be as good, the sample will be significantly larger. We also found two BCGs (2%) with blue colors, and it would be interesting to estimate the fraction of blue BCGs in the Universe up to redshift $z = 0.7$. We wonder if these BCGs evolve differently from the red BCGs that we detect.

Acknowledgements. We thank the referee, M. West, for his constructive comments and suggestions. F.D. acknowledges continuous support from CNES since 2002. IM acknowledges financial support from the State Agency for Research of the Spanish MCIU through the "Center of Excellence Severo Ochoa" award to the Instituto de Astrofísica de Andalucía (SEV-2017-0709), and through the programs AYA2016-76682C3-1-P and PID2019-106027GB-C41. Based on observations made with the NASA/ESA *Hubble* Space Telescope, and obtained from the *Hubble* Legacy Archive, which is a collaboration between the Space Telescope Science Institute (STScI/NASA), the Space Telescope European Coordinating Facility (ST-ECF/ESA) and the Canadian Astronomy Data Centre (CADC/NRC/CSA).

References

Andreon, S., Newman, A. B., Trinchieri, G., et al. 2014, A&A, 565, A120
Aragon-Salamanca, A., Baugh, C. M., & Kauffmann, G. 1998, MNRAS, 297, 427
Ascaso, B., Aguerri, J. A. L., Varela, J., et al. 2010, ApJ, 726, 69
Bai, L., Yee, H., Yan, R., et al. 2014, ApJ, 789, 134
Bartalucci, I., Arnaud, M., Pratt, G. W., Démoclès, J., & Lovisari, L. 2019, A&A, 628, A86
Bellstedt, S., Lidman, C., Muzzin, A., et al. 2016, MNRAS, 460, 2862
Bernardi, M. 2009, MNRAS, 395, 1491
Bertin, E. 2011, in Astronomical Data Analysis Software and Systems XX, eds. I. N. Evans, A. Accomazzi, D. J. Mink, & A. H. Rots, ASP Conf. Ser., 442, 435
Bertin, E., & Arnouts, S. 1996, A&AS, 117, 393
Brodwin, M., Greer, C. H., Leitch, E. M., et al. 2015, ApJ, 806, 26
Bruzual, G., & Charlot, S. 2003, MNRAS, 344, 1000
Castignani, G., Pandey-Pommier, M., Hamer, S. L., et al. 2020, A&A, 640, A65
Cerulo, P., Orellana, G. A., & Covone, G. 2019, MNRAS, 487, 3759
Chan, J. C. C., Wilson, G., Rudnick, G., et al. 2019, ApJ, 880, 119
Chiu, I., Mohr, J., McDonald, M., et al. 2015, MNRAS, 455, 258
Collins, C. A., & Mann, R. G. 1998, MNRAS, 297, 128
Collins, C. A., Stott, J. P., Hilton, M., et al. 2009, Nature, 458, 603
Cooke, K. C., Kartaltepe, J. S., Tyler, K. D., et al. 2019a, ApJ, 881, 150
Cooke, E. A., Smail, I., Stach, S. M., et al. 2019b, MNRAS, 486, 3047
Czakon, N. G., Sayers, J., Mantz, A., et al. 2015, ApJ, 806, 18
Dahle, H. 2006, ApJ, 653, 954
De Lucia, G., & Blaizot, J. 2007, MNRAS, 375, 2
De Propris, R., West, M. J., Andrade-Santos, F., et al. 2020, MNRAS, 500, 310
DeMaio, T., Gonzalez, A. H., Zabludoff, A., et al. 2019, MNRAS, 491, 3751
Donahue, M., Connor, T., Fogarty, K., et al. 2015, ApJ, 805, 177
Donahue, M., Ettori, S., Rasia, E., et al. 2016, ApJ, 819, 36
Donnarumma, A., Ettori, S., Meneghetti, M., & Moscardini, L. 2009, MNRAS, 398, 438
Durret, F., Márquez, I., Acebrón, A., et al. 2016, A&A, 588, A69
Durret, F., Tarricq, Y., Márquez, I., Ashkar, H., & Adami, C. 2019, A&A, 622, A78
Edwards, L. O. V., Salinas, M., Stanley, S., et al. 2019, MNRAS, 491, 2617
Ellien, A., Durret, F., Adami, C., et al. 2019, A&A, 628, A34
Fassbender, R., Böhringer, H., Nastasi, A., et al. 2011, New J. Phys., 13, 125014
Fogarty, K., Postman, M., Connor, T., Donahue, M., & Moustakas, J. 2015, ApJ, 813, 117
Fogarty, K., Postman, M., Larson, R., Donahue, M., & Moustakas, J. 2017, ApJ, 846, 103
Fogarty, K., Postman, M., Li, Y., et al. 2019, ApJ, 879, 103
Gonzalez, A. H., Decker, B., Brodwin, M., et al. 2015, ApJ, 812, L40
Green, T. S., Edge, A. C., Stott, J. P., et al. 2016, MNRAS, 461, 560
Guennou, L., Adami, C., Durret, F., et al. 2014, A&A, 561, A112
Hashimoto, Y., Henry, J. P., & Boehringer, H. 2014, MNRAS, 440, 588
Hennig, C., Mohr, J. J., Zenteno, A., et al. 2017, MNRAS, 467, 4015
Herbonnet, R., Sifón, C., Hoekstra, H., et al. 2020, MNRAS, 497, 4684
Hicks, A. K., Ellingson, E., Bautz, M., et al. 2008, ApJ, 680, 1022
Hicks, A. K., Pratt, G. W., Donahue, M., et al. 2013, MNRAS, 431, 2542
Hlavacek-Larrondo, J., Allen, S. W., Taylor, G. B., et al. 2013, ApJ, 777, 163
Hoekstra, H., Donahue, M., Conselice, C. J., McNamara, B. R., & Voit, G. M. 2010, ApJ, 726, 48
Jee, M. J., White, R. L., Ford, H. C., et al. 2005, ApJ, 634, 813
Jee, M., Dawson, K., Hoekstra, H., et al. 2011, ApJ, 737, 59
Jee, M. J., Ko, J., Perlmutter, S., et al. 2017, ApJ, 847, 117
Jørgensen, I., Chiboucas, K., Hibon, P., Nielsen, L. D., & Takamiya, M. 2018, ApJS, 235, 29
Just, D. W., Kirby, M., Zaritsky, D., et al. 2019, ApJ, 885, 6
Kluge, M., Neureiter, B., Riffeser, A., et al. 2020, ApJS, 247, 43
Kormendy, J. 1977, ApJ, 218, 333
Kravtsov, A. V., & Borgani, S. 2012, ARA&A, 50, 353
Lauer, T. R., Postman, M., Strauss, M. A., Graves, G. J., & Chisari, N. E. 2014, ApJ, 797, 82
Lidman, C., Suherli, J., Muzzin, A., et al. 2012, MNRAS, 427, 550
Limousin, M., Richard, J., Jullo, E., et al. 2016, A&A, 588, A99
Lin, Y.-T., Ostriker, J. P., & Miller, C. J. 2010, ApJ, 715, 1486
Lin, Y.-T., Brodwin, M., Gonzalez, A. H., et al. 2013, ApJ, 771, 61
Margalef-Bentabol, B., Conselice, C. J., Mortlock, A., et al. 2016, MNRAS, 461, 2728
Márquez, I., Durret, F., Delgado, R. G., et al. 1999, A&AS, 140, 1
Márquez, I., Masegosa, J., Durret, F., et al. 2003, A&A, 409, 459
Martinet, N., Clowe, D., Durret, F., et al. 2016, A&A, 590, A69
Martinet, N., Durret, F., Adami, C., & Rudnick, G. 2017, A&A, 604, A80
Martini, P., Miller, E. D., Brodwin, M., et al. 2013, ApJ, 768, 1
McDonald, M., Stalder, B., Bayliss, M., et al. 2016, ApJ, 817, 86
Merten, J., Meneghetti, M., Postman, M., et al. 2015, ApJ, 806, 4
Mo, W., Gonzalez, A., Jee, M. J., et al. 2016, ApJ, 818, L25
Noble, A. G., Webb, T. M. A., Ellingson, E., et al. 2011, MNRAS, 419, 1983
Okabe, N., & Smith, G. P. 2016, MNRAS, 461, 3794
Okabe, T., Oguri, M., Peirani, S., et al. 2020, MNRAS, 496, 2591
Patel, P., Maddox, S., Pearce, F. R., Aragon-Salamanca, A., & Conway, E. 2006, MNRAS, 370, 851
Peng, C. Y., Ho, L. C., Impey, C. D., & Rix, H.-W. 2002, AJ, 124, 266
Pierpaoli, E., Borgani, S., Scott, D., & White, M. 2003, MNRAS, 342, 163
Postman, M., Lauer, T. R., Donahue, M., et al. 2012a, ApJ, 756, 159
Postman, M., Coe, D., Benítez, N., et al. 2012b, ApJS, 199, 25
Ragone-Figueroa, C., Granato, G. L., Borgani, S., et al. 2020, MNRAS, 495, 2436
Richard-Laferrière, A., Hlavacek-Larrondo, J., Nemmen, R. S., et al. 2020, MNRAS, 499, 2934
Sanders, J. S., Fabian, A. C., Russell, H. R., & Walker, S. A. 2017, MNRAS, 474, 1065
Santos, J. S., Tozzi, P., Rosati, P., Nonino, M., & Giovannini, G. 2012, A&A, 539, A105
Sarron, F., Martinet, N., Durret, F., & Adami, C. 2018, A&A, 613, A67
Sayers, J., Montaña, A., Mroczkowski, T., et al. 2019, ApJ, 880, 45
Sazonova, E., Alatalo, K., Lotz, J., et al. 2020, ApJ, 899, 85
Schlafly, E. F., & Finkbeiner, D. P. 2011, ApJ, 737, 103
Schlegel, D., Finkbeiner, D., & Davis, M. 1998, ApJ, 500, 525
Sereno, M. 2015, MNRAS, 450, 3665
Sereno, M., & Covone, G. 2013, MNRAS, 434, 878
Sereno, M., & Zitrin, A. 2011, MNRAS, 419, 3280
Simard, L., Mendel, J. T., Patton, D. R., Ellison, S. L., & McConnachie, A. W. 2011, ApJS, 196, 11
Stott, J. P., Collins, C. A., Sahlén, M., et al. 2010, ApJ, 718, 23
Stott, J. P., Collins, C. A., Burke, C., Hamilton-Morris, V., & Smith, G. P. 2011, MNRAS, 414, 445
Thomas, D., Maraston, C., Schawinski, K., Sarzi, M., & Silk, J. 2010, MNRAS, 404, 1775
Tozzi, P., Santos, J. S., Jee, M. J., et al. 2015, ApJ, 799, 93
van der Burg, R. F. J., Muzzin, A., Hoekstra, H., et al. 2014, A&A, 561, A79
van der Burg, R. F. J., Muzzin, A., Hoekstra, H., et al. 2015, A&A, 577, A19
West, M. J., de Propris, R., Bremer, M. N., & Phillipps, S. 2017, Nat. Astron., 1, 0157
Whiley, I. M., Aragón-Salamanca, A., De Lucia, G., et al. 2008, MNRAS, 387, 1253
Zhang, Y., Miller, C., McKay, T., et al. 2016, ApJ, 816, 98
Zitrin, A., Meneghetti, M., Umetsu, K., et al. 2012, ApJ, 762, L30

2.2 Detection and photometric properties of a large sample of BCGs from the Canada France Hawaii Telescope Legacy Survey

As a follow-up to Chu, Durret, and Márquez (2021), we study a significantly larger sample of 1371 BCGs of clusters detected in the CFHTLS by Sarron et al. (2018) up to redshift $z = 0.7$. Although the redshift coverage is not as large as in our first sample, and the images from the CFHTLS have lower spatial resolution than those from HST, the big sample size allows us to increase the statistics of our study up to $z = 0.7$ by almost a factor of 20.

2.2.1 Construction of the BCG catalogue, automatic detection

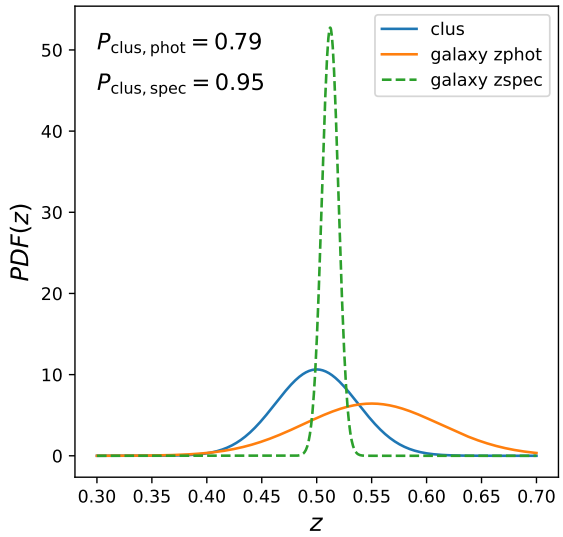

FIGURE 2.3: Redshift PDF of the cluster (blue) and the BCG (orange). The green dotted PDF corresponds to the PDF of the BCG after correcting for the shift in redshift between the photometric and spectroscopic redshift if available.

As in Chu, Durret, and Márquez (2021), building our BCG catalogue from the catalogue of galaxy clusters from Sarron et al. (2018) was the first step. Although we described an effective tool for BCG detection in the previous paper, we chose to develop a new one for this sample. This is because since only photometric redshifts are available for these clusters, the extraction of the red sequence will not be as precise because of the large redshift uncertainties. Instead, we opt for a more probabilistic approach, which relies on the photometric redshift of the cluster and of each galaxy, computed by Sarron et al. (2018). These z-phots were estimated beforehand by the TERAPIX team with the SED fitting LEPHARE code (Arnouts et al., 1999), which also returns the redshift probabilistic distribution functions (PDF) of the galaxies. An example is given in Figure 2.3, which shows the PDF of the cluster in blue which was obtained by summing the PDFs of all galaxies, and the PDF of a galaxy obtained from its z-phot (in orange) and from its z-spec (in dotted green). If the spectroscopic redshift of a galaxy is available (which is not always the case), the position of the PDF obtained with the photometric redshift of the galaxy is shifted to the galaxy's spectroscopic redshift, and its width is also corrected as the uncertainty on spectroscopic

redshifts is much smaller than on photometric ones (of the order of $0.005 \times (1 + z)$ and $0.04 \times (1 + z)$ respectively). As a result, the final PDF obtained with a known z-spec is narrower and more peaked than the one obtained with only a z-phot. Then, from the convolution of the PDF of the cluster and of the galaxy, we can derive a probability for the galaxy to be at the same redshift as the cluster.

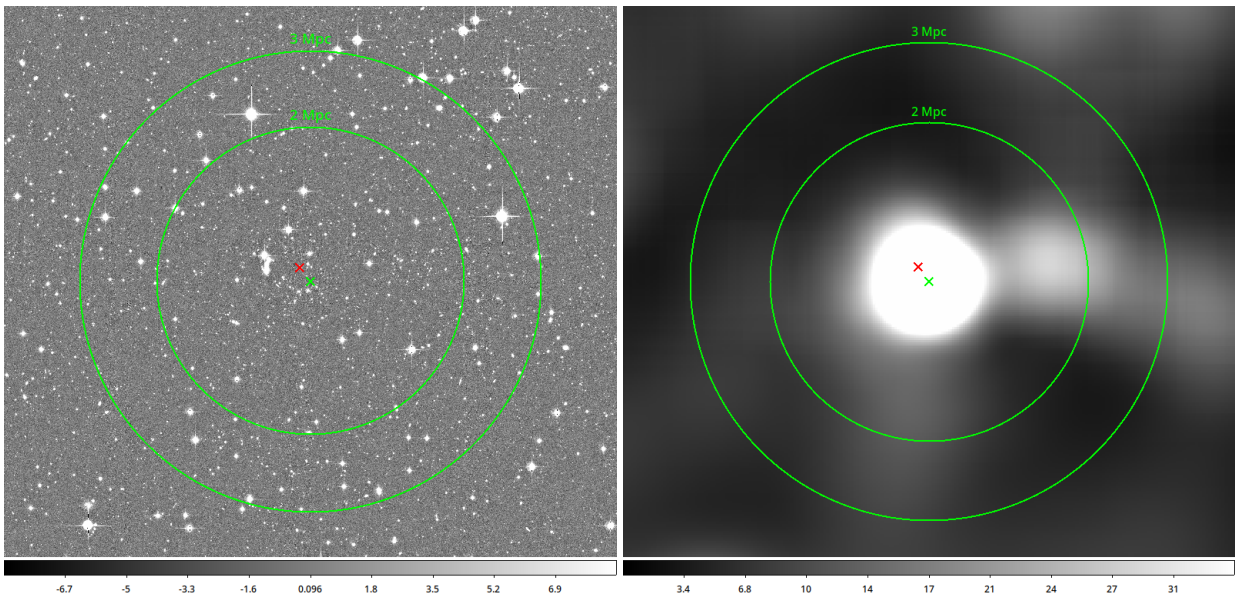

FIGURE 2.4: On the left, the optical image in the *r* band of the cluster W4-325, on the right the associated density map. The green circles represent radii of 2 Mpc and 3 Mpc from the cluster center indicated by the green cross. The red cross shows the position of the BCG.

This probability along with galaxy density maps, enables us to determine if a galaxy is likely to be at the cluster's redshift, and if its location agrees with the galaxy distribution of the cluster. The brightest galaxy which has both a redshift probability above a defined threshold, and a position that is coherent with the area of the cluster as measured on density maps, is defined as the BCG. We show on Figure 2.4 the image of a cluster at z-phot = 0.47 and the associated density map. Two circles centered on the cluster coordinates (as given in Sarron et al., 2018) are traced to illustrate the physical distances corresponding to 2 Mpc and 3 Mpc, creating a ring of width 1 Mpc. This ring is far enough from the cluster's center and we can consider that it only contains the background. A BCG is not always located at the very center of its host cluster, as was shown by several studies (see Chu, Durret, and Márquez, 2021, and references therein). Moreover, clusters do not always have a simple spheroidal or ellipsoidal shape, and obtaining precise estimates of their sizes is not easy. This is why we do not just identify the BCG as being the brightest galaxy located within a given distance from the cluster center.

To determine whether or not a galaxy is in the cluster's vicinity, we compare its signal-to-noise ratio (S/N), SN, on the cluster density map to the S/N in the background, SN_{bkg}, defined as the mean S/N computed in the ring illustrated in the images. This allows us to trace the "borders" of the cluster. If $SN \geq SN_{lim} = SN_{bkg} + 3\ \sigma_{SN,bkg}$, with $\sigma_{SN,bkg}$ the S/N dispersion in the background, then the galaxy is considered to be inside the cluster.

To further confirm that it is at the right distance as well (same redshift), we compare its redshift probability, P_z, to the mean probability of the galaxies in the ring (in the background), $P_{z,bkg}$. If $P_z \geq P_{z,lim} = P_{z,bkg} + 3\ \sigma_{Pz,bkg}$, with $\sigma_{Pz,bkg}$ the P_z dispersion of the galaxies in the background, then

we consider that the galaxy is at the same redshift as the cluster. These thresholds are well defined if the cluster has a simple elongated shape, if it is isolated in the cosmic web, and if it does not have a close neighbour or a strong filament connected to it.

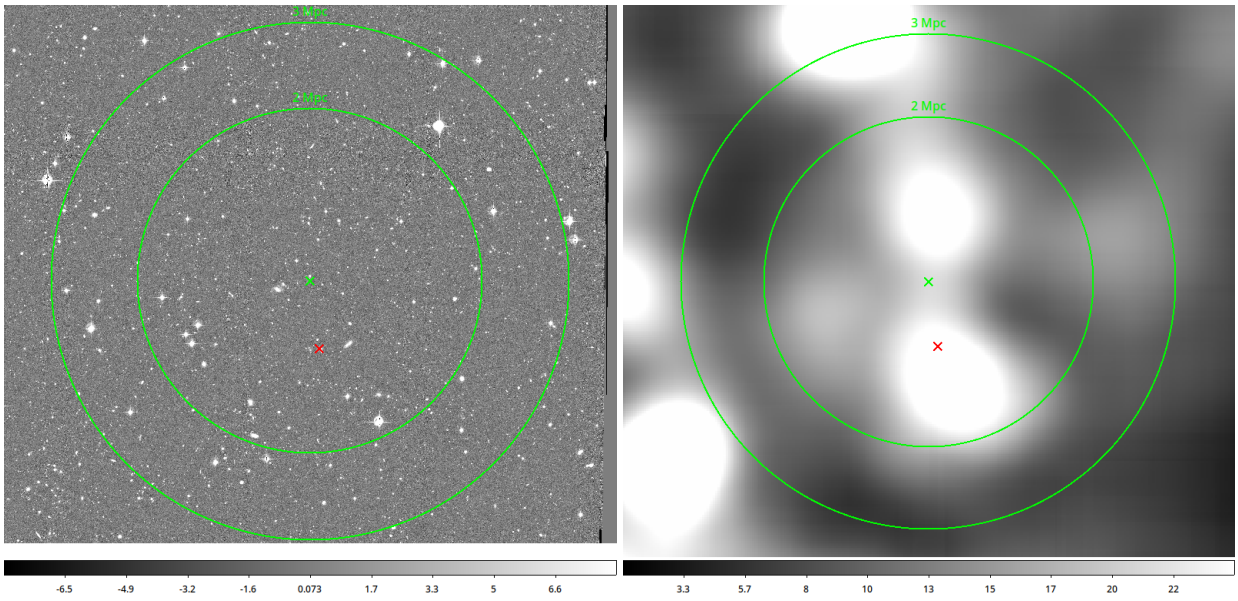

FIGURE 2.5: On the left, the optical image in the *r* band of the cluster W1-639, on the right the associated density map. The green circles represent a physical distance of 3 Mpc and 2 Mpc radius from the cluster center indicated by the green cross. The red cross shows the position of the BCG.

We adjust these thresholds when one of these conditions is not fulfilled. Cluster coordinates were determined on density maps which are a superposition of the signals of multiple structures covering a rather large redshift bin (of the order of 0.1). As a result, if two structures with similar redshifts appear close to each other, the cluster center coordinates will have large uncertainties as its signal will be contaminated by its neighbour. The presence of a nearby substructure will increase the SN_{bkg} and $\sigma_{SN,bkg}$ in the background, and some galaxies at a similar redshift may end up in the background ring meaning the probability $P_{z,bkg}$ and $\sigma_{Pz,bkg}$ will also increase. An example is given in Figure 2.5, in which two structures overlap and the center coordinates appear in the middle of the two. As a result, the density at the cluster's center appears comparable to that of the background. Although it is not the case in this example, we could imagine that the two substructures were large enough so they would be partially contained in the ring. In such a case, the redshift probability of some of the galaxies in the background (which is no longer well defined as it contains part of the cluster) may be comparable to those of cluster members. It is thus difficult to estimate good thresholds in these peculiar cases. I thus decided to adjust manually these thresholds, by testing different combinations of SN_{lim} and $P_{z,lim}$, and chose the combination that returned the best detection rate.

This method was visually verified by two of the authors, who checked carefully the position, morphology and redshift probability of all the BCG candidates detected by the algorithm before choosing the final BCG. We also built a sample of BCGs with available spectroscopic redshifts to confirm our detections. We estimate that this algorithm has a 70% success rate, which was calculated as the ratio of correctly detected BCGs by the algorithms over the total number of BCGs.

2.2.2 Luminosity profiles and results

Similarly to Chu, Durret, and Márquez (2021), we modeled the luminosity profiles of BCGs with a single and two Sérsic components. We agree with Chu, Durret, and Márquez (2021): we report no evolution of the effective radius, absolute magnitude or Sérsic index with redshift up to $z = 0.7$. This confirms the early formation of BCGs more than 6 Gyrs ago.

Alignment of BCGs with their host clusters

We confirm the alignments of BCGs with their host cluster by demonstrating that more than 50% of BCGs at $z < 0.7$ are aligned with their clusters within 30 degrees. We measure the position angles of the clusters similarly to West et al. (2017) by computing moments of inertia, except we use the density maps of the clusters (see Figure 2.4 and Figure 2.5) instead of considering the red sequence galaxies. This is because, for the same reason as we did not use the red sequence for the detection method, as we only have photometric redshifts, the red sequence will be badly defined and thus the mass distribution will not be well modeled. The moment of inertia I of an object with mass M is defined as:

$$I = \int di = \int_0^M r^2 dm \tag{2.2}$$

with r the distance of a point mass from the rotation axis of the object. Here, we consider the extended signal of the cluster on the density maps as the object for which we want to measure the main axis (its position angle). It is composed of a number N of pixels with intensity i. To compute the moment of inertia of the cluster, we sum all the pixels in a radius R_{500} (radius which encloses 500 times the critical density of the Universe at the redshift of the cluster) centered on the cluster center on the density map. In order to find the main axis of the cluster, we compute the moment of inertia by rotating the axis from 0 to 360 degrees by steps of 1 degree first, then after measuring the axis for which the moment of inertia is minimal, we increase the resolution to 0.1 degree. This two-step measurement was done to save on computing time, as images can be quite big, making the calculation heavy. The position angle of the cluster is defined as the axis with the lowest moment of inertia. We chose a radius of R_{500} because it is a characteristic physical parameter of a cluster, and it is a good compromise between having a size big enough to contain most of the cluster, and small enough not to be affected by possible contaminations by nearby filaments, groups, or clusters which may bias our measurements.

To estimate the uncertainties on the position angle of the cluster, we use bootstrap resampling (again, similarly to West et al., 2017): instead of considering all the pixels enclosed in the same aperture of radius R_{500}, only half are considered to measure the main axis of the cluster in the same way described before using the moments of inertia. We chose to cut in half the pixel sample as we find that less than this number returns high uncertainties on the PA (not enough pixels to map the cluster distribution correctly), and more increases the computing time without significantly decreasing the uncertainties; so this was the best compromise to obtain correct measurements without spending a considerable amount of time to compute them. The pixels are randomly selected, and the measure is repeated a hundred times. The dispersion on all the iterations gives the uncertainty on the position angle of the cluster.

The lower fraction of clusters with PA alignments within 30 degrees of their host clusters found here compared to Chu, Durret, and Márquez (2021) comes from the measurement of the position angles of the clusters on the density maps. These density maps were generated by considering large bins in redshift, which makes the measurements of cluster position angles less precise.

Origin of the inner component

The main result of this study is the distinction between a one Sérsic model and a two Sérsic model, and what causes the separation between the two. In Chu, Durret, and Márquez (2021), two-Sérsic BCGs represented more than 50% of the final sample and were mostly at low redshifts ($z < 0.4$). Here, we only reach $z = 0.7$, while Chu, Durret, and Márquez (2021) reaches $z = 1.8$. If the BCGs studied in Chu, Durret, and Márquez (2021) and this paper were the same, we would thus expect the fraction of two-Sérsic BCGs over the whole sample to increase here, or to have similar fractions over the same redshift range, which is to say 69%. Instead, we find that two-Sérsic BCGs in this study only represent 5% of the whole BCG population. As was demonstrated in Chu, Durret, and Márquez (2021), the different resolution of the CFHTLS from HST can not explain such a decrease in the fraction of two-Sérsic BCGs. Instead, we looked for other possible causes which would affect the fitting of the luminosity profiles of galaxies.

We first suspected the Intra Cluster Light (ICL) to be the main source of contamination on our images. ICL has very faint surface brightness and can be difficult to distinguish from the outskirts of the central galaxies, as the stars of the ICL and the stars of the BCG can meddle with each other. So far, only the acquisition of spectroscopic data can enable us to separate the two. On images, the ICL will just look like an extension of the profile of the BCG which would then appear more diffuse. To estimate how much the ICL affects the luminosity profiles of the BCGs in our sample, we made use of images of ICL kindly provided by Yolanda Jiménez-Teja (Jiménez-Teja and Dupke, 2016) and compared the models returned by `GALFIT` on images of BCG+ICL and images on which we subtracted the ICL. The algorithm presented in Jiménez-Teja and Benítez (2012) and Jiménez-Teja and Dupke (2016) creates an ICL map by, in a very simplified description, first detecting the sources in the image and modeling their profile with Chebyshev-Fourier functions (CHEFs). The flux of all the galaxies is then removed from the image. The BCG modeled by CHEFs is added back, which gives an image containing only the BCG and background flux, as well as the ICL that could not be removed. On this image, the curvature of the BCG+ICL profile is measured. The main assumption of this study is that the BCG and the ICL have different luminosity profiles, and thus, that ICL takes over above a certain radius resulting in a change of slope. This is how they delimit the borders of the BCGs. The BCG is then modeled once again but by considering only the flux contained in the borders measured previously, and by first estimating the surface brightness of the ICL in the regions surrounding the BCG and taking this value as the background. The modeled BCG is then removed which returns the final image of the ICL. We show in this way that, even though ICL does indeed extend the profile at higher radii (bigger effective radius, fainter effective surface brightness, higher Sérsic index), it is not responsible for the presence of an outer and inner component.

Apart from the resolution of the instruments, the depth of the images is one of the main differences between our two surveys. Indeed, the images of the CFHTLS have an 80% completeness in the i filter at $m_{80} = 24.7$, whereas HST images can detect objects of magnitudes up to $m_{80} = 28.0$. Our study shows, from the comparison of fits obtained on the CFHTLS WIDE and DEEP

images, that the depth of the images is the parameter that mainly affects the structure of the BCG: deep images with $m_{80} > 26.5$ mag arcsec^{-2} mostly require two-component BCGs, whereas images which do not reach this depth are mostly fit with a single component.

2.2.3 Summary

To summarize, this paper reports the lack of evolution in absolute magnitude, size and surface brightness in a very large sample of BCGs from $z = 0.7$ to $z = 0.15$. We conclude that BCGs were mostly assembled before $z = 0.7$, in agreement with results from Chu, Durret, and Márquez (2021). We also highlight the importance of deep surveys for such studies in order to properly model the structures of BCGs. As part of the future Euclid space mission which will survey 15000 deg^2 of the sky, the Euclid deep fields should enable us to achieve this. Similarly, the future Rubin-LSST (Legacy Survey of Space and Time) mission will cover uniformly 30000 deg^2 of the sky in six filters for photometric redshift estimation, with deep images. This work, thanks to the very big sample studied, allows to bring statistically significant evidence for an earlier formation epoch for BCGs.

We also detail another method to detect automatically BCGs on optical images, but in this case, making use of photometric redshifts. Compared to the method applied in Chu, Durret, and Márquez (2021), which needs spectroscopic redshifts of the clusters and only two filters to extract the red sequence, this method requires more prior measurements: several filters for SED-fitting in order to obtain satisfying z-phots and PDF(z) of galaxies, the photometric redshift of the cluster, as well as density maps which need to be generated. We find that it is still quite effective (success rate of 70%). We also argue that it may be applied to more surveys as only few catalogues of clusters with spectroscopy are available. Photometric redshifts, contrary to spectroscopic redshifts, are quite easily measured. Obtaining catalogues of photometric redshifts of all galaxies in the field can be a time consuming task, but with the development of SED fitting algorithms such as the LEPHARE code, it is possible to obtain photometric redshifts with quite good accuracy. The uncertainties on the z-phots of individual galaxies are of the order of 0.04-0.05 $\times$ $(1 + z_{clus})$, and for clusters the uncertainties are estimated to be 0.025 $\times$ $(1 + z_{clus})$ (Sarron et al., 2018). In expectation of the future Euclid or Rubin-LSST surveys, this method will allow to detect a large number of BCGs and to help build significant catalogues of BCGs for future studies.

2.2.4 The paper

A&A 666, A54 (2022)
https://doi.org/10.1051/0004-6361/202243504

Astronomy & Astrophysics

Physical properties of more than one thousand brightest cluster galaxies detected in the Canada-France-Hawaii Telescope Legacy Survey

A. Chu[1], F. Sarron[2,3], F. Durret[1], and I. Márquez[4]

[1] Sorbonne Université, CNRS, UMR 7095, Institut d'Astrophysique de Paris, 98bis Bd Arago, 75014 Paris, France
e-mail: aline.chu@iap.fr
[2] Jodrell Bank Centre for Astrophysics, University of Manchester, Oxford Road, Manchester, UK
[3] IRAP, Institut de Recherche en Astrophysique et Planétologie, Université de Toulouse, UPS-OMP, CNRS, CNES, 14 avenue E. Belin, 31400 Toulouse, France
[4] Instituto de Astrofísica de Andalucía, CSIC, Glorieta de la Astronomía s/n, 18008 Granada, Spain

Received 9 March 2022 / Accepted 28 June 2022

ABSTRACT

Context. Brightest cluster galaxies (BCGs) are very massive elliptical galaxies found at the centres of clusters. Their study gives clues to the formation and evolution of the clusters in which they are embedded.
Aims. We analyse here in a homogeneous way the properties of a sample of more than 1000 BCGs in the redshift range $0.15 < z < 0.7$, based on images from the Canada-France-Hawaii Telescope Legacy Survey.
Methods. Based on a recent catalogue of 1371 clusters, we applied our automatic BCG detection algorithm and successfully identified 70% of the BCGs in our sample. We analysed their 2D photometric properties with GALFIT. We also compared the position angles of the BCG major axes with those of the overall cluster to which they belong.
Results. We find no evolution of the BCG properties with redshift up to $z = 0.7$, in agreement with previous results by Chu et al. (2021, A&A, 649, A42), who analysed a sample an order of magnitude smaller, but reaching a redshift $z = 1.8$. The Kormendy relation for BCGs is tight and consistent with that of normal elliptical galaxies and BCGs measured by other authors. The position angles of the BCGs and of the cluster to which they belong agree within 30 degrees for 55% of the objects with well-defined position angles.
Conclusions. The study of this very large sample of more than 1000 BCGs shows that they were mainly formed before $z = 0.7$ as we find no significant growth for the luminosities and sizes of central galaxies. We discuss the importance of the intracluster light in the interpretation of these results. We highlight the role of image depth in the modelling of the luminosity profiles of BCGs, and give evidence of the presence of an inner structure which can only be resolved on deep surveys with limiting apparent magnitude at 80% completeness $m_{80} > 26$ mag arcsec^{-2}.

Key words. galaxies: clusters: general – galaxies: evolution – galaxies: formation

1. Introduction

Located at the intersection of cosmic filaments in the large-scale structures, galaxy clusters present in their centres, at the bottom of the cluster potential well, a supermassive galaxy that is also most often the brightest galaxy in the cluster. This galaxy is referred to as the brightest cluster galaxy (BCG).

It is commonly believed that BCGs are supermassive elliptical galaxies with quenched star formation and little to no gas left. Their gas was consumed during mergers that formed stars at earlier epochs, as predicted by Thomas et al. (2010), among others, who find that most of the stellar population present in such galaxies was already formed in situ before the cluster was formed at $z \simeq 2$. However, BCGs with huge reservoirs of molecular gas and strong ongoing star formation have been observed and identified (see McDonald et al. 2016; Fogarty et al. 2019; Castignani et al. 2020). Some of these particular BCGs also have irregular shapes instead of the regular elliptical morphology expected. Sometimes, they can even be reminiscent of jellyfish galaxies, such as RX J1532+3020 that shows traces of a recent merger, with UV-emitting filaments and knots indicating recent starbursts (Castignani et al. 2020). Such cases remain rare, as shown by Chu et al. (2021), who reported that only two BCGs out of 98 were blue galaxies (negative rest frame blue minus red colour) with a high star formation rate (SFR $> 100\,M_\odot\,\mathrm{yr}^{-1}$). Cerulo et al. (2019) found that only 9% of the BCGs that constitute their sample of 74275 BCGs up to $z = 0.35$ have colours bluer than 2σ from the median colour of the red sequence.

Brightest cluster galaxies can form via numerous dynamical and environmental processes, such as galactic cannibalism, cooling flows from the central AGN, or dynamical friction, but the relative importances of these processes on the growth of BCGs and on the stellar mass assembly are still controversial (see Castignani et al. 2020, and references therein). In addition, it is unclear whether BCGs are still evolving today, as authors have found conflicting results.

Observations show that at low and intermediate redshifts ($z < 1$), or even at local redshifts, some BCGs can still be undergoing major mergers that could potentially affect the growth of the central galaxy. This agrees with Bernardi (2009) and Ascaso et al. (2010), for example, who find that the sizes of BCGs have grown by a factor of 2 since $z = 0.5$.

The galaxies that compose the cluster and constitute the red sequence of the cluster, including the BCG, are mostly red elliptical galaxies with little gas content. Major mergers were shown to have little effect on the mass growth of BCGs and to be unlikely to trigger a new starburst phase (De Lucia & Blaizot 2007). De Lucia & Blaizot (2007) show in simulations that half of the final mass of BCGs is already in place by redshift 0.5. Thomas et al. (2010) find that most of the stars in BCGs were already formed before $z = 2$, and De Lucia & Blaizot (2007) show that at least 80% were already formed by $z = 3$. These studies indicate that it is likely that the stellar population in these galaxies has settled earlier than 10 Gyr ago at least. This is consistent with Stott et al. (2011) who find no significant change in the size or shape of these galaxies since $z = 1.3$. Additionally, Chu et al. (2021) find that the physical properties of BCGs, such as effective radius and surface brightness, show little to no evolution since redshift $z = 1.8$, and conclude that BCGs were thus mainly formed before $z = 1.8$. BCGs undergoing major mergers (12 clusters) were also detected in this last study, and were found to have properties that did not differ from those of other BCGs.

Understanding how BCGs were formed and how they evolve can help us to understand how the clusters that host them were formed (see e.g., Lauer et al. 2014). BCGs are the result of billions of years of successive galaxy mergers that can leave an imprint on the galaxy. Numerous studies have shown that clusters are preferentially aligned in the cosmic web, along the filaments that connect them, and that neighbouring clusters separated by less than 30 Mpc tend to 'point to each other' (see Binggeli 1982). BCGs were also found to share this same tendency with their host clusters; Donahue et al. (2015), West et al. (2017), Durret et al. (2019), De Propris et al. (2020) and Chu et al. (2021) have found that BCGs tend to align with the major axis of the host cluster. This means that BCGs tend to have a preferential orientation pointing to the filaments of the cosmic web along which galaxies and groups are falling towards the bottom of the cluster potential well where the BCG is expected to reside. BCGs are aligned by tidal interaction (Faltenbacher et al. 2009) and show stronger alignments for brighter galaxies, for rich and more massive clusters, and for low redshifts (see Faltenbacher et al. 2009; Niederste-Ostholt et al. 2010; Hao et al. 2011). Niederste-Ostholt et al. (2010) find that the second to fifth ranked galaxies of the cluster also tend to show signs of alignment, although not as strongly as the BCG. West et al. (2017) show that other galaxies in the cluster, excluding the BCG, have no preferential orientations in the cluster.

The present study uses data from the Canada-France-Hawaii Telescope Legacy Survey (CFHTLS) and concentrates on the redshift range between 0.15 and 0.7. Although the resolution is not as good as that of the *Hubble* Space Telescope (HST), we increased the sample size by almost a factor of 20 (there are 74 BCGs in the same redshift range in Chu et al. 2021), making this analysis one of the largest studies on BCGs, thus allowing us to go deep into the study of the luminosity profiles of these galaxies.

The intracluster light (ICL) is also brought up in this study. The ICL is composed of stars that were stripped from their host galaxies and are now trapped in the potential of the cluster, but are not gravitationally bound to any individual galaxy in the cluster. This ICL constitutes a very diffuse and faint component of the cluster, which is thus very difficult to detect and can merge with the extended envelope of the central galaxy. One challenge is to distinguish the BCG from the ICL. Some works have shown, by studying the velocity dispersion as a function of the distance to the BCG centre, an increase in the dispersion observed at longer distances (Cui et al. 2014; Jiménez-Teja et al. 2021). This discrepancy shows the border between ICL and BCG. However, spectroscopic observations are currently necessary to achieve this. In the absence of such spectroscopic data, algorithms that attempt to detect the ICL on deep large-scale images are being developed and should allow us to detect low surface brightness objects even more efficiently on optical images in the near future. This topic is bound to become all the more important with the release of deep sky surveys (see e.g., Jiménez-Teja & Dupke 2016; Kluge et al. 2020, 2021; Ellien et al. 2021). In this paper we also discuss and estimate how much the ICL may impact the luminosity profiles of BCGs at these redshifts.

The paper is organized as follows. The data and the method used to detect the BCGs are presented in Sect. 2. In Sect. 3 we describe how the luminosity profiles were modelled, and analyse the results obtained. In Sect. 4 we estimate in a preliminary study the impact of the ICL on the models fitted, and in Sect. 5 the impact of the depth of the images. We measure the alignment of BCGs with their host clusters in Sect. 6. Finally, we discuss the results and present our conclusions in Sect. 7.

Throughout this paper we assume a ΛCDM model with $H_0 = 70\,\mathrm{km\,s^{-1}\,Mpc^{-1}}$, $\Omega_\mathrm{M} = 0.3$, and $\Omega_\Lambda = 0.7$. We compute the scales and physical distances using the astropy.coordinates package[1]. All magnitudes are given in the AB system.

2. Obtaining the BCG catalogue

2.1. The data

This work is based on the cluster catalogue of 1371 clusters by Sarron et al. (2018), extracted in the 154 deg^2 region covered by the CFHTLS with the AMASCFI cluster finder. The survey is 80% complete in AB up to a magnitude $m_\mathrm{i} = 24.8$ in the CFHTLS i filter, for point sources. The code detects clusters as galaxy overdensities in overlapping photometric redshift slices. Multiple detections that occur in such a configuration are then cleaned using a minimal spanning tree (MST) algorithm. The cluster candidates have a mass $M_{200} > 10^{14}\,M_\odot$ and are limited to redshift $z \leq 0.7$. By running the AMASCFI cluster finder on mock data created using lightcones from the Millennium simulations (Springel et al. 2005; Henriques et al. 2012) and modified to mimic CFHTLS data, Sarron et al. (2018) estimated that this cluster sample is 90% pure and 70% complete overall. At $z \leq 0.7$, they find that the purity is fairly constant with redshift ∼90%, while the completeness steadily decreases with increasing redshift and decreasing cluster mass from ∼100% down to ∼50% at $z \sim 0.6$ and $M_{200} \sim 10^{14}\,M_\odot$. The large number of clusters in this catalogue, with known selection function, allowed Sarron et al. (2018) to discuss the properties and evolution of cluster galaxies with redshift in various mass bins.

Photometric redshifts are available for each galaxy in the field in the CFHTLS TERAPIX T0007 release. These photo-zs were computed with the LePhare code (Arnouts et al. 1999; Ilbert et al. 2006) based on five filters in the optical.

For the purpose of this work we used the redshift probability distribution function (PDF) for each cluster, $\mathrm{PDF}_c(z)$, computed by Adami et al. (2020) on the Sarron et al. (2018) catalogue. We note however, that contrary to Adami et al. (2020), we did not split $\mathrm{PDF}_c(z)$ with multiple peaks into sub-detections. We made this choice in order to stay as close as possible to the original catalogue released in Sarron et al. (2018). Briefly, the cluster redshift PDF is computed by summing (stacking) the $\mathrm{PDF}_\mathrm{gal}(z)$ of

[1] https://docs.astropy.org/en/stable/coordinates/

galaxies (provided for each galaxy in the photometric redshift release of the CFHTLS T0007) less than 0.5 Mpc from the cluster centre and removing the expected field stacked $\mathrm{PDF}_{\mathrm{field}}(z)$ in that region.

The cluster redshift $\mathrm{PDF}_c(z)$ allows us to compute for each galaxy in the cluster vicinity the probability that the galaxy and the cluster are at the same redshift: P_z. This is done by convolving the redshift PDFs following the formalism of Castignani & Benoist (2016) as in Adami et al. (2020):

$$P_z \propto \int \mathrm{PDF}_c(z)\,\mathrm{PDF}_{\mathrm{gal}}(z)\,\mathrm{d}z. \quad (1)$$

We note that since then Sarron & Conselice (2021) have proposed a slightly updated version of this formalism that better accounts for the combined uncertainties of cluster redshift and cluster galaxy redshift in the P_z estimate. However, the correction amounts to a few percent in the worst case, and we thus decided to reuse the Adami et al. (2020) results directly in the present work. By taking into account the distance between the galaxy and the cluster centre, we also generated the probability that a galaxy was part of the cluster, $\mathrm{PDF}_{\mathrm{member}}(z)$, following Adami et al. (2020).

However, Sarron et al. (2018) detected clusters using galaxy density maps (without magnitude or luminosity weighting) computed in large redshift bins. The exact centre assigned to each cluster is then taken as the signal-to-noise ratio (S/N) weighted mean position of its individual sub-detections merged in the MST cleaning process. This implies that the centre assigned by Sarron et al. (2018) is close to an unweighted barycentre of galaxies in the cluster region. This position may differ significantly from the BCG position in some cases (e.g., in highly substructured clusters). Moreover, tests on simulations showed that the uncertainties on the centre coordinates as defined by Sarron et al. (2018) can reach hundreds of kiloparsecs in the worst cases. Considering the distance to the cluster centre would thus negatively bias our detection rate.

In the following subsection we describe our method for detecting BCGs on optical images from the CFHTLS. This method makes use of the probability for each galaxy to be at the same redshift as the cluster, $P_z(z)$, and not the probability for the galaxy to be part of the cluster, $P_{\mathrm{member}}(z)$.

2.2. Detection of BCGs

We retrieved the CFHTLS images from the Canadian Astronomy DATA Centre[2] and identified in each cluster the position of its BCG. The BCG is defined as the brightest galaxy in the cluster that lies within a radius of 1.2 Mpc from the centre defined in Sarron et al. (2018), after filtering out foreground and/or background objects.

Lack of spectroscopic data has led astronomers to develop methods that only make use of photometric properties. In Chu et al. (2021), spectroscopic redshifts of the clusters allowed us to accurately extract the red sequence, which was then used to identify the BCG. With the present dataset, we rely on photometric redshifts to distinguish cluster members from field objects.

Similarly to Chu et al. (2021), we first proceeded by removing foreground galaxies, taking into account the uncertainties on the redshift. Spectroscopic redshifts, if available, were retrieved from the NASA/IPAC Extragalactic Database (NED) to remove all sources that are not within the redshift 68% confidence interval. Point sources were identified in NED, or via the CLASS_STAR parameter (CLASS_STAR < 0.95) in SExtractor. To identify foreground galaxies, we calculated the pseudo absolute magnitude (at the cluster's redshift) for each object. Foreground galaxies would in this way appear abnormally bright ($M_{\mathrm{abs}} < -26$). Edge-on spirals were excluded as well by filtering out any object with a major-to-minor axis ratio higher than 2.6.

In order to identify the BCG among the remaining galaxies in the catalogue, we measured the S/N at the galaxy's coordinates on the density map from Sarron et al. (2018), and considered the galaxy's probability of being at the cluster's redshift (see Eq. (1)). The S/N, compared to the S/N peak ($\mathrm{SN}_{\mathrm{peak}}$) defined in a radius of 5 Mpc centred on the cluster centre, gives information on the location of the galaxy in its host cluster. Taking into account the S/N of the galaxy measured on density maps, instead of simply taking the distance to the cluster centre as defined in Sect. 2, allows the size and extent of the cluster to be considered as well. It was shown that BCGs do not always lie at the very centre of the host cluster (see Chu et al. 2021, and references therein), so defining a strict limit in distance appears to be hazardous. In an attempt to define the size of the cluster, we computed the S/N in the background of the density maps, $\langle \mathrm{SN}_{\mathrm{bkg}} \rangle$, in a ring between 2 and 3 Mpc from the defined cluster centre. All objects with $\mathrm{S/N} < \mathrm{SN}_{\mathrm{lim}}$, with $\mathrm{SN}_{\mathrm{lim}} = \langle \mathrm{SN}_{\mathrm{bkg}} \rangle + 3\sigma_{SN,bkg}$, and with $\sigma_{\mathrm{SN,bkg}}$ the S/N RMS of the pixels in the background were considered not bound to the cluster, and were thus rejected. Similarly, to determine if a galaxy is part of the cluster, we compared the probability that it is at the cluster's redshift, P_z, with the same probability computed for galaxies in the background, $\langle P_{z,\mathrm{bkg}} \rangle$. The background was again taken in a ring between 2 and 3 Mpc from the cluster centre. Objects with $P_z \geq P_{z,\mathrm{lim}}$, with $P_{z,\mathrm{lim}} = \langle P_{z,\mathrm{bkg}} \rangle + 3\sigma_{\mathrm{Pz,bkg}}$, and $\sigma_{\mathrm{Pz,bkg}}$ the P_z RMS of the galaxies in the background, were considered as belonging to the cluster and the others were rejected. Any object that did not agree with these two conditions was eliminated as a BCG candidate.

These limits are well defined if the cluster has a simple elongated shape, and if the signal related to the cluster is not contaminated by another cluster or filament on the density map. Otherwise, the presence of such structures can increase the noise in the background, resulting in too high dispersions for the background S/N and P_z. This can result in a limiting $\mathrm{SN}_{\mathrm{lim}}$ that is higher than the S/N at the peak of the density map, or a limiting $P_{z,\mathrm{lim}}$ higher than a probability of unity, which renders the detection impossible. In these cases, we redefine the S/N and P_z lower limits and set $\mathrm{SN}_{\mathrm{lim}} = \mathrm{SN}_{\mathrm{peak}} - 2$ and $P_{z,\mathrm{lim}} = 0.70$. These limits were chosen after testing different values; they return the best detection rate for our method. We explain how this rate was estimated in the following.

In order to evaluate our method, detections by the algorithm were validated or corrected individually. Two members of our team visually inspected every image, and compared the position of the detected BCG to the distribution of galaxies on the density maps. We also confirmed that no brighter galaxy in the catalogue was more likely to be the actual BCG by comparing the S/N and P_z values to those of the detected BCG. We considered that a brighter galaxy with P_z or S/N similar to the BCG, but slightly below and close to the defined limits, is more likely to be the BCG. If a galaxy was determined to be a better candidate, upon our verification we replaced the BCG detected by our algorithm with the new candidate. We estimate that the method successfully detected about 70% of the BCGs in our sample. For the remaining 30%, the BCG assigned by the algorithm was not the best candidate we chose upon inspection, and we thus manually corrected the detection in our final catalogue.

[2] https://www.cadc-ccda.hia-iha.nrc-cnrc.gc.ca/

From our final catalogue of BCGs, we constructed a subsample of 496 BCGs with known spectroscopic redshifts. We can thus confirm that the BCGs selected in this subsample are indeed the BCGs of their clusters, and better estimate the detection rate of our algorithm. We find that 70% of these BCGs automatically assigned by the algorithm were accurately detected.

There are 133 clusters (i.e. 10% of the initial sample of 1371 clusters) that we excluded, as we were still uncertain, even after verification, which galaxy was the BCG. These clusters have a S/N $\geq$ 4 on the density maps generated by Sarron et al. (2018). This is consistent with Sarron et al. (2018), who estimate their catalogue to be 90% pure. The missing 10% of BCGs might thus correspond to the 10% of false detections in the initial cluster catalogue. We compare the distribution in redshift of the 10% of clusters that have no BCG in our catalogue, and the variation in the cluster catalogue purity with redshift in Sarron et al. (2018), to check if the 10% of false detections we excluded indeed correspond to the 10% of false detections from Sarron et al. (2018). And, indeed, we find similar distributions in redshift. The fraction of clusters in our initial catalogue with no BCG detected increases with redshift, as they compose only ~5% of the clusters at $z < 0.4$ (averaged), and ~10% at $z \geq 0.4$. The purity in Sarron et al. (2018) similarly decreases with redshift. For S/N $\geq$ 4 the catalogue is ~95% pure at $z < 0.4$, and ~90% pure at $z \geq 0.4$. We can thus assume that the clusters we excluded are indeed the 10% impurity from Sarron et al. (2018).

Consequently, our final catalogue of BCGs is supposed to be nearly perfectly pure. We cannot say that it is 100% pure as we do not have spectroscopic redshifts for all objects and cannot certify that the selected galaxy is indeed the BCG. We can only identify which galaxy is the best candidate given the information that we have. Our final sample consists of 1238 detected BCGs and is available at the CDS[3].

Making use of our subsample of clusters with spectroscopic redshifts, we estimate the error on the photometric redshift of our whole sample of CFHTLS detected BCGs; 66% of these BCGs have spectroscopic redshifts within $z_{\rm clus} \pm 0.025 \times (1 + z_{\rm clus})$, the expected 1σ uncertainty on the cluster photometric redshift (Sarron et al. 2018). On the other hand, 2.6% of these galaxies have spectroscopic redshifts greater than 3σ of the photometric redshift of the cluster, which means that the absolute difference between the two redshifts is greater than $3 \times 0.025 \times (1 + z_{\rm clus})$. This validates that the photometric redshift uncertainties of the BCG and the clusters are well defined, and that virtually all the BCGs in our final catalogue are bona fide.

The colours of the detected BCGs were also computed to better estimate the fraction of 'blue' BCGs in that redshift range. We define the $(g-i)$ colour by considering the magnitudes measured in the CFHTLS g and i filters, in a 35 kpc aperture diameter. We apply a K-correction (given by an EZGAL Bruzual & Charlot 2003 model for elliptical galaxies; see Chu et al. 2021) and correct for reddening by galactic extinction. We consider a galactic reddening law $A_{\rm V} = 3.1$, reddening values for the CFHTLS filters from Schlafly & Finkbeiner (2011), and dust maps from Schlegel et al. (1998). We consider that a galaxy is blue if its $(g-i)$ colour is negative. As a result, we find that there are 7% (89) blue BCGs in our sample. These BCGs with blue colours also tend to be at higher redshifts: 68 of the 89 blue BCGs (76%) are at $z > 0.5$. Their photometric properties are discussed and compared to those of red BCGs in the following.

[3] http://simbad.u-strasbg.fr/simbad/

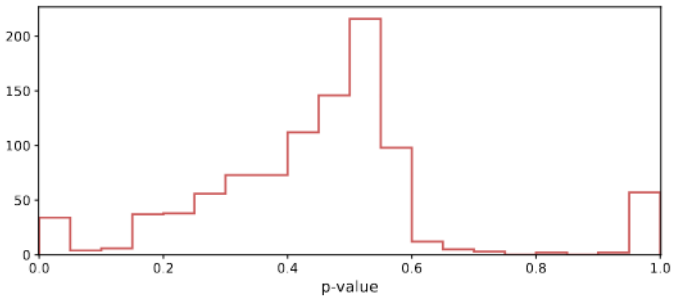

Fig. 1. Histogram of the computed p-values. BCGs that could not be fitted with a single component have a default p-value = 0, and those that could not be fitted with two components have a p-value = 1.

3. Properties of the BCGs

3.1. Method

We fit the 2D luminosity profiles of the 1238 BCGs of our sample with GALFIT in the CFHTLS i band. Up to redshift $z = 0.7$ this filter falls above the 4000 Å break, and hence enables us to consider a homogeneous red and old stellar population for all the BCGs. The method used is the same as described in Chu et al. (2021): we first mask neighbouring sources using SExtractor segmentation maps and sharp-subtracted images (see Márquez et al. 1999, 2003) and model the PSF with PSFex (Bertin 2009). The initial parameters are given by SExtractor by modelling the galaxy with a bulge and a disc. We first run GALFIT to fit the BCGs with one Sérsic component, trying different values of the Sérsic index n between 0.5 and 10 until the fit converges. We reject any non-physical fit with effective radius larger than half the size of the fitting region, which is to say $R_{\rm e} \leq 2.5\, r_{\rm Kron}/2$ pixels, where $r_{\rm Kron}$ is the Kron radius measured by SExtractor. Then, we try to add a second Sérsic component to better model the inner part of the galaxy. If the fit with a single Sérsic profile converges, we use the output parameters for the single-Sérsic model as initial guesses for the external component of the double-Sérsic model. The initial parameters for the inner component are taken once again from SExtractor by considering the parameters returned for the bulge component. If the model with one Sérsic component did not manage to converge, we reinitialize the parameters for the external component and inner component with SExtractor.

The choice between a single-Sérsic and double-Sérsic model is made with an F-test (as was done in Margalef-Bentabol et al. 2016; Chu et al. 2021). The F-test is a statistical test that relies on the residuals and the number of degrees of freedom of two models. The computed p-value, which depends on the F-value (a ratio of reduced χ squares), must be lower than a probability P_0 in order to reject the null hypothesis: if two models give comparable fits, the p-value tends to unity. On the other hand, if the second more complex model gives significantly better results than the first, this value tends to zero and we can reject the null hypothesis. We assigned a p-value = 0 to BCGs that could not be fitted with a single component and a p-value = 1 to those that could not be fitted with two components. Here P_0 is defined as the limit between the low p-values computed and the higher values, which is around $P_0 = 0.15$ (see Fig. 1). This value of P_0 is lower than that defined in Margalef-Bentabol et al. (2016) and Chu et al. (2021), as the p-value is computed taking into account the number of resolution elements. Since the resolution of the CFHTLS is not as good as that of the HST, the value of P_0 defined here appears lower. We also visually checked the fits and

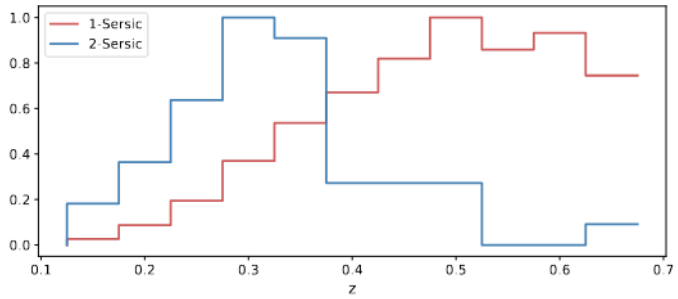

Fig. 2. Normalized histograms of the distribution of redshifts z for BCGs fitted with single-Sérsic (red) and double-Sérsic (blue) models.

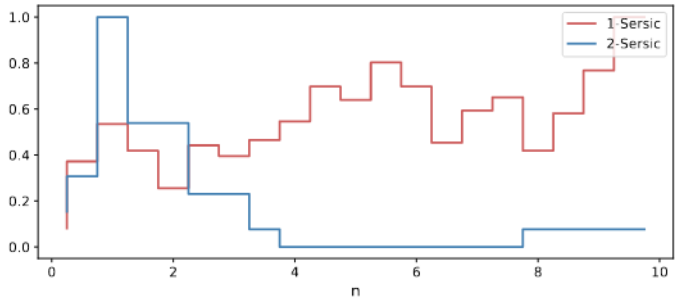

Fig. 3. Normalized histograms of the Sérsic indices n for BCGs fitted with single-Sérsic (red) and double-Sérsic (blue) models. For BCGs fitted with two components, we consider the Sérsic index of the outer component.

residuals of galaxies that have p-values close to this limit to make sure that P_0 is well defined. We verified that for a p-value $p \geq P_0$, the residuals of the single-Sérsic and double-Sérsic models are similar, and for $p < P_0$, the galaxy profile is better fitted with two components.

3.2. Results

Out of the 1238 detected BCGs, 30 were not successfully fitted with either model, bringing our sample to 1208 galaxies. We then only considered galaxies with relative errors on the effective radius, mean surface brightness, and Sérsic index smaller than 20%. Excluding the objects with large uncertainties, we ended up with 1107 BCGs, of which 930 BCGs (84%) are well modelled with one Sérsic component and 177 BCGs (16%) are better modelled with two Sérsic components.

As in Chu et al. (2021), we also excluded all galaxies fitted with two Sérsics that have an inner component (the component with the smaller R_e) that contributes more than 30% to the total luminosity of the galaxy. In the following we consider that the outer component of the double-Sérsic model contains most of the light in the galaxy. This will allow a comparison with a model with one Sérsic component.

Our final sample is thus made of 974 BCGs, of which 930 BCGs (95%) are better modelled with one Sérsic component and 44 BCGs (5%) with two Sérsic components. Among them, there are 80 blue BCGs (8%) which were all well modelled with a single Sérsic component. In the following we consider the measured properties of the outer component of the double-Sérsic BCGs, which is then compared to the properties of the single-Sérsic BCGs. We show the normalized redshift distribution of the sample for the two chosen models in Fig. 2. We find single-Sérsic BCGs at all redshifts, whereas we mainly find BCGs better fitted with two components at lower redshifts (77% of BCGs better fitted with two Sérsics are at redshift $z < 0.4$).

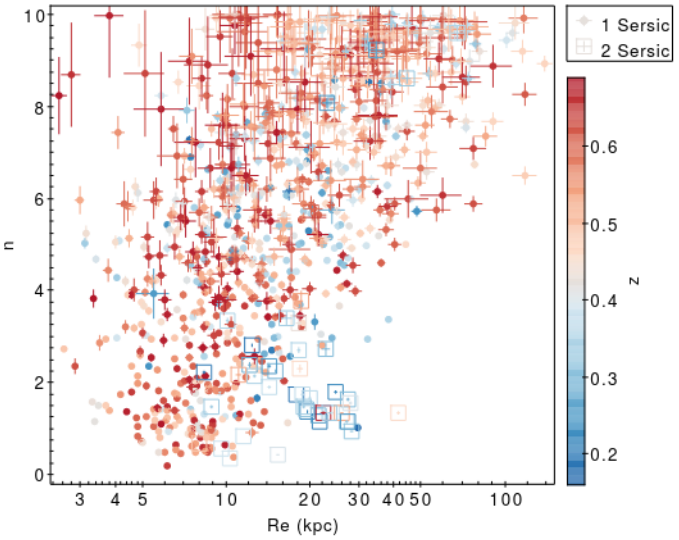

Fig. 4. Sérsic index n as a function of effective radius R_e, colour-coded with redshift. Dots correspond to BCGs fitted with one Sérsic component and empty squares to BCGs fitted with two Sérsic components. For BCGs fitted with two components the properties of the outer component are considered.

The histogram of the BCG Sérsic indices is shown in Fig. 3. The single-Sérsic model fits BCGs with all values of the Sérsic index n, and the distribution appears mostly flat. When a double-Sérsic model is required, the outer component has a very small value of n (mostly between 1 and 2) and the distribution appears more peaked.

Similar results were found in Chu et al. (2021). A first natural interpretation could be that as the redshift increases, the spatial resolution decreases. At lower redshifts, because the galaxies are better resolved, it is possible to distinguish the inner component from the outer component in some galaxies. As a result, galaxies at higher redshifts would be correctly fitted with a single profile, as the centre is not correctly resolved. However, Chu et al. (2021) show that this is not true: degrading the resolution of low-redshift BCGs to the resolution at $z = 1$ returns comparable results, implying that the models are resolution-independent. Moreover, we find similar distributions of z and n with the HST and CFHTLS samples, which strengthens our point, since the HST resolution is much higher than that of the CFHTLS.

We display in Fig. 4 the Sérsic index n as a function of the effective radius R_e in logarithmic scale, colour-coded with redshift. Two-component BCGs are mainly concentrated in a zone with small Sérsic index ($n < 2$) and large effective radius ($R_e > 20$ kpc), and they are also low-redshift objects ($z < 0.4$). When considering only those well fitted with one Sérsic, we find that the Sérsic indices increase as a function of the logarithm of the effective radius. Here, we find $n = (5.13 \pm 0.21)\log(R_e) + (-0.29 \pm 0.26)$ (with a correlation coefficient $R = 0.62$ and significant with a p-value $p \ll 10^{-5}$)[4]. In the following, we consider $R = 0.20$ as the minimum value showing a faint trend, and define $p = 0.05$ as our significance level.

The absolute magnitude and effective radius as a function of redshift are displayed in Fig. 5. Absolute magnitudes range

[4] Linear regressions were made using the Python scipy lingress function: https://scipy.org/

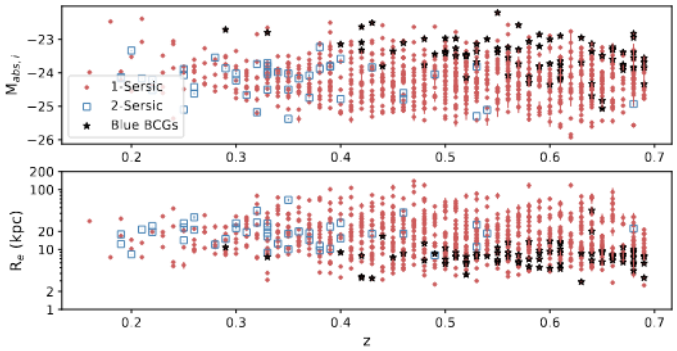

Fig. 5. Absolute magnitude (*top*) and effective radius (*bottom*) measured in the CFHTLS *i* filter, as a function of redshift. BCGs fit with a single component are represented by red dots, BCGs better fit with two components have their outer parameter represented by empty blue squares. Blue BCGs (see Sect. 2) are identified by dark stars. For BCGs fitted with two components the properties of the outer component are considered.

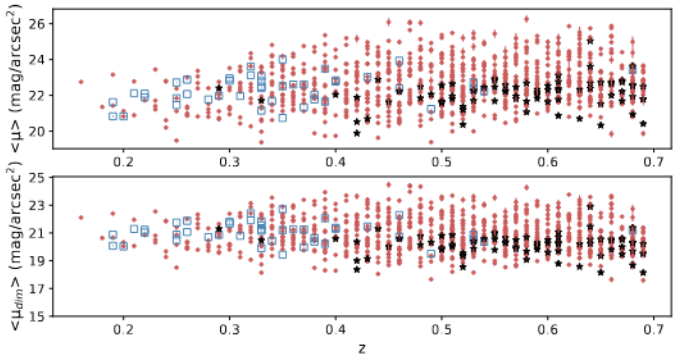

Fig. 6. Mean surface brightness as a function of redshift not corrected (*top*) and corrected (*bottom*) for cosmological dimming. The symbols are the same as in Fig. 5. For BCGs fitted with two components the surface brightness of the outer component is considered.

between −26 and −22 with no dependence on redshift. The effective radius is also redshift-independent. A very faint trend for BCGs to become brighter and bigger with redshift up to $z = 1.8$ is reported in Chu et al. (2021) (correlation coefficient $R = -0.29$ with a p-value $p = 0.007$ for the absolute magnitude to become brighter, and $R = -0.40$ in logarithmic scale with $p < 10^{-3}$ for the size of BCGs to increase). Within the same redshift range as the present study, they measure no correlation for either of these two properties ($R = 0.11$ for the absolute magnitude and $R = 0.27$ for the effective radius, with $p = 0.31$ and $p = 0.01$ respectively). By increasing the sample size by more than a factor of ten, we therefore confirm that BCGs have not grown in luminosity or size since $z = 0.7$ (lower correlations $R = 0.06$ and $R = 0.14$, respectively, with $p = 0.06$ and $p \ll 0.05$).

The mean surface brightness, not corrected and corrected by a factor of $(1 + z)^4$ for cosmological dimming, shows no significant dependence with redshift (Fig. 6). As a result, none of the measured parameters (brightness, surface brightness, size, Sérsic index) is observed to evolve with redshift up to $z = 0.7$.

Blue BCGs, identified by dark stars in the previous figures, also do not show any signs of evolution, but they seem to occupy preferential locations in these relations. For the most part, blue BCGs tend to be at higher redshifts (76% at $z > 0.5$), less bright (mean absolute magnitude for blue BCGs $M_{\rm abs,i,blue} = -23.5$, for red BCGs $M_{\rm abs,i,red} = -24.2$), and smaller (mean effective radius for blue BCGs $R_{\rm e,blue} = 8$ kpc, for red BCGs $R_{\rm e,red} = 22$ kpc) (see Fig. 5), and to have brighter mean surface brightnesses than their red BCG counterparts (mean surface brightness for blue BCGs $\mu_{\rm blue} = 22.1$, for red BCGs $\mu_{\rm red} = 22.6$) (see Fig. 6).

3.3. Kormendy relation for BCGs

The Kormendy relation (Kormendy 1977) between the mean surface brightness and the effective radius is shown in Fig. 7 before (left) and after (right) correcting for the $(1 + z)^4$ cosmological dimming effect. With more than 1000 objets, here the Kormendy relation is very well defined ($R > 0.88$, $p = 0$). Without correction for cosmological dimming, we measure the relation as $\langle\mu\rangle = (3.34 \pm 0.05) \log R_{\rm e} + (18.65 \pm 0.07)$. Similarly to Bai et al. (2014) and Chu et al. (2021), we find that the slope of the Kormendy relation stays constant with redshift. The relation is also independent of the model used (single- or double-Sérsic profiles).

After correcting for cosmological dimming, we find $\langle\mu\rangle = (3.49 \pm 0.04) \log R_{\rm e} + (16.72 \pm 0.05)$. This removes the redshift dependence observed in the left figure, and tightens the relation observed.

3.4. Properties of the double-Sérsic BCG inner component

As in Chu et al. (2021), we do not find any correlation for any of the properties of the inner component of the double-Sérsic BCGs with redshift. The similar sample sizes of about 40 BCGs in Chu et al. (2021) and the present paper do not enable us to better constrain the inner part of these galaxies, and we do not have good enough statistics for our analysis to become significant. Even so, we note that compared to the outer component, the inner component tends to be brighter by at least one magnitude (we recall the selection criterion we applied on double-Sérsic BCGs to retain only those with an inner component that does not contribute much to the total luminosity of the galaxy) and tends to be smaller in size by at least a factor of 3.

The Kormendy relation is also very well defined for the inner component at smaller effective radii and brighter mean surface brightnesses ($R = 0.93$, $p \ll 0.05$) than the relation illustrated in Fig. 7. For the inner component, the relation uncorrected for cosmological dimming is $\langle\mu\rangle = (4.69 \pm 0.29) \log R_{\rm e} + (17.94 \pm 0.15)$.

4. Effect of the ICL on luminosity profiles of galaxies

Despite its faint nature, the ICL may contribute in the outskirts of BCGs and have an influence on their luminosity profiles at large radii. We try here to quantify how much the ICL affects the BCG profiles in model fitting.

We make use of the ICL and background images, kindly provided by Y. Jimenez-Teja, to estimate the effect of the ICL on the shape and photometry measured by GALFIT. Jiménez-Teja et al. (2018) study the ICL fraction in a sample of clusters from the CLASH and Frontier Fields (FF) surveys observed with the HST. We compared the fits obtained with GALFIT on the original HST images with those obtained after subtracting the ICL using the maps provided by Y. Jimenez-Teja. We prefer to use these HST data rather than our current CFHTLS sample for this study as we have spectroscopic redshifts available for the HST sample, better spatial resolution, and the clusters studied in

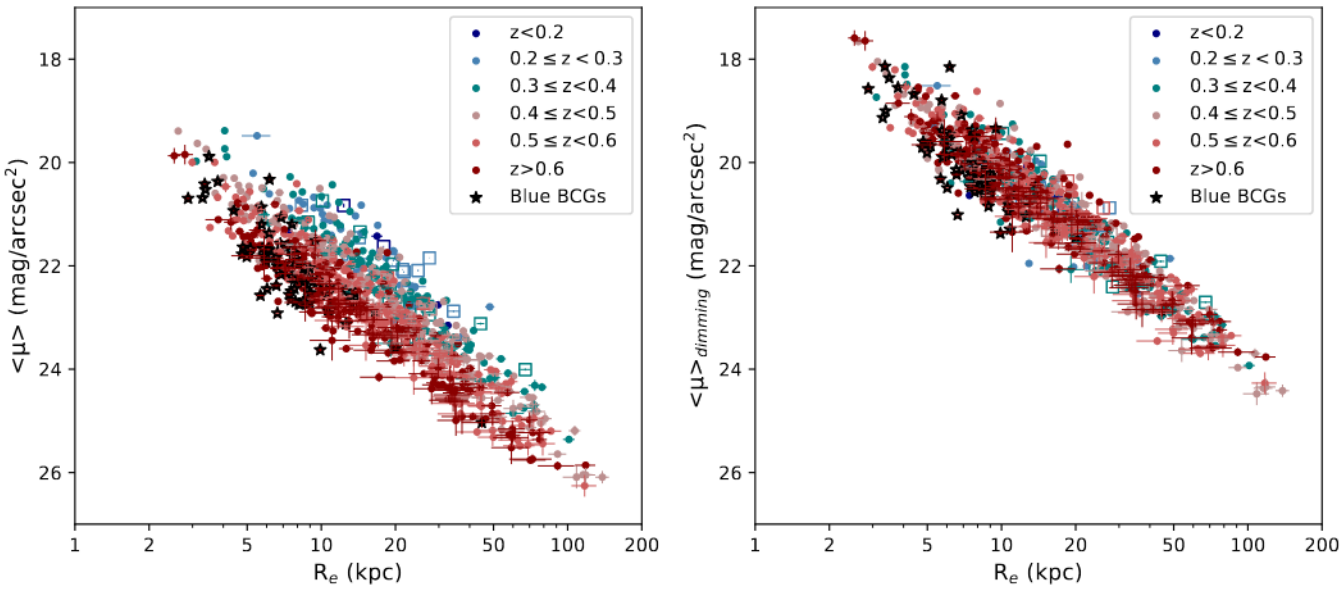

Fig. 7. Kormendy relation before (*left*) and after (*right*) correcting for cosmological dimming. The symbols with various colours correspond to different redshift intervals. For BCGs fitted with two components we consider the properties of the outer component.

Table 1. Sample of the seven clusters from Jiménez-Teja et al. (2018) studied and successfully modelled with GALFIT.

Name	RA_{BCG} (J2000)	Dec_{BCG} (J2000)	z
Abell 2744	3.59204	−30.40573	0.306
Abell 383	42.01412	−3.53921	0.1871
Abell 611	120.23672	36.05658	0.288
MACS J1115.9+0129	168.96625	1.49862	0.349
MACS J1149+2223	177.29874	22.39854	0.5444
RX J2129.6+0005	322.41648	0.08923	0.234
MS 2137−2353	325.06316	−23.66114	0.313

Notes. The columns are full cluster name, coordinates of the BCG, and redshift.

Jiménez-Teja et al. (2018) have deep images on which the ICL was well studied and detected. To check which model between the single-Sérsic and the double-Sérsic models fits our galaxies best, the BCGs are first modelled with GALFIT on the original images. We find that all BCGs need a second component according to the F-test described in Sect. 3.

We then subtract the ICL and background from our images and run GALFIT on these final images, which only contain the BCG. We then compare the returned parameters, and check if subtracting the ICL allows us to remove the inner component needed on the original images. This should indeed allow us to understand if the double-Sérsic model BCGs observed mostly at low redshifts ($z \leq 0.4$) are an effect of the ICL being more easily detectable at lower z.

From a sample of 11 clusters up to $z = 0.54$, four BCGs could not be fitted properly with GALFIT with one or two components. The remaining seven clusters studied here are shown in Table 1. We find that all BCGs, even after subtracting the ICL, are still better fitted using two Sérsic profiles. Thus, we deduce that the ICL does not affect the inner structure of the galaxy, and the need for a second component is not caused by the ICL. By comparing the parameters obtained on the original and ICL subtracted images, by letting all parameters free in GALFIT, we found that the presence of the ICL could disturb the profile of the outer component of the model (in particular, higher effective radius by about a factor of two or three). To better estimate how much the ICL can affect our models, we chose to model one more time the BCGs on the original images, but we fixed the inner component with the parameters obtained on the images without ICL. As the ICL mainly affects the outskirts of the profile, the inner region of the BCG is supposed to be hardly modified. By fixing the inner component, we make sure that we only take into account the differences caused by the ICL.

The parameters measured with two components can be found in Table 2. For all seven BCGs, the absolute magnitude M_{ABS} of the external component is brighter after removing the ICL (with a difference $\Delta M_{ABS} \leq 2$). After subtracting the ICL, the BCGs also have brighter effective surface brightness values, with Abell 2744 presenting the biggest difference of almost 3 mag/arcsec^2. Additionally, for all cases, the effective radii increase in the presence of ICL, some of them drastically. The measured effective radius can be up to 13 times bigger when the ICL is still present in the images. This is the case for MACS J1149+2223.

To further illustrate this, we plot the Kormendy relation obtained with the seven BCGs, before and after subtracting the ICL (Fig. 8). The relation after subtracting the ICL is shifted at lower R_e and brighter $\langle\mu\rangle$, which is consistent with our previous remarks. The slope of the Kormendy relation does not depend on the presence of the ICL.

The outer component profile on ICL-subtracted images still presents a low Sérsic index with $n < 2$ for all BCGs. The Sérsic indices without ICL are smaller than those measured with ICL, resulting in a flatter profile in the outskirts. This is to be expected, as the ICL would extend the profile at higher radii with very faint surface brightness, and the stars that constitute the ICL would blend with the stars that are bound to the BCG in the outskirts. The galaxy would thus appear less compact, bigger, and more diffuse in the presence of ICL.

Since the component with very low Sérsic index ($n < 2$) is still present even after removing the ICL from the original

Table 2. Parameters obtained from fitting the luminosity profiles with two Sérsic components for the ICL sample.

Name	External component				Inner component			
	m_{ABS} (mag)	$\langle\mu_e\rangle$ (mag arcsec^{-2})	R_e (kpc)	n	m_{ABS} (mag)	$\langle\mu_e\rangle$ (mag arcsec^{-2})	R_e (kpc)	n
Abell 2744	−25.93	24.76	155.33	3.13	−23.52	19.39	4.34	2.47
	−24.38	21.96	21.04	0.81				
Abell 383	−25.20	22.01	38.09	0.83	−24.53	19.83	10.22	1.96
	−25.00	21.58	28.52	0.63				
Abell 611	−25.46	22.01	36.34	1.26	−23.70	20.21	7.05	2.68
	−25.19	21.61	26.73	1.03				
MACS J1115.9+0129	−25.26	22.95	46.50	1.68	−22.66	19.50	2.88	1.69
	−24.74	22.22	26.21	1.06				
MACS J1149.5+2223	−26.94	25.72	276.22	3.85	−22.81	20.78	4.23	1.88
	−25.24	23.04	36.75	1.23				
RX J2129.7+0005	−25.54	22.18	44.48	2.02	−22.09	19.15	2.24	1.22
	−25.27	21.75	32.14	1.63				
MS 2137−2353	−25.11	20.71	16.30	2.1	−22.21	20.95	4.80	3.21
	−24.86	20.34	12.27	1.69				

Notes. The columns are full cluster name; absolute magnitude, mean effective surface brightness, effective radius, and Sérsic index for the outer component; and absolute magnitude, mean effective surface brightness, effective radius, and Sérsic index for the inner component. For each cluster the parameters for the outer component are given for the original images (top row) and the ICL subtracted images (bottom row) with fixed inner component.

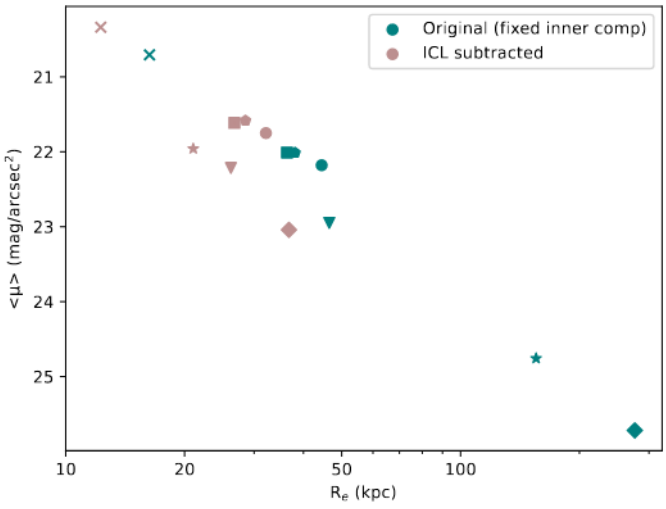

Fig. 8. Kormendy relation obtained for the seven BCGs in our sample before (blue) and after (red) subtracting the ICL on the original images. Each cluster is represented by a different symbol.

images, we thus conclude that the dichotomy observed in the distribution of Sérsic indices and redshifts, following the best model used, is not related to the ICL. Drawing any conclusions regarding the evolution of the size of BCGs with redshift can be tricky, however, as the ICL can affect the profile at large radius.

We tried to take the ICL into account by adding a third Sérsic profile when fitting the original images, and by fixing the parameters of the first two components to those obtained on the ICL subtracted images. Although a Sérsic profile might not be the best choice to model the ICL, our goal was only to check if GALFIT would be able to detect a third component in addition to the BCG. If successful, we could then try to fit three Sérsic profiles instead of two to our whole sample in order for it not to be affected by the ICL contribution.

The test was done on the cluster RX J2129 (chosen arbitrarily from the BCGs that were well fitted previously). A third component was successfully detected and was modelled with faint surface brightness (μ_{ICL} = 25.24), large effective radius ($R_{e,ICL}$ = 190 kpc, i.e. more than four times bigger than that of the outer component), and very low Sérsic index (n = 0.4). Though this result was expected, as the ICL is by nature a very extended envelope with faint surface brightness, GALFIT returns a very elongated component (b/a = 0.2), whereas the ICL map appears close to circular. We thus conclude that GALFIT does not manage to correctly model the ICL and has difficulties in properly fitting components with very faint surface brightness. Adding a third component, in addition to being even more time consuming, is not possible with GALFIT to correct for the effect of the ICL on the outer profile of BCGs.

5. Effect of the depth of the images

As demonstrated above, the presence of BCGs with two Sérsic components observed mostly at low redshifts ($z < 0.4$) is neither due to the lower resolution at higher redshifts nor to the presence of ICL at low redshifts. In Chu et al. (2021), we degraded the resolution of low-redshift clusters to that at redshift z = 1 and in Sect. 4 we remove the ICL from our images to check if these two parameters can influence the choice of the best fitting model, according to the F-test. In both cases we found that we still need two components to properly fit the BCGs that were better modelled with two Sérsics on the original images.

Although we increased by more than a factor of ten the sample size up to z = 0.7 from Chu et al. (2021), we find similar numbers for galaxies better fitted by two Sérsic profiles. Either this is related to the evolution of BCGs, or another observational bias comes into play. To confirm this, we study how the depth of the images affects the model distribution shown in Fig. 2 and in Chu et al. (2021).

We measure the magnitude at 80% completeness, m_{80}, of our catalogues and show the distribution of the model chosen as a

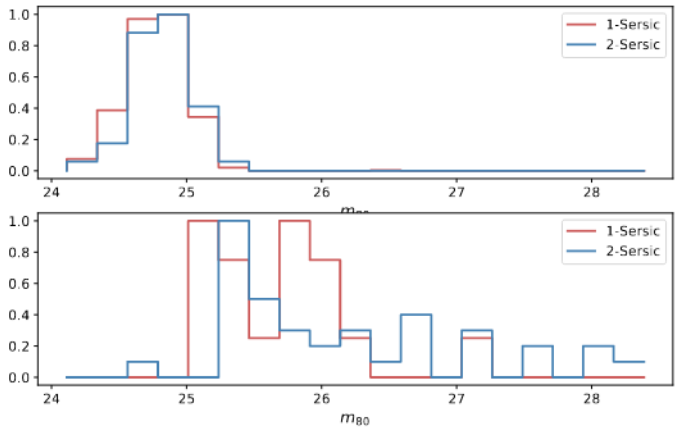

Fig. 9. Normalized distributions of the magnitudes at 80% completeness for the sample in this paper (*top*) and in Chu et al. (2021, *bottom*). The red histograms represent BCGs well fitted with a single component; blue histograms are BCGs better fitted with two components.

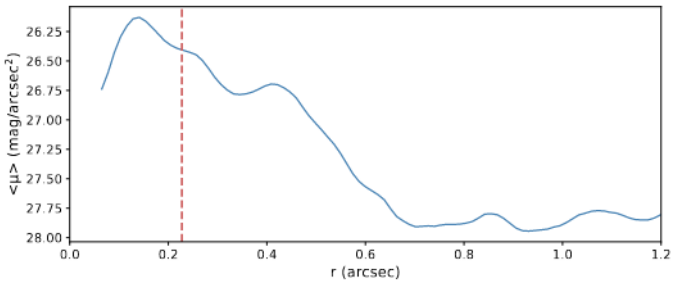

Fig. 10. Surface brightness profile of the ICL in the cluster RX J2129. The surface brightness was computed in a circular aperture, centred on the cluster centre, with a radius r. The red vertical line represents the Kron radius of the BCG.

function of m_{80} (see Fig. 9). The images in Chu et al. (2021) obtained with HST are deeper than those used in the present study, based on the CFHTLS. In Chu et al. (2021, Fig. 9, bottom plot) the distribution of m_{80} has a peak at $m_{80} = 25.4$, and can reach $m_{80} = 28.0$. With our CFHTLS sample, we measure a peak at $m_{80} = 24.7$ (Fig. 9, top plot), and no cluster has $m_{80} > 25.5$. This is consistent with the value indicated in the TERAPIX documentation[5].

With the HST data, out of 54 BCGs up to $z = 0.7$, 37 (69%) were better modelled with two Sérsics. BCGs better modelled with two components have images that go deeper than $m_{80} = 25.2$. For the deepest images ($m_{80} > 26.5$), the BCGs that need an additional component become dominant. Only one BCG was well fitted with a single Sérsic; the other 13 BCGs in that redshift range were better fitted with the more complex model. In the present study, in the same redshift range, we find that only 5% of BCGs need an additional component. Not only does the depth of the CFHTLS images not go as deep as the HST images, but it is also limited to a magnitude $m_{80} = 25$, which is below the magnitude of the peak measured for HST for those fitted with two components. We can guess that if deeper images were available for the CFHTLS, the structure of the BCGs would be better resolved and the number of two-component BCGs would increase.

In another attempt to highlight the influence of the depth of the images on the model used to fit the BCGs, we made use of the Deep fields of the CFHTLS. Eight BCGs in our sample were observed both in the Wide and Deep surveys, allowing us to compare directly the effect of the depth of the images on the luminosity profiles of the BCGs. Using the Deep survey, we find that six out of eight BCGs have a two-component structure. On the other hand, all but one of the same objects observed in the Wide survey lack an inner component. Additionally, the p-values computed on the Wide images ($p_W > 0.35$ on average) are much higher than those obtained on the Deep images ($p_D < 0.1$), indicating that the residuals of the two models tend to become similar as the images become shallower. For one BCG still lacking an inner component on the Deep image, the Wide p-value ($p_W = 0.59$) drops to $p_D = 0.18$ for the Deep image. This suggests that an even deeper image would allow us to resolve the inner component that is currently 'hidden'. This BCG is also the farthest galaxy in our sample of eight BCGs, at $z = 0.65$. On the contrary, the BCG that was better modelled with two components in both images is the one at the lowest redshift, $z = 0.19$.

It may be important to note that in Chu et al. (2021), double-Sérsic BCGs are also observed at redshifts higher than $z > 0.4$. Although they are more dominant at lower redshifts and not as much at higher redshift, we still account for two-component galaxies up to $z = 1.8$. By plotting a $z - m_{80}$ diagram, we distinguish two populations at $z > 0.7$. The first is the dominant population of single-Sérsic BCGs at $z > 0.7$, modelled on images with $m_{80} < 26\,\mathrm{mag\,arcsec^{-2}}$; the second is the population of double-Sérsic BCGs, modelled on images with $m_{80} > 27\,\mathrm{mag\,arcsec^{-2}}$. Consequently, if deeper surveys were available, we could assume that not only would the fraction of two-component BCGs increase at low redshifts, but this would happen at higher redshifts as well.

We also checked if the ICL could be detected in our images, and thus if the ICL affects our study, by measuring its surface brightness on the images provided by Jiménez-Teja et al. (2018) and comparing it with the limit computed for the CFHTLS images. We were able to do this, as images provided by Jiménez-Teja et al. (2018) are very deep images limited to magnitude 27.7 in the F814W ACS filter. Taking the example of RX J2129, the profile in surface brightness is shown in Fig. 10. We find a maximum surface brightness of $26\,\mathrm{mag\,arcsec^{-2}}$ in the centre of the cluster. The profile becomes dimmer the farther we go from the centre, and reaches a surface brightness of $28\,\mathrm{mag\,arcsec^{-2}}$ at distances $r > 0.7$ arcsec ($r > 2.6$ kpc) from the centre. When compared to the surface brightness limit of our CFHTLS sample ($\mu_{\mathrm{CFHTLS},80} = 21.5\,\mathrm{mag\,arcsec^{-2}}$), the ICL is too faint to be observed in our images. We measured a surface brightness $\mu_{\mathrm{ICL}} = 26\,\mathrm{mag\,arcsec^{-2}}$ for the ICL, which is fainter than the surface brightness limit measured on the CFHTLS images. We can thus confirm that the results shown previously are physical and are not affected by ICL.

6. Alignment of BCGs with their host clusters

With the purpose of studying the alignment of BCGs with their host clusters, we measured their positions angles (PA) and ellipticities with GALFIT. Out of the 974 BCGs that were fitted by either one or two Sérsic profiles, 126 have a minor-to-major axis ratio $b/a \geq 0.9$. As in Chu et al. (2021), we exclude these galaxies as an ellipticity close to unity leads to high uncertainties

[5] https://www.cfht.hawaii.edu/Science/CFHTLS/T0007/

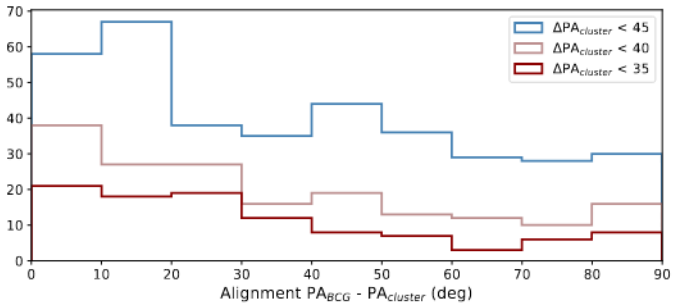

Fig. 11. Histograms of the alignments (absolute difference of PAs) between BCGs and their host clusters. The histograms were obtained after excluding circular objects and systems, and excluding clusters with large PA uncertainties ($\Delta PA_{cluster} > 45$ degrees in blue, $\Delta PA_{cluster} > 40$ degrees in light red, $\Delta PA_{cluster} > 35$ degrees in dark red).

on the measurement of the PA, and also to an ill-defined PA. We thus end up with 848 BCGs.

We measured the cluster ellipticities by fitting ellipses on the density maps with a 3σ clipping, applying the ellipse function in the Python photutils package[6]. All clusters with $b/a \geq 0.9$ were excluded. This reduced the sample to 639 clusters.

Similarly to West et al. (2017), we measured the PA of clusters by computing the moments of inertia on the galaxy density maps provided by Sarron et al. (2018), and estimated the uncertainties with bootstrap resamplings. For each cluster, we generated 100 bootstraps of half of the pixels of the density maps, in a radius $R_{500,c}$ corresponding to the radius within which the mean density is 500 times the critical density of the Universe at the redshift of the cluster, $\rho_c(z)$. The size of $R_{500,c}$ was computed from the $R_{200,c}$ radius obtained for each cluster in Sarron et al. (2018). The conversion was done using the relation given in Sun et al. (2009): $R_{500,c} = 0.669\ R_{200,c}$. This $R_{200,c}$ was derived from the M_{200} estimate of Sarron et al. (2018) inferred from an X-ray derived mass to optical richness scaling relation:

$$R_{200,c} = \left(\frac{3M_{200,c}}{4\pi 200\rho_c(z)}\right)^{\frac{1}{3}}. \quad (2)$$

We initially wanted to exclude all clusters that present large uncertainties on their PAs. However, we found that most clusters tend to have very high uncertainties of around 45 degrees. This can be explained by the fact that, as stated in Sect. 2, clusters are detected in density maps that cover a wide redshift bin (on average, the width of the redshift bin is $\delta z = 0.15$), which means one detection can overlap with another cluster at a nearby redshift. The presence of filaments, which link clusters in the cosmic web, can also bias the measured PA. For all these reasons, the uncertainties computed by bootstrap resampling can be large if the cluster is not rich (and thus has a low S/N on density maps), if it is circular, or if it is not isolated.

We chose to cut the samples by removing clusters with uncertainties bigger than 45, 40, and 35 degrees. This reduced our samples to 420, 203, and 116 clusters and BCGs, respectively.

The alignments (differences between the cluster and BCG PAs) for the final samples are illustrated in Fig. 11. For all three histograms, even with the largest uncertainties on the PA of the cluster, we still observe a peak at lower differences. We measure, respectively (for errors of 45, 40, and 35 degrees), $44 \pm 2\%$, $51 \pm 3\%$, and $57 \pm 4\%$ of BCGs aligned within 30 degrees with their host clusters (uncertainties on the alignment fractions were computed by bootstrap resampling). On the contrary, only 24%, 22%, and 18% of BCGs differ by more than 60 degrees from the major axis of the cluster. This shows a tendency for BCGs to align with the major axis of their host clusters that is discussed in Sect. 7. To assess the confidence that our observation is not due to random fluctuations in a sample with a finite number of clusters, we computed the expected uncertainty on f_{random} through bootstrap realisations of sampling from a random distribution for $N = 420$ and 116 clusters, respectively. This allows us to estimate that the observed alignment is not due to random fluctuations at 3.4σ ($\Delta PA_{cluster} < 45$ deg) and 4σ ($\Delta PA_{cluster} < 35$ deg), respectively.

Furthermore, we find that BCGs in very massive clusters of $M_{cluster} > 5\ 10^{14}\ M_\odot$ (and thus the most massive BCGs, by converting cluster mass to BCG mass using the relation given in Bai et al. 2014), and bigger BCGs with $R_{e,BCG} > 30$ kpc, tend to be better aligned than the less massive ones. All BCGs in that size and mass range, from Chu et al. (2021, 2 BCGs) and in the present paper (12 BCGs), are found to be better aligned than 30 degrees with the major axis of their host clusters. It is difficult to confirm this with less massive galaxies, however, because of the large scatter in the $M_{cluster}$ versus $|PA_{cluster} - PA_{BCG}|$ relation (similarly, M_{BCG} versus $|PA_{cluster} - PA_{BCG}|$) and the $R_{e,BCG}$ versus $|PA_{cluster} - PA_{BCG}|$ relations.

7. Discussion and conclusions

Making use of the galaxy cluster catalogue of Sarron et al. (2018), we developed an algorithm to detect BCGs in optical images from the CFHTLS. We estimate that 70% of the BCGs in our sample were successfully detected. The final sample of BCGs built and studied in this paper consists of 1238 BCGs.

This method requires large images in order to properly estimate the background (at least 2 Mpc to be far enough from the cluster centre), as well as images in several filters to obtain a good photometric redshift estimate of the galaxies in the cluster field. With the CFHTLS, five filters were available to fit the objects with the LePhare code, enabling Sarron et al. (2018) to estimate photometric redshifts with a typical accuracy of $0.05 \times (1 + z)$.

Several studies such as McDonald et al. (2016), Cerulo et al. (2019), Fogarty et al. (2019), Castignani et al. (2020) and Chu et al. (2021) have identified BCGs with unusual blue colours, showing signs of recent starbursts. However, such BCGs are scarce, and increasing their statistics is necessary to better understand the processes that lead these galaxies to behave differently from their red counterparts. By computing the $(g - i)$ colours of the BCGs, we also estimate the fraction of blue ($g - i < 0$) BCGs in the Universe up to $z = 0.7$. We find that 9% of BCGs in our sample are blue, which is consistent with the estimates given in the cited papers.

By applying the same method as in Chu et al. (2021), we modelled the luminosity profiles of the BCGs by fitting two models, one with a single Sérsic component and one with two Sérsic components. The model was chosen using the statistical F-test: we observed two populations with a separation at $z = 0.4$, below which some BCGs tend to require an additional component to take into account the brighter bulge. Up to $z = 0.7$, in Chu et al. (2021), we found that 77% of BCGs were better modelled with two components, while here only 5% are better modelled with two Sérsics in the same redshift range. Even though we significantly increase the size of our sample, the number of

[6] https://photutils.readthedocs.io/en/stable/isophote.html

two-component BCGs did not increase, and we find that the fraction of double-Sérsic BCGs actually decreases. In order to understand and explain why these galaxies with a more important bulge exist mostly at lower redshifts, we checked for any observational bias that could affect our study.

Although the spatial resolutions of this sample and of the sample in Chu et al. (2021) are different, we still find similar distributions for the best model, with double-Sérsic BCGs found mainly at lower redshifts ($z < 0.4$). We also find similar distributions for the Sérsic indices, with two-component BCGs having lower indices ($n < 2$), and single-component BCGs presenting indices that cover a wide range between 0 and 10, with a flatter distribution. This hints that the resolution of the images does not play a large role in model fitting. We confirmed this in Chu et al. (2021) by degrading the resolution of HST images at low z and verifying that the fits returned by GALFIT were unchanged.

We already took into account the distance at which the galaxies are observed by considering a filter that is above the 4000 Å break, and thus by always modelling the same red stellar population. However, it is all the more difficult to detect objects with faint surface brightness at high redshifts, without deep exposure times. We thus pondered if ICL, which has very faint surface brightness, might be detectable at lower redshifts, and would thus constitute the second component observed.

By removing the ICL contribution, using images provided by Jiménez-Teja et al. (2018), we show that the presence of ICL can affect the outskirts of the galaxy, and can flatten the profiles at large radii. The presence of ICL can decrease the outer Sérsic index, and increase the size of the BCG. Nonetheless, a second component with low Sérsic index is still needed even after subtracting the ICL. The presence of double-Sérsic BCGs with low index at low redshift is thus also not an effect of the ICL. Moreover, the images studied here are not deep enough to detect the ICL, which is too faint, with a surface brightness $\mu_{\rm ICL} \geq 26\,{\rm mag\,arcsec^{-2}}$. We conclude that our study is not affected by the presence of ICL.

It should be noted that Kluge et al. (2020, 2021), who study a sample of 170 local BCGs up to $z = 0.08$, find a fraction of 71% of BCG+ICL systems that are well described with a single Sérsic component. The remaining 29% are better fitted with an additional component. This outer component of the double-Sérsic BCG+ICL system would trace the unrelaxed star material that might have been accreted in the recent past.

In this study we find that 95% of the BCGs in our sample at higher redshifts are well modelled with a single Sérsic component, and 5% need two components. The very different fractions between the two studies could be due to the depth of the images and/or to the presence of ICL. The limiting magnitude in Kluge et al. (2020, 2021) is deeper, $\mathrm{SB_{lim}} = 30\,g'\,{\rm mag\,arcsec^{-2}}$, which allows them to detect the ICL surrounding the BCG. In the present study the magnitude at 80% completeness in the i CFHTLS filter is $m_{80} = 24.7$. We also show for a small sample of seven BCGs from Jiménez-Teja et al. (2018) that the presence of a second component is independent from the presence of ICL. If the ICL does not play a role in the existence of a second component, then it cannot explain the difference between Kluge et al. (2020, 2021) and our study. A large sample of BCGs with deep images, as in Kluge et al. (2021), should be used to disentangle the ICL contribution with a similar method to the one we applied to the ICL-subtracted images from Jiménez-Teja et al. (2018).

Lastly, we compare the completeness of our catalogues. We recall that in Chu et al. (2021) 85% of BCGs at redshift $z \leq 0.4$ are two-component galaxies, whereas here they only represent 16% of our sample at $z \leq 0.4$. We find that double-Sérsic component BCGs in Chu et al. (2021) tend to appear in images that have a depth of the order of $m_{80} > 26.5\,{\rm mag\,arcsec^{-2}}$. Our current CFHTLS data do not go as deep as the HST images, and the structure of the BCG is thus not as well determined. We could assume that repeating this study with deeper images would reveal the existence of an inner component at $z \leq 0.4$ for most of the BCGs that are well modelled with a single Sérsic component in this paper. The presence of such an inner structure would indicate that bulges of BCGs may have formed first, and the extended envelope would have formed later on, at $z \leq 0.4$. As Edwards et al. (2019) state, the cores and inner regions of BCGs were already formed long ago and stopped evolving, whereas the outer regions as well as the ICL started developing recently via minor mergers. This would also agree with the assumption that the ICL was formed at later times ($z < 1.0$), as stated by Jiménez-Teja et al. (2018) and references therein. Montes & Trujillo (2017) claim that the ICL saw most of its formation happen at $z = 0.5$; this would agree with the discrepancy between the two models we observe around $z = 0.4$, which could hint at a more important contribution of the ICL to the luminosity profile of BCGs at $z \leq 0.4$. According to Lauer et al. (2014), from a study of 433 $z \leq 0.08$ BCGs, although the inner portions would have already been assembled before the cluster was formed, the envelope would be expanded by dry mergers as the BCG spends time in the dense centre of the cluster. These dry mergers would not make the BCG brighter, but they would contribute greatly to the extension of its outer envelope. This inside-out scenario has been confirmed by many authors (De Lucia & Blaizot 2007; van Dokkum et al. 2010; Bai et al. 2014; Ragone-Figueroa et al. 2018; Edwards et al. 2019; Dalal et al. 2021). As they experience more interactions with other galaxies, and thus as their envelope forms as they accrete more and more matter, BCGs can be expected to evolve from single-Sérsic into double-Sérsic BCGs.

In Chu et al. (2021), double-Sérsic BCGs are observed up to $z = 1.8$, even though they are not dominant at higher redshifts. These two-component galaxies are found in the deepest images with limiting magnitudes $m_{80} > 27\,{\rm mag\,arcsec^{-2}}$. The remaining population of single-Sérsic BCGs are modelled on images with $m_{80} < 26\,{\rm mag\,arcsec^{-2}}$. The separation between the two models at higher redshifts that depends on the depth of the images highlights the importance of deep surveys. We would expect to detect two components in all BCGs, but this requires deep images and long exposure times. Even though the depth of the images could be a solution to resolving the structure of these central galaxies, we can still wonder if other cluster properties may be linked to the properties of this inner component. We do not find any correlation between the properties of the inner component and redshift, or with the cluster properties. Moreover, the small sample size of double-Sérsic BCGs does not enable us to draw any significant conclusions. Deeper surveys are needed to confirm our results and assumptions, and determine any link between the presence of an inner component and BCG growth.

In order to understand whether BCGs are still growing today, we looked for correlations between redshift and the physical properties of BCGs measured with GALFIT. We find no evolution as a function of redshift for the effective radius and absolute magnitude. In Chu et al. (2021), no correlation could be found for the mean surface brightness when no dimming correction was applied, up to $z = 1.8$. A trend could be seen up to $z = 0.7$ ($R = 0.29$, $p = 0.013$), but in fact this trend was caused by cosmological dimming. After correcting for this effect, the trend is no longer measured ($R < 0.1$). We once again verified this result, as no correlation could be found here between the

corrected mean surface brightness and redshift. The large size of our sample enables us to confirm the results shown in Chu et al. (2021) up to $z = 0.7$, namely that BCGs were mainly formed before 0.7 ($z = 1.8$ in our previous study), and have properties that appear to have remained stable since then.

Following the work of Graham & Colless (1997) and Bai et al. (2014), we demonstrate that the Sérsic index varies as the logarithm of the effective radius: $n = (5.13 \pm 0.21)\log(R_e) + (-0.29 \pm 0.26)$, while Graham & Colless (1997) find approximately $n \propto 3.22 \log(R_e)$. Our relation is steeper than that found by these authors, which means the measured Sérsic indices are more sensitive to small variations of the effective radius.

We also plot the Kormendy relation for BCGs, which is very well defined with our sample. Our relation, not corrected for cosmological dimming, $\langle\mu\rangle = (3.34 \pm 0.05)\log R_e + (18.65 \pm 0.07)$, agrees within 1σ with that given in Bai et al. (2014) and Chu et al. (2021), and within 3σ with Durret et al. (2019):
$\langle\mu\rangle = (3.50 \pm 0.18)\log R_e + (18.01 \pm 0.23)$ (Bai et al. 2014);
$\langle\mu\rangle = (3.33 \pm 0.73)\log R_e + C$ (Chu et al. 2021);
$\langle\mu\rangle = (2.64 \pm 0.35)\log R_e + (19.7 \pm 0.5)$ (Durret et al. 2019).

The dependence with redshift is due to cosmological dimming, which moves the relation to fainter surface brightnesses without affecting the sizes of the BCGs. The slope measured is also steeper than that of Bai et al. (2014) measured for non BCG early type galaxies: $\langle\mu\rangle = (2.63 \pm 0.28)\log R_e + C$.

Following the work of Donahue et al. (2015), West et al. (2017), Durret et al. (2019), De Propris et al. (2020) and Chu et al. (2021), we show that the major axis of the BCG tends to align with that of the host cluster. We find that at least $(44 \pm 2)\%$ of BCGs are aligned with their host clusters within 30 degrees. By only considering the best measured PAs (uncertainties smaller than 35 degrees), this percentage goes up to $(57 \pm 4)\%$. If BCGs had a random orientation, we would expect a uniform distribution, and thus only $f_{\rm random} = 33\%$ of BCGs aligned with the major axis of their host clusters within 30 degrees. We confirm that the measured alignment fractions are not due to random fluctuations as the number of clusters studied is finite. We also confirm the results by Faltenbacher et al. (2009), Niederste-Ostholt et al. (2010) and Hao et al. (2011) who find stronger alignments for brighter and bigger galaxies. In the hierarchical scenario of structure formation, matter and galaxies fall into the centre of clusters along cosmic filaments. This would create tidal interactions that can explain the observed alignment of BCGs with their host clusters. Thus, contrary to other cluster members, as was found by West et al. (2017) who show that non BCGs members of a cluster have a random orientation in the cluster, the BCG properties are linked to the cluster.

This study shows, with increased statistics, evidence for an early formation of the brightest central galaxies in clusters. Most of their matter content was already in place by $z = 0.7$, and we showed in Chu et al. (2021) that this conclusion can most likely be applied up to $z = 1.8$. New datasets in the infrared (JWST, *Euclid*) should enable us to confirm this result at higher redshifts with better statistics. In the present paper, we also estimate in a first approach the contribution of the ICL to such studies.

Acknowledgements. We are very grateful to Y. Jiménez-Teja for providing us with her ICL images. We also thank A. Ellien for discussions on the ICL. We thank the referee for her/his constructive comments and suggestions. F.D. acknowledges continuous support from CNES since 2002. I.M. acknowledges financial support from the State Agency for Research of the Spanish MCIN through the "Center of Excellence Severo Ochoa" award to the Instituto de Astrofísica de Andalucía (SEV-2017-0709), and through the program PID2019-106027GB-C41. Based on observations obtained with MegaPrime/MegaCam, a joint project of CFHT and CEA/DAPNIA, at the Canada-France-Hawaii Telescope (CFHT) which is operated by the National Research Council (NRC) of Canada, the Institut National des Sciences de l'Univers of the Centre National de la Recherche Scientifique (CNRS) of France, and the University of Hawaii. This work is based in part on data products produced at Terapix and the Canadian Astronomy Data Centre as part of the Canada-France-Hawaii Telescope Legacy Survey, a collaborative project of NRC and CNRS. This research has made use of the NASA/IPAC Extragalactic Database (NED) which is operated by the California Institute of Technology, under contract with the National Aeronautics and Space Administration.

References

Adami, C., Sarron, F., Martinet, N., & Durret, F. 2020, A&A, 639, A97
Arnouts, S., Cristiani, S., Moscardini, L., et al. 1999, MNRAS, 310, 540
Ascaso, B., Aguerri, J. A. L., Varela, J., et al. 2010, ApJ, 726, 69
Bai, L., Yee, H., Yan, R., et al. 2014, ApJ, 789, 134
Bernardi, M. 2009, MMNRAS, 395, 1491
Bertin, E. in Astronomical Data Analysis Software and Systems XX, eds. I. N. Evans, A. Accomazzi, D. J. Mink, & A. H. Rots, ASP Conf. Ser., 442, 435
Binggeli, B. 1982, A&A, 107, 338
Bruzual, G., & Charlot, S. 2003, MNRAS, 344, 1000
Castignani, G., & Benoist, C. 2016, A&A, 595, A111
Castignani, G., Pandey-Pommier, M., Hamer, S. L., et al. 2020, A&A, 640, A65
Cerulo, P., Orellana, G. A., & Covone, G. 2019, MNRAS, 487, 3759
Chu, A., Durret, F., & Márquez, I. 2021, A&A, 649, A42
Cui, W., Murante, G., Monaco, P., et al. 2014, MNRAS, 437, 816
Dalal, R., Strauss, M. A., Sunayama, T., et al. 2021, MNRAS, 507, 4016
De Lucia, G., & Blaizot, J. 2007, MNRAS, 375, 2
De Propris, R., West, M. J., Andrade-Santos, F., et al. 2020, MNRAS, 500, 310
Donahue, M., Connor, T., Fogarty, K., et al. 2015, ApJ, 805, 177
Durret, F., Tarricq, Y., Márquez, I., Ashkar, H., & Adami, C. 2019, A&A, 622, A78
Edwards, L. O. V., Salinas, M., Stanley, S., et al. 2019, MNRAS, 491, 2617
Ellien, A., Slezak, E., Martinet, N., et al. 2021, A&A, 649, A38
Faltenbacher, A., Li, C., White, S. D. M., et al. 2009, Res. Astron. Astrophys., 9, 41
Fogarty, K., Postman, M., Li, Y., et al. 2019, ApJ, 879, 103
Graham, A., & Colless, M. 1997, MNRAS, 287, 221
Hao, J., Kubo, J. M., Feldmann, R., et al. 2011, ApJ, 740, 39
Henriques, B. M. B., White, S. D. M., Lemson, G., et al. 2012, MNRAS, 421, 2904
Ilbert, O., Arnouts, S., McCracken, H. J., et al. 2006, A&A, 457, 841
Jiménez-Teja, Y., & Dupke, R. 2016, ApJ, 820, 49
Jiménez-Teja, Y., Dupke, R., Benítez, N., et al. 2018, ApJ, 857, 79
Jiménez-Teja, Y., Vílchez, J. M., Dupke, R. A., et al. 2021, ApJ, 922, 268
Kluge, M., Neureiter, B., Riffeser, A., et al. 2020, ApJS, 247, 43
Kluge, M., Bender, R., Riffeser, A., et al. 2021, ApJS, 252, 27
Kormendy, J. 1977, ApJ, 218, 333
Lauer, T. R., Postman, M., Strauss, M. A., Graves, G. J., & Chisari, N. E. 2014, ApJ, 797, 82
Margalef-Bentabol, B., Conselice, C. J., Mortlock, A., et al. 2016, MNRAS, 461, 2728
Márquez, I., Durret, F., Delgado, R. G., et al. 1999, A&AS, 140, 1
Márquez, I., Masegosa, J., Durret, F., et al. 2003, A&A, 409, 459
McDonald, M., Stalder, B., Bayliss, M., et al. 2016, ApJ, 817, 86
Montes, M., & Trujillo, I. 2017, MNRAS, 474, 917
Niederste-Ostholt, M., Strauss, M. A., Dong, F., Koester, B. P., & McKay, T. A. 2010, MNRAS, 405, 2023
Ragone-Figueroa, C., Granato, G. L., Ferraro, M. E., et al. 2018, MNRAS, 479, 1125
Sarron, F., & Conselice, C. J. 2021, MNRAS, 506, 2136
Sarron, F., Martinet, N., Durret, F., & Adami, C. 2018, A&A, 613, A67
Schlafly, E. F., & Finkbeiner, D. P. 2011, ApJ, 737, 103
Schlegel, D., Finkbeiner, D., & Davis, M. 1998, ApJ, 500, 525
Springel, V., White, S. D. M., Jenkins, A., et al. 2005, Nature, 435, 629
Stott, J. P., Collins, C. A., Burke, C., Hamilton-Morris, V., & Smith, G. P. 2011, MNRAS, 414, 445
Sun, M., Voit, G. M., Donahue, M., et al. 2009, ApJ, 693, 1142
Thomas, D., Maraston, C., Schawinski, K., Sarzi, M., & Silk, J. 2010, MNRAS, 404, 1775
van Dokkum, P. G., Whitaker, K. E., Brammer, G., et al. 2010, ApJ, 709, 1018
West, M. J., de Propris, R., Bremer, M. N., & Phillipps, S. 2017, Nat. Astron., 1, 0157

Chapter 3

Fossil groups

Fossil groups (FGs) are groups of galaxies (less than a hundred members) which present a brightest galaxy that is at least two magnitudes brighter than the second ranked galaxy of the group, located within half the Virial radius of the cluster from the brightest group galaxy (BGG). They are also X-ray luminous, with an X-ray luminosity at least brighter than $L_X = 10^{42}\ h_{50}^{-2}$ erg s^{-1} (Jones et al., 2003). FGs lack bright galaxies, with only the BGG standing out. Their discovery is quite recent, as Ponman et al. (1994) discovered the first candidate FG (now confirmed) in 1994, less than 30 years ago. Their late discovery, and the rareness of these systems, make it still difficult to understand how these peculiar systems formed.

Two main scenarios have been proposed. First, FGs may be the remnants of early mergers of groups of galaxies and the BGG may have accreted all the massive galaxies in the group a long time ago, which would explain the low number of bright galaxies. In this case, FGs would not evolve anymore and would remain in their final form. This is supported by Jones et al. (2003), D'Onghia et al. (2005), and Zarattini et al. (2022). In the second scenario, FGs would only be a temporary stage in the groups' lives before they capture more galaxies and become similar to normal groups (von Benda-Beckmann et al., 2008; Kundert, D'Onghia, and Aguerri, 2017; Aguerri and Zarattini, 2021). Contradictory studies tend to be mostly in favor of the first scenario, but no clear conclusion has been made yet.

3.1 Data samples

In order to better understand how these special groups form and which conditions made them evolve differently from their peers, it is necessary to obtain large enough samples of FGs to undertake statistically meaningful studies on these objects. In this goal, we have built two different samples of FG BGGs. An on-going project is based on the galaxy group catalogue of Sarron et al. (2018) and will be presented later in this chapter.

In the main study presented here, we make use of Tinker's catalogue of galaxies with available spectroscopy to identify candidate FGs by selecting groups in which the BGG is two magnitudes brighter than all the other members. As of now, these remain labeled as "candidates" as we did not check their X-ray data yet, so they only satisfy one out of the two conditions to be a FG. However, we selected groups with a mass halo $M_{halo} \geq 10^{13}\ M_\odot$. The masses of the halos indicate that, although we lack X-ray data, they are massive enough to be likely gravitationally bound groups with a relatively high X-ray luminosity expected. We plan to submit in 2023 an XMM-Newton proposal to observe candidate FGs for which we will not find X-ray data in the archive. This gave us a sample of 88 candidate FG BGGs between $z = 0.02$ and $z = 0.18$.

We then selected the FG candidates which have good images in the Canada France Imaging Survey (CFIS) survey. The full description of CFIS can be found on the CFHT website[1]. The Principal Investigators are Jean-Charles Cuillandre and Alan McConachie, with about one hundred collaborators from both countries. CFIS has scientific aims in various fields of astronomy. Based on observations made with the Canada France Hawaii Telescope and the MegaCam camera, CFIS is a Large Program that has been allocated 271 nights over six semesters (17A to 19B, from Feb. 1st 2017, to Jan. 31st 2020), and has since been extended (+75 nights) to July 31st, 2022 due to adverse weather conditions. It has two survey components:

- CFIS-r (Wide + Image Quality + Deep) will image $\sim$ 5000 square degrees over 154 nights in the r-band. Covering the sky above a declination of 30 degrees, and outside the galactic plane, it will produce a panoramic survey with exquisite image quality ($\sim$ 0.6 arcseconds) to a depth of r = 24.1 (point source, S/R = 10, 2 arcsecond diameter aperture).
- CFIS-u (continuation of the Legacy for the U-band All-sky Universe - Luau - program) will survey $\sim$ 10000 square degrees over 117 nights, covering the region above a declination of 0 degrees, and outside the galactic plane, to a u-band depth of 23.6 (point source, S/R = 10, 2 arcseconds diameter aperture).

CFIS is now part of the Ultraviolet Near Infrared Optical Northern Survey (UNIONS), which includes CFIS (u and r bands), Pan-STARRS (griz bands) and the Subaru telescope (g and z bands). All these data are available to the consortium members. More information on UNIONS can be found on this[2] website.

Thanks to the depth of the CFIS images, we are able to continue part of the study in Chu et al. (2022) in which we estimate how the ICL can affect the luminosity profiles of BCGs and, more importantly, to resolve the structure of BCGs, which was the main issue with our last work with CFHTLS data.

3.2 Methods and results

We studied three main questions: first, what are the physical properties of FG BGGs and how do they compare to non-FG BGGs; then how does the ICL affect our study; and finally, how did the stellar population of these galaxies evolve with time.

To alleviate the text, we will refer to FG candidates as FGs in the following.

3.2.1 Physical properties of brightest galaxies of fossil and non-fossil groups

Although this is still a work in progress, we bring preliminary answers to each of these questions. For the first one, properties of BGGs of FGs and non-FGs were obtained, similarly to Chu, Durret, and Márquez (2021) and Chu et al. (2022), by modeling the luminosity profiles of the brightest galaxies with `GALFIT`, using one or two Sérsic models, in the available CFIS u (35 BGGs), r (25 BGGs), and $rLSB$ (r low surface brightness, 19 BGGs) filters. The $rLSB$ images are obtained from the r images passed through the Elixir-LSB reduction pipeline to compute image backgrounds as homogeneously as possible, allowing a study of low surface brightness features in the images.

[1] https://www.cfht.hawaii.edu/Science/CFIS/
[2] https://www.skysurvey.cc/

Twelve BGGs have images both in the u and r filters. A sample of 100 non-FGs was obtained from the same Tinker parent sample by selecting groups with a BGG that has a magnitude gap smaller than two magnitudes with the second ranked galaxy. Among them, we selected 30 groups with good CFIS data and with comparable masses, brightnesses and colours to those of FGs.

Because of the very small redshift interval ($0.02 \leq z \leq 0.18$), it was not possible to quantify the evolution of their properties (luminosity, size) over time. Instead, we only tried to characterize the properties of FG BGGs. We find that, as could be expected, BGGs in the u band can mainly be modeled with a single component. Indeed, the signal to noise ratio (S/N) in the blue filter is lower than in the redder filters, as BGGs are mainly early-type galaxies characterized by a passive stellar population and the blue filter captures the young stellar component of these galaxies. In r and $rLSB$, BGGs are mostly modeled with two surface brightness components. This is in agreement with Chu et al. (2022), in which we concluded that most BCGs may be two-Sérsic galaxies, but that deep images in the red passbands were necessary in order to distinguish the more complex structure of these galaxies. The r and $rLSB$ CFIS images are deep enough to detect this second component.

What was unexpected, however, is the lower fraction of two-Sérsic BGGs in the $rLSB$ images than in the r images. Indeed, by bringing out low surface brightness features, we would have expected the ICL to be more noticeable on these images. The presence of ICL would have, in theory, extended the profile at higher radii of these galaxies. In Chu et al. (2022), we showed that ICL would not cause the appearance of a second component, so while we may not really expect the fraction of two-Sérsic BGGs to increase significantly in the $rLSB$ images, its decrease is even less expected. We suspect that the Elixir-LSB reduction pipeline may be responsible for this, as it may clean the fainter scattered light surrounding the BCG, thus changing its profile. This can be seen on Figure 3.1: top left is the original image and the top right is the sky background measured by the Elixir-LSB pipeline. The bottom image is the resulting image after subtraction of the background to the original image. Flux around the galaxy has been removed, and the galaxy appears less extended.

We find, from the parameters returned by `GALFIT`, that although the effective radii and the Sérsic indices of FG and non-FG BGGs are similar, FG BGGs are in general brighter in absolute magnitude and mean effective surface brightness. These results indicate that BGGs of FG and non-FGs may be different, and BGGs of FGs may have experienced more important mergers than non-FG BGGs. Indeed, the lack of bright galaxies in the vicinity of BGGs hints at the cannibalization of multiple massive galaxies.

This hypothesis is enforced by the measured Kormendy relations: in all filters, the Kormendy relation of BGGs of FGs appears very similar to the one obtained from BCGs of clusters detected in the CFHTLS by Chu et al. (2022), whereas the relation of BGGs of non-FGs is offset from the relations of FGs BGGs and CFHTLS BCGs. This again shows that BGGs of FGs and non-FGs are different, but more interestingly, that BGGs of FGs may have undergone an evolution similar to that of BCGs. We suggest that BGGs of FGs may have undergone major mergers similar to those undergone by cluster BCGs a long time ago, and cannibalized all the bright galaxies in the FG vicinity. The fact that FG BGGs resemble BCGs suggests that FGs may be the ending stage of normal groups of galaxies. Indeed, from this result, we might think that FGs have already experienced more mergers than normal groups. The second scenario in which FGs are just a temporary stage before they experience another merger and capture more galaxies and become

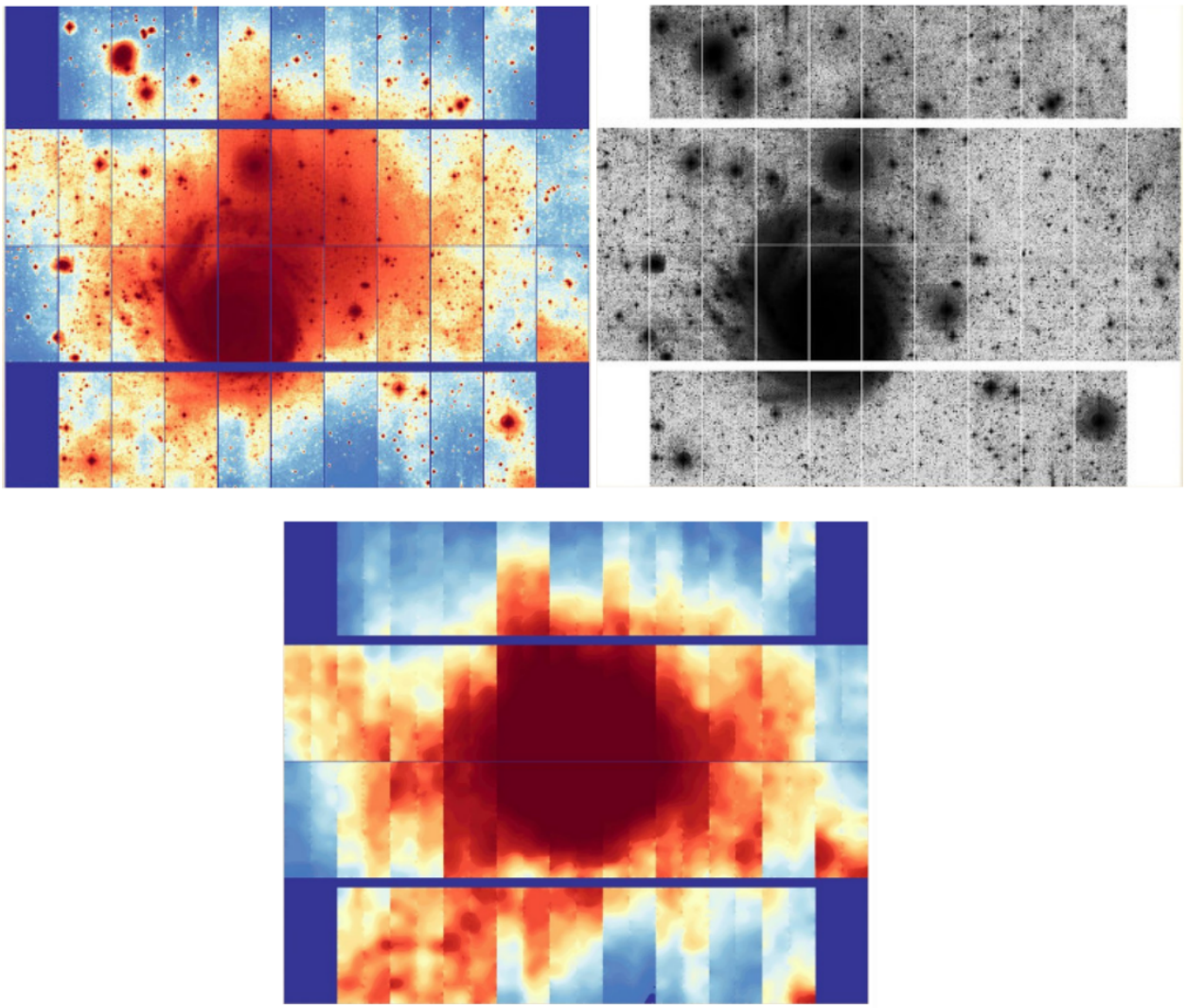

FIGURE 3.1: Illustration of the ELIXIR-LSB reduction pipeline: the original image (top left), to which is subtracted the sky background measured by the pipeline (top right), which enables to bring out low surface brightness features on the final image (bottom). Credit: J-C Cuillandre & CFIS collaboration.

similar to normal groups then appears less likely.

3.2.2 Contribution of the ICL

We also estimate how much the ICL affects our study, similarly to what was done in Chu et al. (2022). The first step was to obtain images of the ICL which we could subtract to the CFIS images to obtain clean signals of our BGGs which are not contaminated by other sources of light. The extraction of the ICL was done using the code `DAWIS` (The Detection Algorithm with Wavelets for Intracluster light Studies) which has been developed and optimised by Ellien et al., 2021 to detect low surface brightness sources in images, in particular (but not limited to) ICL.

`DAWIS` follows a multiresolution vision based on wavelet representation to detect sources, embedded in an iterative procedure called synthesis-by-analysis approach to restore the complete unmasked light distribution of these sources with very good quality. The code first models the

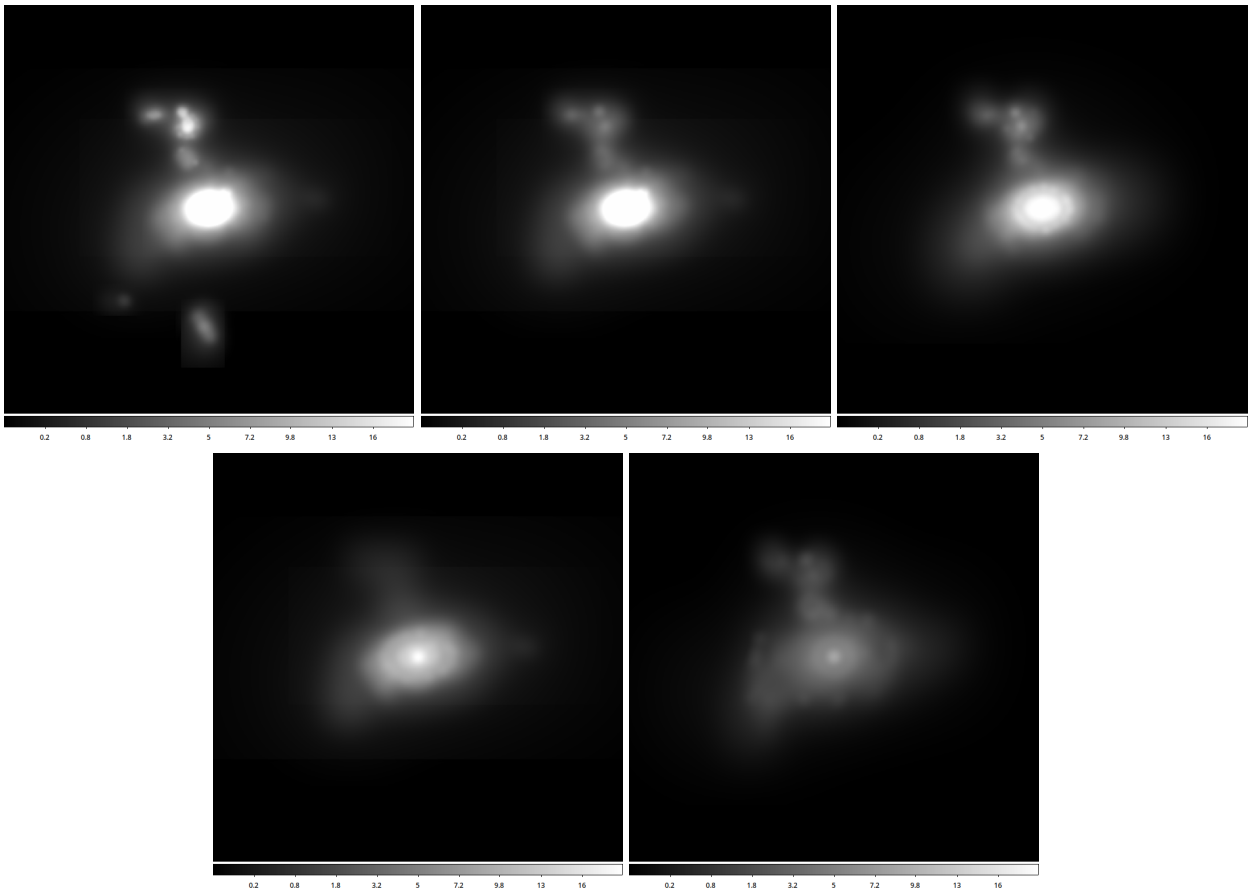

FIGURE 3.2: ICL maps generated by the DAWIS (Ellien et al., 2021) code by considering thresholds of 20, 40, 60 kpc (top row) and 80 and 100 kpc (bottom row) for ICL extraction.

brightest sources and then removes them from the image. The process is repeated by using the resulting image from the previous iteration until all sources were removed from the image and the residuals are only due to noise. The algorithm is built so sources can be classified based on criteria depending on the analysis goal. The case of ICL detection and the measurement of ICL fractions are discussed by Ellien et al., 2021, with tests on mock images of galaxy clusters with various ICL profiles and comparisons with more traditional ICL detection methods. In our case, DAWIS classified sources larger than a given size threshold as belonging to the ICL. Several thresholds were tested (20, 40, 60, 80 and 100 kpc) and 100 kpc was chosen, as smaller scales were more easily contaminated by other structures (foreground galaxies, stars). As can be seen on Figure 3.2, ICL maps with the different thresholds are represented. Lower thresholds appear very bright in the center as they include light from the BCG. By increasing the limit, we remove less light from the BCG and the signal of the ICL is cleaner.

DAWIS was applied here to the rLSB images of 19 FG and 30 non-FGs with rLSB images available to extract the ICL contribution. We then subtracted this ICL contribution to the original image and fit the BGG with GALFIT. Overall, the same observations are made before and after subtracting the ICL: BGGs of FGs are brighter in absolute magnitude and surface brightness, and have sizes similar to non-FG BGGs. The difference in the brightnesses of the two samples is even stronger once the signal has been cleaned of the ICL. We confirm results from Chu et al. (2022) and show that ICL makes the profiles of BGGs of FGs and non-FGs more extended, with bigger effective

radii, dimmer, with fainter surface brightnesses, and makes them appear shallower, with higher Sérsic indices.

3.2.3 Stellar history

In order to track the evolution of the stellar population in FG BGGs, we retrieved the SDSS spectra of 79 of 88 FGs (9 were not available) and 29 of the 30 non-FGs that we studied morphologically. We will study the full sample of 100 non-FGs in the coming weeks. We excluded from the study BGGs which were identified as AGNs, and we thus end with 73 FGs and 21 non-FGs. We fitted the spectra with the eBOSS `Firefly`[3] (Wilkinson et al., 2017) code. `Firefly` is a chi-squared minimisation fitting code to spectroscopic data which fits a number of starburst components to model the observed spectrum, which allows to derive the star formation history of the corresponding galaxies. This code was applied to the whole SDSS survey, and catalogs containing the measured stellar properties such as age, metallicity, stellar mass or star formation history are available (Comparat et al., 2017). However, since we wanted access to all the properties returned by `Firefly` (the properties of each starburst were removed from the final catalogues available on the SDSS website), we ran `Firefly` once again on each spectrum we retrieved. To model the spectra, we used combinations of several initial mass functions (IMF) (Kroupa, Salpeter) and stellar population libraries (MILES, ELODIE, STELIB). A description of each model and their results with `Firefly` is given in Wilkinson et al. (2017). In this way, we obtained information about the stellar mass and metallicity, weighted by mass or light, SFR, or the age of the Universe at each starburst. To lighten the study, we decided to focus on only two different models: Kroupa-MILES and Kroupa-STELIB. The stellar libraries MILES and ELODIE are quite similar, as they both fit bimodal distributions in light-weighted starburst ages, with one of two peaks being recent ($\approx$ 3 Gyrs ago). STELIB returns unimodal solutions with a broader distribution. The χ^2 distribution for all three libraries is also very similar. We thus decided to simply select the two libraries which cover the largest redshift range. The choice of a Kroupa IMF was done as Wilkinson et al. (2017) describe their studies based on the Kroupa IMF, and state that the difference observed between the Kroupa and Salpeter IMF is minimal. This thus allows us a simple comparison with their studies. Preliminary results show that, for the Kroupa+MILES model:

- FG : 61% of the mass was formed at $t > 8$ Gyrs
- Non-FG : 54% of the mass was formed at $t > 8$ Gyrs

and for the Kroupa+STELIB model:

- FG : 71% of the mass was formed at $t > 8$ Gyrs
- Non-FG : 74% of the mass was formed at $t > 8$ Gyrs

In the first model, BGGs of FGs have built most of their mass earlier than non-FGs, which suggests an earlier formation epoch. FG BGGs might have cannibalized most of the massive galaxies of their group earlier than non-FGs. This agrees with our previous observations with the Kormendy relations that show different evolutions of FGs and non-FGs BGGs. On the contrary, the second model exhibits similar stellar build-ups for the two categories at $t > 8$ Gyrs. This would mean that

[3] http://www.icg.port.ac.uk/firefly/

FGs started evolving differently from their peers more recently, less than 8 Gyrs ago. However, it is still difficult to determine which model is the most accurate. This work is still in progress, in particular because until now we have analyzed only 29 non-FG spectra out of the entire sample.

3.3 Perspectives

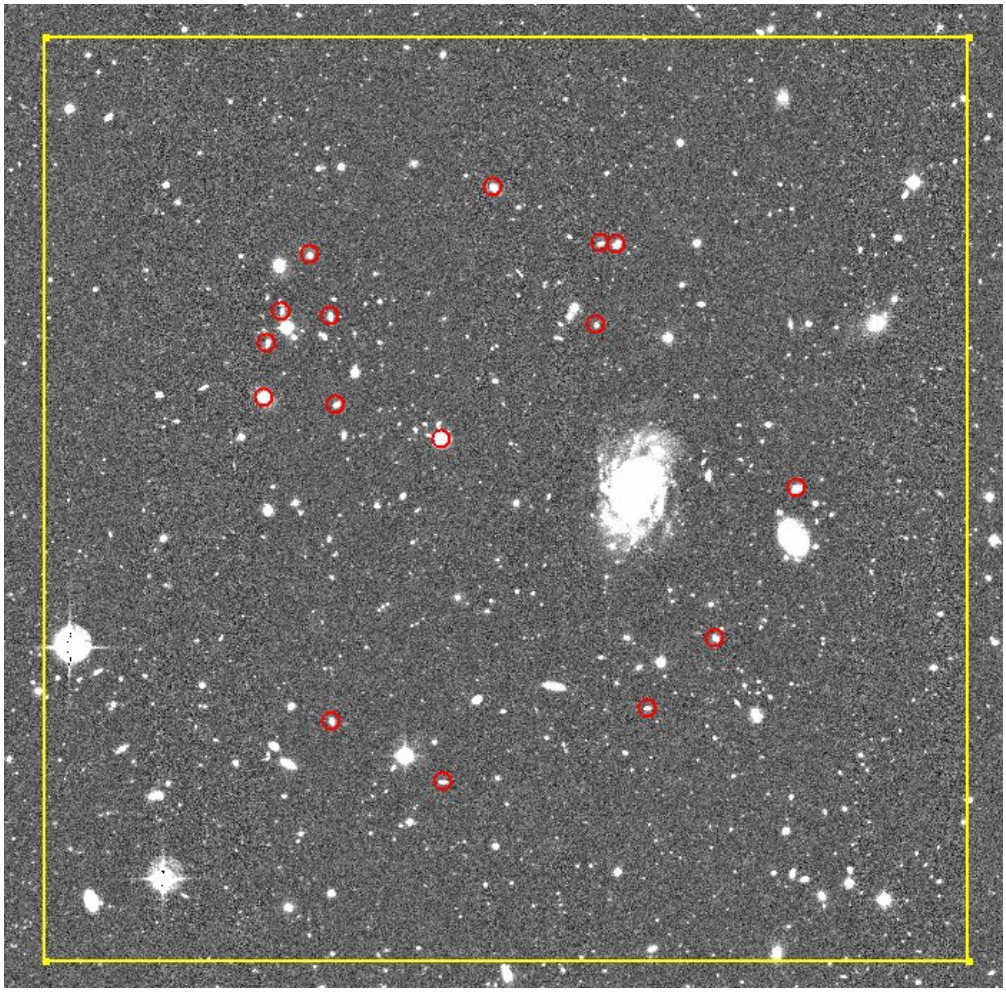

FIGURE 3.3: Example of the candidate fossil group W1-FG122 detected in the CFHTLS and for which we have applied for telescope time with the DOLORES multi-object spectrograph on Telescopio Nazionale Galileo. The red circles indicate the galaxies brighter than r=21.5 with a high probability of belonging to the FG according to their photometric redshift. The yellow square shows the size of the DOLORES MOS field (8.6×8.6 arcmin^2).

This study will give insight on the formation and the evolution of FGs, and what properties distinguish them from normal groups of galaxies. We also offer a comparison with brightest galaxies of clusters, and try to constrain the stellar formation history of FGs and non-FGs. The corresponding paper is included below and will be submitted to A&A in a few weeks.

As mentioned before, another work in progress focuses on a catalogue of potential FGs from the CFHTLS. Since only photo-zs are available for most of the galaxies in this catalogue, and with the aim of detecting and confirming new FGs, we ran several observations with spectrographs

at multiple observatories and instruments. So far, we have only obtained observations using 2-meter class telescopes such as the Nordic Optical Telescope (Roque de los Muchachos Observatory, La Palma in the Canary Islands), the 2.2m at the Calar Alto Observatory, or the 1.93m at the Observatoire de Haute Provence (France). This limited our observations to galaxies with apparent magnitudes in the CFHTLS r filter $r < 19$ mag. We are currently in the process of asking for more observing time with 4-meter class telescopes to be able to measure the redshifts of fainter objects. We show as an example Figure 3.3 with the field we want to observe for a candidate FG.

3.4 The paper

The paper included in this manuscript has been submitted to Astronomy & Astrophysics and is currently in revision.

Astronomy & Astrophysics manuscript no. output
March 6, 2023

A UNIONS view of the brightest central galaxies of candidate fossil groups ⋆

A. Chu[1], F. Durret[1], A. Ellien[2], F. Sarron[3], C. Adami[4], I. Márquez[5], N. Martinet[4], T. de Boer[6], K. C. Chambers[6], J.-C. Cuillandre[7], S. Gwyn[8], E. A. Magnier[6], and A. W. McConnachie[8]

[1] Sorbonne Université, CNRS, UMR 7095, Institut d'Astrophysique de Paris, 98bis Bd Arago, 75014, Paris, France
[2] Anton Pannekoek Institute for Astronomy & GRAPPA, University of Amsterdam, Science Park 904, 1098 XH Amsterdam, The Netherlands
[3] IRAP, Institut de Recherche en Astrophysique et Planétologie, Université de Toulouse, UPS-OMP, CNRS, CNES, 14 avenue E. Belin, F-31400 Toulouse, France
[4] Aix-Marseille Univ., CNRS, CNES, LAM, Marseille, France
[5] Instituto de Astrofísica de Andalucía, CSIC, Glorieta de la Astronomía s/n, 18008, Granada, Spain
[6] Institute for Astronomy, University of Hawaii, 2680 Woodlawn Drive, Honolulu HI 96822, USA
[7] Université Paris-Saclay, Université Paris Cité, CEA, CNRS, AIM, 91191, Gif-sur-Yvette, France
[8] Herzberg Astronomy and Astrophysics, National Research Council, 5071 West Saanich Road, Victoria, BC, Canada, V9E2E7

Received

ABSTRACT

Context. The formation process of fossil groups (FGs) is still under debate, and, due to the relative rarity of FGs, large samples of such objects are still missing.
Aims. The aim of the present paper is to increase the sample of known FGs, and to analyse the properties of their brightest group galaxies (BGG) and compare them with a control sample of non-FG BGGs.
Methods. Based on the large spectroscopic catalogue of haloes and galaxies publicly made available by Tinker, we extract a sample of 87 FG and 100 non-FG candidates. For all the objects with data available in UNIONS (initially the Canada France Imaging Survey, CFIS), in the u and r bands, and/or in an extra r-band processed to preserve all low surface brightness features (rLSB hereby), we made a 2D photometric fit of the BGG with GALFIT with one or two Sérsic components. We also analysed how the subtraction of intracluster light contribution modifies the BGG properties. From the SDSS spectra available for the BGGs of 65 FGs and 82 non-FGs, we extracted the properties of their stellar populations with Firefly. To complement our study, we investigated the origin of the emission lines in a nearby FG, dominated by the NGC 4104 galaxy, to illustrate in detail the possible origin of emission lines in the FG BGGs, involving the presence or absence of an AGN.
Results. Morphologically, a single Sérsic profile can fit most objects in the u band, while two Sérsics are needed in the r and rLSB bands, both for FGs and non-FGs. Non-FG BGGs cover a larger range of Sérsic index *n*. FG BGGs follow the Kormendy relation (mean surface brightness versus effective radius) previously derived for almost one thousand brightest cluster galaxies (BCGs) by Chu et al. (2022) while non-FGs BGGs are in majority located below this relation, with fainter mean surface brightnesses. This suggests that FG BGGs have evolved similarly to BCGs, and non-FG BGGs have evolved differently from both FG BGGs and BCGs. All the above properties can be strongly modified by the subtraction of intracluster light contribution. Based on spectral fitting, the stellar populations of FG and non-FG BGGs do not differ significantly.
Conclusions. The morphological properties and the Kormendy relation of FG and non-FG BGGs differ, suggesting they have had different formation histories. However, it is not possible to trace differences in their stellar populations or in their large scale distributions.

Key words. Galaxies: fossil groups, morphology.

1. Introduction

Fossil groups (FGs) were discovered by Ponman et al. (1994). They are particular groups of galaxies with high X-ray luminosities but with fewer bright galaxies than groups or clusters of galaxies. Jones et al. (2003) later gave the commonly accepted definition of FGs as satisfying three conditions: they are extended X-ray sources with an X-ray luminosity of at least $L_X = 10^{42}\ h_{50}^{-2}$ erg s^{-1}, with a Brightest Group Galaxy (BGG) at least two magnitudes brighter than other group members, the distance between the two brightest galaxies being smaller than half the group virial radius. The formation of these peculiar objects and why they present such a low amount of optically emitting matter are still under debate. Jones et al. (2003) have suggested that FGs are the remnants of early mergers, and that they are cool-core structures which accreted most of the large galaxies in their environment a long time ago, a scenario supported by hydrodynamical simulations by D'Onghia et al. (2005). However, FGs could also be a short temporary stage of group evolution before they capture more galaxies in their vicinity, as reported for instance by von Benda-Beckmann et al. (2008), based on N-body simulations.

FGs can be studied through their optical (Vikhlinin et al. 1999; Santos et al. 2007) or X-ray (Romer et al. 2000; Adami

⋆ Based on observations obtained with CFHT, SDSS, CAHA, and OHP observatories (see acknowledgements for more details).

et al. 2018) properties. Some optical studies support the scenario that FGs are the result of a large dynamical activity at high redshift, but in an environment that is too poor for them to evolve into a cluster of galaxies through the hierarchical growth of structures. For example, La Barbera et al. (2009) found that the optical properties of BGGs in FGs are identical to those of giant isolated field galaxies. Girardi et al. (2014) found a similar relation between their X-ray and optical luminosities for FGs and for normal groups, suggesting that all groups contain the same amount of optical material, but that in FGs it is concentrated in a giant central elliptical galaxy that has cannibalized most of the surrounding bright galaxies. At X-ray wavelengths, based on Chandra X-ray observations, Bharadwaj et al. (2016) found that FGs are mostly cool-core systems, suggesting that these structures are no longer dynamically active.

However recent observations tend to contradict the findings that FGs are dynamically relaxed systems that have not undergone recent merging events. For example, Kim et al. (2018) reported that the prototypical FG NGC 1132 shows an asymmetrical disturbed X-ray profile, and suggested that it is dynamically active. Similarly, Lima Neto et al. (2020) detected shells around the BGG of NGC 4104 and, based on N-body simulations, showed that this FG has probably experienced a relatively recent merger between its BGG and another bright galaxy with a mass of about 40% of that of the BGG. More details on FGs can be found in the recent review by Aguerri & Zarattini (2021).

To make up for the lack of large samples of FGs, Adami et al. (2020) made a statistical study of FGs, extracted from the catalog of 1371 groups and clusters detected by Sarron et al. (2018) in the Canada-France-Hawaii Telescope Legacy Survey (CFHTLS). These systems were detected based on photometric redshifts (Ilbert et al. 2006). Adami et al. (2020) found that groups with masses larger than 2.4×10^{14} $M_\odot$ had the highest probability to be FGs and discussed their location in the cosmic web relatively to nodes and filaments (for a similar study, see also Zarattini et al. 2022). They concluded that FGs were most probably in a poor environment making the number of nearby galaxies insufficient to compensate for the accretion by the central group galaxy.

Numerical simulations of FGs by Dariush et al. (2007) have shown a good agreement with both optical and X-ray observations, and predict that fossil systems will be found in significant numbers (3-4% of the population), even for quite rich clusters. They find that FGs assemble a higher fraction of their mass at high redshifts than non-fossil groups, with the ratio of the currently assembled halo mass to final mass, at any epoch, being about 10–20% higher for FGs. Their interpretation is that FGs represent undisturbed, early-forming systems in which large galaxies have merged to form a single dominant elliptical.

The role of the BGG is therefore crucial to explain the lack of bright galaxies in FGs. The aim of the present paper is to analyse the physical properties of the BGGs of FGs and compare them to those of non-fossil groups and clusters. For this, we gathered a sample of FGs as large as possible from the sample of groups detected by Tinker from SDSS data (Section 2). In each FG candidate, we detected the BGG and measured its morphological properties. We then compared the properties of FG BGGs to those of a control sample of non-FGs, as well as to the brightest galaxies of clusters and massive groups of galaxies previously studied by Chu et al. (2021, 2022) to study how FG BGGs compare to the BCGs and BGGs of more imposing systems (Section 3). We also analysed the stellar populations of FG and non-FG BGGs and investigated the origin of the BGG spectroscopic emission lines, taking as an example a very nearby fossil group BGG NGC 4104 (Section 4.2). Finally, our results are discussed in Section 5.

2. Data

2.1. Selection of FGs

Tinker has made available catalogues[1] with data for 559,038 galaxies. These catalogues give, among other quantities, positions, spectroscopic redshifts from the SDSS survey, k-corrected and evolution corrected (to z=0.1) g and r band absolute magnitudes, galaxy stellar masses, and total halo masses. For each galaxy, the group to which it belongs is indicated.

The group-finding algorithm described by Tinker (2021) is based on the halo-based group finder of Yang et al. (2005), further vetted by Campbell et al. (2015). The standard implementation of the group finder yields central galaxy samples with a purity and completeness of 85–90 per cent (Tinker et al. 2011). To assign stellar masses to haloes and subhaloes, Tinker (2021) uses the stellar mass function from Cao et al. (2020), which utilizes the principal component analysis galaxy stellar masses of Chen et al. (2012).

We first eliminated all the galaxies that were alone in a group, because a single galaxy in a halo does not form a group, and obtained a catalogue of 201,007 galaxies that were at least in a pair. We then selected the galaxies belonging to groups where the magnitude difference in the r band between the brightest and second brightest galaxy was at least 2 magnitudes, and for which the distance between these two galaxies was smaller than half the virial radius, r_{vir}:

$$R_{virial} = (M_{halo} \times 4.30091 \times 10^{-9})/(100 \times H(t)^2)^{1/3},$$

where the corresponding mass M_{halo} is given in the Tinker catalogue, G is the gravitational constant and $H(t)$ the Hubble constant at the group redshift. We thus obtained a catalogue of 2453 galaxies. We note that in this process, we do not take into account the possibility to have a projected galaxy at less than half the virial radius, which could in fact physically (in 3D) be at more than half the virial radius (because of the lack of precision of the spectroscopic redshift or because of high proper velocity). Such a galaxy could artificially be placed in the group luminosity function between the BGG and the second ranked galaxy, and therefore unqualify the group as a fossil group. However, such a case would just limit the size of our sample, wrongly eliminating some of the fossil groups. This effect will not pollute our fossil group sample by inserting non fossil groups.

We extracted from the above catalogue a list with the brightest galaxy of each group, and this led to a catalog of 1112 galaxies that may be considered as BGGs. This means that in fact most groups were made of pairs. In order to avoid considering objects that could not be real groups, such as isolated galaxies with a few small satellites, we added a condition on the halo mass: $M_{halo} > 10^{13}$ $M_\odot$, giving 88 FG candidates. This limit was chosen to match the lowest mass that we found for a FG in our search for FGs in the CFHTLS: 1.1×10^{13} $M_\odot$ (Adami et al. 2020). In absence of X-ray data for all our objects except one, this condition also gives more confidence that these systems may indeed be FGs. Indeed, N. Clerc kindly matched our FG catalogue with his XCLASS catalogue of X-ray sources derived from XMM-Newton data and only found one match for FG17 (e.g. FG #17 of Table A.1), with $L_X = 5 \times 10^{41}$ h_{50}^{-2} erg s^{-1} in the [0.5 - 2] keV energy band. This value is slightly lower than the limit of 10^{42}

[1] https://www.galaxygroupfinder.net/catalogs

h_{50}^{-2} erg s^{-1} defined by Jones et al. (2003). For the other FGs, this does not mean that they are not X-ray emitters, but simply that they are not located in regions observed by XMM-Newton.

The last step was to use photometric catalogs from UNIONS[2] to check if no galaxies were missed in spectroscopy. The Ultraviolet Near Infrared Optical Northern Survey (UNIONS) collaboration combines wide field imaging surveys of the northern hemisphere. UNIONS consists of the Canada-France Imaging Survey (CFIS), conducted at the 3.6-meter CFHT on Maunakea, parts of Pan-STARRS, and the Wide Imaging with Subaru HyperSuprime-Cam of the Euclid Sky (WISHES). CFHT/CFIS is obtaining deep u and r bands; Pan-STARRS is obtaining deep i and moderate-deep z band imaging, and Subaru is obtaining deep z-band imaging through WISHES and g-band imaging through the Waterloo-Hawaii IfA g-band Survey (WHIGS). These independent efforts are directed, in part, to securing optical imaging to complement the Euclid space mission, although UNIONS is a separate collaboration aimed at maximizing the science return of these large and deep surveys of the northern skies.

We searched in the UNIONS photometric archive all objects (galaxies or stars) that 1) fall within $0.5\times R_{virial}$ of a FG center, 2) are missing from the Tinker catalog, and 3) have magnitudes between that of the BGG and that of the second brightest galaxy. Stars were removed with central surface brightness versus total magnitude plots.

2.2. Additional spectroscopic observations of FGs

At the end of this selection process, we found three galaxies not present in the Tinker spectroscopy and potentially contributing to the first two magnitude range. This affected two FG candidates: FG65 and FG73 (see Table A.1).

For FG65, we obtained long-slit spectroscopy with MISTRAL at Observatoire de Haute-Provence for the two relatively bright galaxies (RA=228.7630093°, DEC=42.0503814° and RA=228.769596°, DEC=42.0548771°, 1 hour exposures), which both have magnitudes differing by less than 2 magnitudes from the BGG. Both proved to be part of the same foreground galaxy at z=0.0149, and not related to the FG BGG at z=0.13479. This confirmed the fossil nature of the FG65 group.

We also observed a galaxy (RA=238.45581°, DEC=56.4229°, 1 hour exposure) within the FG73 FG candidate with CAFOS at the Calar Alto Hispano Alemán Telescope. This galaxy proved to be at a redshift of 0.1055, very close to the redshift of the putative BGG (z=0.1080), and to have less than two magnitudes difference with the BGG. FG73 was therefore removed from the FG final list because the two magnitude difference criterium between the brightest and second brightest galaxies was not satisfied.

We thus obtained the final catalogue of 87 FG candidates listed in Table A.1.

2.3. Basic properties of FGs

The histograms of the halo masses and BGG stellar masses of the FG candidates and of the comparison sample (see below) are shown in Figs. 1 and 2 respectively. These quantities are taken from Tinker's catalogues. The halo masses are in the $[10^{13},10^{14}]$ $M_\odot$ range, with 65 FGs (74%) having halo masses $\leq 2\times10^{13}$ $M_\odot$. The BGG stellar masses are in the $[10^{10.8},10^{12}]$ $M_\odot$ range, except for one galaxy (FG22) that has a lower mass of $10^{10.4}$ $M_\odot$.

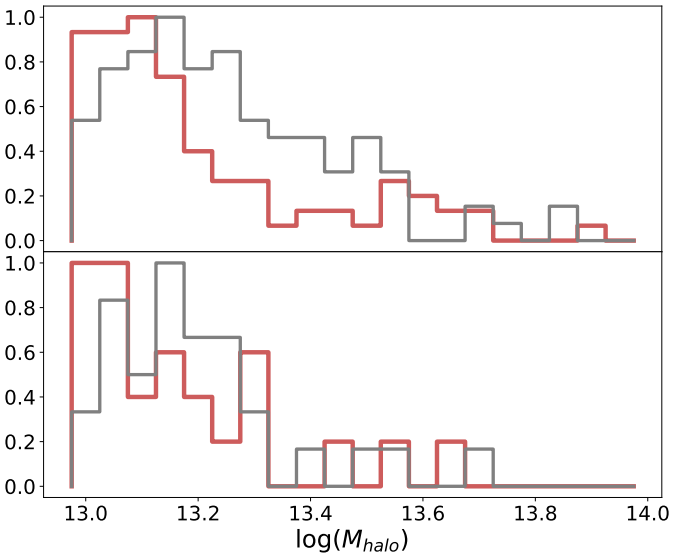

Fig. 1. Normalized histograms of the logarithms of the halo masses for FGs (red) and non-FGs (grey). Top: the 87 FGs and 100 non-FGs. Bottom: 25 FGs and 30 non-FGs analysed morphologically.

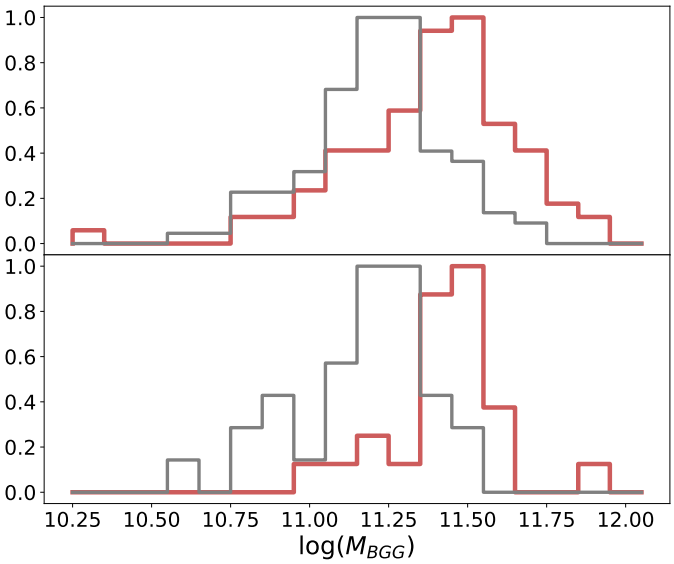

Fig. 2. Same as Fig. 1 for the normalized histograms of the logarithms of the BGG stellar masses.

The redshift histogram of the groups is shown in Fig. 3. Most of the FGs are in the [0.02,0.12] range, with only five FGs in the [0.12,0.18] range. The absolute magnitude histograms in the g and r bands, together with the (g-r) colour histogram, are shown in Fig. 4 for the groups. BGGs have typical absolute magnitudes in the r band in the [−23, −21] range, with typical (g-r) colors in the [0.8,1.0] range.

We searched for images of these 87 FG candidates in the UNIONS image database in the u and r bands. These images were retrieved from the DR3, which includes observations made before January of 2021, and covers 7000 deg^2 in u and 3600

[2] https://www.skysurvey.cc

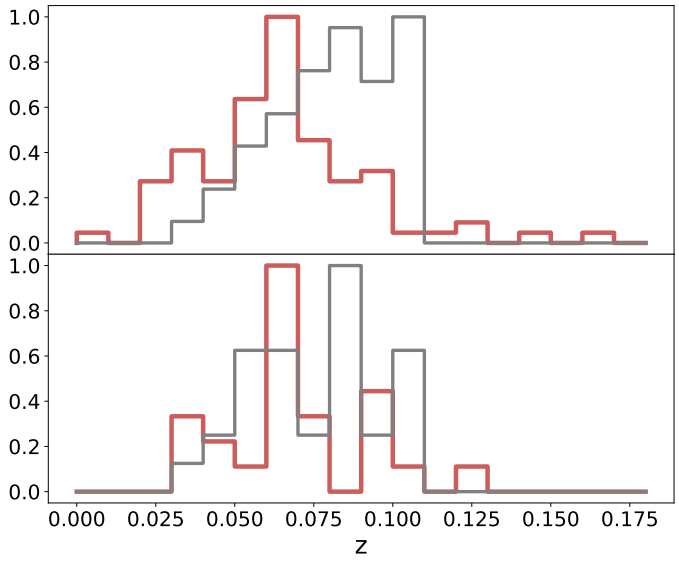

Fig. 3. Same as Fig. 1 for the normalized redshift histograms.

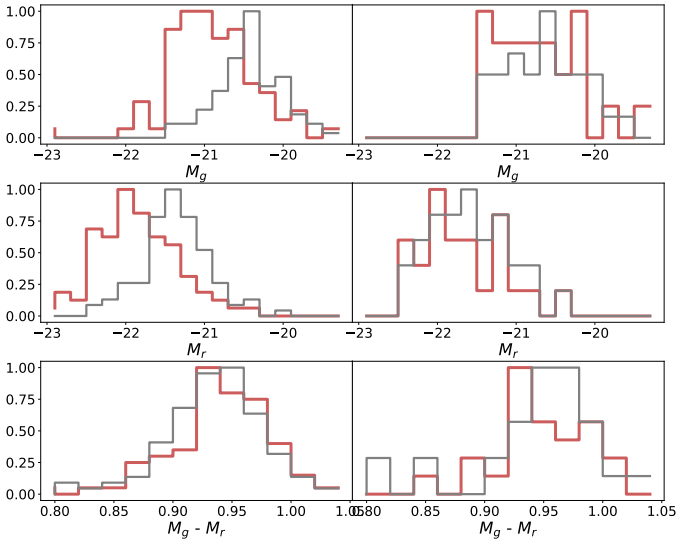

Fig. 4. Normalized histograms of the absolute magnitudes of the BGGs in the g (top) and r (middle) bands, and of the (g-r) colour (bottom), for FGs (red) and non-FGs (grey). Left: the 87 FGs and 100 non-FGs. Right: 25 FGs and 30 non-FGs analysed morphologically.

deg^2 in r. We found images for 35 FGs in the u band and for 25 FGs in the r band, among which 12 FGs having both u and r band images. We indicate in Table A.1 (last column) the FGs with UNIONS images available.

Chu et al. (2022) have shown that subtracting the contribution of intracluster light (ICL) could modify the properties derived for BCGs. Therefore, with the aim of estimating how subtracting the ICL could modify the properties derived for the BGG, we also exploited the r band images processed to preserve all low surface brightness features (hereafter referred to as rLSB). As explained e.g. by Žemaitis et al. (2023), the images were obtained using an observing technique that is optimised for low surface brightness (LSB) surveys at CFHT (e.g., Ferrarese et al. 2012; Duc et al. 2015).

There were 19 FGs available in rLSB. For all these objects, we extracted images of 4000×4000 pixels^2 centred on the BGG, either just by cropping the tiled UNIONS rLSB images, or by first assembling two to four tiled images with the SExtractor and SWarp softwares (Bertin & Arnouts 1996; Bertin et al. 2002; Bertin 2006)[3] and then cropping them to this size. In the latter case, special care was taken to assemble tiles that had been background subtracted in order not to lose faint signal in the outskirts of BGGs.

2.4. Control sample of non-fossil groups

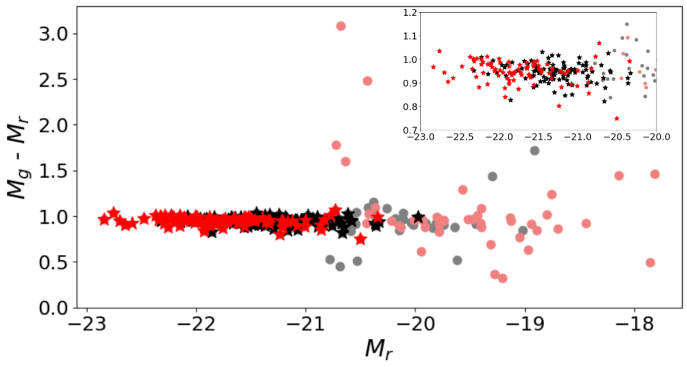

Fig. 5. (g-r) colour magnitude diagram for four samples: light red dots: galaxies within 1 arcmin of FG BGGs; red stars: FG BGGs; grey dots: all galaxies within 1 arcmin of non-FG BGGs; black stars: non-FG BGGs. The x-axis is the absolute magnitude in the r band. A zoomed-in version of the plot at the brightest magnitudes is shown on the top right.

In order to compare the properties of BGGs of FGs with those of non-fossil groups (hereafter non-FGs), we built a catalogue of non-FGs in a similar way, but this time imposing a magnitude difference between the brightest and second brightest galaxies smaller than 2. This condition, together with that of $M_{halo} > 10^{13}$ M$_\odot$ gave 100 non-FG candidates. None of them had a match in the XCLASS X-ray catalogue of N. Clerc.

The catalogues of the 87 FG candidates and of the 100 non-FGs are available in electronic form at the CDS via anonymous ftp to cdsarc.u-strasbg.fr (130.79.128.5) or via http://cdsweb.u-strasbg.fr/cgi-bin/qcat?J/A+A/. They contain the following columns: number, RA, DEC, spectroscopic redshift, BGG stellar mass, absolute magnitude in the g and r SDSS bands, virial radius, and halo mass. Among the 100 non-FGs, we chose 30 non-FGs having good quality UNIONS images in u, r, and rLSB. They are listed in Table A.2. This subsample of non-FGs is comparable in number to that of FG candidates for which UNIONS data are available. The BGGs of this control sample were chosen to match as well as possible the absolute magnitude and colour histograms of our FG sample. This can be checked by looking at Figs. 1 - 4. A Kolmogorov-Smirnov test on the FG and non-FG samples shows that these two samples have only a 40% probability to be statistically different.

For each FG and non-FG, we extracted from the Tinker catalogue (which gives absolute magnitudes in the g and r bands) all the galaxies belonging to the same halo within 1 arcmin around the BGG. The colour-magnitude diagram shown in Fig. 5 shows that all FG BGGs follow a very well-defined sequence. With a colour g-r=−1.29, only one BGG is bluer than g-r=0 and falls outside the plot; it appears to be a spiral galaxy, but we kept it in

[3] https://www.astromatic.net/

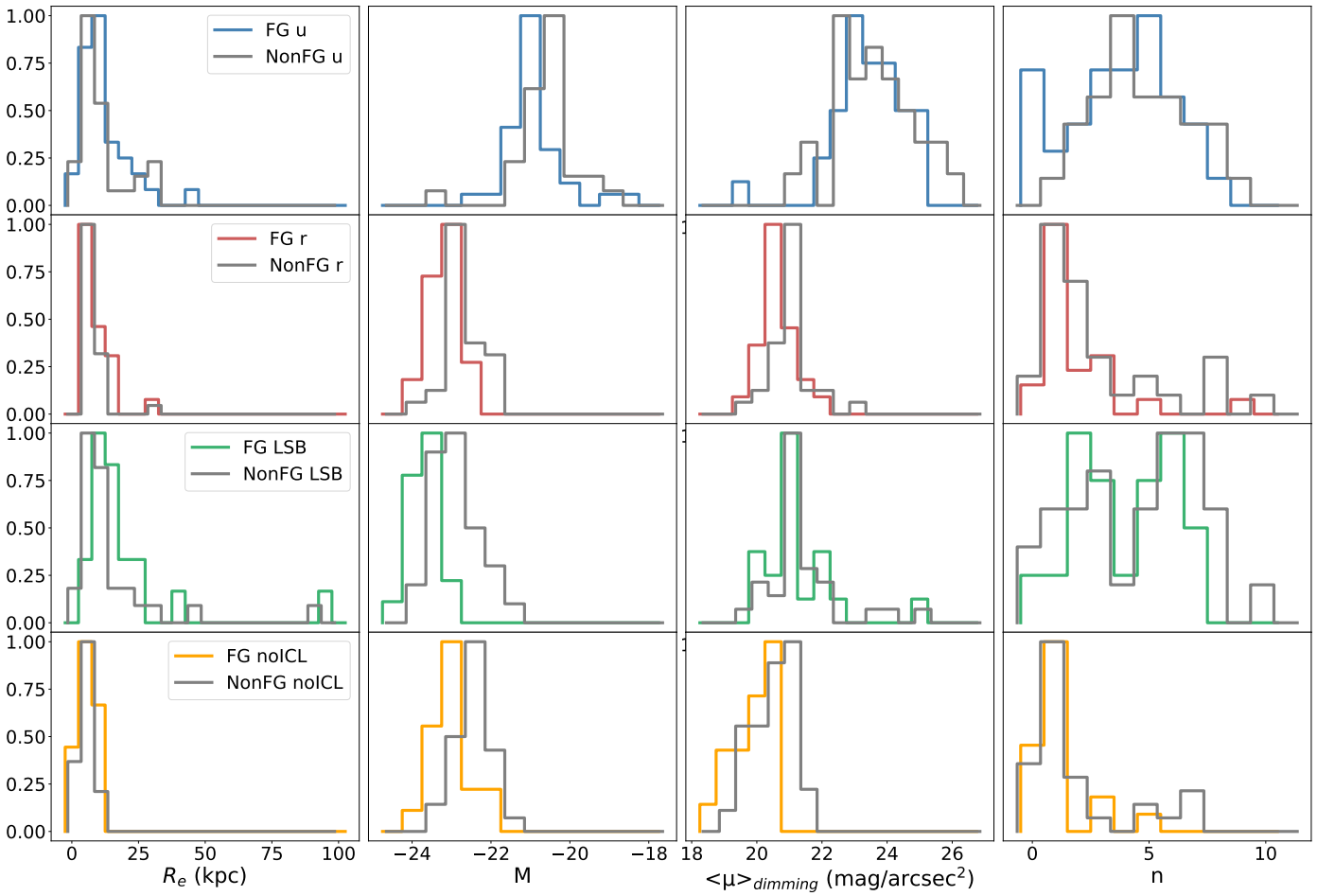

Fig. 6. From left to right: normalized histograms of the effective radius, absolute magnitude, mean surface brightness corrected for cosmological dimming, and Sérsic index n. From top to bottom: 35 candidate FGs (in blue) and 30 non-FGs (grey) in the u band; 25 candidate FGs (in red) and 30 non-FGs (grey) in the r band; 19 candidate FGs (green) and 30 non-FGs (grey) in the rLSB band; same as above in the rLSB band after ICL subtraction (yellow for FGs).

the sample. BGGs of non-FGs surprisingly follow very well this sequence, whereas the galaxies which are not BGGs tend to be fainter and show a notably larger dispersion.

3. Morphological properties of the FG BGGs

3.1. Method

We now consider the 25 and 30 BGGs of FGs and non-FGs for which r band data are available in UNIONS. Following Chu et al. (2021) and Chu et al. (2022), the 2D profile of each BGG was fit with GALFIT (Peng et al. 2002) with a single Sérsic model and with a double Sérsic model. GALFIT initial parameters were obtained with SExtractor, using a bulge + disk model. A mask and a point spread function were created following the method described in Chu et al. (2021). The choice between a single and double Sérsic model was made based on the statistical F-test (Margalef-Bentabol et al. 2016) and the computed p-value, which indicates if complexifying the model, i.e increasing the number of degrees of freedom, is necessary. Since the current sample has the same resolution as Chu et al. (2022), we adopt the same p-value limit to distinguish between the two different models: $P_0 = 0.15$.

3.2. Morphological properties of FGs

The numbers of BGGs of FGs and non-FGs for which one Sérsic law (S1) or two Sérsic laws (S2) are needed to fit their 2D profiles in the various bands are given in Table 1. For FGs, we can see that in the u band most BGGs can be fit with a single Sérsic (83%). In contrast, a major part of the profiles in the r band require two components (92%). If we now consider the BGGs from the rLSB data, only 53% require two Sérsics.

The fact that a single Sérsic fits most of the u band images of BGGs can be due to the lower signal to noise ratio in the u band that makes the detection of a faint outer component difficult, while this outer low surface brightness component is better detected in the deeper r band images. Following the same interpretation, it appears surprising that the percentage of BGGs better fit by two Sérsics is smaller in the deeper rLSB data than in the r band data. This can be explained by the fact that the Elixir-LSB pipeline, during the refined background subtraction procedure, removes light from around the BGGs. We cannot guarantee whether this light has BGG origin, is due to instrumental contamination, or a mixture of both. This nevertheless means that part of our two Sérsic fits in the r band are potentially contaminated by MegaCam scattered light. We decide to keep both bands for comparison purposes: the r band, with more flux but

Table 1. Number of BGGs of fossil and non-fossil groups for which one or two Sérsic laws are needed to fit their 2D profiles in the various bands: u, r, rLSB, and rLSB after subtraction of the ICL contribution.

	FG				Non-FG			
	u	r	rLSB	rLSB-ICL	u	r	rLSB	rLSB-ICL
One-Sérsic	29	2	9	3	27	6	14	6
Two-Sérsic	6	23	10	16	3	24	16	24

potentially contaminated, and the rLSB band that is 'cleaner' but might be missing light from the BGG outer profiles.

The same 2D profile fitting was applied to the control sample of non-FGs. As for FGs, we see in Table 1 that most BGGs in the u band are fit with a single Sérsic (90%) while in the r band 80% are better fit with two Sérsics, and in rLSB, 53% are better fit with two Sérsics. The difference between FGs and non-FGs is therefore of a few percent, a value that is not significant in view of the dispersion.

As will be described in Sect. 3.4, we computed the ICL contribution and subtracted it from the BGGs to see how the Sérsic parameters changed. If we look at Table 1, we can see that only three FG BGGs out of 19 (16%) can be fit with a single Sérsic, and for non-FG BGGs six out of 30 BGGs (20%) are fit with a single Sérsic. The subtraction of the ICL contribution therefore does not make the second Sérsic component disappear, as already observed by Chu et al. (2022). The effect of ICL on the morphological properties of BGGs will be discussed further in Sect. 3.4. Unexpectedly, we find more BGGs of FGs and non-FGs that are better modeled by two-Sérsic profiles on ICL-subtracted rLSB images than on rLSB images. This will be discussed in Sect. 5.

As seen in Fig. 6, the effective radii are comparable for the BGGs of FGs and non-FGs in all filters. The absolute magnitudes of FG BGGs appear brighter (by up to one magnitude) than those of non-FG BGGs. The same is observed for the mean surface brightnesses, except in the u filter, where they appear similar.

The histograms of the Sérsic indices n are more concentrated towards low values in r for FGs: only 2 FGs out of 25 (8%) have n >4 while 8 non-FGs out of 30 (27%) have n>4. In rLSB, there are 10 FGs out of 19 (53%) and 18 non-FGs out of 30 (60%) with n>4. This high value of n may be linked to the presence of ICL (see Sect. 3.4).

Because the difference in Sérsic indices between FGs and non-FGs is not apparent in all bands, and the effective radii are about the same, the only clear difference that we find between the physical properties of FGs and non-FGs is that FG BGGs are intrinsically brighter. This may be due to a selection bias, as our sample of FG BGGs is overall brighter than our sample of non-FG BGGs (see Fig. 4). Despite our efforts to build two samples with similar properties, we could not find as many non-FG BGGs as bright as FG BGGs. This may indicate that, in a given group mass range, FG BGGs are indeed brighter and most of the mass of the group is concentrated in the BGG.

3.3. Kormendy relation

We now consider the relation found by Kormendy (1977) (mean effective brightness $< \mu >$ as a function of effective radius R_e), that can be fit with the following law:

$$< \mu >= (a \pm \sigma_a) \times log(R_e) + (b \pm \sigma_b).$$

The slopes and intercepts with their errors are given in Table 2 in the u, r, rLSB and ICL subtracted rLSB bands, before and after correction for cosmological dimming, applied as in Chu et al. (2022). For better comparison with that study, we convert the surface brightnesses measured in the u, r, rLSB and ICL subtracted rLSB bands into those in the i band using the Fukugita et al. (1995) tables. We can see in Table 2 that the dispersion is smaller for FGs than for non-FGs in all bands, and that the relations in u and r are parallel within the dispersion. Except in the rLSB band, the slopes are larger for non-FGs than for FGs, but in view of the dispersion this difference is not significant.

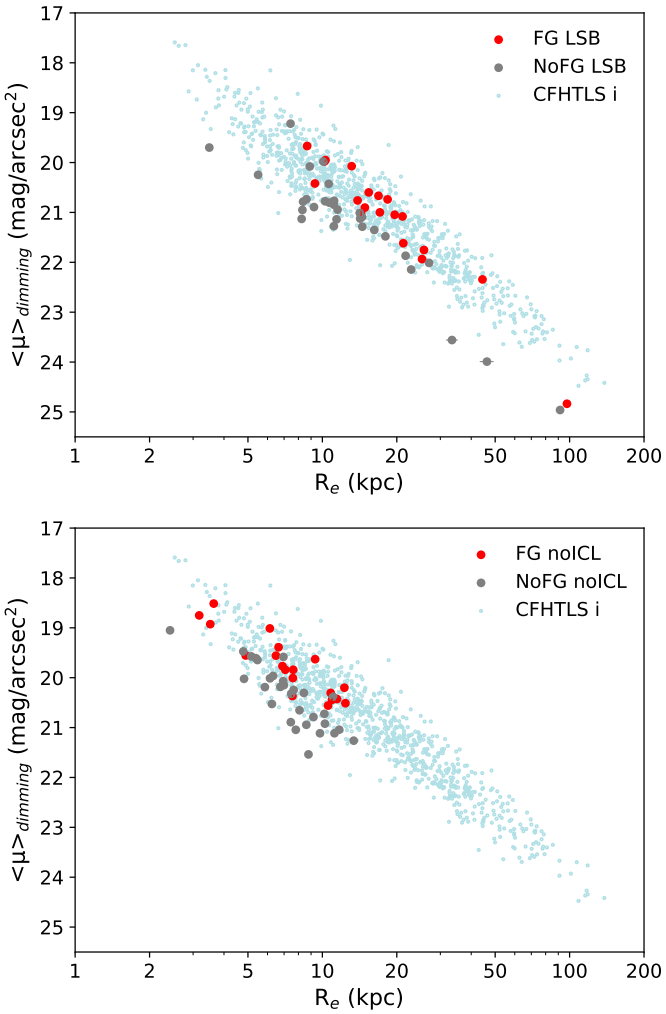

Fig. 7. Kormendy relation for FGs in red and Non-FGs in grey, superimposed on the relation found for almost one thousand BCGs by Chu et al. (2022) in cyan. Both plots are obtained in the rLSB band, the top plot without ICL subtraction and the bottom plot after ICL subtraction. The points for FGs and non-FGs have been shifted from the r to the i band, and all points are corrected for cosmological dimming.

The Kormendy relation derived in the i band for almost one thousand BCGs by Chu et al. (2022) was: $< \mu >= (3.34 \pm 0.05) \times log(R_e) + (18.65 \pm 0.07)$ and $< \mu >= (3.49 \pm 0.04) \times log(R_e) +$

Table 2. Slopes (a) with their error (σ_a) and intercepts (b) with their error (σ_b) for the Kormendy relation. For each filter, we give the values without (u, r, rLSB, rLSB-ICL) and with (udimm, rdimm, rLSBdim, rLSB-ICLdimm) redshift dimming correction. Magnitudes were converted to the CFHTLS i magnitudes to compare the present results with those of Chu et al. (2022).

	FG				Non-FG			
	a	σ_a	b	σ_b	a	σ_a	b	σ_b
u	3.41	0.28	17.15	0.31	3.72	0.44	17.13	0.47
udimm	3.31	0.30	16.95	0.33	3.68	0.44	16.83	0.47
r	3.80	0.32	16.82	0.34	3.95	0.68	17.24	0.69
rdimm	3.26	0.39	17.07	0.41	3.76	0.68	17.09	0.69
rLSB	4.48	0.23	15.79	0.29	4.03	0.31	17.07	0.35
rLSBdimm	4.47	0.30	15.47	0.38	4.00	0.31	16.75	0.35
rLSB-ICL	3.41	0.30	17.16	0.27	3.69	0.44	17.53	0.39
rLSB-ICLdimm	3.10	0.36	17.10	0.32	3.44	0.44	17.41	0.38

(16.72 ± 0.05) before and after correction for cosmological dimming respectively. This relation was found to be independent of the model used (one or two Sérsic profiles). If we compare the Kormendy relations found here for FGs and non-FGs to those of Chu et al. (2022), we see that FGs are located on this relation, while non-FGs are located in majority below the relation, as illustrated in Fig. 7, and this is true both before and after ICL subtraction. However, in view of the large dispersion the difference in the intercepts is not statistically significant.

Therefore the BGGs of FGs appear to have properties closer to those of BCGs than non-FG BGGs, suggesting that BGGs in FGs and BCGs have undergone comparable evolutions, while non-FGs have evolved somewhat differently, reaching fainter surface brightnesses.

3.4. Influence of the ICL contribution on the estimation of the morphological properties of FGs

Chu et al. (2022) have estimated the importance of the ICL contribution on the morphological properties of seven BCGs computed with GALFIT. For this, they fit the 2D properties of the BCGs on the original images, and then subtracted to these images the contribution of the ICL derived by Jiménez-Teja et al. (2018) and fit again the BCGs. Their main result was that two Sérsics were still necessary to fit the BCGs, and therefore that the need for a second component could not only be attributable to ICL. In all cases, the effective radii increase in the presence of ICL, some of them drastically (by an order of magnitude). For all seven BCGs, the absolute magnitude of the external component is fainter after removing the ICL (with a difference that can reach two magnitudes). After subtracting ICL, BCGs also have brighter effective surface brightnesses, with a difference that can almost reach 3 mag arcsec^{-2}.

Similarly, to better quantify the effect of the ICL in the present study, we now compare the values of the various physical parameters galaxy by galaxy before and after ICL subtraction. This demands an estimation of the ICL contribution for each FG. For this, we use `DAWIS` (Detection Algorithm with Wavelets for Intracluster light Studies; Ellien et al. 2021), a wavelet based algorithm optimized for the detection and characterization of LSB structures in deep optical images. In a nutshell, `DAWIS` applies a wavelet transform to the analysed image and detects sources in the new wavelet representation. The light profiles in the original image of these sources are then modeled from their wavelet representation through a restoration procedure. `DAWIS` follows a semi-greedy procedure, meaning that sources are restored iteratively. The brightest detected sources are modeled first and removed from the image, and the whole wavelet procedure is then applied again on the residual image. New sources are detected, modeled and removed, until convergence to a noise only residual map. This provides a refined modeling of all detected sources, from very bright objects down to very faint structures. Note that the detected sources are not necessarily entire astrophysical objects, but rather sub-structures of such objects. `DAWIS` was applied to each FG for which we have an image in the rLSB band, providing for each of them a list of sources and their light profiles.

For each BGG, we extracted from the `DAWIS` output list a sub-list of sources that are identified as contributing to ICL. This sub-list was estimated using the following criteria: the source must be unimodal and centered on the BGG center, and its spatial radial extent must be greater or equal to a given radius. We tried different values for the spatial extent, going from 40 kpc up to 100 kpc. Low values lead to brighter ICL contribution, contaminated by smaller sources such as pieces of foreground and background galaxies. For our study we chose to remove a clean ICL contribution, potentially missing some of it, rather than a contribution contaminated by galaxies, and set the radius to 100 kpc. The light profiles of these sources are summed into a 2D ICL profile, and this profile is then subtracted from the BGG light profile. More details about this procedure and `DAWIS` can be found in Ellien et al. (2021) and Brough et al. (in preparation).

The results after ICL subtraction are illustrated in Fig. 8 and Table 3, We can see that for FGs, the ICL increases the effective radius by a mean factor of 3.7, and the ICL adds light to the BGG by up to 1.3 magnitude. With ICL, the mean surface brightness can be up to 5 mag arcsec^{-2} brighter, with a mean at 1.3, and the Sérsic index n tends to be larger (by 2.8 on average). There seems to be a bimodality in the Sérsic index histogram. The peak at $n < 2$ comes from BGGs that were better modeled with two Sérsic profiles before and after ICL subtraction, and the peak at $n > 3$ originates from 1-Sérsic profile BGGs on LSB images that become 2-Sérsic BGGs after ICL subtraction.

For non-FGs, the ICL increases the effective radius by a mean factor of 2.4 and the absolute magnitude with ICL is up to 1.2 magnitude brighter. The mean surface brightness before subtraction of the ICL can be up to 1.2 mag arcsec^{-2} fainter, with a mean of about 0.8, and the Sérsic index n tends to be larger with ICL, with a large dispersion from one BGG to another. We can note that when the ICL is subtracted, the Sérsic index distributions become comparable for FGs and non-FGs (refer to Fig. 6). The distributions of the properties of BGGs obtained for FGs and non-FGs after ICL subtraction also become more comparable to those measured in the r filter (see Fig. 6). This is not surprising, as the r images before LSB processing should resemble rLSB images after the removal of low brightness features.

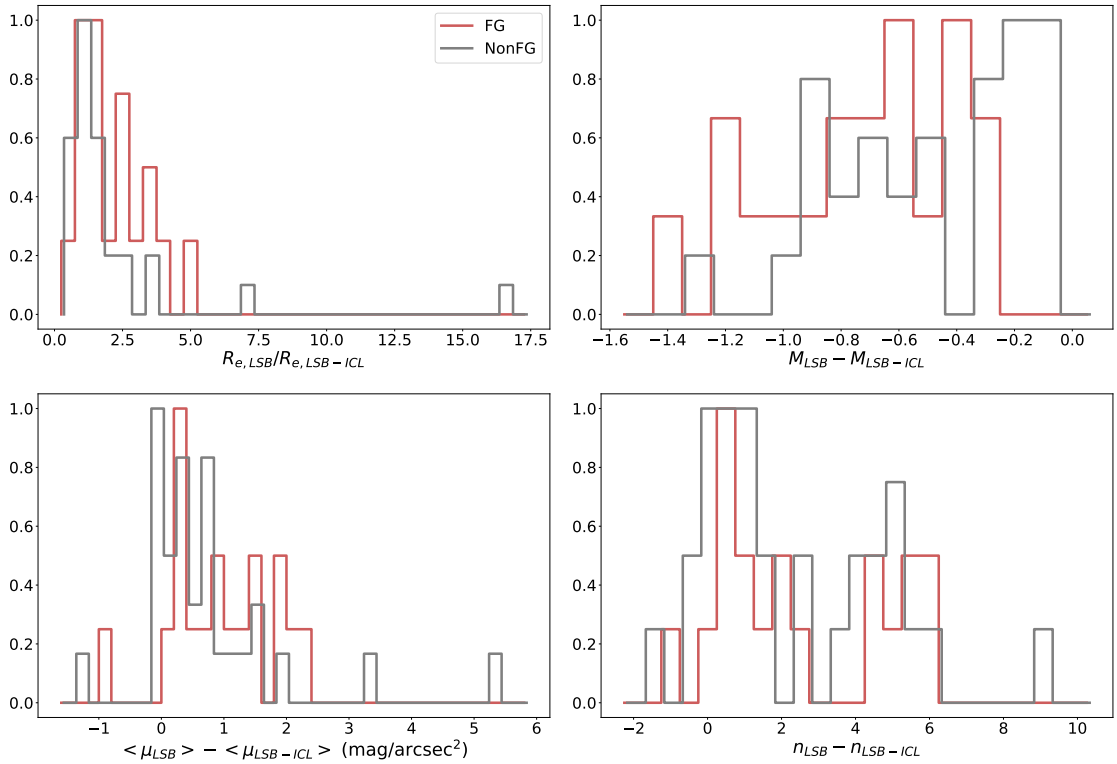

Fig. 8. Normalized histograms of the difference between the values obtained before and after subtraction of the ICL for the 19 candidate FGs (in red) and 30 non-FGs (in grey): effective radius (top left), absolute magnitude (top right), mean surface brightness (bottom left), and Sérsic index n (bottom right).

Table 3. Mean morphological parameters (with their dispersion in parentheses) for FGs and non-FGs in the u, r, and rLSB bands, and after subtracting the ICL contribution. The columns are: effective radius R_e, absolute magnitude M_{abs}, mean surface brightness μ_{mean} corrected for cosmological dimming, and Sérsic parameter n.

	R_e	M_{abs}	μ_{mean}	n
FG u	14.0 (8.8)	-20.6 (0.8)	23.7 (1.0)	4.2 (2.3)
Non-FG u	13.2 (8.7)	-20.4 (0.7)	23.8 (1.2)	5.2 (2.0)
FG r	11.7 (4.8)	-23.0 (0.4)	20.9 (0.5)	2.3 (1.9)
Non-FG r	10.6 (4.6)	-22.4 (0.5)	21.3 (0.6)	3.3 (2.5)
FG rLSB	22.0 (19.5)	-23.4 (0.4)	21.5 (1.1)	4.4 (2.1)
Non-FG rLSB	16.7 (16.4)	-22.6 (0.5)	21.6 (1.2)	5.0 (2.7)
FG no ICL	7.9 (2.9)	-22.8 (0.5)	20.2 (0.6)	1.6 (1.2)
Non-FG no ICL	7.7 (2.4)	-22.2 (0.4)	20.8 (0.6)	2.4 (2.1)

However, we can note that there is still a significant difference between the properties measured on the r and rLSB-ICL images. Indeed, BGGs on the r filter appear bigger, brighter, and have fainter mean surface brightnesses and higher Sérsic indices (see Table 3) than on rLSB-ICL images, all which indicate the presence of ICL even on the r images. This illustrates the fact that ICL modifies somewhat the apparent morphological properties, and that its contribution should be carefully subtracted before analysing the physical properties of BCGs and BGGs.

4. Stellar populations of BGGs

4.1. Data

We retrieved the spectra of the FG and non-FG BGGs of our sample in the SDSS. Among the 87 FGs, nine spectra were not available, leaving us with 78 BGGs. Among the 100 non-FGs, 4 spectra were not available, so we analysed 96 spectra. We fit these spectra with Firefly (Wilkinson et al. 2017) and eliminated the spectra corresponding to AGN as classified by the SDSS: 13 in FGs and 14 in non-FGs. This was done because it is difficult to extract stellar populations from spectra dominated by an AGN. The AGN fractions are very similar between BGGs of FGs and non-FGs, 20% and 17% respectively. We were therefore left with 66 FG BGG and 82 non-FG BGG spectra. Since Wilkinson et al. (2017) have shown that Kroupa and Salpeter IMFs gave comparable results, we limited our analysis to a Kroupa IMF. We used the STELIB and MILES stellar libraries, to estimate the robustness of our results.

4.2. Results

We find that the stellar populations of FG and non-FG BGGs cannot be distinguished with this relatively straightforward analysis. As an illustration, we show the fraction of stellar mass created as a function of age in Fig. 9. Firefly fits the galaxy observed

spectra using multiple star-formation bursts with various luminosities, masses, metallicities and ages. The software returns the number of bursts, and for each burst: its age, metallicity, and the fraction it contributed to the luminosity and stellar-mass of the galaxy. From these, we computed the fraction of stellar mass formed in a range of galaxy age by summing the fractions of total stellar-mass of all the star-formation bursts that occurred in the considered age range.

We find that 76% and 71% of the total stellar mass of FG and non-FG BGGs respectively was already formed 8 Gyr ago, using the STELIB library. These percentages become 61% and 66% for the MILES library. These results agree with Fig. 5, where we see that the BGGs of FGs and non-FGs have very similar colours. Therefore, although the morphological properties of FG and non-FG BGGs somewhat differ, this is not the case for their stellar populations. Fig. 9 shows that the choice between the MILES and STELIB libraries does not change much the results.

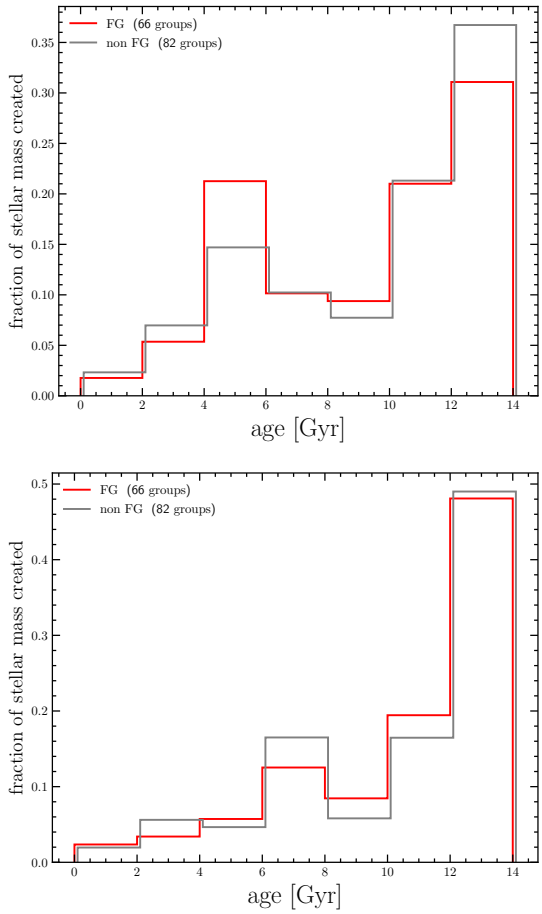

Fig. 9. Histograms of the fraction of stellar mass created as a function of age for FGs (red) and non-FGs (grey), for a Kroupa IMF, using the MILES (top) and STELIB (bottom) libraries.

There are 39 BGGs in FGs with emission lines (among which 9 may have a broad Hα component) out of 78. Each time Hα is detected, it is associated with the [NII]6584 emission line. For the BGGs of non-FGs, 30 out of 96 show emission lines (with no broad Hα line apparent).

These emission lines can originate from star-formation processes (e.g. driven by recent merging events) or from AGN activity (even if no broad Hα line is detected). However, the spectroscopy available to us comes from the SDSS survey, with a fiber of 3 arcsec diameter. Given the angular extent of the considered BGGs, at most 10% of their area within a Petrosian radius is covered by the fiber, and mainly in the center of the galaxies. Detected emission lines are therefore probably coming from AGN activity, with rare cases where it can be produced by star-forming processes detected in the disk.

The respective percentages of Hα-[NII] emission line galaxies are 50% for FGs and 31% for non-FGs. This suggests that BGGs contain more frequently an AGN in the centers of FGs than in non-FGs.

4.3. Emission lines in FG BGGs: the case of NGC 4104

As seen in the previous section, a non negligible part of our FG BGGs show emission lines and we think that these are mainly due to AGN activity. In order to investigate more precisely the location of the emitting regions in BGGs and see if some merging-induced star-formation activity can be detected, we concentrated on a specific example: NGC 4104 (not a member of our present sample of FG candidates).

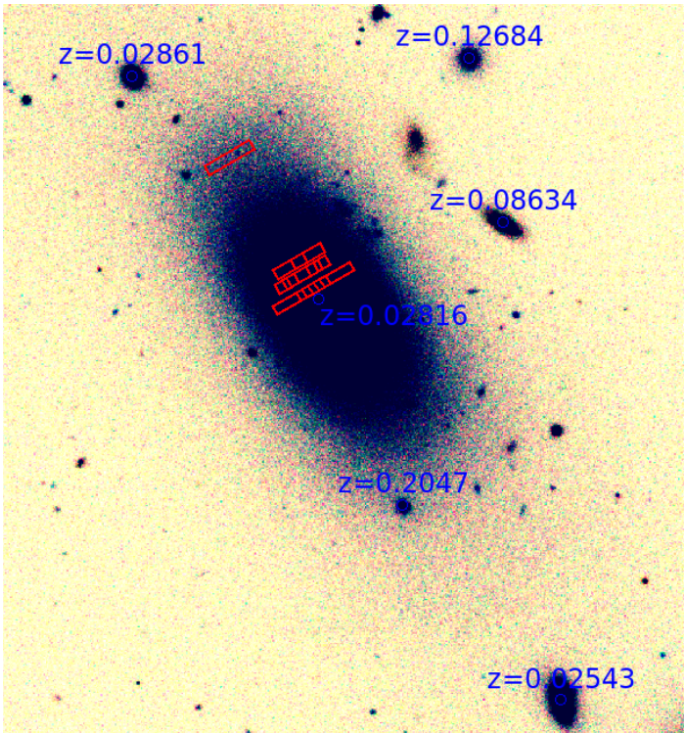

Fig. 10. SDSS g', r', i' trichromic image (~2.9'×3.5') of NGC 4104. The redshifts indicated come from the SDSS. The red rectangles show the regions where we extracted MISTRAL spectra.

It is a well known galaxy (see Fig. 10) at z~0.02816, BGG of the eponym fossil group recently studied by e.g. Lima Neto et al. (2020). It constitutes a good laboratory to investigate the possibility of having merging-induced star-formation activity because it was most probably subject to relatively recent merging activity (Lima Neto et al. 2020). Given the fact that it is a nearby galaxy, it is also easy to study in detail its spectral and morphological characteristics.

Despite the BGG status of NGC 4104 (classified as S0 by the RC3 catalog de Vaucouleurs et al. 1991, and as Elliptical by the SDSS), SDSS spectroscopy (identified as spec-2227-53820-0518 in the Science Archive Server) clearly shows strong emission lines in its center (see Fig. 10 for the location of the SDSS

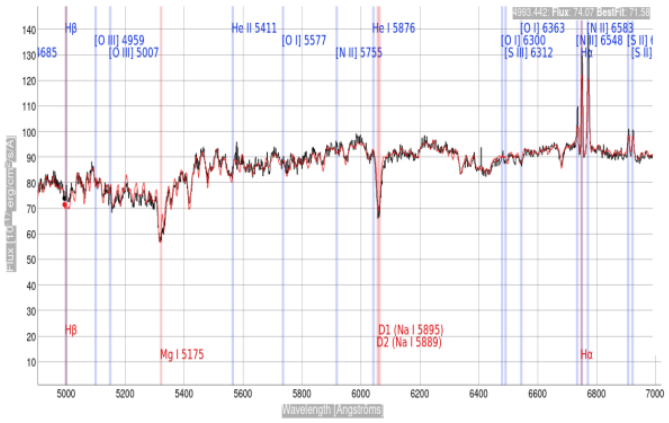

Fig. 11. SDSS spectroscopy of NGC 4104, with emission (blue labels) and absorption (red labels) lines.

spectroscopic extraction area). In this region, we have a noticeable lack of emission at the Hβ and [OIII] wavelengths. The Hα, [NII] and [SII] lines are very prominent, in addition to MgI and NaD absorption lines (see Fig. 11).

In order to investigate the origin of these emission lines, and to see if they are present over the entire galaxy, we partially mapped NGC 4104 at the Observatoire de Haute Provence with the MISTRAL single-slit spectro-imager (see http://www.obs-hp.fr/guide/mistral/MISTRAL_spectrograph_camera.shtml) in March 2022. We used the blue setting (1 hour exposure, resolution R∼750, and covered the wavelength range [4200, 8000]Å) to obtain spectra in four different slits (see Fig. 10). The three slits close to the galaxy center provided high enough signal-to-noise to allow extraction of spectra in 15 different regions (see Fig. B.1). The outermost slit has too low a signal-to-noise to detect any significant lines (including emission lines).

We do not detect any emission line in the galaxy external regions with the other slits. Only central regions (l1, l2, l4, c1, c2, c3, c5, and c6 on Fig. B.1) show [NII], [SII], and sometimes weak to bright Hα emission, very similarly to what is visible in the SDSS spectrum. We show in Fig. B.1 a zoom on the [6700, 6940]Å wavelength interval. The table GalSpecInfo of the SDSS DR17 database lists NGC 4104 as an AGN, with an old stellar population of the order of 13 Gyr. In order to investigate more precisely the nature of this galaxy we first applied the pipes_vis visualization tool (Leung et al. 2021), based on the BAGPIPES tool (Carnall et al. 2018) to the normalized SDSS spectrum. We selected a Wild et al. (2020) model, adding dust (Charlot & Fall 2000) and a nebular component (Leung et al. 2021).

First, based on Lima Neto et al. (2020), we assumed a stellar mass for NGC 4104 of $10^{11.3}$ $M_\odot$ and a redshift of 0.03. We also fixed to 100 the α and β slopes of the Wild et al. (2020) burst (decline and incline steepness of the burst, index of double power law), to 2.0 the η_{dust} (additional scaling factor for dust in star forming clouds), to 0.7 the n_{CF00} (slope of the attenuation law) of the dust component, and to 0.01 Gyr the t_{bc} parameter in pipes_vis (time during which the star forming clouds remain).

We then fixed the galaxy velocity dispersion to 150 km/s in order to reproduce the [SII] doublet aspect. The log(U) value (ionization parameter) has to be lower than −3.5 in order to have [NII] stronger than Hα. We fixed log(U) to this value.

We had to introduce a passive population older than ∼6 Gyr to explain the depth of the absorption lines. We fixed the age of the Universe when the older population formed to 8 Gyr. We also fixed to 1 Gyr the SFR decay timescale of the older population.

To explain the absence of [OIII] emission and the weakness of Hβ, we fixed the metallicity to Z=2.5 and the Av (extinction in V band) to 2.

Finally, we added a small burst in the Wild et al. (2020) model, with 5% of the mass of the older population contained in the burst, ∼1 Gyr ago (12.8 Gyr after the Big Bang), in order to explain visible emission lines and to have deep enough MgI and NaD lines. Values contained in the burst of more than 10% of the mass of the older population do not allow to reproduce the spectrum characteristics, whatever the values of the other parameters.

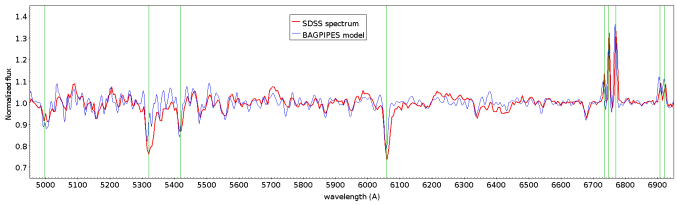

Fig. 12. A modelisation of the normalized SDSS spectrum of NGC 4104 with the pipes_vis tool.

With this set of parameters, we are able to reasonably reproduce the SDSS spectrum (see Fig. 12). This probably shows that we are dealing with a relatively old stellar population (∼6 Gyr old). This is consistent with the 4-6 Gyr old merger proposed by Lima Neto et al. (2020). Any emission lines induced by the old merger have probably now vanished. In addition, a recent burst/merger (∼ 1 Gyr old) is also likely. It may possibly have reactivated the central AGN and be at the origin of the emission lines presently observed in the centre of NGC 4104. The star-forming Hα emission induced by this late merging event would require a few hundred Myr to also vanish, and this is not in contradiction with the age of the recent burst (∼ 1 Gyr).

As a comparison to the other FGs, we also applied Firefly to the SDSS spectrum of NGC 4104 with a Kroupa IMF and the STELIB and MILES stellar libraries. For these two models, we find that 73% and 69% of the total stellar population was formed more than 8 Gyr ago, which is consistent with the previous results. The subtraction of the stellar population fitting results in a pure-emission spectrum, that can be used to locate the line ratios in the BPT (Baldwin et al. 1981) diagrams (Kewley et al. 2013). The line ratios [OIII]/Hβ and [NII]/Hα locate the nuclear spectrum of NGC 4104 in the region occupied by LINER nuclei.

We also investigated the AGN nature of the spectra in MISTRAL covered regions where [NII] and Hα emissions were strong (namely, regions c1, c2 and c5 of Fig. B.1). [OIII] and Hβ were not detectable, so Fig. 13 only shows vertical lines for these three regions. We clearly see that, even without [OIII] and Hβ lines, the NGC 4104 c1, c2, c5, and central regions all have AGN characteristics.

As a conclusion, the emission lines of NGC 4104 originate mainly from the galaxy centre and each of the regions exhibiting emission lines have AGN characteristics. The remaining areas of the galaxy have passive characteristics. The emission lines of NGC 4104 are therefore largely due to the AGN activity, in agreement with an AGN-origin for the emission lines that we detected in at least part of our general sample of BGGs (see previous section).

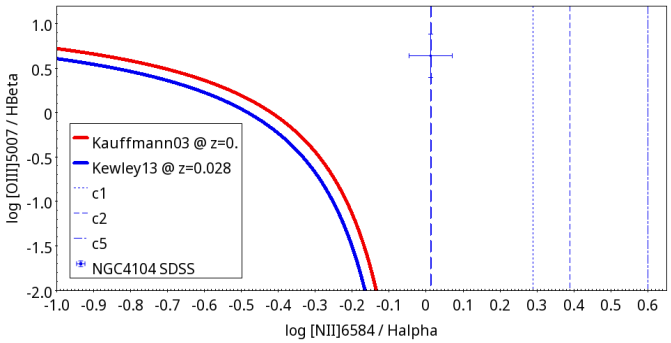

Fig. 13. log([OIII]5007/Hβ) versus log([NII]6584A/Hα) for the SDSS spectrum (central area, see e.g. Fig. B.1) and the c1, c2, and c5 MISTRAL regions. Regions under the red and blue curves are normal galaxies, according to Kauffmann et al. (2003) and Kewley et al. (2013) respectively, while regions above these curves are active objects (AGN, LINERS).

5. Discussion and Conclusions

The aim of this paper is to increase the number of known FGs to shed light on their formation process. Here, we increase the sample by 87 FG candidates confirmed spectroscopically, and with a high probability of being real FGs in view of their estimated large halo mass, though the confirmation of the X-ray condition on their X-ray luminosity ($L_X > 10^{42}$ erg s^{-1}) is still missing. For the FGs with UNIONS data available (35 in the u band, 25 in the r band and 19 in the rLSB band (r band treated with the Elixir-LSB software), we analyse the morphological properties of their brightest group galaxy (BGG), and compare these properties with those of a control sample of 30 non-FG BGGs.

The 2D photometric fits of the BGGs made with GALFIT with one or two Sérsic components show that a single Sérsic component is sufficient in most objects in the u band, while two Sérsics are needed in the r band, both for FGs and non-FGs. However, non-FGs cover a larger range of Sérsic index n than FGs. Therefore, FG BGGs appear to have homogeneous profiles whereas non-FG BGGs cover a larger range of profiles.

After the subtraction of ICL in the rLSB images, the fraction of two-Sérsic BGGs increases. This is rather unexpected, since ICL forms a faint halo around the BGG and adds flux to the envelope of the BGG. We could thus expect a higher fraction of two-Sérsic BGGs when ICL is included. However, the ICL distribution does not necessarily follow a Sérsic profile. In a more general way, it seems that Sérsic profiles generally do not trace physical components, and only act as an analytical description of galaxies.

FG BGGs appear to follow the Kormendy relation previously derived for BCGs by Chu et al. (2022), whereas the relation for non-FG BGGs is shifted to fainter surface brightnesses. This implies that FG BGGs have morphological properties closer to those of BCGs, and may have evolved similarly to BCGs. Chu et al. (2021) have confirmed that BCGs have not evolved since z=1.8. Therefore, a similar evolution of FG BGGs and of BCGs favours the scenario in which FGs have formed long ago and have stopped evolving because their environment lacked galaxies that the group could accrete.

We have analysed the properties of the stellar populations of FG and non-FG BGGs derived from the analysis of their SDSS spectra with Firefly, assuming a Kroupa IMF and using the STELIB and MILES stellar libraries. We find no significant difference between FGs and non-FGs (65 and 82 galaxies respectively), so the stellar populations of BGGs must have evolved in comparable ways in FGs and non-FGs.

Detailed observations of the FG NGC 4104 illustrate the fact that the BGGs of some FGs may show emission lines in their spectra. However, only a small percentage of BGGs are blue and star-forming, and so potentially exhibiting star-formation induced Hα lines. The others, as NGC 4104, show emission lines originating from their centre and mainly due to their AGN activity. In NGC 4104, this AGN was probably reactivated in a recent past by some merging activity, therefore questioning the passive status of the central regions of FGs.

In conclusion, BGGs of FGs and non-FGs are found to differ morphologically, suggesting they have had somewhat different formation histories, but not sufficiently to make their stellar populations significantly different.

As a parallel project to increase the number of known FGs, we are presently confirming spectroscopically the subsample of FG candidates detected in the CFHTLS survey with a high probability by Adami et al. (2020). This will be the topic of a future paper.

Acknowledgements. We thank the referee, Rémi Cabanac, for his careful and constructive reading of the manuscript. We are grateful to Nicolas Clerc for matching our FG and non-FG catalogues with his XCLASS X-ray catalogue. F.D. acknowledges support from CNES. I.M. acknowledges financial support from the State Agency for Research of the Spanish MCIU, through the "Center of Excellence Severo Ochoa" award to the Instituto de Astrofísica de Andalucía (SEV-2017-0709), and through PID2019-106027GB-C41. F.S. acknowledges support from a CNES Postdoctoral Fellowship. This work is based on data obtained as part of UNIONS (initially CFIS), using data from a CFHT large program of the National Research Council of Canada and the French Centre National de la Recherche Scientifique. Based on observations obtained with MegaPrime/MegaCam, a joint project of CFHT and CEA Saclay, at the Canada-France-Hawaii Telescope (CFHT) which is operated by the National Research Council (NRC) of Canada, the Institut National des Science de l'Univers (INSU) of the Centre National de la Recherche Scientifique (CNRS) of France, and the University of Hawaii. Pan-STARRS is a project of the Institute for Astronomy of the University of Hawaii, and is supported by the NASA SSO Near Earth Observation Program under grants 80NSSC18K0971, NNX14AM74G, NNX12AR65G, NNX13AQ47G, NNX08AR22G, and by the State of Hawaii. Funding for the Sloan Digital Sky Survey IV has been provided by the Alfred P. Sloan Foundation, the U.S. Department of Energy Office of Science, and the Participating Institutions. SDSS-IV acknowledges support and resources from the Center for High-Performance Computing at the University of Utah. The SDSS web site is www.sdss.org. SDSS-IV is managed by the Astrophysical Research Consortium for the Participating Institutions of the SDSS Collaboration including the Brazilian Participation Group, the Carnegie Institution for Science, Carnegie Mellon University, the Chilean Participation Group, the French Participation Group, Harvard-Smithsonian Center for Astrophysics. Based in part on observations made at Observatoire de Haute Provence (CNRS), France. This research has made use of the MISTRAL database, based on observations made at Observatoire de Haute Provence (CNRS), France, with the MISTRAL spectro-imager, and operated at CeSAM (LAM), Marseille, France. Based on observations collected at Centro Astronomico Hispano en Andalucia (CAHA) at Calar Alto, operated jointly by Instituto de Astrofisica de Andalucia (CSIC) and Junta de Andalucia. Based on observations taken with the Nordic Optical Telescope on La Palma (Spain).

References

Adami, C., Giles, P., Koulouridis, E., et al. 2018, A&A, 620, A5
Adami, C., Sarron, F., Martinet, N., & Durret, F. 2020, A&A, 639, A97
Aguerri, J. A. L. & Zarattini, S. 2021, Universe, 7, 132
Baldwin, J. A., Phillips, M. M., & Terlevich, R. 1981, PASP, 93, 5
Bertin, E. 2006, in Astronomical Society of the Pacific Conference Series, Vol. 351, Astronomical Data Analysis Software and Systems XV, ed. C. Gabriel, C. Arviset, D. Ponz, & S. Enrique, 112
Bertin, E. & Arnouts, S. 1996, A&AS, 117, 393
Bertin, E., Mellier, Y., Radovich, M., et al. 2002, in Astronomical Society of the Pacific Conference Series, Vol. 281, Astronomical Data Analysis Software and Systems XI, ed. D. A. Bohlender, D. Durand, & T. H. Handley, 228
Bharadwaj, V., Reiprich, T. H., Sanders, J. S., & Schellenberger, G. 2016, A&A, 585, A125

Campbell, D., van den Bosch, F. C., Hearin, A., et al. 2015, MNRAS, 452, 444
Cao, J.-z., Tinker, J. L., Mao, Y.-Y., & Wechsler, R. H. 2020, MNRAS, 498, 5080
Carnall, A. C., McLure, R. J., Dunlop, J. S., & Davé, R. 2018, MNRAS, 480, 4379
Charlot, S. & Fall, S. M. 2000, ApJ, 539, 718
Chen, Y.-M., Kauffmann, G., Tremonti, C. A., et al. 2012, MNRAS, 421, 314
Chu, A., Durret, F., & Márquez, I. 2021, A&A, 649, A42
Chu, A., Sarron, F., Durret, F., & Márquez, I. 2022, A&A, 666, A54
Dariush, A., Khosroshahi, H. G., Ponman, T. J., et al. 2007, MNRAS, 382, 433
de Vaucouleurs, G., de Vaucouleurs, A., Corwin, H. G., J., et al. 1991, S&T, 82, 621
D'Onghia, E., Sommer-Larsen, J., Romeo, A. D., et al. 2005, ApJ, 630, L109
Duc, P.-A., Cuillandre, J.-C., Karabal, E., et al. 2015, MNRAS, 446, 120
Ellien, A., Slezak, E., Martinet, N., et al. 2021, A&A, 649, A38
Ferrarese, L., Côté, P., Cuillandre, J.-C., et al. 2012, ApJS, 200, 4
Fukugita, M., Shimasaku, K., & Ichikawa, T. 1995, PASP, 107, 945
Girardi, M., Aguerri, J. A. L., De Grandi, S., et al. 2014, A&A, 565, A115
Ilbert, O., Arnouts, S., McCracken, H. J., et al. 2006, A&A, 457, 841
Jiménez-Teja, Y., Dupke, R., Benítez, N., et al. 2018, The Astrophysical Journal, 857, 79
Jones, L. R., Ponman, T. J., Horton, A., et al. 2003, MNRAS, 343, 627
Kauffmann, G., Heckman, T. M., Tremonti, C., et al. 2003, MNRAS, 346, 1055
Kewley, L. J., Maier, C., Yabe, K., et al. 2013, ApJ, 774, L10
Kim, D.-W., Anderson, C., Burke, D., et al. 2018, ApJ, 853, 129
Kormendy, J. 1977, ApJ, 218, 333
La Barbera, F., de Carvalho, R. R., de la Rosa, I. G., et al. 2009, AJ, 137, 3942
Leung, H.-H., Wild, V., Carnall, A., & Papathomas, M. 2021, Research Notes of the American Astronomical Society, 5, 171
Lima Neto, G. B., Durret, F., Laganá, T. F., et al. 2020, A&A, 641, A95
Margalef-Bentabol, B., Conselice, C. J., Mortlock, A., et al. 2016, MNRAS, 461, 2728
Peng, C. Y., Ho, L. C., Impey, C. D., & Rix, H.-W. 2002, The Astronomical Journal, 124, 266
Ponman, T. J., Allan, D. J., Jones, L. R., et al. 1994, Nature, 369, 462
Romer, A. K., Nichol, R. C., Holden, B. P., et al. 2000, ApJS, 126, 209
Santos, W. A., Mendes de Oliveira, C., & Sodré, Laerte, J. 2007, AJ, 134, 1551
Sarron, F., Martinet, N., Durret, F., & Adami, C. 2018, A&A, 613, A67
Tinker, J., Wetzel, A., & Conroy, C. 2011 [arXiv:1107.5046]
Tinker, J. L. 2021, ApJ, 923, 154
Vikhlinin, A., McNamara, B. R., Hornstrup, A., et al. 1999, ApJ, 520, L1
von Benda-Beckmann, A. M., D'Onghia, E., Gottlöber, S., et al. 2008, MNRAS, 386, 2345
Žemaitis, R., Ferguson, A. M. N., Okamoto, S., et al. 2023, MNRAS, 518, 2497
Wild, V., Taj Aldeen, L., Carnall, A., et al. 2020, MNRAS, 494, 529
Wilkinson, D. M., Maraston, C., Goddard, D., Thomas, D., & Parikh, T. 2017, MNRAS, 472, 4297
Yang, X., Mo, H. J., van den Bosch, F. C., & Jing, Y. P. 2005, MNRAS, 356, 1293
Zarattini, S., Aguerri, J. A. L., Calvi, R., & Girardi, M. 2022, A&A, 668, A38

Appendix A: Lists of FG candidates and non-FGs

The list of the 87 FG candidates is given in Table A.1 with the principal properties of their BGG. The list of the 30 non-FGs for which the morphological properties were analysed are shown in Table A.2. The full list of 100 non-FGs will be available in electronic form at the CDS, together with the list of 87 FG candidates.

Appendix B: Spectra of NGC 4104

Illustrations of the observations obtained with the MISTRAL spectrograph at Observatoire de Haute Provence are given in Fig. B.1.

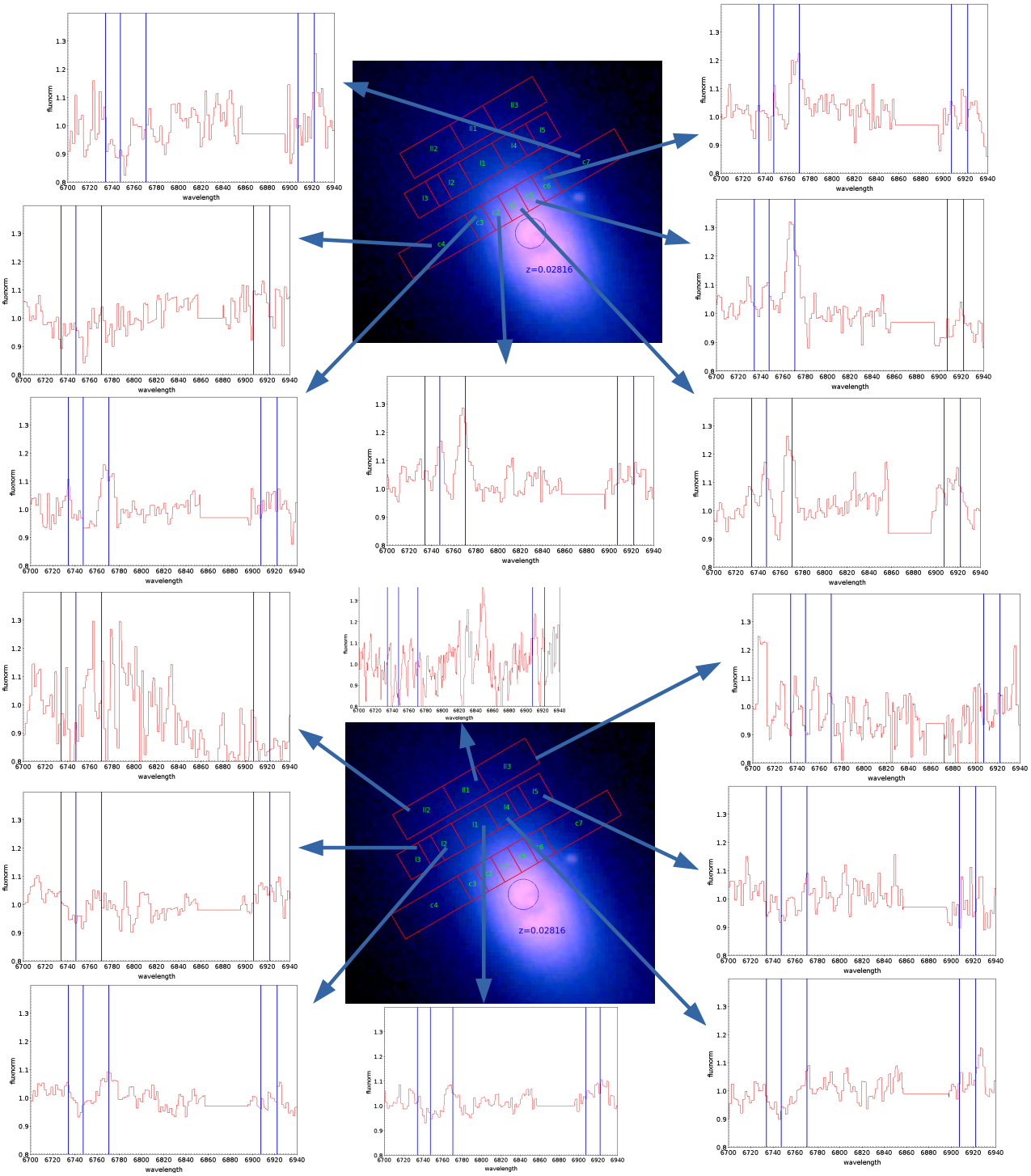

Fig. B.1. MISTRAL spectroscopic observations of 15 different regions of NGC 4104. Spectra are normalized in flux. The location of the SDSS fiber is shown as the blue central circle. Wavelength domain is limited to [6700, 6940]Å

Table A.1. Sample of 87 FG candidates. The columns are: running number, J2000 right ascension and declination (in degrees), spectroscopic redshift, logarithm of the BGG mass, absolute magnitudes in the g and r bands, virial radius, logarithm of the halo mass, UNIONS data when available with relevant photometric band(s).

Number	RA	DEC	z	$\log M_{BGG}$	$Mabs_g$	$Mabs_r$	R_{virial} (Mpc)	$\log M_{halo}$	UNIONS
1	4.6490	-10.5378	0.1463	11.521	-21.358	-22.369	0.6069	13.053	
2	10.6416	-9.9117	0.0585	11.194	-21.325	-22.327	0.4548	13.436	
3	22.3493	15.4461	0.1727	11.279	-19.754	-20.503	0.6696	13.628	u
4	24.9841	-9.2424	0.0421	11.807	-20.801	-21.759	0.4630	13.109	
5	26.3686	-10.0933	0.0550	11.493	-20.868	-21.811	0.7318	13.131	
6	58.2920	-5.4971	0.1230	11.525	-21.666	-22.587	0.7250	13.055	
7	117.6895	17.1722	0.0727	11.586	-20.272	-21.221	0.4433	13.020	
8	118.8856	27.7361	0.0748	11.721	-21.282	-22.286	0.5019	13.672	u
9	120.0094	51.6025	0.0823	11.644	-20.168	-21.120	0.5096	13.054	r rLSB
10	124.8362	20.2687	0.0816	11.753	-21.506	-22.476	0.4569	13.070	u
11	128.8010	31.7042	0.0684	11.424	-21.369	-22.295	0.4432	13.689	u r rLSB
12	131.0486	23.5347	0.0768	11.464	-21.091	-22.050	0.4653	13.577	u
13	131.1130	53.4878	0.0616	11.408	-21.085	-21.925	0.4823	13.467	
14	131.7862	19.6311	0.0312	11.025	-22.859	-21.569	0.4403	13.607	u
15	132.5318	2.6479	0.0597	11.562	-20.921	-21.866	0.6485	13.517	
16	136.8240	16.7384	0.0522	11.389	-20.574	-21.552	0.4463	13.160	
17	137.5553	38.7321	0.0978	11.531	-20.399	-21.346	0.6854	13.198	u r rLSB
18	139.7271	50.0207	0.0343	11.495	-20.761	-21.739	0.4935	13.150	
19	141.3023	5.3517	0.0760	11.658	-20.682	-21.606	0.5196	13.121	
20	142.1698	12.6173	0.0282	10.986	-21.118	-22.104	0.4655	13.133	
21	144.5160	42.9743	0.0468	11.207	-20.680	-21.613	0.4771	13.102	u r rLSB
22	150.5563	11.3197	0.0550	11.284	-19.868	-20.831	0.4730	13.101	
23	150.7645	16.6710	0.0706	11.591	-21.217	-22.207	0.4664	13.063	
24	151.9548	39.7382	0.0808	11.621	-21.008	-21.952	0.5842	13.186	r rLSB
25	154.8047	15.0122	0.0815	11.512	-20.524	-21.498	0.6847	13.007	
26	155.9830	7.9813	0.1033	11.604	-21.229	-22.230	0.5261	13.189	
27	157.3174	15.4637	0.0570	11.261	-21.377	-22.259	0.4406	13.605	
28	161.1391	45.5408	0.1122	11.577	-20.049	-21.001	0.5509	13.043	r rLSB
29	162.1012	5.2697	0.0699	11.235	-20.415	-21.334	0.5064	13.111	
30	164.5891	3.6572	0.0567	11.312	-21.166	-22.145	0.4939	13.235	
31	165.8158	54.1113	0.0703	11.510	-21.037	-21.990	0.5013	13.263	r rLSB
32	175.0114	15.7188	0.0844	11.483	-20.261	-21.208	0.4708	13.156	
33	175.5136	3.0047	0.0406	11.151	-20.327	-21.209	0.4457	13.210	u
34	178.8740	49.7966	0.0535	11.139	-20.907	-21.818	0.4519	13.180	u
35	179.8952	40.6662	0.0666	11.425	-20.782	-21.727	0.4915	13.306	u r
36	180.1458	32.6646	0.0715	11.463	-20.595	-21.566	0.5057	13.328	u r rLSB
37	181.2686	40.7910	0.0525	11.050	-20.526	-21.520	0.4447	13.210	u r
38	181.3191	21.0103	0.0746	11.565	-21.133	-22.111	0.5507	13.100	u
39	181.4802	25.2690	0.1007	11.722	-20.689	-21.624	0.5222	13.024	u
40	181.5380	-2.9481	0.0256	10.847	-21.123	-22.091	0.7142	13.389	
41	182.3114	67.6405	0.0599	11.234	-20.413	-21.392	0.4919	13.103	
42	183.1793	61.9709	0.0496	11.323	-20.877	-21.818	0.4802	13.110	
43	184.6847	44.7812	0.0383	11.233	-21.255	-22.150	0.4753	13.326	r rLSB
44	192.5297	52.8502	0.0330	11.385	-20.683	-21.649	0.4422	13.063	
45	198.8502	7.8469	0.0926	11.614	-21.053	-21.931	0.5359	13.727	
46	201.2748	6.3122	0.0825	11.437	-20.423	-21.364	0.4478	13.249	
47	202.5798	11.5118	0.0377	11.184	-21.247	-22.226	0.5317	13.405	
48	203.7632	35.4873	0.0635	11.011	-20.667	-21.559	0.4752	13.103	u
49	204.6871	15.4295	0.0745	11.343	-21.080	-22.011	0.5456	13.027	
50	205.0684	56.5015	0.0998	11.580	-21.328	-22.321	0.7522	13.499	r
51	207.4004	28.4404	0.0746	11.404	-21.001	-22.005	0.4925	13.282	u
52	210.5004	45.5619	0.0654	11.477	-20.185	-21.081	0.4571	13.022	r
53	211.7204	-1.7302	0.0700	11.443	-20.505	-21.461	0.4704	13.145	
54	216.6863	9.1793	0.0550	11.335	-20.687	-21.649	0.4883	13.044	
55	218.8973	50.1900	0.0691	11.456	-20.003	-20.859	0.4993	13.021	r rLSB
56	219.1753	9.9292	0.0586	11.726	-21.873	-22.841	0.6403	13.901	
57	219.6765	30.4659	0.0707	11.648	-20.980	-21.876	0.4580	13.201	u
58	223.2020	32.3799	0.0878	11.873	-21.724	-22.760	0.7595	14.007	u
59	225.6145	19.7352	0.0972	11.550	-19.964	-20.867	0.6811	13.002	

Table A.1. Continued.

Number	RA	DEC	z	$\log M_{BGG}$	$Mabs_g$	$Mabs_r$	R_{virial} (Mpc)	$\log M_{halo}$	
60	225.8131	36.1477	0.0733	11.649	-21.754	-22.699	0.5928	13.734	u
61	226.1660	53.8232	0.0379	11.403	-20.567	-21.559	0.5158	13.133	r
62	227.3765	46.4927	0.0378	11.195	-19.350	-20.342	0.5162	13.072	r
63	227.4669	-0.3847	0.0711	11.775	-20.964	-21.874	0.4527	13.129	
64	228.2578	28.4928	0.0786	11.390	-20.520	-21.464	0.4803	13.037	u
65	228.7253	42.0131	0.1348	11.968	-20.222	-21.162	0.9219	13.185	u r rLSB
66	232.6162	-0.2305	0.0869	11.774	-20.435	-21.238	0.6042	13.090	
67	233.3931	33.6996	0.0677	11.502	-21.141	-22.153	0.4443	13.212	u r rLSB
68	233.4166	24.4047	0.0434	11.335	-20.677	-21.642	0.4801	13.158	u
69	234.9934	48.5938	0.0677	11.391	-20.930	-21.872	0.5596	13.091	r rLSB
70	235.6059	13.9567	0.0926	11.635	-20.781	-21.717	0.4694	13.026	
71	236.6317	12.1427	0.0720	11.800	-20.121	-21.008	0.6834	13.113	
72	237.0568	29.9150	0.0960	11.500	-21.384	-22.344	0.5031	13.069	u r rLSB
74	239.8565	42.2635	0.0605	11.420	-20.906	-21.841	0.5515	13.068	r rLSB
75	242.3237	4.0439	0.0551	10.939	-20.982	-21.903	0.4439	13.197	
76	246.6880	24.1490	0.0589	11.117	-20.538	-21.497	0.4370	13.164	u
77	251.8154	33.9324	0.0673	11.622	-20.905	-21.875	0.4699	13.596	r rLSB
78	252.4850	35.2121	0.0996	11.589	-19.763	-20.775	0.4768	13.000	u r rLSB
79	255.2097	23.0110	0.0094	11.906	-21.262	-22.206	0.8850	13.252	u
80	255.8944	58.9176	0.0762	11.516	-20.669	-21.656	0.4717	13.026	u r rLSB
81	317.6327	0.8951	0.0681	11.319	-20.853	-21.800	0.4475	13.109	u
82	322.3274	11.2010	0.0890	11.755	-21.004	-21.990	0.4537	13.310	u
83	327.4432	-7.4425	0.0903	11.582	-21.746	-22.652	0.6729	13.590	u
84	336.5609	0.6678	0.0364	11.016	-20.888	-21.877	0.4711	13.091	u
85	340.9873	1.0005	0.0580	11.195	-20.881	-21.756	0.5032	13.297	u
86	342.3251	12.6305	0.1337	10.374	-19.661	-20.730	0.4602	13.072	u
87	346.9538	0.9405	0.0418	11.459	-21.107	-22.059	0.4846	13.596	u
88	348.8094	-1.2422	0.0251	10.848	-20.366	-21.327	0.4662	13.012	

Table A.2. Control sample of 30 non-FG candidates. The columns are: name, J2000 right ascension and declination (in degrees), spectroscopic redshift, logarithm of the BGG mass, absolute magnitudes in the g and r bands, logarithm of the halo mass. The availability of UNIONS data is not indicated, since they all have UNIONS data in the u, r, and rLSB bands.

Name	RA	DEC	z	$\log M_{BGG}$	$Mabs_g$	$Mabs_r$	R_{Virial} (Mpc)	$\log M_{halo}$
NonFG6	121.2352	31.2595	0.0732	11.363	-20.550	-21.495	0.4882	13.152
NonFG8	121.5296	39.3424	0.0645	11.480	-19.942	-20.897	0.5038	13.190
NonFG9	121.6227	33.2801	0.0838	10.829	-20.221	-21.072	0.4785	13.131
NonFG12	123.3757	30.3811	0.0753	11.197	-19.908	-20.894	0.4397	13.017
NonFG15	124.1161	33.3768	0.1084	11.150	-20.659	-21.640	0.6743	13.588
NonFG16	124.7523	34.9870	0.0623	11.159	-20.596	-21.592	0.5076	13.198
NonFG17	125.0182	41.3390	0.1021	11.216	-20.396	-21.356	0.5278	13.266
NonFG19	126.1656	32.3262	0.0683	11.357	-20.572	-21.526	0.5401	13.282
NonFG22	126.5740	29.5435	0.1100	11.251	-20.850	-21.837	0.5273	13.268
NonFG23	126.8353	34.2165	0.0876	10.973	-20.556	-21.531	0.5129	13.223
NonFG24	127.3892	31.6653	0.0900	11.595	-20.422	-21.453	0.5514	13.318
NonFG29	128.2929	30.4762	0.1075	11.301	-20.196	-21.128	0.4921	13.177
NonFG30	128.3209	30.9804	0.0936	11.243	-19.755	-20.676	0.4963	13.182
NonFG31	128.9864	30.1257	0.0933	10.824	-20.749	-21.711	0.4650	13.097
NonFG33	129.4784	36.9984	0.0548	11.574	-20.437	-21.297	0.4853	13.137
NonFG34	129.5675	35.0896	0.0647	11.434	-20.314	-21.331	0.4675	13.092
NonFG48	131.7605	31.4298	0.0660	11.346	-19.842	-20.664	0.6012	13.420
NonFG56	133.3498	37.3566	0.1036	11.083	-21.203	-22.141	0.5211	13.250
NonFG58	133.6843	35.5656	0.0882	11.258	-21.218	-22.227	0.7549	13.726
NonFG63	134.0557	37.7081	0.0938	10.904	-21.090	-22.034	0.4891	13.163
NonFG67	135.3629	34.4643	0.0655	11.307	-20.122	-21.080	0.5484	13.301
NonFG69	136.0299	30.8830	0.0635	11.212	-20.990	-21.967	0.5083	13.201
NonFG78	140.8148	33.5107	0.0424	10.670	-20.200	-21.173	0.4663	13.080
NonFG82	142.0339	35.8988	0.1108	11.454	-20.930	-21.906	0.4497	13.061
NonFG84	143.2806	32.2718	0.0735	10.961	-21.084	-22.079	0.5072	13.202
NonFG86	143.7315	32.8416	0.0610	11.287	-19.442	-20.364	0.5401	13.279
NonFG90	144.2122	30.2841	0.1111	11.305	-21.027	-21.855	0.4677	13.112
NonFG95	148.1868	40.7628	0.0925	11.150	-21.372	-22.324	0.4461	13.043
NonFG96	148.3277	34.7647	0.0502	11.332	-20.690	-21.682	0.4690	13.090
NonFG98	148.5450	32.4480	0.0869	11.200	-20.812	-21.764	0.6378	13.506

Chapter 4

Off-centre supermassive black holes in bright central galaxies

Galaxy clusters are rich environments, hosts of hundreds to thousands of galaxies, which makes them propitious environments to galaxy mergers. In Section 1, we have described the importance of galactic mergers for the formation of galaxies. Apart from mergers, other physical contributors are to be taken into account to explain the evolution of these clusters. Among these are black holes (BHs), and more specifically, supermassive black holes (SMBHs).

BCGs are believed to host SMBHs in their centers. The many mergers that BCGs experience can bring matter such as gas into the center of the galaxy, and this matter will be absorbed by the SMBH; mergers can also bring massive stars or BHs, with which the SMBH can merge to form an even greater SMBH. As stated in the introduction (see Section 1.2.3), these BHs are believed to be key ingredients in the shaping of their host galaxies, and more specifically in the quenching of star formation in elliptical galaxies. This quenching would mainly consist in the heating of the surrounding gas by AGN feedback (cooling flow problem).

However, Boldrini, Mohayaee, and Silk (2020) have shown that AGN feedback in dwarf galaxies is not effective if the central BH is off-centered, and Smith et al. (2018) indicated that this may also be the case for more massive galaxies. The work I present here was first motivated by observations made in Chu, Durret, and Márquez (2021), in which we find that some BCGs are farther than tens or even hundreds of kiloparsecs from the X-ray center of their host cluster. We wondered if this offset was the sign of an off-centered SMBH in the cluster. Indeed, BCGs are more likely to experience mergers in their lifetimes, and we suspect some of these mergers to be able to eject the SMBH from its central position.

4.1 Method

We study here a large sample of 370 galaxy clusters in the Illustris-TNG300 simulation from Barnes et al. (2018). Illustris-TNG[1] is a large cosmological hydrodynamical simulation of galaxy formation. TNG-300 corresponds to the largest cosmological box size of 300 Mpc (see Figure 4.1), and enables us to collect a large sample of clusters and to study the clustering of systems. The galaxy formation model of the simulation includes: the radiative cooling of gas; the formation of stars and SMBHs and their feedback; the formation, merging and accretion of nearby gas by SMBHs; and other mechanisms and processes to explain galactic formation and evolution. Our aim is to

[1] https://www.tng-project.org/

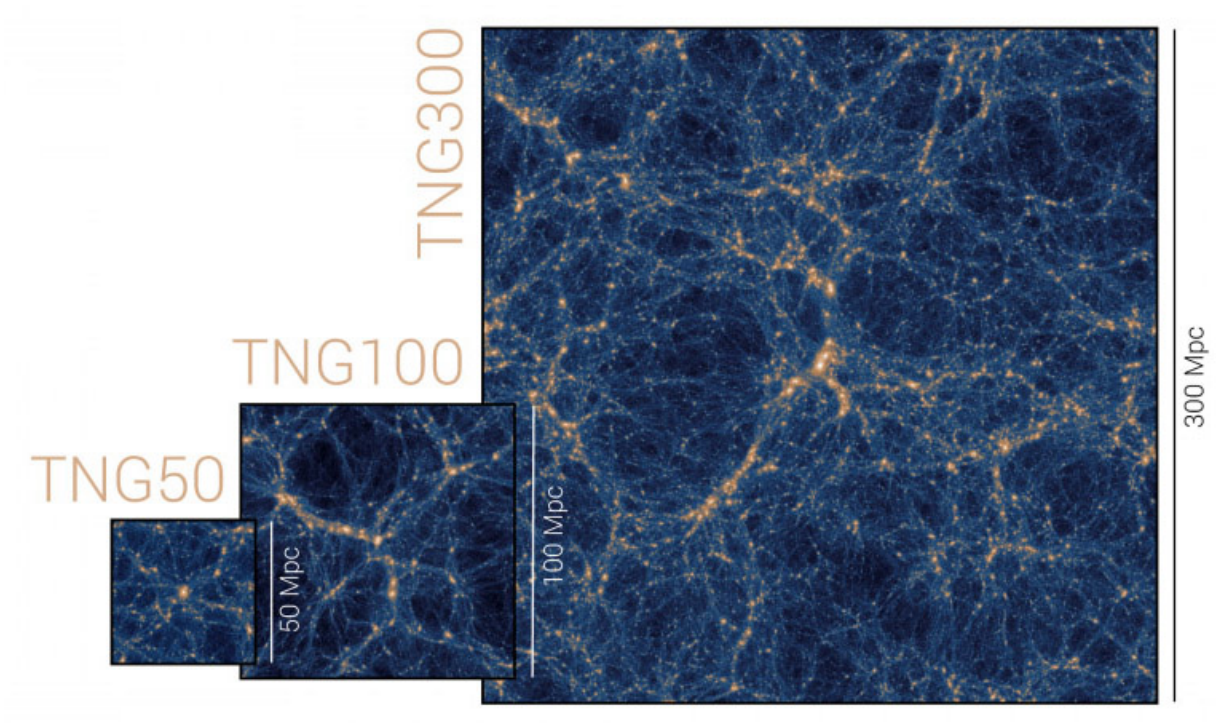

FIGURE 4.1: The Illustris-TNG simulation comes in three different sizes: 50, 100 and 300 Mpc. In this work, we use the largest box which enables us to study a significant number of clusters. Clusters can be identified as the knots, i.e. high density regions, and are connected to each other with filaments. In between filaments, voids can also be spotted throughout the whole image.

verify if galaxy mergers can indeed kick away the SMBH from its central position using information from the simulation and orbital integration methods, i.e, we track the orbit of the SMBH in the potential of the BCGs through multiple galaxy mergers.

I emphasize that we do not retrieve the orbit of the SMBH directly from the Illustris-TNG300 simulation. Indeed, simulations tend to pin the SMBH at the center of the cosmological box to obtain effective AGN feedback and to ensure that SMBHs gain mass rapidly through mergers during the early epochs of the Universe. Dynamical friction, which allows the SMBH to sink down to the bottom of the potential well of the BCG, is also not well treated in simulations, hence the repositioning of the SMBH (see Weinberger et al., 2017; Morton, Khochfar, and Oñorbe, 2021; Bahé et al., 2021). We only use data from the simulation to obtain the BCGs' and satellites' properties, and we then integrate the orbit of the SMBH using orbital integration methods independent from the simulation. This enables us to overcome problems linked to the repositioning of the SMBH and to resolve the orbit of the SMBH with better precision. As such, the orbits we compute are not limited by the constraints imposed by the Illustris-TNG300 simulation.

4.1.1 Reconstruction of the BCG's merger history

Barnes et al. (2018) have identified 370 galaxy clusters at $z = 0$ with a median halo mass $M_{500} > 8.8 \times 10^{13}$ $M_{\odot}$. The catalogue gives information on the cluster ID in the simulation and its properties at redshift $z = 0$. Since our goal is to retrace the merger history of the BCG, it is thus necessary to know, at each time step, which galaxy is the BCG and if a satellite is a potential merger candidate.

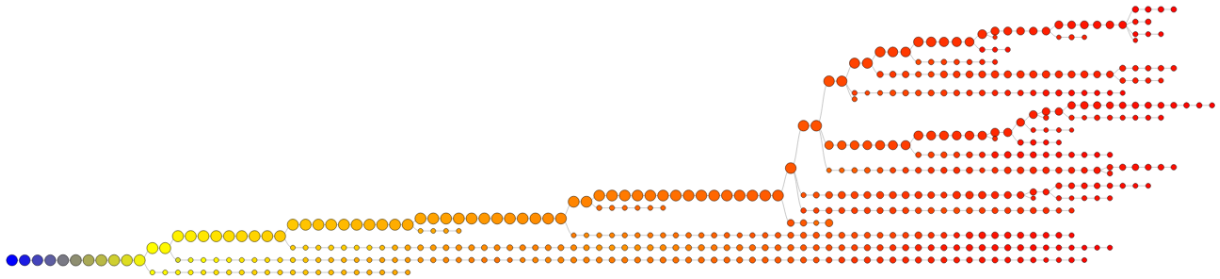

FIGURE 4.2: Merger tree of a BCG in the Illustris-TNG300 simulation (right to left) from soon after the Big Bang ($z = 20$) to today ($z = 0$). Each dot represents a galaxy at a given time. The bigger dots which form a continuous line represent the BCG of the cluster. The smaller dots represent the satellites that have merged with the main galaxy.

However, Illustris-TNG300 does not give us these informations directly, we thus had to find a method in order to draw numerically the merger tree of the BCG from $z = 2$ to $z = 0$. We chose to stop at $z = 2$, as we found in Chu, Durret, and Márquez (2021) that BCGs were most likely formed before that time. A cluster merger tree is shown in Figure 4.2. From left to right, we identify the BCG as the most massive galaxy in the cluster (or halo), which on the diagram corresponds to the bigger dots. At snapshot n, or in other words at a given time, Illustris-TNG gives the ID in the simulation of the First Progenitor (FP) of a galaxy, which is the BCG at snapshot $n - 1$ (snapshot $n = 99$ being equivalent to $z = 0$, and snapshot $n = 0$ to $z = 20$, soon after the Big Bang). It is thus possible to track the BCG through time. Identifying the satellite with which the BCG merged, however, is not as straightforward. The main idea is that two galaxies that merge together will have the same "child", i.e., descendant. In order to find the two "parents", i.e. progenitors, of a BCG resulting from the merging of two galaxies, we need to find two galaxies in the parent halo that both share the BCG as their descendant. One of the two progenitors is obviously the previous BCG at a time step earlier, the other one is the satellite. We checked in the simulation that the total mass of the satellite was always smaller than the total mass of the BCG.

4.1.2 Orbital integration of the satellites in the potential of the BCG

We retrieve the tridimensional velocities, positions, stellar, DM and gas masses of the BCG at $z = 2$. Then, we follow the merger history of the BCG, and at each merger, we get the same properties for the merging satellite. Using these properties, we are able to compute the orbit of the satellite via orbital integration method in the potential of the BCG, which we model by a Hernquist profile (Hernquist, 1990) for the DM distribution:

$$\rho(r) = \frac{\rho_s}{\left(\frac{r}{r_s}\right)\left(1 + \frac{r}{r_s}\right)^3} \tag{4.1}$$

with ρ_s the central density and r_s the scale radius; and by a Plummer profile (Plummer, 1911) for the stellar distribution:

$$\rho(r) = \frac{3M_0}{4\pi a^3}\left(1+\frac{r^2}{a^2}\right)^{-\frac{5}{2}} \tag{4.2}$$

with M_0 the total mass of the BCG and a the Plummer radius which is a scale distance close to the half mass radius (radius which encloses half of the total mass of the satellite). To compute their orbits, as a first approximation, we consider the satellites as point masses (the masses are given by the simulation), which fall into the potential of the BCG defined earlier and which suffer dynamical friction which takes into account the size of the satellite. Tracking the orbit of the satellite relatively to the center of the BCG enables us to check if the satellite can affect the central region of the BCG as it is falling into the BCG's potential. Indeed, in order to kick away the central BH, two conditions need to be met:

1. The distance d between the center of the satellite and the center of the BCG must be smaller than the half mass radius $r_{\rm hm}^{\rm sat}$ of the satellite. In order to simplify this model, we neglect mass loss and mass transfer between the two galaxies during the merger, so this condition needs to be met at the first passage of the satellite for this to be true. As a result, we look for all the satellites which fall in a radial orbit in the potential of the BCG.

$$d \leq r_{\rm hm}^{\rm sat}. \tag{4.3}$$

2. The total mass of the satellite $M_{\rm tot}^{\rm sat}$ must be greater than the mass of the BCG enclosed in an aperture of radius d, with d the distance between the two galaxy centers. We thus select only satellites which are massive enough to affect the central region of the BCG.

$$M_{\rm tot}^{\rm sat} \geq M_{\rm int}^{\rm BCG}(d). \tag{4.4}$$

If a satellite fulfills these two conditions, we define the time of the event as T_d. The orbits of the satellites relative to the BCG center are computed using the code `galpy` (Bovy, 2015), which is a python package for galactic-dynamics calculations, and more specifically in this case, for numerical orbit integration calculation. `galpy` enables to take into account dynamical friction as well, which is defined by Chandrasekhar as the loss of momentum and energy of a moving object as it suffers the gravitational force of its environment (Chandrasekhar, 1943a; Chandrasekhar, 1943b; Chandrasekhar, 1943c)

In this way, we go through the merger history of the BCG from $z = 2$ to $z = 0$ and identify all massive satellites which fall in a radial orbit in the potential of the BCG, potentially affecting the central region of the BCG and thus the dynamics of the SMBH. We retrieve the time T_d at which each of these satellites meet Equations (4.3) and (4.4) and order them in chronological order. From the Illustris-TNG database, we can only know which two galaxies are going to merge between two redshifts (the time resolution of the simulation). By integrating the orbit of these objects, we have better precision as to when the event happens. As a result, we complete the merger tree of the cluster by indicating when a satellite and which satellite falls with a radial orbit in the potential of the BCG and can potentially offset the central SMBH. Taking into account only these radial mergers, we now track back the orbit of the central SMBH.

4.1.3 Orbital integration of the SMBH in the potential of the BCG

We define the SMBH as an object with mass $M_{SMBH} = 0.06\ M^*_{BCG}$ (Magorrian et al., 1998), with M^*_{BCG} the stellar mass of the BCG at the first T_d. The mass of the SMBH is fixed constant throughout. We suppose that it is initially on a circular orbit at a radius 100 times its Schwarzschild radius. This value was chosen to ensure that the SMBH would be orbiting in the central region of the galaxy, but the factor of 100 was arbitrary. We tested several values and the factor does not really affect our results. Similarly to the method described for satellites in Section 4.1.2, we compute the orbit of the SMBH with `galpy`. The SMBH is described as a point mass which goes through the potential of the BCG and suffers dynamical friction. Following a radial merger, the SMBH gets kicked away to distances up to a hundred kpc, and then, as it suffers dynamical friction from its environment, loses energy and falls back to the center of its host cluster. As the next merger happens, the SMBH may have not had time to go back to its initial position, and so it may not be affected. Thus, not all radial mergers will affect the SMBH. Once the SMBH goes back to the center and a radial merger happens, we update the SMBH velocity and position with the outputs of `galpy`. We thus trace the dynamical history of the SMBH from $z = 2$ to $z = 0$.

4.2 Results

Our results show that almost half of the BCGs (170 out of 370 BCGs) in our sample present SMBHs that have been at least once off-centered during their lifetime, and these BCGs for the most part spent more than half of their lives off-centered. We also show that the more massive a galaxy is, the more likely it is to present an off-centered SMBH still today. Boldrini, Mohayaee, and Silk (2020) show that massive galaxies are centrally less dense than less massive ones. Our result of larger off-centering of massive galaxies can be understood considering that dynamical friction is less effective in massive galaxies, meaning that the SMBH will take more time to lose its angular momentum and sink to the center (Boldrini, Mohayaee, and Silk, 2020).

These mergers can remove the SMBH from the central regions of its host galaxy for an extended period of time, and can eject the SMBH to distances of a few pc to a hundred kpc. These results are very interesting as the off-centering may have significant consequences on the growth and evolution of the BCG SMBH, in particular, off-centering can prevent the SMBH mass growth. We argue that a good fraction of SMBHs may not have been able to grow much since the last 10 Gyrs, as they spent most of their time outside the dense central regions of the BCGs and did not accrete matter efficiently.

As mentioned in Section 4.1, simulations tend to reposition the SMBH to the center of the cosmological box at each time step, allowing the SMBH to accrete in the denser center of the galaxies and thus to increase their masses. By showing that SMBHs can leave the central regions to less dense regions where the accretion will be less effective, we argue that simulations may overestimate the mass of the SMBHs. The absence of growth, i.e. the absence of accretion into the central SMBH, also indicates that feedback becomes inefficient (Boldrini, Mohayaee, and Silk, 2020). Hence,we question the role of AGN feedback in the cooling flow problem, and suggest that other processes need to be taken into account to explain the low SFR measured in clusters. This work shows evidence for the necessity to take into account the off-centering of the SMBH and to obtain in simulations good models of dynamical friction in simulations which tend to reposition

the SMBH at the center of its halo. Such simulations will enable to properly model SMBH growth and better understand which processes affect the formation and evolution of galaxies and estimate their relative importance.

By retrieving reconstructed images of the star density of the 370 simulated BCGs at $z = 0$, we attempted to determine the physical properties and characteristics of BCGs with an off-center SMBH at $z = 0$ that can distinguish them from BCG with a still central SMBH. We checked for the presence of a stream or tail, which would hint at a recent merger; an alignment of the stream with the axis of the galaxy, which would indicate a radial merger; the intensity of the stream, as an indicator of the strength of the merger; or the morphology or state (relaxed, disturbed) of the galaxy which again would give evidence for a recent merger, and thus for a SMBH that would not have had time yet to fall to its central position. However, we did not find any consistent link between the presence of streams and a decentering of the BHs.

4.3 The paper

The paper included in this manuscript has been submitted to the Monthly Notices of the Royal Astronomical Society and is currently in revision.

MNRAS **000**, 1–7 (2015) Preprint 6 March 2023 Compiled using MNRAS LATEX style file v3.0

Off-centre supermassive black holes in bright central galaxies

Aline Chu [1]★, Pierre Boldrini [1,2]† and Joe Silk [1,3,4]
[1]*Sorbonne Université, CNRS, UMR 7095, Institut d'Astrophysique de Paris, 98 bis bd Arago, 75014 Paris, France*
[2]*Université de Lorraine, CNRS, Inria, LORIA, F-54000 Nancy, France*
[3]*Department of Physics and Astronomy, The Johns Hopkins University, Baltimore MD 21218, USA*
[4]*Beecroft Institute for Particle Astrophysics and Cosmology, Department of Physics, University of Oxford, Oxford OX1 3RH, UK*

Accepted XXX. Received YYY; in original form ZZZ

ABSTRACT

Supermassive black holes (SMBHs) are believed to reside at the centre of massive galaxies such as brightest cluster galaxies (BCGs). However, as BCGs experienced numerous galaxy mergers throughout their history, the central BH can be significantly kicked from the central region by these dynamical encounters. By combining the TNG300 simulations and orbital integrations, we demonstrate that mergers with satellite galaxies on radial orbits are a main driver for such BH displacements in BCGs. BHs can get ejected to distances varying between a few parsecs to hundreds of kiloparsecs. Our results clearly establish that SMBH offsets are common in BCGs and more precisely a third of our BHs are off-centred at $z = 0$. This orbital offset can be sustained for up to at least 6 Gyr between $z = 2$ and $z = 0$ in half of our BCGs. Since the dense gas reservoirs are located in the central region of galaxies, we argue that the consequences of off-center SMBHs in BCGs are to quench any BH growth and BH feedback.

Key words: galaxy clusters – supermassive black hole – brightest cluster galaxy – off-centre black holes – orbital integrations

1 INTRODUCTION

Galaxy clusters are the largest virialized structures known today. These rich systems of hundreds to thousands of galaxies are the perfect targets to study how environment can impact the formation of galaxies and their evolution. Located at the intersection of the filaments which compose the cosmic web, clusters are believed to form mainly by accreting small galaxies and groups which fall along the filaments, or by mergers with other systems (Kravtsov & Borgani 2012). Galaxies, gas clumps and globular clusters, which are captured by the cluster potential, would sink to the central region of the cluster. Indeed, these satellites are bound to merge with the central galaxy, which is often referred to as the Brightest Cluster Galaxy (BCG) (Crawford et al. 1999; Bernardi et al. 2007).

BCGs are among the most massive galaxies observed in the Universe (Dubinski 1998). These peculiar elliptical galaxies, which generally lie at the bottom of the cluster potential well, are more likely to encounter other objects due to their special location, and thus, to undergo many mergers during their lifetimes which promotes their growth. BCGs form via environmental processes (Castignani et al. 2020, and references therein), and suffer and reflect all the processes which formed and shaped their host clusters. Hence, BCGs have properties which are closely linked to those of their host clusters (see Lauer et al. 2014; Sohn et al. 2022).

In the local Universe, black holes (BHs) are nearly ubiquitous in galaxies (Kormendy & Ho 2013; Saglia et al. 2016; van den Bosch 2016). In particular, BCGs host among the most massive BHs ever detected, the supermassive black holes (SMBH). Recently, measurements were reported of SMBH masses in excess of 10^{10} $M_\odot$ (McConnell et al. 2011; Hlavacek-Larrondo et al. 2012, 2015; McConnell & Ma 2013a; Thomas et al. 2016). We expect the central BHs to grow at the same time as their host galaxies by accreting matter brought in by infalling galaxies. That is the reason why central BH masses seem to be correlated with the stellar and bulge masses of their host galaxies (Magorrian et al. 1998; Gültekin et al. 2009; Marleau et al. 2013; McConnell & Ma 2013b; Sahu et al. 2019). A prominent example is the SMBH of Holm 15A, the BCG of the galaxy cluster Abell 85, which is the most massive BH directly detected via stellar dynamics with a mass of about 4×10^{10} $M_\odot$, i.e. 2% of the total stellar mass of the central galaxy (Mehrgan et al. 2019).

However, it has been demonstrated that BHs are not necessarily located exactly at the bottom of the cluster potential, inside and at the center of the central galaxy. In particular, tens of thousands of active galactic nuclei (AGN) are not located at the centers of their host dwarf galaxies. These observations exhibit BH offsets between tens of parsecs to a few kiloparsecs (Menezes et al. 2014, 2016; Reines et al. 2020; Shen et al. 2019). Many scenarios have been proposed to explain these off-centre BHs (Sundararajan et al. 2010; Tremmel et al. 2018; Barth et al. 2009; Comerford & Greene 2014; Merritt & Milosavljević 2005; Volonteri & Perna 2005; Loeb 2007; Komossa 2012; Boldrini et al. 2020). It is important to notice that most of these scenarios need to invoke interactions and mergers with other galaxies or dark matter (DM) substructures (Bellovary et al. 2019; Pfister et al. 2019; Bellovary et al. 2021, 2018; Boldrini et al. 2020).

This BH feature was also found in more massive galaxies such as Andromeda (M31). It has been shown that its SMBH is offset by 0.26 pc from the centre of the galaxy (Kormendy & Bender 1999).

★ E-mail: chu@iap.fr
† E-mail: boldrini@iap.fr

As there are several indications of a recent merger activity in M31, it was demonstrated that the accretion of a satellite on a highly eccentric orbit naturally explains this off-centre BH in our neighbor galaxy (Boldrini 2020). As BCGs are the results of numerous galaxy mergers throughout their history, we suspect that some mergers could have significantly offset the SMBH located at the center of BCGs to distances even larger than of the order of a kiloparsec.

In this paper, we aim to examine the impact of mergers between BCGs and satellite galaxies, within galaxy clusters, on the SMBH of BCGs. In fact, we track the orbit of the central SMBH in 370 BCGs by using orbital integration methods after analysing the merger history of the central galaxies provided by the TNG300 simulation. The paper is organized as follows. Our method is based on the coupling between TNG300 data and orbital integration methods and is described in details in Section 2. We present our results in Section 3, and discuss the implications of this BH behaviour in Section 4. Section 5 presents our conclusions and perspectives.

2 METHOD

Using a large sample of 370 galaxy clusters detected by Barnes et al. (2018) in TNG300 (Nelson et al. 2018; Pillepich et al. 2017; Springel et al. 2017; Nelson et al. 2017; Naiman et al. 2018; Marinacci et al. 2018), we track the orbit of a test SMBH throughout the merger history of the BCG, by integrating its orbit in the fixed potential of the BCG using the publicly available code `galpy`[1] (Bovy 2015). The sample is limited to masses $M_{500} > 10^{13.75}$ $M_\odot$ and has a median mass $M_{500} = 8.8 \times 10^{13}$ $M_\odot$ at $z = 0$. The following describes our approach.

2.1 Merger history of BCGs with TNG300

For each cluster in TNG300, we identify the BCG at $z = 0$, which is assumed to be the most massive galaxy in the cluster at $z = 0$. Going back through its merger history tree until $z = 2$, we search for all the main mergers that the BCG has undergone. Indeed, BCGs were shown to have photometric properties and shapes that do not change much in that redshift range, hinting at an earlier formation epoch (Chu et al. 2021, 2022). Moreover, other studies such as De Lucia & Blaizot (2007) and Thomas et al. (2010) have shown evidence that the stellar population in such galaxies has most likely settled since $z = 2$ as most of the stars in BCGs were already formed in-situ a long time ago, and the stellar masses measured today are found not to be significantly different from their masses 9 billion years ago (Collins et al. 2009). More precisely, BCGs only grow a factor of 1.8 in mass between $z = 1$ and $z = 0$ (Burke & Collins 2013).

We identify the BCG at snapshot n and go back one snapshot to $n - 1$ to look for its first progenitor (FP) (the most massive galaxy in the cluster at snapshot $n - 1$). If a merger happened, we also identify the most massive satellite galaxy with which the BCG has merged, which is referred to as the next progenitor (NP) in the TNG300 simulation. At snapshot $n - 1$, the NP will also have the BCG as a descendant. We thus retrieve all FPs and NPs at each snapshot present in the parent halo (or cluster). If two galaxies are merging, we retrieve their positions, velocities, half-mass radii, stellar and DM masses, which will be used to integrate the orbit of the satellite in the potential of the BCG. We find that BCGs in this sample have undergone between 12 and 130 mergers since z = 2.

[1] Available at `https://github.com/jobovy/galpy`

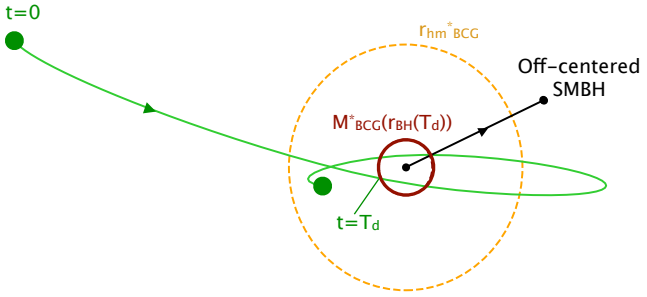

Figure 1. *Dynamical heating from satellites of BCG:* Scheme illustrating the radial orbit of a satellite (green points), falling into the potential of the BCG, which kicks away the central BH (black point) after its passage. It results in an off-centered SMBH. The maroon circle represents the region of the BCG where Equations (1) and (2) are satisfied. We note T_d the time at which both of these conditions are met. The dotted orange circle represents the half-mass radius of the BCG stellar component.

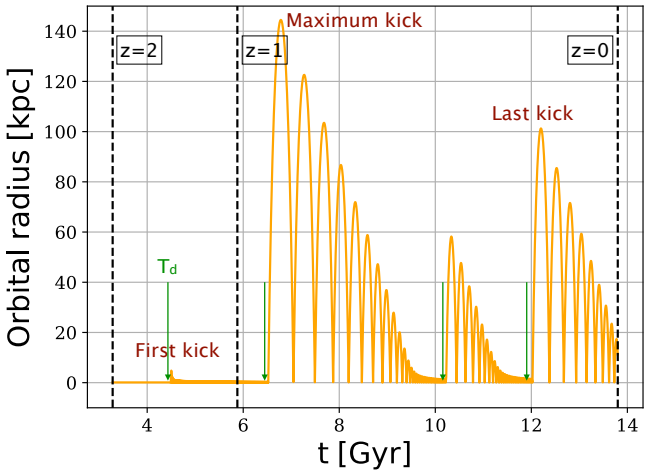

Figure 2. *Black hole kicks in BCGs:* Orbital radius of a $M_{SMBH} = 2.6 \times 10^{10}$ $M_\odot$ SMBH in a BCG potential composed of a DM halo of M_{DM} =8.1×10^{12} $M_\odot$ and a stellar component of M_* =4.4×10^{11} $M_\odot$ between $z = 2$ and $z = 0$. The SMBH has experienced 17 mergers since $z = 2$ but only 4 mergers have satisfied our kicking criteria described by Equations (1), (2) and (6), showed by green arrows. The BH can be ejected to hundreds of kiloparsecs. Between mergers, we observe the orbital decay of the BH due to dynamical friction. At $z = 0$, the BH is still significantly off-centered by about 10 kpc.

2.2 Orbital integrations with `galpy`

For each satellite galaxy (or NP), we integrate its orbit forward in time in the potential of the BCG (or FP) from $z = 2$ until $z = 0$. The potential of the BCG consists in a Hernquist and Plummer profile for the DM and stellar components respectively, which is computed considering the properties found in TNG300. All masses and scale radii are taken from the cosmological simulation. The DM and stellar masses of the BCG remain fixed along all the orbital integrations. In fact, we neglect the mass contribution of satellites from galaxy mergers. The satellite is assumed to be a point mass, which suffered the dynamical friction from the BCG. Its total half-mass radius r_{hm}^{NP} is incorporated in the dynamical friction force. Therefore, we also neglect the mass loss of the satellite, which could reduce the impact of the merger with the BCG.

We aim to determine if the satellite galaxy, via the merger, dynamically heats the central region of the BCG and more particularly its SMBH. The satellite needs to be massive enough and pass close enough to the center of the BCG on its first orbit to be able to transfer energy to the central region of the galaxy during the merger. Two conditions need to be met:

- The distance d between the centers of the satellite and the BCG must be smaller than the half-mass radius of the NP $r_{\rm hm}^{\rm sat}$:

$$d \leq r_{\rm hm}^{\rm sat}. \quad (1)$$

This condition needs to be true on the satellite's first passage in the potential of the BCG (radial merger). Indeed, through each orbit, the satellite will transfer its mass to the total mass of the BCG with which it is merging until all its mass has been consumed by the BCG. In order to simplify the problem, we neglect the mass loss of the satellite, which is valid only on its first passage.

- The total mass of the satellite galaxy must be bigger than the total mass of the FP contained in a radius d:

$$M_{\rm tot}^{\rm sat} \geq M_{\rm int}^{\rm BCG}(d). \quad (2)$$

Only under this condition, the BCG potential can be displaced due to the mass deposit from the satellite (Goerdt et al. 2010; Read et al. 2006). Then the BH can vacate the central region of the galaxy. In our mass calculations, we take into account the DM and stellar components.

The two previous conditions are equivalent to checking if the satellite has a radial orbit. Indeed, the satellite must pass by the center or very close to the center of the BCG in order to affect the central SMBH. We note T_d the time at which both of these conditions are met. We update at each T_d the stellar and DM masses of the BCG given by the TNG300 simulation. Figure 1 illustrates a satellite which falls in the potential of the BCG passing by its center, in a radius $r_{\rm hm}^{\rm sat}$ as described in Equation 1. The SMBH is significantly kicked by the satellite galaxy (see Figure 1).

Using the simulation information, we are able to follow the orbit of satellites throughout the merger history of the BCG with `galpy`, by considering their initial positions, velocities, and masses. Then, a SMBH with a constant mass is placed at the centre of each BCG potential. As we are not using the BH as a PartType5 particle from the simulation, the mass of the SMBH was calculated based on the Magorrian et al. (1998) relation: $\rm M_{SMBH} = 0.06\ M_*^{BCG}$, with $\rm M_*^{BCG}$ the stellar mass of the BCG at the first $\rm T_d$. We suppose that the SMBH is initially on a circular orbit at a arbitrary radius, which is 100 times its Schwarzschild radius, as the SMBH should lie in the central region of its host galaxy. After a careful check, choosing a smaller radius does not significantly affect our results. If both Equations (1) and (2) are satisfied, the SMBH is kicked at $\rm T_d$ with a velocity based on the analytic expansion derived in Naab et al. (2009):

$$v_{\rm kick}^{\rm first} = \sqrt{\frac{(1+\eta\epsilon^2)}{(1+\eta)}}\, v_{\rm c}^{\rm SMBH}(100 \times R_{\rm s}), \quad (3)$$

with $v_{\rm c}^{\rm SMBH}$, which is the circular velocity of the SMBH at 100 times its Schwarzschild radius $R_{\rm s}$,

$$\eta = M_{\rm tot}^{\rm sat}/M_{\rm int}^{\rm BCG}(d), \quad (4)$$

and

$$\epsilon = \frac{v^{\rm sat}}{v_{\rm c}^{\rm SMBH}}, \quad (5)$$

where $v^{\rm sat}$ the velocity norm of the satellite galaxy at $\rm T_d$ (see Figure 2). Our criterion (2) is established to maximise the energy transferred to the SMBH via the velocity kick, described by Equations (3) and (4). All the velocities are calculated relative to the BCG. We then integrate the BH orbit with its new velocity by applying dynamical friction to it with a constant mass.

At each subsequent merger, we check if the SMBH, which might have been kicked from the center of the galaxy, passes close to the inner region of the BCG heated by the satellite. We, therefore, use the orbital radii of the SMBH and distance d between the centers of the satellite and the BCG to define a simple criterion in order to establish if the BH can be affected after this new merger:

$$r_{\rm orb}^{\rm SMBH} \leq d. \quad (6)$$

In order to satisfy this condition, the BH must have had sufficient time to come back to the BCG centre before the next merger happens. Then, the SMBH is kicked once again with a new velocity:

$$v_{\rm kick}^{\rm sub} = \sqrt{\frac{(1+\eta\epsilon)}{(1+\eta)}}\, v_{\rm N}^{\rm SMBH}. \quad (7)$$

The only difference with Equation (3) is that the SMBH is no longer in a circular orbit and now has a velocity norm $v_{\rm N}^{\rm SMBH}$.

First, we plot the orbit of the SMBH within a BCG which went through multiple mergers throughout its history. As an example, Figure 2 depicts the four kicks that a $\rm M_{SMBH} = 2.6 \times 10^{10}\ M_\odot$ BH has experienced in a BCG potential composed of a DM halo of $\rm M_{DM} = 8.1{\times}10^{12}\ M_\odot$ and a stellar component of $\rm M_* = 4.4{\times}10^{11}\ M_\odot$ between $z = 2$ and $z = 0$. The maximum distance reached by the SMBH is about 150 kpc. The SMBH has been heated by a first merger between $z = 2$ and $z = 1$ and by three more mergers between $z = 1$ and $z = 0$. We emphasize that the number of mergers shown in Figure 2 may not be equal to the total number of mergers experienced by the BCG. Indeed, the BCG has experienced 17 mergers since $z = 2$ but only 4 mergers have satisfied our kicking criteria described by Equations (1), (2) and (6). In this example, the BCG undergoes its last merger almost 2 Gyrs ago, the SMBH was kicked up to 100 kpc away from the center, which is to say beyond $r_{\rm hm}^{\rm BCG} = 32$ kpc at $z = 0$. After being kicked, we observe the orbital decay of the SMBH in the BCG potential due to dynamical friction. We argue that the SMBH needs to return to the central region to be kicked again (see Figure 2). In other words, chances of encounter between an offcenter BH and a falling satellite are very small. In the case of dynamical interactions out of the central regions of BCGs, the collision would have little impact. Indeed, it is really hard to satisfy the criterion (2) in these regions of BGCs as the major impact of satellites takes place especially in the central region where the enclosed mass of BCG is smaller (at large distances d, $\rm M_{tot}^{sat}$ would need to be comparable to the total mass of the BCG $\rm M_{int}^{BCG}(\mathit{d})$). We stress that at $z = 0$, the BH is still significantly off-centered by about 10 kpc.

We apply this procedure to our full sample of 370 galaxy clusters from TNG300.

3 RESULTS

Here we present our results by considering our full sample of 370 BCGs and thus 370 orbiting BHs, tracked with orbital integrations.

As depicted by Figure 3, not all mergers undergone by the BCGs perturb the central BH. We derive that BHs are mainly kicked by satellites which have stellar masses $M_*^{\rm sat} > M_*^{\rm BCG}/100$. We confirm that massive satellites on a radial orbit are rare (only 229 mergers out of all 6628 mergers accounted for all 370 clusters meet Equations

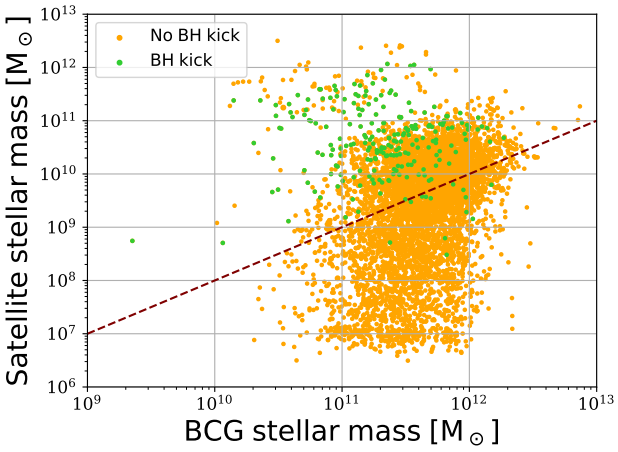

Figure 3. *Mergers in our full sample:* Satellite stellar mass as a function of the BCG stellar mass . We distinguish two different categories of mergers in our full sample of 370 BCGs: mergers which have kicked the central BH (green points, 229 mergers), and mergers which have not affected the BH (orange points, 6628 mergers). The dotted line represents a constant ratio of 100 in mass. The majority of mergers leave the BH unaffected. BHs are mainly kicked by satellites which have stellar masses $M_*^{\rm sat} > M_*^{\rm BCG}/100$.

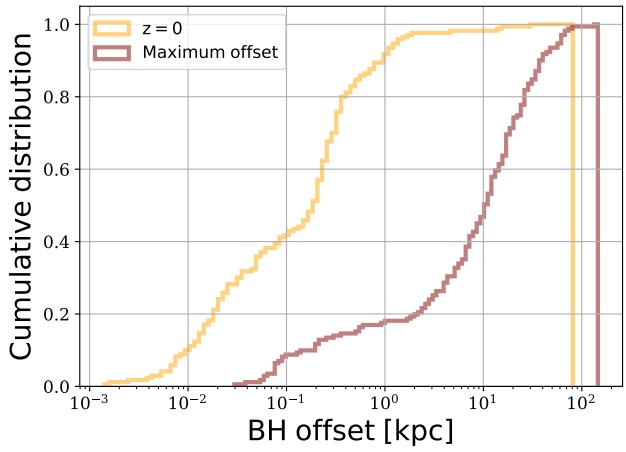

Figure 4. *Off-centered black holes in BCGs:* Cumulative histograms showing the BH offset at $z = 0$ in yellow, and the maximum offset measured since $z = 2$ in maroon. In almost half of our sample (170 BCGs), the SMBH is still off-centered ($r > 0.01$ kpc) at $z = 0$. About 60% of these SMBHs are located at $r > 0.1$ kpc at present time, and more than 80% of these SMBHs were off-centered by at least 1 kpc during their dynamical history.

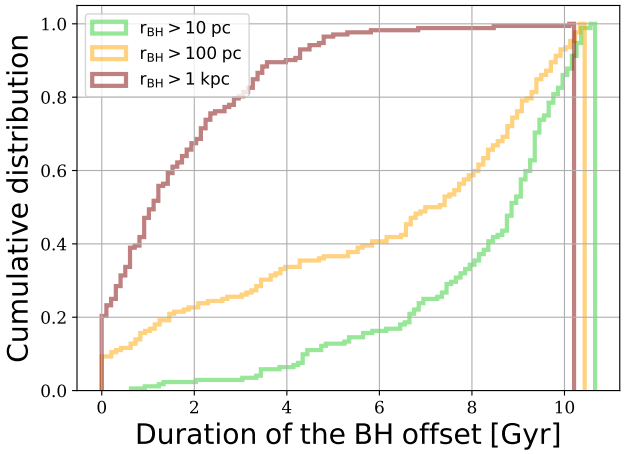

Figure 5. *Black hole offset time:* Cumulative histogram of the total duration of our 170 BHs with an offset > 10, 100 and 1000 pc since $z = 2$. A huge percentage 85% (60%) of the BCGs exhibit a SMBH off-centered with $r >$ 10 pc ($r > 100$ pc) for at least 6 Gyrs. Besides, these BHs spend less than 3 Gyrs above 1 kpc.

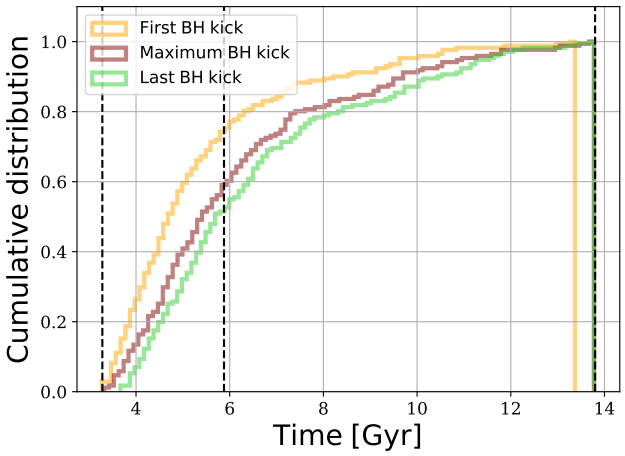

Figure 6. *Offset epochs:* Cumulative histograms showing the times when the first (yellow), the maximum (maroon) and the last (green) kick happened. The vertical black dashed lines show z=2, 1 and 0. 70% of our 170 BHs experienced their first kick before $z = 1$. The merger which kicked the central SMBH to the maximum distance does not take place at a particular time since $z = 2$, but still happens much earlier than the last merger. 65% of the clusters have undergone their last mergers after $z = 1$. That is the reason why it is very likely that SMBHs in BCGs are still off-centered at $z = 0$.

(1) and (2)), but their rareness does not invalidate their efficiency in displacing the BH of BCGs. That is the reason why almost half of BHs (~170) of our sample were off-centered during their orbital history. Some of the more massive satellites also appear to not have decentered the BH, as indicated by the orange island of points. Out of all mergers with a stellar mass ratio $M_*^{\rm sat} > M_*^{\rm BCG}/100$, 220 satellites kicked away the BHs from their central positions, but still, 3280 satellites did not affect the central BH. Those that did not manage to move the BH are mainly massive satellites which did not satisfy Equation (1), i.e. their orbits are not radial. A small fraction of these massive satellites actually have a radial orbit (5%), but the BH was still off-centered at the moment of the merger and was thus not affected. Thus, we predict two different populations of BHs: those that have resided at the centre of their BCGs and those that have been off-centered. Hence, we expect that these BHs exhibit differences in accretion, growth and feedback.

For all the 170 BHs heated by satellite galaxies, we analyse their orbit between $z = 2$ and $z = 0$. Figure 4 shows the cumulative distribution of the SMBH offset at $z = 0$ and the maximum offset measured since $z = 2$. In almost all BCGs, the SMBH is still off-

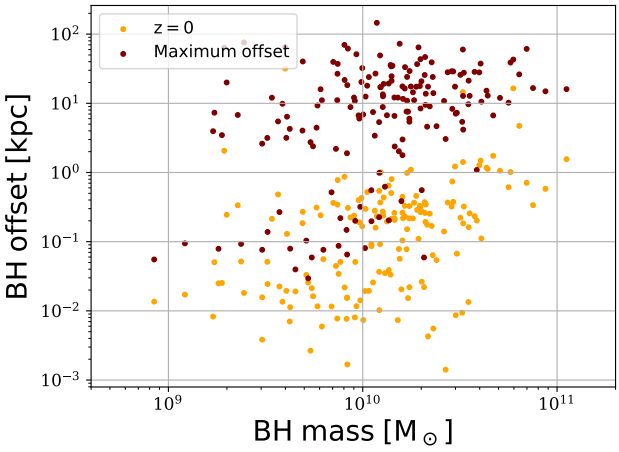

Figure 7. *Dynamical friction on black holes:* BH offset as a function of its mass at $z = 0$ (yellow dots) and at the time of the maximum offset (maroon dots). More massive BH exhibits larger offsets than less massive ones because dynamical friction acting on BHs becomes significantly weaker as the total galaxy mass grows.

centered at $z = 0$. About 60% of these SMBHs are located at $r > 0.1$ kpc at present time, and almost all SMBHs were off-centered by at least 1 kpc during their dynamical history. The maximum offset reached by these BHs is about 200 kpc (see Figure 4). We also demonstrate that even if BHs have been significantly displaced at a specific redshift, BHs have sufficient time to decrease their offset.

We now evaluate the time spent by the SMBH at distances longer than 10, 100 and 1000 pc from the BCG center. Figure 5 illustrates the cumulative histogram of the duration of the SMBH offset. We state that 85% (60%) of the BCGs exhibit a SMBH with an offset of 10 pc (100 pc) for more than 6 Gyr since $z = 2$. This means that SMBHs in BCGs spent more than half of their lifetime off-centered. We also notice that these BHs spend less than 3 Gyrs above 1 kpc.

Besides, we show on Figure 6 the cumulative distribution of the specific times at which the first merger, the merger which has led to the maximum offset, and the last merger happened. We establish that 70% of our 170 BHs experienced their first kick before $z = 1$. Hence, SMBHs do not inhabit the center of the BCG potential already at early times of the Universe. Most of BHs have undergone their most important merger in terms of dynamical heating, i.e. the one that displaces the most our BHs, after $z = 1$, but much earlier than their last mergers. We then establish that the energy given by subsequent mergers is one of the key ingredient that permits BHs to reach these far distances of the order of a tens of kpc. More precisely, as a result of the first merger, BHs gain energy from the satellite by changing its velocity according to Equation (3). Before the second kick, BHs have eccentric orbits and thus are more energetic. This dynamical behaviour allows them to reach velocities which are higher than the escape velocity computed at their position, until large radius from the galaxy centre. Finally, we demonstrate that 65% of the clusters have undergone their last mergers after $z = 1$. This phenomenon naturally explains why it is very likely that SMBHs in BCGs are still off-centered at $z = 0$. Indeed, these BHs do not have a sufficient time to loose their angular momentum via dynamical friction and then reach the central region of the galaxy, where they are expected to reside.

Finally, Figure 7 displays the BH offset as a function of the BH mass, both at $z = 0$ and at the time the SMBH suffered its most significant kick. We recall that M_{BH} was fixed at the mass derived from the BCG mass at the first T_d. We report a correlation between BH mass and its offset. Indeed, more massive BH exhibits larger offsets than less massive ones at $z = 0$. As a result, it is more likely to find off-centered SMBHs in the most massive BCGs. In the hierarchical structure formation model, the density at the centre decreases as the total galaxy mass grows. In fact, dynamical friction acting on BHs becomes significantly weaker and then BHs take more time to sink towards the centre of their BCGs, as demonstrated in Figure 7.

4 DISCUSSION

BH offsets of a few dozen parsecs were shown to have huge consequences on the physics that reign at the center of galaxies (Smith et al. 2018; Bahé et al. 2022). Even at such small distances, Boldrini et al. (2020) have pointed out that accretion by the SMBH in dwarf galaxies would become inefficient, due to the lower density of gas at higher radii from the center. Smith et al. (2018) indicated that this might also be the case for more massive galaxies, such as BCGs.

Our results clearly establish that SMBH offsets are common in BCGs as they have undergone frequent dynamical perturbations. Indeed, about a third of our SMBH sample are off-centred at the present time, and half of SMBHs were off-centered by at least 1 kpc during their dynamical history. Similarly to what was shown for dwarf galaxies (Bellovary et al. 2021), we demonstrate that the reason for off-center locations is also mainly due to galaxy-galaxy mergers and more precisely mergers with satellites on radial orbits. The orbital offset in BCGs can sustain up to at least 6 Gyr between $z = 2$ and $z = 0$ in half of our BCGs. Our result reinforces the prediction of a population of off-centered BHs, not only in dwarf galaxies (Governato et al. 1994; Rashkov & Madau 2014; Micic et al. 2011; Islam et al. 2004; Volonteri et al. 2003; Schneider et al. 2002; Bellovary et al. 2018; Boldrini et al. 2020), but also in very massive galaxies such as BCGs.

The fact that half of our SMBHs spend almost all their dynamical history offset from the BCG center should have major consequences on the BH and galaxy formation and evolution as there is an interplay between the feeding/feedback mechanisms of the SMBH and the host galaxy (Silk & Rees 1998). In particular, it was pointed out that BHs must intersect with a highly accretable clump at some time in order to accrete gas efficiently (Smith et al. 2018). Hence, as off-centered BHs seems to be very common in BCGs, we expect that they accrete gas very inefficiently as gas clumps are centrally located. As a result, off-centered BHs should experience essentially no growth at all. It was already demonstrated that in cosmological simulations, SMBH offset has a dramatic effect on BH growth (Bahé et al. 2022). It is established that SMBHs gain mass via gas accretion (Soltan 1982; Rees 1978) and via BH mergers. Even if BH mergers are strongly subdominant to gas accretion for SMBHs (Ni et al. 2022; Zhang et al. 2021), we pointed out that both mechanisms are effectively halted by mergers of satellites on radial orbits in BCGs.

According to our results, we expect that growth and feedback for a non-negligible SMBH population in BCGs was quenched between $z = 2$ and $z = 1$ until $z = 0$. For this reason, we predict the presence of a population of SMBHs with very different masses. It will result in a larger scatter in mass compared to what cosmological simulations predict. However, observations of BHs show the presence of a scatter around the M_{BH} - M_{BCG} relation (Gaspari et al. 2019; Bogdán et al. 2018; Savorgnan et al. 2016; Main et al. 2017; McConnell & Ma 2013a). Such scatter is evidence of the complex co-evolution of

SMBHs with their host galaxies in clusters (Volonteri et al. 2021). In particular, we establish that the growth of these SMBHs seems to be governed by one property of their host clusters, i.e. the number of satellites on radial orbits.

The absence of gas accretion by the SMBHs will also obviously influence their feedback (Heckman & Best 2014). If the SMBHs is not accreting, BH feedback also becomes inefficient. Nevertheless, it is well established that the BH feedback can alter the DM distribution of galaxies. In fact, the repeating episodes of gas ejection and recycling can flatten the cuspy DM profile until the formation of a constant density in the central region of galaxies, called the DM core. This effect on the DM profile has been studied in massive galaxies in the Horizon-AGN simulation (Peirani et al. 2017, 2019) and in the NIHAO-AGN simulations (Macciò et al. 2020).They showed that BH feedback can very slightly flatten the DM profile of BCGs. Our result, i.e the quenching of BH feedback due the BH offset, reinforces the prediction concerning the inefficiency of this mechanism to create DM cores in massive galaxies such as BCGs.

This work highlights a major problem encountered in simulations which pin the SMBH to the center of potential of the cosmological box (Bahé et al. 2021). Doing so has many advantages: keeping the BH at the center renders sub-grid AGN models effective, and this ensures that the initial merger-driven growth of BHs can proceed rapidly as this early phase is highly uncertain. This also avoids the question of dynamical friction, which is still treated poorly within simulations (Morton et al. 2021). This results in higher accretion rates, overestimated BH growth and higher counts of BH-BH mergers (see Bahé et al. 2021; Barausse et al. 2020, and references therein). We confirm that BH repositioning in simulations (see Section 2.2 of Weinberger et al. 2017, which details the repositioning of the BH in the TNG simulation) is nonphysical and show the need of new repositioning and dynamical friction models in order to correctly model the dynamics in galaxy clusters. There have now been many efforts on testing and incorporating dynamical friction from gas and stars in cosmological simulations (e.g Tremmel et al. 2015; Pfister et al. 2019; Chen et al. 2022), which do produce off-center SMBHs.

5 CONCLUSION

Making use of the work of Barnes et al. (2018), we study how satellites affect the dynamics in the central region of 370 different BCGs from the TNG300 simulation, between redshift $z = 2$ and $z = 0$. By using orbital integration methods, we show how galaxies which fall in the potential of the BCG can heat dynamically the center of BCGs, and kick away the central SMBH to distances from a few parsecs up to a hundred kiloparsecs. Our study demonstrates that half of SMBHs in BCGs, more particularly those in the most massive galaxies, were kicked away since $z = 2$, but only a third are still off-centered by more than 200 pc today. These BHs spent most of their lives outside the central region of their host, which has consequences on the physics that reign at the center of clusters.

As gas is mostly condensed in the center of galaxies, BHs, if offcentered, do not encounter as many gas clumps. As a result, BHs can not accrete gas efficiently. Consequently, the growth of SMBH may have been overestimated. Indeed, the lack of efficient accretion means that they do not gain much mass in their lifetime. As the central SMBH can not accrete matter efficiently, AGN feeback also becomes inefficient.

Following this study, analyzing how mergers can affect the distribution of DM in the central regions of BCGs might also be an interesting subject of research. Indeed, the multiple passage of satellites in the central region of BCGs may be responsible for ejecting DM out of the center of the galaxy, resulting in the flattening of the central DM density.

The presence of such a population of offcentered BHs in BCGs brings up the question of their detections and the identification of BCGs which may host a SMBH which has been kicked away in the recent past. Traces in the morphology of the BCG such as stellar tails or streams may hint at the passage of a massive satellite and thus at a recent merger. Observations of the central regions of these galaxies with integral field units such as the Multi Unit Spectroscopic Explorer (MUSE) may enable us to pinpoint the location of a potential offcentered BH by looking for the presence of a broadline region, characteristic of Seyfert galaxies or associated with the presence of an AGN (Gaskell 2009). This is still a challenging project as Elitzur et al. (2014) show that the broadline emission decreases as the accretion rate of the BH decreases as well. If offcentered, we would thus not expect an intense emission.

In this paper, we only considered the central BH of the BCG. However, satellites may harbor a SMBH as well in their centers. We could thus expect a population of wandering BHs of different masses in the BCG. The characterization of this population of BHs and the knowledge of their orbits in the potential of the BCGs may give us a better idea of the rate of BH-BH mergers observed in the future.

ACKNOWLEDGEMENTS

We thank Josh Borrow and Mark Vogelsberger for providing the Illustris data, and for useful comments. We also thank Florence Durret, Warren Massonneau and Yohan Dubois for fruitful discussions concerning this project. This work was supported by the EXPLOR-AGRAM Inria AeX grant.

DATA AVAILABILITY

The data that support the plots within this paper and other findings of this study are available from the corresponding author upon reasonable request.

REFERENCES

Bahé Y. M., et al., 2022, MNRAS, 516, 167
Bahé Y. M., et al., 2021, The importance of black hole repositioning for galaxy formation simulations, doi:10.48550/ARXIV.2109.01489, https://arxiv.org/abs/2109.01489
Barausse E., Dvorkin I., Tremmel M., Volonteri M., Bonetti M., 2020, ApJ, 904, 16
Barnes D. J., et al., 2018, MNRAS, 481, 1809
Barth A. J., Strigari L. E., Bentz M. C., Greene J. E., Ho L. C., 2009, ApJ, 690, 1031
Bellovary J. M., Cleary C. E., Munshi F., Tremmel M., Christensen C. R., Brooks A., Quinn T. R., 2018, Monthly Notices of the Royal Astronomical Society, 482, 2913
Bellovary J. M., Cleary C. E., Munshi F., Tremmel M., Christensen C. R., Brooks A., Quinn T. R., 2019, MNRAS, 482, 2913
Bellovary J. M., et al., 2021, Monthly Notices of the Royal Astronomical Society, 505, 5129
Bernardi M., Hyde J. B., Sheth R. K., Miller C. J., Nichol R. C., 2007, AJ, 133, 1741
Bogdán Á., Lovisari L., Volonteri M., Dubois Y., 2018, ApJ, 852, 131
Boldrini P., 2020, MNRAS, 498, L31
Boldrini P., Mohayaee R., Silk J., 2020, Monthly Notices of the Royal Astronomical Society: Letters, 495, L12–L16

Bovy J., 2015, ApJS, 216, 29
Burke C., Collins C. A., 2013, MNRAS, 434, 2856
Castignani G., Pandey-Pommier M., Hamer S. L., Combes F., Salomé P., Freundlich J., Jablonka P., 2020, A&A, 640, A65
Chen N., Ni Y., Tremmel M., Di Matteo T., Bird S., DeGraf C., Feng Y., 2022, MNRAS, 510, 531
Chu A., Durret F., Márquez I., 2021, A&A, 649, A42
Chu Sarron Durret Márquez 2022, A&A, 666, A54
Collins C., et al., 2009, Nature, 458, 603
Comerford J. M., Greene J. E., 2014, ApJ, 789, 112
Crawford C. S., Allen S. W., Ebeling H., Edge A. C., Fabian A. C., 1999, MNRAS, 306, 857
De Lucia G., Blaizot J., 2007, Monthly Notices of the Royal Astronomical Society, 375, 2–14
Dubinski J., 1998, The Astrophysical Journal, 502, 141
Elitzur M., Ho L. C., Trump J. R., 2014, Monthly Notices of the Royal Astronomical Society, 438, 3340
Gaskell C. M., 2009, New Astronomy Reviews, 53, 140
Gaspari M., et al., 2019, ApJ, 884, 169
Goerdt T., Moore B., Read J. I., Stadel J., 2010, ApJ, 725, 1707
Governato F., Colpi M., Maraschi L., 1994, MNRAS, 271, 317
Gültekin K., et al., 2009, ApJ, 698, 198
Heckman T. M., Best P. N., 2014, ARA&A, 52, 589
Hlavacek-Larrondo J., Fabian A. C., Edge A. C., Hogan M. T., 2012, MNRAS, 424, 224
Hlavacek-Larrondo J., et al., 2015, ApJ, 805, 35
Islam R. R., Taylor J. E., Silk J., 2004, MNRAS, 354, 427
Komossa S., 2012, Advances in Astronomy, 2012, 364973
Kormendy J., Bender R., 1999, ApJ, 522, 772
Kormendy J., Ho L. C., 2013, ARA&A, 51, 511
Kravtsov A. V., Borgani S., 2012, Annual Review of Astronomy and Astrophysics, 50, 353–409
Lauer T. R., Postman M., Strauss M. A., Graves G. J., Chisari N. E., 2014, The Astrophysical Journal, 797, 82
Loeb A., 2007, Phys. Rev. Lett., 99, 041103
Macciò A. V., Crespi S., Blank M., Kang X., 2020, MNRAS, 495, L46
Magorrian J., et al., 1998, AJ, 115, 2285
Main R. A., McNamara B. R., Nulsen P. E. J., Russell H. R., Vantyghem A. N., 2017, MNRAS, 464, 4360
Marinacci F., et al., 2018, Monthly Notices of the Royal Astronomical Society
Marleau F. R., Clancy D., Bianconi M., 2013, MNRAS, 435, 3085
McConnell N. J., Ma C.-P., 2013a, ApJ, 764, 184
McConnell N. J., Ma C.-P., 2013b, The Astrophysical Journal, 764, 184
McConnell N. J., Ma C.-P., Gebhardt K., Wright S. A., Murphy J. D., Lauer T. R., Graham J. R., Richstone D. O., 2011, Nature, 480, 215
Mehrgan K., Thomas J., Saglia R., Mazzalay X., Erwin P., Bender R., Kluge M., Fabricius M., 2019, ApJ, 887, 195
Menezes R. B., Steiner J. E., Ricci T. V., 2014, ApJ, 796, L13
Menezes R. B., Steiner J. E., da Silva P., 2016, ApJ, 817, 150
Merritt D., Milosavljević M., 2005, Living Reviews in Relativity, 8, 8
Micic M., Holley-Bockelmann K., Sigurdsson S., 2011, MNRAS, 414, 1127
Morton B., Khochfar S., Oñorbe J., 2021, arXiv e-prints, p. arXiv:2103.15848
Naab T., Johansson P. H., Ostriker J. P., 2009, ApJ, 699, L178
Naiman J. P., et al., 2018, Monthly Notices of the Royal Astronomical Society, 477, 1206
Nelson D., et al., 2017, Monthly Notices of the Royal Astronomical Society, 475, 624
Nelson D., et al., 2018, The IllustrisTNG Simulations: Public Data Release, doi:10.48550/ARXIV.1812.05609, https://arxiv.org/abs/1812.05609
Ni Y., et al., 2022, MNRAS, 513, 670
Peirani S., et al., 2017, MNRAS, 472, 2153
Peirani S., et al., 2019, MNRAS, 483, 4615
Pfister H., Volonteri M., Dubois Y., Dotti M., Colpi M., 2019, MNRAS, 486, 101
Pillepich A., et al., 2017, Monthly Notices of the Royal Astronomical Society, 475, 648
Rashkov V., Madau P., 2014, ApJ, 780, 187
Read J. I., Wilkinson M. I., Evans N. W., Gilmore G., Kleyna J. T., 2006, MNRAS, 366, 429
Rees M. J., 1978, in Berkhuijsen E. M., Wielebinski R., eds, Vol. 77, Structure and Properties of Nearby Galaxies. p. 237
Reines A. E., Condon J. J., Darling J., Greene J. E., 2020, ApJ, 888, 36
Saglia R. P., et al., 2016, ApJ, 818, 47
Sahu N., Graham A. W., Davis B. L., 2019, The Astrophysical Journal, 887, 10
Savorgnan G. A. D., Graham A. W., Marconi A., Sani E., 2016, ApJ, 817, 21
Schneider R., Ferrara A., Natarajan P., Omukai K., 2002, ApJ, 571, 30
Shen Y., Hwang H.-C., Zakamska N., Liu X., 2019, ApJ, 885, L4
Silk J., Rees M. J., 1998, A&A, 331, L1
Smith B. D., Regan J. A., Downes T. P., Norman M. L., O'Shea B. W., Wise J. H., 2018, Monthly Notices of the Royal Astronomical Society, 480, 3762
Sohn J., Geller M., Vogelsberger M., Borrow J., 2022
Soltan A., 1982, MNRAS, 200, 115
Springel V., et al., 2017, Monthly Notices of the Royal Astronomical Society, 475, 676
Sundararajan P. A., Khanna G., Hughes S. A., 2010, Phys. Rev. D, 81, 104009
Thomas D., Maraston C., Schawinski K., Sarzi M., Silk J., 2010, Monthly Notices of the Royal Astronomical Society, 404, 1775
Thomas J., Ma C.-P., McConnell N. J., Greene J. E., Blakeslee J. P., Janish R., 2016, Nature, 532, 340
Tremmel M., Governato F., Volonteri M., Quinn T. R., 2015, MNRAS, 451, 1868
Tremmel M., Governato F., Volonteri M., Pontzen A., Quinn T. R., 2018, ApJ, 857, L22
Volonteri M., Perna R., 2005, MNRAS, 358, 913
Volonteri M., Haardt F., Madau P., 2003, ApJ, 582, 559
Volonteri M., Habouzit M., Colpi M., 2021, Nature Reviews Physics, 3, 732
Weinberger R., et al., 2017, MNRAS, 465, 3291
Zhang T.-C., Guo Q., Qu Y., Gao L., 2021, Research in Astronomy and Astrophysics, 21, 212
van den Bosch R. C. E., 2016, ApJ, 831, 134

This paper has been typeset from a TEX/LATEX file prepared by the author.

Chapter 5

Conclusions and perspectives

In this thesis, I have worked on different aspects of the physics of Brightest Cluster Galaxies, from an observational point of view as well as from a numerical simulation point of view, in an attempt to better probe the formation and evolution of these special galaxies. Starting from galaxy clusters, to fossil groups, and finally to the central supermassive black holes of clusters, my work has covered a number of subjects related to extragalactic astronomy.

5.1 Summary

In Chapter 2, I describe the analysis of the two different BCG samples that we built. The first one is a sample of 149 BCGs observed with HST at redshifts 0.1 - 1.8. This represents one of the largest samples of BCGs in the literature that covers almost all the cluster history since its formation and with such exquisite resolution. The second sample consists in 1371 clusters detected in the CFHTLS with redshifts between 0.1 - 0.7. This sample is remarkable thanks to its big size, which allows statistically significant studies.

First, I developed new tools in order to detect BCGs automatically on optical and near infrared images, obtained from spatial or ground-based observatories. Two methods were used in order to take into account the nature of the cluster redshift: spectroscopic or photometric. We show that these methods are quite effective, as we manage to detect successfully all red BCGs in the HST sample and about two-thirds of the BCGs in the CFHTLS sample. I then modeled these galaxies with the `GALFIT` fitting algorithm. I automatized this step as well so that masks, PSFs, initial photometry and then profile fitting could be done on a large number of galaxies with minimal human intervention. The results of these studies show that the physical properties of BCGs do not evolve much since z = 1.8, and we conclude that BCGs were most likely formed before 10 Gyrs ago. Interestingly, although their sizes or luminosities do not grow significantly in that time lapse, their structures may have changed through time. Indeed, we count more galaxies whose luminosity profiles can be modeled by two Sérsic profiles rather than one at lower redshift. We suspect that this is mainly due to an observational bias due to the depth of the surveys instead of a real evolution in their structures. Studies by De Lucia and Blaizot (2007), Bai et al. (2014) or Edwards et al. (2019) suggest an inside-out growth scenario in which the central region of BCGs forms first, and then the outer regions of the galaxies grow through dry mergers. From Chu, Durret, and Márquez (2021), we would expect the inner component (the central region) of the BCG to have already been in place by z = 1.8, as we do observe two-component BCGs already at these times. However, the depth of our surveys does not enable us to estimate the evolution of the

fraction of two-Sérsic BCGs over the whole population of BCGs over time. Such a study would allow to estimate when the core and then the outskirts of these bright galaxies formed.

We also reduce the scatter in the Kormendy relation, and show that the scaling relations for BCGs over all redshifts up to $z = 0.7$ and $z = 1.8$ are very well defined with little dispersion, which is useful on a cosmological point of view to test models. We confirm that BCGs have a strong tendency to align with the major axis of their host clusters, with an alignment fraction within 30 degrees of 70% in Chu, Durret, and Márquez (2021). This can be taken as evidence for the effect of mergers on the central galaxy. From our samples, we estimate a fraction of less than 9% of blue BCGs over the total population of observed BCGs which tend to be mainly at $z > 0.4$. The subject of ICL is also considered to estimate how much this faint component can modify the luminosity profiles of BCGs and thus, bias their photometric properties.

We focus on the peculiar groups that are Fossil Groups in Chapter 3. We increase the number of candidate and confirmed FGs to better infer why and in which aspects these groups evolved differently from their peers. We characterize the physical properties of FG BGGs and compare them with those of non-FG BGGs. We show that FG BGGs tend to have brighter surface brightnesses and luminosities than BGGs of non-FGs, and that their formation is more comparable to that of BCGs of clusters than that of BGGs of non-FGs, as infered from the Kormendy relation. These results are valid considering or not the ICL in the analysis. Consequently, we suggest that FGs may have formed long ago in a similar fashion as clusters, with FG BGGs cannibalizing all the bright galaxies of the group, and then stopping their evolution, as their environment was not rich enough to bring other galaxies or groups in the vicinity of the FG. The stellar populations of the BGGs of FGs and non-FGs, as deduced from spectra-fitting with the FIREFLY code, show no clear difference of evolution between the two. We conclude that FGs and non-FGs may have evolved differently as inferred by their different morphologies and physical properties, but still have comparable stellar histories.

Finally, we discuss in Chapter 4 the impact of galaxy mergers on the central regions of BCGs, according to simulations. Based on a sample of 370 galaxy clusters identified in the Illustris-TNG300 simulation, we find that radial mergers, although not numerous in the whole history of the galaxy, can kick away the central SMBH from the center of the BCG, to distances ranging from a few parsecs to hundreds of kiloparsecs. Half of BCGs had their SMBHs displaced at least once since the last 10 Gyrs, and these SMBHs have for the most part spent the majority of their lives off-centered. As a result, because of the lack of accretion as they moved to less dense environments, these SMBHs would not be able to grow and the inefficient accretion leads to inefficient feedback as well. Consequently, we suggest that the mass of SMBHs in simulations and the importance of AGN feedback may be overestimated in cosmological models which try to explain the formation of galaxies.

5.2 Perspectives

The work presented in this thesis can still be improved and pushed further in many ways. Machine learning could be implemented in the detection method to make it more robust and at the same time attempt to characterize and classify the detected BCGs according to their physical properties and morphologies. Even without machine learning, though, these algorithms may be applied to future large surveys in order to increase significantly the statistics on the number of

identified BCGs. In particular, we look forward to the future Euclid and LSST missions that will detect about one hundred thousand clusters in the visible and near infrared range and enable us to complete cluster catalogs at lower redshifts.

Euclid is the future spatial telescope developed by the European Space Agency (ESA) and the Euclid consortium, expected to be launched next year, in 2023. It will observe in the visible to the near-infrared wavelengths, with the aim of observing and analyzing the shapes of galaxies through time (up to $z \approx 2$). This will enable researchers to better constrain DM and understand how it affected the expansion of the Universe and how structures formed. Euclid will survey 15000 $\deg^2$ of the sky, and will detect billions of galaxies, ten of thousands of galaxy clusters and groups, while providing us with multi-band photometry from ground-based surveys for the estimation of photometric redshifts.

The Rubin-LSST is an astronomical observatory located in Chile which aims to survey the entire southern sky with an 8 meter telescope every ten days, allowing to observe fainter and fainter objects at each iteration over the next decade. Ultimately, the survey will provide images with unprecedented depth.

These future surveys will enable us to obtain deep images of the whole sky and thus to better estimate the fraction of 2-Sérsic BCGs and more specifically, to better constrain the epoch of formation of the core and external regions of these galaxies. Although the inside-out scenario of structure formation is widely accepted now, observationally, more works have to be carried out to confirm this even further. It might also be worth verifying if two-component BCGs have an inner structure that is linked with the presence of an AGN. Cross-correlating our BCG catalogues with catalogues of radio sources may be the next step of this study. Moreover, Euclid and LSST, thanks to their depth, will allow the detection of ICL. The ICL fraction may be estimated with higher accuracy to better understand the impact of mergers on the central galaxy. It may also be interesting to study how would compare the ICL in fossil groups and rich clusters, given the different evolutionary histories of these environments. LSST wil also bring a unique capability in studying filaments, and comparing the location of FGs, groups and clusters in the cosmic web might be a very interesting future project.

We also look forward to the future James Webb Space Telescope (JWST) surveys, which will complete observations in the infrared up to 28.3 μm with excellent resolution. The successor of the Hubble Space Telescope will enable us to go back to the first galaxies in the Universe, up to the epoch of reionization. As mentioned in Chapter 2, apart from the shallow depth of our images, another problem lies in the choice of the filter used to model these massive galaxies. In order to carry on a homogeneous study of the red stellar population of BCGs, the same rest-frame wavelength interval needs to be modeled. However, at higher redshift especially ($z > 1.0$), data in the near infrared filters of the HST WFC3 instrument although appropriate, are not often available in the archive. We can hope with the JWST NIRCam and MIRI near and mid-infrared imager instruments to complete observations of clusters at the redder wavelengths. The sky coverage of the JWST, compared to Euclid or LSST, will not enable us to obtain big surveys in the infrared with good resolution; but pointed observations can enable us to complement data obtained with HST.

The main expectation however is the discovery and confirmation of proto-clusters, the progenitors of galaxy clusters, up to $z = 6$. I would be very interested in extending our study on the characterization of BCGs of clusters to brightest galaxies of proto-clusters, in the hope of determining since when did clusters start forming and stopped evolving. This is also very interesting

from a cosmological point of view, in order to establish how clusters were formed. Via a hierarchical evolution scenario, clusters are expected to have formed via the assembling of several groups and galaxies together over time. We may also wonder if the BCG was already formed as the cluster came together. The existence of BCGs in proto-clusters is a strong test of the early formation paradigm of BCGs.

In our samples, we identified 2% of blue BCGs in our HST sample and 9% in our CFHTLS sample. The existence of these blue BCGs is rather surprising considering that most BCGs are red quescient galaxies, so the question of the processes which triggered star formation can be brought up. Our subsample of about 89 blue BCGs from the CFHTLS may be subject to another study to analyze better their morphologies and estimate their stellar content.

As mentioned in Chapter 3, the work presented in this manuscript is still not complete. Indeed, those are only preliminary, as we only considered 30 out of 100 non-FGs as a first test to compare the stellar populations of FG and non-FG BGGs. The remaining non-FGs need to be included in this study.

Another project concerning FGs is currently in progress. This work consists in the analysis of fossil groups detected by Sarron et al. (2018) in the CFHTLS. As only photometric redshifts are available for this catalogue, the fossil groups here are only candidates. In the aim of building a bigger sample of confirmed fossil groups, we proceeded to observe 14 FG candidates, with observations still on-going today, with the Nordic Optical Telescope at La Palma with the ALFOSC spectrograph instrument, with the 2.2m telescope at Calar Alto mounted with the CAFOS instrument, or at the Observatoire de Haute Provence, France, with the MISTRAL instrument. Our observations have been limited to bright BGGs as we only used 2-meter class telescopes so far. We are in the process of asking for observing time with 4-meter class telescopes such as the TNG telescope at La Palma to obtain the spectra of fainter galaxies and potentially higher-z BGGs. However, even if we were to measure similar redshifts between the first and second ranked galaxy of the groups with a magnitude gap of 2 magnitudes (first condition), this would not be enough to confirm the fossil nature of the group, since the second condition requires a high X-ray luminosity. Our catalogues are thus to be cross-correlated with XMM-Newton catalogues to retrieve the X-ray luminosity if available. For fossil group candidates which satisfy the first condition and that do not have X-ray data, we plan to submit observation proposals with XMM-Newton to fill in the gaps.

We also aim to measure emission lines of any BGG that would show signs of star formation. The future survey obtained from observations with the Dark Energy Spectroscopic Instrument (DESI) instrument should allow the detection of many fossil groups. DESI is attached to the 4-meter Mayall telescope at the Kitt Peak National Observatory. It will provide us with the spectra of tens of millions of galaxies and other distant objects. DESI will thus give us a detailed 3D map of the Universe which will go back up to 11 Gyrs ago.

Finally, X-ray data may also be retrieved for clusters which show traces of a recent merger, in hope of detecting an off-center SMBH. The first hint would be an offset between the BCG coordinates and the coordinates of the clusters measured on X-ray images. In Chu, Durret, and Márquez (2021), we find that all BCGs are off-centered by at least 1 kpc from the associated X-ray emission, with an offset reaching up to 330 kpc. The lower limit of 1 kpc can be explained by the Chandra resolution which does not enable us to resolve objects below this value at these redshifts.

The separation between the BCG and X-ray centers may be linked to the dynamical state of the

cluster at the moment the observation was made. I retrieved the central densities, cooling times or central entropies of clusters in Chu, Durret, and Márquez (2021) as derived from their X-ray emission. We find that the less dense the core of the cluster and/or the higher the central entropy, the more important the measured offset. Cool-core clusters, as defined by Hudson et al. (2010), are centrally dense and dynamically relaxed clusters, characterized by a low central entropy and, as hinted by its name, should have short cooling times. However, the distinction between cool-core systems and non cool-core systems is not obvious. Hudson et al. (2010) shows that the cooling time is the best indicator to distinguish between the different classes, and that it is correlated with the central entropy. They find that cool-core clusters present a systematic drop in their temperature profile, and generally have a brighter BCG located at the X-ray peak. On the other hand, what they call weak cool-core clusters, or transition clusters (medium cool-core clusters) tend to have a less significant drop in their temperature profiles, and a moderate central entropy, with a BCG that is moderately bright located near the X-ray peak. On the contrary, non cool-core clusters have flat temperature profiles and higher entropies. We might thus expect to observe off-centered SMBHs mainly in non cool-core clusters. This may be subject to a future paper.

A natural follow-up of this study would be to detect these off-center SMBHs via observations. X-rays may give us a clue at the presence of an off-centered SMBH, but this will not enable us to localize the position of the SMBH precisely. Indeed, the X-ray peak is not necessarily associated with the position of the SMBH; and the resolution of X-rays telescopes such as the Chandra X-ray Observatory or XMM-Newton will not enable us to resolve the center of clusters, and thus to localize the position of the SMBH under the kpc.

One way of solving this problem would be to use integral field units (IFUs) such as the Multi Unit Spectroscopic Explorer (MUSE) on the ESO Very Large Telescope (VLT) to map the BCG, and to look for the presence of an off-centered pixel relatively to the BCG center with a broadline emission in its spectrum. As broadline emission is linked to AGNs (Gaskell, 2009), this may give us a clue on the position of the SMBH in the cluster. However, MUSE may only enable us to resolve the central regions of BCGs below one kpc for relatively local BCGs. Using the Wide Field Mode with a field of view of 4' $\times$ 4', the resolution of a pixel is 1 kpc at $z = 0.35$, and is below 100 pc for $z < 0.03$. This mode may be used to observe the more massive BCGs which are more likely to present large offsets than less massive ones (see Section 4.2). The Narrow Field Mode may allow to resolve the centers at higher redshifts (resolution below 100 pc at $z < 0.26$) but the field of view will be much smaller than the Wide Field Mode (7.5" $\times$ 7.5"). This may also be used to resolve the centers of the less massive galaxies which may present smaller offsets between the galaxy center and the SMBH. Moreover, it is important to note that the intensity of the broadline emission decreases with decreasing accretion by the SMBH (Elitzur, Ho, and Trump, 2014). It may therefore be difficult to apply this method to detect off-center SMBHs which may not be associated with strong AGNs because of the lack of accretion. Although difficult and challenging, Chen et al. (2022) have managed to detect AGNs separated by more than a kpc from the center of their BCGs in high redshift galaxies. Catalogues of radio sources may also be retrieved to identify off-centered AGNs.

As mergers can disturb the central SMBH, it would also be interesting to study how they would affect the DM distribution in the center of the BCG, which can be done by retrieving the DM properties in Illustris. Indeed, such a study might help better understand and constrain the DM profile in clusters: as mergers happen and satellites fall in the potential of the BCG and pass

by the core, DM could be ejected.

Lastly, we might expect the existence of, not a single one, but a population of wandering SMBHs in clusters. Indeed, in this work, we only considered the SMBH of the BCG, but satellites may host SMBHs as well. It would thus be interesting to characterize this population of SMBHs in clusters. By integrating the orbits of the "main" SMBH of the BCG, and those of the SMBHs harbored by satellites as well, we might be able to better estimate the rate of SMBH-SMBH mergers which will be observed in the future.

Bibliography

Abell, G. O. (Jan. 1962). "Membership of Clusters of Galaxies". In: *Problems of Extra-Galactic Research*. Ed. by George Cunliffe McVittie. Vol. 15, p. 213.

Abell, George O. (May 1958). "The Distribution of Rich Clusters of Galaxies." In: 3, p. 211. DOI: 10.1086/190036.

Aguerri, J. Alfonso L. and Stefano Zarattini (May 2021). "Properties of Fossil Groups of Galaxies". In: *Universe* 7.5, p. 132. DOI: 10.3390/universe7050132. arXiv: 2106.13255 [astro-ph.CO].

Allen, Steven W., August E. Evrard, and Adam B. Mantz (2011). "Cosmological Parameters from Observations of Galaxy Clusters". In: *Annual Review of Astronomy and Astrophysics* 49.1, pp. 409–470. DOI: 10.1146/annurev-astro-081710-102514. eprint: https://doi.org/10.1146/annurev-astro-081710-102514. URL: https://doi.org/10.1146/annurev-astro-081710-102514.

Arnaboldi, M. et al. (Sept. 2012). "A tale of two tails and an off-centered envelope: diffuse light around the cD galaxy NGC 3311 in the Hydra I cluster". In: 545, A37, A37. DOI: 10.1051/0004-6361/201116752. arXiv: 1205.5289 [astro-ph.CO].

Arnouts, S. et al. (Dec. 1999). "Measuring and modelling the redshift evolution of clustering: the Hubble Deep Field North". In: 310.2, pp. 540–556. DOI: 10.1046/j.1365-8711.1999.02978.x. arXiv: astro-ph/9902290 [astro-ph].

Bacon, R., G. Monnet, and F. Simien (Nov. 1985). "Mass-to-light ratio of elliptical galaxies." In: 152, pp. 315–324.

Bahcall, Neta A. (Nov. 1974). "Optical Properties of X-Ray Clusters of Galaxies". In: 193, pp. 529–534. DOI: 10.1086/153190.

Bahcall, Neta A., Xiaohui Fan, and Renyue Cen (Aug. 1997). "Constraining Ω with Cluster Evolution". In: 485.2, pp. L53–L56. DOI: 10.1086/310814. arXiv: astro-ph/9706018 [astro-ph].

Bahé, Yannick M. et al. (2021). *The importance of black hole repositioning for galaxy formation simulations*. DOI: 10.48550/ARXIV.2109.01489. URL: https://arxiv.org/abs/2109.01489.

Bai, Lei et al. (2014). "The inside-out growth of the most massive galaxies at 0.3< z< 0.9". In: *The Astrophysical Journal* 789.2, p. 134.

Baldry, Ivan K. et al. (Jan. 2004). "Quantifying the Bimodal Color-Magnitude Distribution of Galaxies". In: 600.2, pp. 681–694. DOI: 10.1086/380092. arXiv: astro-ph/0309710 [astro-ph].

Barbosa, C. E. et al. (Jan. 2018). "Sloshing in its cD halo: MUSE kinematics of the central galaxy NGC 3311 in the Hydra I cluster". In: 609, A78, A78. DOI: 10.1051/0004-6361/201731834. arXiv: 1710.08941 [astro-ph.GA].

Barnes, David J. et al. (Dec. 2018). "A census of cool-core galaxy clusters in IllustrisTNG". In: 481.2, pp. 1809–1831. DOI: 10.1093/mnras/sty2078. arXiv: 1710.08420 [astro-ph.CO].

Baugh, C. (2000). "Correlation Function and Power Spectra in Cosmology". In: *Encyclopedia of Astronomy and Astrophysics*. Ed. by P. Murdin, 2136, p. 2136. DOI: 10.1888/0333750888/2136.

Baum, W. A. (Apr. 1959). "Population Inferences from Star Counts, Surface Brightness and Colors". In: 71.419, pp. 106–117. DOI: 10.1086/127346.

Bellstedt, Sabine et al. (May 2016). "The evolution in the stellar mass of brightest cluster galaxies over the past 10 billion years". In: *Monthly Notices of the Royal Astronomical Society* 460.3, p. 2862. ISSN: 0035-8711. DOI: 10.1093/mnras/stw1184. eprint: https://academic.oup.com/mnras/article-pdf/460/3/2862/13772859/stw1184.pdf. URL: https://doi.org/10.1093/mnras/stw1184.

Bender, Ralf et al. (July 2015). "Structure and Formation of cD Galaxies: NGC 6166 in ABELL 2199". In: 807.1, 56, p. 56. DOI: 10.1088/0004-637X/807/1/56. arXiv: 1411.2598 [astro-ph.GA].

Bertin, E. and S. Arnouts (June 1996). "SExtractor: Software for source extraction." In: 117, p. 393. DOI: 10.1051/aas:1996164.

Bertone, Gianfranco and Dan Hooper (2018). "History of dark matter". In: 90.4. DOI: 10.1103/revmodphys.90.045002. URL: https://doi.org/10.1103%2Frevmodphys.90.045002.

Binney, James (Oct. 1976). "Is the Flattening of Elliptical Galaxies Necessarily Due to Rotation?" In: *Monthly Notices of the Royal Astronomical Society* 177.1, pp. 19–29. ISSN: 0035-8711. DOI: 10.1093/mnras/177.1.19. eprint: https://academic.oup.com/mnras/article-pdf/177/1/19/9333245/mnras177-0019.pdf. URL: https://doi.org/10.1093/mnras/177.1.19.

Birkinshaw, Mark (1999). "The Sunyaev–Zel'dovich effect". In: *Physics Reports* 310.2, pp. 97–195. ISSN: 0370-1573. DOI: https://doi.org/10.1016/S0370-1573(98)00080-5. URL: https://www.sciencedirect.com/science/article/pii/S0370157398000805.

Biviano, Andrea (2000). *From Messier to Abell: 200 years of science with galaxy clusters*. DOI: 10.48550/ARXIV.ASTRO-PH/0010409. URL: https://arxiv.org/abs/astro-ph/0010409.

Boldrini, Pierre, Roya Mohayaee, and Joseph Silk (2020). "Subhalo sinking and off-centre massive black holes in dwarf galaxies". In: *Monthly Notices of the Royal Astronomical Society: Letters* 495.1, L12–L16. ISSN: 1745-3933. DOI: 10.1093/mnrasl/slaa043. URL: http://dx.doi.org/10.1093/mnrasl/slaa043.

Bovy, Jo (2015). "galpy: A python LIBRARY FOR GALACTIC DYNAMICS". In: *The Astrophysical Journal Supplement Series* 216.2, p. 29. DOI: 10.1088/0067-0049/216/2/29. URL: https://doi.org/10.1088/0067-0049/216/2/29.

Bruzual, G and Stephane Charlot (2003). "Stellar population synthesis at the resolution of 2003". In: *Monthly Notices of the Royal Astronomical Society* 344.4, p. 1000.

Carter, D. et al. (Apr. 1981). "The dynamics of the giant dumbell galaxy IC 2082." In: 195, 15P–20. DOI: 10.1093/mnras/195.1.15P.

Castignani, G. et al. (Aug. 2020). "Molecular gas in CLASH brightest cluster galaxies at z $\sim$ 0.2 - 0.9". In: 640, A65, A65. DOI: 10.1051/0004-6361/202038081. arXiv: 2004.01786 [astro-ph.GA].

Castro-Rodriguéz, N. et al. (2009). "Intracluster light in the Virgo cluster: large scale distribution*". In: *A&A* 507.2, pp. 621–634. DOI: 10.1051/0004-6361/200809774. URL: https://doi.org/10.1051/0004-6361/200809774.

Cattaneo, A. et al. (July 2009). "The role of black holes in galaxy formation and evolution". In: 460.7252, pp. 213–219. DOI: 10.1038/nature08135. arXiv: 0907.1608 [astro-ph.CO].

Cavaliere, A. G., H. Gursky, and W. H. Tucker (June 1971). "Extragalactic X-ray Sources and Associations of Galaxies". In: 231.5303, pp. 437–438. DOI: 10.1038/231437a0.

Cerulo, P, G A Orellana, and G Covone (2019). "The evolution of brightest cluster galaxies in the nearby Universe – I. Colours and stellar masses from the Sloan Digital Sky Survey and Wide

Infrared Survey Explorer". In: *Monthly Notices of the Royal Astronomical Society* 487.3, p. 3759. ISSN: 1365-2966. DOI: 10.1093/mnras/stz1495. URL: http://dx.doi.org/10.1093/mnras/stz1495.

Chandrasekhar, S. (Mar. 1943a). "Dynamical Friction. I. General Considerations: the Coefficient of Dynamical Friction." In: 97, p. 255. DOI: 10.1086/144517.

— (Mar. 1943b). "Dynamical Friction. II. The Rate of Escape of Stars from Clusters and the Evidence for the Operation of Dynamical Friction." In: 97, p. 263. DOI: 10.1086/144518.

— (July 1943c). "Dynamical Friction. III. a More Exact Theory of the Rate of Escape of Stars from Clusters." In: 98, p. 54. DOI: 10.1086/144544.

Chen, Yu-Ching et al. (2022). "Varstrometry for Off-nucleus and Dual Subkiloparsec AGN (VODKA): Hubble Space Telescope Discovers Double Quasars". In: *The Astrophysical Journal* 925.2, p. 162. DOI: 10.3847/1538-4357/ac401b. URL: https://doi.org/10.3847/1538-4357/ac401b.

Chu et al. (2022). "Physical properties of more than one thousand brightest cluster galaxies detected in the Canada-France-Hawaii Telescope Legacy Survey". In: *A&A* 666, A54. DOI: 10.1051/0004-6361/202243504. URL: https://doi.org/10.1051/0004-6361/202243504.

Chu, A., F. Durret, and I. Márquez (May 2021). "Physical properties of brightest cluster galaxies up to redshift 1.80 based on HST data". In: 649, A42, A42. DOI: 10.1051/0004-6361/202040245. arXiv: 2102.01557 [astro-ph.GA].

Clerc, N. et al. (July 2012). "The cosmological analysis of X-ray cluster surveys – I. A new method for interpreting number counts". In: *Monthly Notices of the Royal Astronomical Society* 423.4, pp. 3545–3560. ISSN: 0035-8711. DOI: 10.1111/j.1365-2966.2012.21154.x. eprint: https://academic.oup.com/mnras/article-pdf/423/4/3545/4910250/mnras0423-3545.pdf. URL: https://doi.org/10.1111/j.1365-2966.2012.21154.x.

Comparat, Johan et al. (2017). *Stellar population properties for 2 million galaxies from SDSS DR14 and DEEP2 DR4 from full spectral fitting*. DOI: 10.48550/ARXIV.1711.06575. URL: https://arxiv.org/abs/1711.06575.

Cooke, Kevin C. et al. (2019). "Stellar Mass Growth of Brightest Cluster Galaxy Progenitors in COSMOS Since z 3". In: *The Astrophysical Journal* 881.2, p. 150. ISSN: 1538-4357. DOI: 10.3847/1538-4357/ab30c9. URL: http://dx.doi.org/10.3847/1538-4357/ab30c9.

Cui, Weiguang et al. (2008). "An Ideal Mass Assignment Scheme for Measuring the Power Spectrum with Fast Fourier Transforms". In: *The Astrophysical Journal* 687.2, pp. 738–744. DOI: 10.1086/592079. URL: https://doi.org/10.1086/592079.

De Lucia, G. and J. Blaizot (2007). "The hierarchical formation of the brightest cluster galaxies". In: *Monthly Notices of the Royal Astronomical Society* 375.1, 2–14. ISSN: 1365-2966. DOI: 10.1111/j.1365-2966.2006.11287.x. URL: http://dx.doi.org/10.1111/j.1365-2966.2006.11287.x.

De Propris, Roberto et al. (2020). "Brightest cluster galaxies: the centre can(not?) hold". In: *Monthly Notices of the Royal Astronomical Society* 500.1, p. 310. ISSN: 1365-2966. DOI: 10.1093/mnras/staa3286. URL: http://dx.doi.org/10.1093/mnras/staa3286.

de Vaucouleurs, Gerard (Jan. 1961). "Integrated Colors of Bright Galaxies in the u, b, V System." In: 5, p. 233. DOI: 10.1086/190056.

DeMaio, Tahlia et al. (2019). "The growth of brightest cluster galaxies and intracluster light over the past 10 billion years". In: *Monthly Notices of the Royal Astronomical Society* 491.3, p. 3751. ISSN: 1365-2966. DOI: 10.1093/mnras/stz3236. URL: http://dx.doi.org/10.1093/mnras/stz3236.

Ding, Xuheng et al. (2022). "Concordance between Observations and Simulations in the Evolution of the Mass Relation between Supermassive Black Holes and Their Host Galaxies". In: *The Astrophysical Journal* 933.2, p. 132. DOI: 10.3847/1538-4357/ac714c. URL: https://doi.org/10.3847/1538-4357/ac714c.

D'Onghia, E. et al. (Sept. 2005). "The Formation of Fossil Galaxy Groups in the Hierarchical Universe". In: 630.2, pp. L109–L112. DOI: 10.1086/491651. arXiv: astro-ph/0505544 [astro-ph].

Dressler, A. (Aug. 1978). "A comprehensive study of 12 very rich clusters of galaxies. I. Photometric technique and analysis of the luminosity function." In: 223, pp. 765–787. DOI: 10.1086/156310.

— (Aug. 1979). "The dynamics and structure of the cD galaxy in Abell 2029." In: 231, pp. 659–670. DOI: 10.1086/157229.

— (Mar. 1980). "Galaxy morphology in rich clusters: implications for the formation and evolution of galaxies." In: 236, pp. 351–365. DOI: 10.1086/157753.

Durret, F. et al. (2019). "Link between brightest cluster galaxy properties and large scale extensions of 38 DAFT/FADA and CLASH clusters in the redshift range 0.2 < z < 0.9". In: *Astronomy & Astrophysics* 622, A78. ISSN: 1432-0746. DOI: 10.1051/0004-6361/201834374. URL: http://dx.doi.org/10.1051/0004-6361/201834374.

Edwards, Louise O V et al. (Sept. 2019). "Clocking the formation of today's largest galaxies: wide field integral spectroscopy of brightest cluster galaxies and their surroundings". In: *Monthly Notices of the Royal Astronomical Society* 491.2, pp. 2617–2638. ISSN: 0035-8711. DOI: 10.1093/mnras/stz2706. eprint: https://academic.oup.com/mnras/article-pdf/491/2/2617/31196256/stz2706.pdf. URL: https://doi.org/10.1093/mnras/stz2706.

Elitzur, Moshe, Luis C. Ho, and Jonathan R. Trump (Jan. 2014). "Evolution of broad-line emission from active galactic nuclei". In: *Monthly Notices of the Royal Astronomical Society* 438.4, pp. 3340–3351. ISSN: 0035-8711. DOI: 10.1093/mnras/stt2445. eprint: https://academic.oup.com/mnras/article-pdf/438/4/3340/3854200/stt2445.pdf. URL: https://doi.org/10.1093/mnras/stt2445.

Ellien, A. et al. (May 2021). "DAWIS: a detection algorithm with wavelets for intracluster light studies". In: 649, A38, A38. DOI: 10.1051/0004-6361/202038419. arXiv: 2101.03835 [astro-ph.GA].

Evrard, August E. (June 1989). "Biased Cold Dark Matter Theory: Trouble from Rich Clusters?" In: 341, p. L71. DOI: 10.1086/185460.

Faber, S. M. and R. E. Jackson (Mar. 1976). "Velocity dispersions and mass-to-light ratios for elliptical galaxies." In: 204, pp. 668–683. DOI: 10.1086/154215.

Fabian, A.C. (2012). "Observational Evidence of Active Galactic Nuclei Feedback". In: *Annual Review of Astronomy and Astrophysics* 50.1, pp. 455–489. DOI: 10.1146/annurev-astro-081811-125521. eprint: https://doi.org/10.1146/annurev-astro-081811-125521. URL: https://doi.org/10.1146/annurev-astro-081811-125521.

Ferrarese, Laura and David Merritt (Aug. 2000). "A Fundamental Relation between Supermassive Black Holes and Their Host Galaxies". In: 539.1, pp. L9–L12. DOI: 10.1086/312838. arXiv: astro-ph/0006053 [astro-ph].

Fogarty, Kevin et al. (2019). "The Dust and Molecular Gas in the Brightest Cluster Galaxy in MACS 1931.8-2635". In: *The Astrophysical Journal* 879.2, p. 103. ISSN: 1538-4357. DOI: 10.3847/1538-4357/ab22a4. URL: http://dx.doi.org/10.3847/1538-4357/ab22a4.

Frenk, Carlos S. et al. (Mar. 1990). "Galaxy Clusters and the Amplitude of Primordial Fluctuations". In: 351, p. 10. DOI: 10.1086/168439.

Gaskell, C. Martin (2009). "What broad emission lines tell us about how active galactic nuclei work". In: *New Astronomy Reviews* 53.7. Proceedings of the VII Serbian Conference on Spectral Line Shapes (VII SCSLSA) held in Zrenjanin, Serbia June 15th-19th 2009, pp. 140–148. ISSN: 1387-6473. DOI: https://doi.org/10.1016/j.newar.2009.09.006. URL: https://www.sciencedirect.com/science/article/pii/S1387647309000608.

Gavazzi, G. et al. (2010). "A snapshot on galaxy evolution occurring in the Great Wall: the role of Nurture at z". In: *A&A* 517, A73. DOI: 10.1051/0004-6361/201014153. URL: https://doi.org/10.1051/0004-6361/201014153.

Gebhardt, Karl et al. (Aug. 2000). "A Relationship between Nuclear Black Hole Mass and Galaxy Velocity Dispersion". In: 539.1, pp. L13–L16. DOI: 10.1086/312840. arXiv: astro-ph/0006289 [astro-ph].

Gil-Marín, Héctor et al. (May 2015). "The power spectrum and bispectrum of SDSS DR11 BOSS galaxies – I. Bias and gravity". In: *Monthly Notices of the Royal Astronomical Society* 451.1, pp. 539–580. ISSN: 0035-8711. DOI: 10.1093/mnras/stv961. eprint: https://academic.oup.com/mnras/article-pdf/451/1/539/4177830/stv961.pdf. URL: https://doi.org/10.1093/mnras/stv961.

Gott J. R., III and M. J. Rees (Dec. 1975). "A theory of galaxy formation and clustering." In: 45, pp. 365–376.

Gu, Meng et al. (2020). "Spectroscopic Constraints on the Buildup of Intracluster Light in the Coma Cluster". In: *The Astrophysical Journal* 894.1, p. 32. DOI: 10.3847/1538-4357/ab845c. URL: https://doi.org/10.3847/1538-4357/ab845c.

Gültekin, Kayhan et al. (June 2009). "The M-σ and M-L Relations in Galactic Bulges, and Determinations of Their Intrinsic Scatter". In: 698.1, pp. 198–221. DOI: 10.1088/0004-637X/698/1/198. arXiv: 0903.4897 [astro-ph.GA].

Hashimoto, Yasuhiro, J. Patrick Henry, and Hans Boehringer (2014). "Multiwavelength investigations of co-evolution of bright cluster galaxies and their host clusters". In: *Monthly Notices of the Royal Astronomical Society* 440.1, p. 588. ISSN: 0035-8711. DOI: 10.1093/mnras/stu311. URL: http://dx.doi.org/10.1093/mnras/stu311.

Hernquist, Lars (June 1990). "An Analytical Model for Spherical Galaxies and Bulges". In: 356, p. 359. DOI: 10.1086/168845.

Herschel, John Frederick William (Jan. 1864). "A General Catalogue of Nebulae and Clusters of Stars". In: *Philosophical Transactions of the Royal Society of London Series I* 154, pp. 1–137.

Herschel, William (Jan. 1785). "On the Construction of the Heavens." In: *Philosophical Transactions of the Royal Society of London Series I* 75, pp. 213–266.

Holmberg, E. (Jan. 1958). "A photographic photometry of extragalactic nebulae." In: *Meddelanden fran Lunds Astronomiska Observatorium Serie II* 136, p. 1.

Hubble, E. P. (Dec. 1926a). "Extragalactic nebulae." In: 64, pp. 321–369. DOI: 10.1086/143018.

— (Sept. 1927). "The classification of spiral nebulae". In: *The Observatory* 50, pp. 276–281.

— (1936). *Realm of the Nebulae*.

Hubble, Edwin. (Jan. 1926b). "No. 324. Extra-galactic nebulae." In: *Contributions from the Mount Wilson Observatory / Carnegie Institution of Washington* 324, pp. 1–49.

Hubble, Edwin (Mar. 1929). "A Relation between Distance and Radial Velocity among Extra-Galactic Nebulae". In: *Proceedings of the National Academy of Science* 15.3, pp. 168–173. DOI: 10.1073/pnas.15.3.168.

Hubble, Edwin and Milton L. Humason (July 1931). "The Velocity-Distance Relation among Extra-Galactic Nebulae". In: 74, p. 43. DOI: 10.1086/143323.

Hudson et al. (2010). "What is a cool-core cluster? a detailed analysis of the cores of the X-ray flux-limited HIFLUGCS cluster sample*". In: *A&A* 513, A37. DOI: 10.1051/0004-6361/200912377. URL: https://doi.org/10.1051/0004-6361/200912377.

Hütsi, G. (2006). "Power spectrum of the SDSS luminous red galaxies: constraints on cosmological parameters". In: *A&A* 459.2, pp. 375–389. DOI: 10.1051/0004-6361:20065377. URL: https://doi.org/10.1051/0004-6361:20065377.

Jedrzejewski, Robert and Paul L. Schechter (July 1989). "Minor-Axis Rotation in Elliptical Galaxies". In: 98, p. 147. DOI: 10.1086/115133.

Jiménez-Teja, Y. and N. Benítez (Feb. 2012). "A New Tool for Image Analysis Based on Chebyshev Rational Functions: CHEF Functions". In: 745.2, 150, p. 150. DOI: 10.1088/0004-637X/745/2/150. arXiv: 1104.0683 [astro-ph.IM].

Jiménez-Teja, Y. et al. (2019). "J-PLUS: Analysis of the intracluster light in the Coma cluster". In: *A&A* 622, A183. DOI: 10.1051/0004-6361/201833547. URL: https://doi.org/10.1051/0004-6361/201833547.

Jiménez-Teja, Y. and R. Dupke (2016). "DISENTANGLING THE ICL WITH THE CHEFs: ABELL 2744 AS A CASE STUDY". In: *The Astrophysical Journal* 820.1, p. 49. ISSN: 1538-4357. DOI: 10.3847/0004-637x/820/1/49. URL: http://dx.doi.org/10.3847/0004-637X/820/1/49.

Jiménez-Teja, Yolanda et al. (2018). "Unveiling the Dynamical State of Massive Clusters through the ICL Fraction". In: *The Astrophysical Journal* 857.2, p. 79. ISSN: 1538-4357. DOI: 10.3847/1538-4357/aab70f. URL: http://dx.doi.org/10.3847/1538-4357/aab70f.

Jones, L. R. et al. (Aug. 2003). "The nature and space density of fossil groups of galaxies". In: 343.2, pp. 627–638. DOI: 10.1046/j.1365-8711.2003.06702.x. arXiv: astro-ph/0304257 [astro-ph].

Kluge, M. et al. (2020). "Structure of Brightest Cluster Galaxies and Intracluster Light". In: *The Astrophysical Journal Supplement Series* 247.2, p. 43. ISSN: 1538-4365. DOI: 10.3847/1538-4365/ab733b. URL: http://dx.doi.org/10.3847/1538-4365/ab733b.

Kluge, M. et al. (2021). "Photometric Dissection of Intracluster Light and Its Correlations with Host Cluster Properties". In: *The Astrophysical Journal Supplement Series* 252.2, p. 27. DOI: 10.3847/1538-4365/abcda6. URL: https://doi.org/10.3847/1538-4365/abcda6.

Komatsu, E. et al. (Feb. 2011). "Seven-year Wilkinson Microwave Anisotropy Probe (WMAP) Observations: Cosmological Interpretation". In: 192.2, 18, p. 18. DOI: 10.1088/0067-0049/192/2/18. arXiv: 1001.4538 [astro-ph.CO].

Kormendy, J. (Dec. 1977). "Brightness distributions in compact and normal galaxies. II. Structure parameters of the spheroidal component." In: 218, p. 333. DOI: 10.1086/155687.

Kravtsov, Andrey V. and Stefano Borgani (2012). "Formation of Galaxy Clusters". In: *Annual Review of Astronomy and Astrophysics* 50.1, pp. 353–409. DOI: 10.1146/annurev-astro-081811-125502. eprint: https://doi.org/10.1146/annurev-astro-081811-125502. URL: https://doi.org/10.1146/annurev-astro-081811-125502.

Kundert, A., E. D'Onghia, and J. A. L. Aguerri (Aug. 2017). "Are Fossil Groups Early-forming Galaxy Systems?" In: 845.1, 45, p. 45. DOI: 10.3847/1538-4357/aa7b88. arXiv: 1706.08542 [astro-ph.GA].

Lauer, Tod R et al. (2014). "Brightest cluster galaxies at the present epoch". In: *The Astrophysical Journal* 797.2, p. 82.

Lee, Yun Hee, Hong Bae Ann, and Myeong-Gu Park (2019). "Bar Fraction in Early- and Late-type Spirals". In: *The Astrophysical Journal* 872.1, p. 97. DOI: 10.3847/1538-4357/ab0024. URL: https://doi.org/10.3847/1538-4357/ab0024.

Lidman, C. et al. (2012). "Evidence for significant growth in the stellar mass of brightest cluster galaxies over the past 10 billion years". In: *Monthly Notices of the Royal Astronomical Society* 427.1, p. 550. ISSN: 1365-2966. DOI: 10.1111/j.1365-2966.2012.21984.x. URL: http://dx.doi.org/10.1111/j.1365-2966.2012.21984.x.

Lin, Yen-Ting et al. (2013). "THE STELLAR MASS GROWTH OF BRIGHTEST CLUSTER GALAXIES IN THE IRAC SHALLOW CLUSTER SURVEY". In: *The Astrophysical Journal* 771.1, p. 61. ISSN: 1538-4357. DOI: 10.1088/0004-637x/771/1/61. URL: http://dx.doi.org/10.1088/0004-637X/771/1/61.

Loubser, S. I. et al. (June 2018). "Diversity in the stellar velocity dispersion profiles of a large sample of brightest cluster galaxies z $\leq$ 0.3". In: 477.1, pp. 335–358. DOI: 10.1093/mnras/sty498. arXiv: 1802.07745 [astro-ph.GA].

Magorrian, John et al. (June 1998). "The Demography of Massive Dark Objects in Galaxy Centers". In: 115.6, pp. 2285–2305. DOI: 10.1086/300353. arXiv: astro-ph/9708072 [astro-ph].

Mana, Annalisa et al. (July 2013). "Combining clustering and abundances of galaxy clusters to test cosmology and primordial non-Gaussianity". In: *Monthly Notices of the Royal Astronomical Society* 434.1, pp. 684–695. ISSN: 0035-8711. DOI: 10.1093/mnras/stt1062. eprint: https://academic.oup.com/mnras/article-pdf/434/1/684/18495961/stt1062.pdf. URL: https://doi.org/10.1093/mnras/stt1062.

Margalef-Bentabol, Berta et al. (Sept. 2016). "The formation of bulges, discs and two-component galaxies in the CANDELS Survey at z< 3". In: 461.3, p. 2728. DOI: 10.1093/mnras/stw1451. arXiv: 1606.07405 [astro-ph.GA].

Marleau, Francine R., Dominic Clancy, and Matteo Bianconi (Sept. 2013). "The ubiquity of supermassive black holes in the Hubble sequence". In: *Monthly Notices of the Royal Astronomical Society* 435.4, pp. 3085–3095. ISSN: 0035-8711. DOI: 10.1093/mnras/stt1503. eprint: https://academic.oup.com/mnras/article-pdf/435/4/3085/3412143/stt1503.pdf. URL: https://doi.org/10.1093/mnras/stt1503.

McDonald, M. et al. (2016). "STAR-FORMING BRIGHTEST CLUSTER GALAXIES AT 0.25 <z< 1.25: A TRANSITIONING FUEL SUPPLY". In: *The Astrophysical Journal* 817.2, p. 86. ISSN: 1538-4357. DOI: 10.3847/0004-637x/817/2/86. URL: http://dx.doi.org/10.3847/0004-637X/817/2/86.

Melnick, J. et al. (Nov. 2012). "Intergalactic stellar populations in intermediate redshift clusters". In: 427.1, pp. 850–858. DOI: 10.1111/j.1365-2966.2012.21924.x. arXiv: 1207.6394 [astro-ph.CO].

Menci, N. et al. (2005). "Bimodal Color Distribution in Hierarchical Galaxy Formation". In: *The Astrophysical Journal* 632.1, pp. 49–57. DOI: 10.1086/432788. URL: https://doi.org/10.1086/432788.

Mihos, J. Christopher et al. (Sept. 2005). "Diffuse Light in the Virgo Cluster". In: 631.1, pp. L41–L44. DOI: 10.1086/497030. arXiv: astro-ph/0508217 [astro-ph].

Morgan, W. W. and Janet Rountree Lesh (Nov. 1965). "The Supergiant Galaxies." In: 142, p. 1364. DOI: 10.1086/148422.

Morton, Ben, Sadegh Khochfar, and Jose Oñorbe (Mar. 2021). "Gaseous Dynamical Friction: A Challenge to Modern Hydrodynamical Schemes". In: *arXiv e-prints*, arXiv:2103.15848, arXiv:2103.15848. arXiv: 2103.15848 [astro-ph.GA].

Murphy, Jeremy D., Karl Gebhardt, and Mason Cradit (Apr. 2014). "The Rising Stellar Velocity Dispersion of M87 from Integrated Starlight". In: 785.2, 143, p. 143. DOI: 10.1088/0004-637X/785/2/143. arXiv: 1403.1581 [astro-ph.GA].

Nair, Preethi B. and Roberto G. Abraham (2010). "ON THE FRACTION OF BARRED SPIRAL GALAXIES". In: *The Astrophysical Journal* 714.2, pp. L260–L264. DOI: 10.1088/2041-8205/714/2/l260. URL: https://doi.org/10.1088/2041-8205/714/2/l260.

Oemler A., Jr. (Nov. 1976). "The structure of elliptical and cD galaxies." In: 209, pp. 693–709. DOI: 10.1086/154769.

Oemler Augustus, Jr. (Nov. 1974). "The Systematic Properties of Clusters of Galaxies. Photometry of 15 Clusters". In: 194, pp. 1–20. DOI: 10.1086/153216.

Patel, P. et al. (2006). "An imaging survey of a uniform sample of brightest cluster galaxies and intracluster light". In: *Monthly Notices of the Royal Astronomical Society* 370.2, p. 851. ISSN: 1365-2966. DOI: 10.1111/j.1365-2966.2006.10510.x. URL: http://dx.doi.org/10.1111/j.1365-2966.2006.10510.x.

Peng, Chien Y et al. (2002). "Detailed structural decomposition of galaxy images". In: *The Astronomical Journal* 124.1, p. 266.

Plummer, H. C. (Mar. 1911). "On the problem of distribution in globular star clusters". In: 71, pp. 460–470. DOI: 10.1093/mnras/71.5.460.

Pointecouteau (2020). "The Sunyaev-Zeldovich effect from clusters of galaxies". In: *EPJ Web Conf.* 228, p. 00020. DOI: 10.1051/epjconf/202022800020. URL: https://doi.org/10.1051/epjconf/202022800020.

Ponman, T. J. et al. (June 1994). "A possible fossil galaxy group". In: 369.6480, pp. 462–464. DOI: 10.1038/369462a0.

Press, William H. and Paul Schechter (Feb. 1974). "Formation of Galaxies and Clusters of Galaxies by Self-Similar Gravitational Condensation". In: 187, pp. 425–438. DOI: 10.1086/152650.

Rindler, W. (Dec. 1956). "Visual Horizons in World Models". In: *Monthly Notices of the Royal Astronomical Society* 116.6, pp. 662–677. ISSN: 0035-8711. DOI: 10.1093/mnras/116.6.662. eprint: https://academic.oup.com/mnras/article-pdf/116/6/662/8077949/mnras116-0662.pdf. URL: https://doi.org/10.1093/mnras/116.6.662.

Rood, Herbert J. et al. (Aug. 1972). "The Structure of the Coma Cluster of Galaxies". In: 175, p. 627. DOI: 10.1086/151585.

Rosito et al. (2021). "The role of AGN feedback in the structure, kinematics, and evolution of ETGs in Horizon simulations". In: *A&A* 652, A44. DOI: 10.1051/0004-6361/202039976. URL: https://doi.org/10.1051/0004-6361/202039976.

Rudick, Craig S., J. Christopher Mihos, and Cameron K. McBride (2011). "THE QUANTITY OF INTRACLUSTER LIGHT: COMPARING THEORETICAL AND OBSERVATIONAL MEASUREMENT TECHNIQUES USING SIMULATED CLUSTERS". In: *The Astrophysical Journal* 732.1,

p. 48. DOI: 10.1088/0004-637x/732/1/48. URL: https://doi.org/10.1088/0004-637x/732/1/48.

Sarazin, Craig L. (Jan. 1986). "X-ray emission from clusters of galaxies". In: *Reviews of Modern Physics* 58.1, pp. 1–115. DOI: 10.1103/RevModPhys.58.1.

Sarron, F. et al. (May 2018). "Evolution of the cluster optical galaxy luminosity function in the CFHTLS: breaking the degeneracy between mass and redshift". In: 613, A67, A67. DOI: 10.1051/0004-6361/201731981. arXiv: 1712.09481 [astro-ph.GA].

Schechter, P. (Jan. 1976). "An analytic expression for the luminosity function for galaxies." In: 203, pp. 297–306. DOI: 10.1086/154079.

Schechter, P. L. (July 1980). "Mass-to-light ratios for elliptical galaxies." In: 85, pp. 801–811. DOI: 10.1086/112742.

Schneider, Peter (2006). *Extragalactic Astronomy and Cosmology*. Berlin, Heidelberg: Springer Berlin Heidelberg. ISBN: 978-3-540-33174-2. DOI: 10.1007/978-3-540-33175-9. URL: http://dx.doi.org/10.1007/978-3-540-33175-9.

Schombert, J. M. (Mar. 1986). "The Structure of Brightest Cluster Members. I. Surface Photometry". In: 60, p. 603. DOI: 10.1086/191100.

Sérsic, J. L. (Feb. 1963). "Influence of the atmospheric and instrumental dispersion on the brightness distribution in a galaxy". In: *Boletin de la Asociacion Argentina de Astronomia La Plata Argentina* 6, pp. 41–43.

Smith, Britton D et al. (Aug. 2018). "The growth of black holes from Population III remnants in the Renaissance simulations". In: *Monthly Notices of the Royal Astronomical Society* 480.3, pp. 3762–3773. ISSN: 0035-8711. DOI: 10.1093/mnras/sty2103. eprint: https://academic.oup.com/mnras/article-pdf/480/3/3762/25520194/sty2103.pdf. URL: https://doi.org/10.1093/mnras/sty2103.

Sobral, David et al. (Apr. 2015). "MC2: boosted AGN and star formation activity in CIZA J2242.8+5301, a massive post-merger cluster at z = 0.19". In: *Monthly Notices of the Royal Astronomical Society* 450.1, pp. 630–645. ISSN: 0035-8711. DOI: 10.1093/mnras/stv521. eprint: https://academic.oup.com/mnras/article-pdf/450/1/630/18509547/stv521.pdf. URL: https://doi.org/10.1093/mnras/stv521.

Spiniello, C. et al. (June 2018). "The Fornax Cluster VLT Spectroscopic Survey II - Planetary Nebulae kinematics within 200 kpc of the cluster core". In: 477.2, pp. 1880–1892. DOI: 10.1093/mnras/sty663. arXiv: 1803.03276 [astro-ph.GA].

Spitzer Lyman, Jr. and Walter Baade (Mar. 1951). "Stellar Populations and Collisions of Galaxies." In: 113, p. 413. DOI: 10.1086/145406.

Stott, J. P. et al. (2011). "Little change in the sizes of the most massive galaxies since z = 1". In: *Monthly Notices of the Royal Astronomical Society* 414.1, p. 445. ISSN: 0035-8711. DOI: 10.1111/j.1365-2966.2011.18404.x. URL: http://dx.doi.org/10.1111/j.1365-2966.2011.18404.x.

Stroe, Andra et al. (Apr. 2015). "The rise and fall of star formation in z 0.2 merging galaxy clusters". In: *Monthly Notices of the Royal Astronomical Society* 450.1, pp. 646–665. ISSN: 0035-8711. DOI: 10.1093/mnras/stu2519. eprint: https://academic.oup.com/mnras/article-pdf/450/1/646/18507380/stu2519.pdf. URL: https://doi.org/10.1093/mnras/stu2519.

Sunyaev, R. A. and Ya. B. Zeldovich (Apr. 1970). "Small-Scale Fluctuations of Relic Radiation". In: 7.1, pp. 3–19. DOI: 10.1007/BF00653471.

Thomas, Daniel et al. (May 2010). "Environment and self-regulation in galaxy formation". In: *Monthly Notices of the Royal Astronomical Society* 404.4, p. 1775. ISSN: 0035-8711. DOI: 10.1111/j.1365-2966.2010.16427.x. eprint: https://academic.oup.com/mnras/article-pdf/404/4/1775/3777097/mnras0404-1775.pdf. URL: https://doi.org/10.1111/j.1365-2966.2010.16427.x.

Toledo, I. et al. (June 2011). "Diffuse intracluster light at intermediate redshifts: intracluster light observations in an X-ray cluster at z= 0.29". In: 414.1, pp. 602–614. DOI: 10.1111/j.1365-2966.2011.18423.x. arXiv: 1101.5497 [astro-ph.CO].

Toomre, Alar (Jan. 1977). "Mergers and Some Consequences". In: *Evolution of Galaxies and Stellar Populations*. Ed. by Beatrice M. Tinsley and D. Campbell Larson Richard B. Gehret, p. 401.

Tremaine, Scott D. and Douglas O. Richstone (Mar. 1977). "A test of a statistical model for the luminosities of bright cluster galaxies". In: 212, pp. 311–316. DOI: 10.1086/155049.

van der Burg et al. (2014). "A census of stellar mass in ten massive haloes at z 1 from the GCLASS Survey". In: *A&A* 561, A79. DOI: 10.1051/0004-6361/201322771. URL: https://doi.org/10.1051/0004-6361/201322771.

Ventimiglia, G. et al. (Sept. 2010). "The dynamically hot stellar halo around NGC 3311: a small cluster-dominated central galaxy". In: 520, L9, p. L9. DOI: 10.1051/0004-6361/201015485. arXiv: 1009.3281 [astro-ph.CO].

Vera, Alonso, and Coldwell (2016). "Effect of bars on the galaxy properties". In: *A&A* 595, A63. DOI: 10.1051/0004-6361/201628750. URL: https://doi.org/10.1051/0004-6361/201628750.

von Benda-Beckmann, Alexander M. et al. (June 2008). "The fossil phase in the life of a galaxy group". In: 386.4, pp. 2345–2352. DOI: 10.1111/j.1365-2966.2008.13221.x. arXiv: 0710.1297 [astro-ph].

Weinberger, Rainer et al. (Mar. 2017). "Simulating galaxy formation with black hole driven thermal and kinetic feedback". In: 465.3, pp. 3291–3308. DOI: 10.1093/mnras/stw2944. arXiv: 1607.03486 [astro-ph.GA].

West, Michael J. et al. (July 2017). "Ten billion years of brightest cluster galaxy alignments". In: *Nature Astronomy* 1, 0157, p. 0157. DOI: 10.1038/s41550-017-0157. arXiv: 1706.03798 [astro-ph.GA].

Whiley, I. M. et al. (2008). "The evolution of the brightest cluster galaxies sincez 1 from the ESO Distant Cluster Survey (EDisCS)". In: *Monthly Notices of the Royal Astronomical Society* 387.3, p. 1253. ISSN: 1365-2966. DOI: 10.1111/j.1365-2966.2008.13324.x. URL: http://dx.doi.org/10.1111/j.1365-2966.2008.13324.x.

Wilkinson, David M. et al. (Dec. 2017). "FIREFLY (Fitting IteRativEly For Likelihood analYsis): a full spectral fitting code". In: 472.4, pp. 4297–4326. DOI: 10.1093/mnras/stx2215. arXiv: 1711.00865 [astro-ph.GA].

Zarattini, S. et al. (Aug. 2022). "Fossil group origins XII. Large-scale environment around fossil systems". In: *arXiv e-prints*, arXiv:2208.13784, arXiv:2208.13784. arXiv: 2208.13784 [astro-ph.GA].

Zhang, Y. et al. (2016). "GALAXIES IN X-RAY SELECTED CLUSTERS AND GROUPS IN DARK ENERGY SURVEY DATA. I. STELLAR MASS GROWTH OF BRIGHT CENTRAL GALAXIES SINCEz 1.2". In: *The Astrophysical Journal* 816.2, p. 98. ISSN: 1538-4357. DOI: 10.3847/0004-637x/816/2/98. URL: http://dx.doi.org/10.3847/0004-637X/816/2/98.

Zwicky, F. (Oct. 1937). "On the Masses of Nebulae and of Clusters of Nebulae". In: 86, p. 217. DOI: 10.1086/143864.

Zwicky, F. (Jan. 2009). "Republication of: The redshift of extragalactic nebulae". In: *General Relativity and Gravitation* 41.1, pp. 207–224. DOI: 10.1007/s10714-008-0707-4.

Zwicky, F. et al. (1961). *Catalogue of galaxies and of clusters of galaxies, Vol. I*.